

*Now this is not the end. It is not even the beginning of the end.
But it is, perhaps, the end of the beginning.*

Winston Churchill

University of Alberta

**LiDAR assisted mapping and deformation history of Crowsnest Pass,
Alberta**

by

Sharlene Erin Hartman

A thesis submitted to the Faculty of Graduate Studies and Research
in partial fulfillment of the requirements for the degree of

Master of Science

Department of Earth and Atmospheric Sciences

©Sharlene Erin Hartman

Fall 2013

Edmonton, Alberta

Permission is hereby granted to the University of Alberta Libraries to reproduce single copies of this thesis and to lend or sell such copies for private, scholarly or scientific research purposes only. Where the thesis is converted to, or otherwise made available in digital form, the University of Alberta will advise potential users of the thesis of these terms.

The author reserves all other publication and other rights in association with the copyright in the thesis and, except as herein before provided, neither the thesis nor any substantial portion thereof may be printed or otherwise reproduced in any material form whatsoever without the author's prior written permission.

Abstract

The Crowsnest Pass area, located in the Rocky Mountain foothills of the Canadian Cordillera, provides an exceptional example of a thin-skinned thrust belt from which the deformational history can be determined. Use of LiDAR (light detection and ranging) data, acquired by high-resolution remote sensing, increased both area covered in the field and accuracy. An anticline cored by Paleozoic carbonate rocks in the hanging wall of the Turtle Mountain thrust, established from a revised geological map and cross-sections, is a fault-propagation fold. Strain analysis, by both Fry and calcite strain gauge methods, shows that deformation was heterogeneous and involved volume loss. The kinematic model that best matches the deformational history of the fold involves both volume loss and deformation along a thrust that was initially localized at one or more nucleation segments and then propagated through adjoining layers.

Acknowledgements

I would like to express my deepest appreciation to Dr. John Waldron, my thesis supervisor, whose contribution in stimulating suggestions and encouragement helped me to complete my project especially in writing this report. Both his enthusiasm and knowledge in structural geology have been both an inspiration and aspiration.

Furthermore I would also like to acknowledge with much appreciation those who helped me in the field, such as Morgan Snyder, David Herbers, Tiffany Miller and Maryam Dzulkefli. A special thanks goes to those from the department that helped me with technical support, Mark Labbe, David Pirie, Martin Von Dollen, Valery Companiytsev, George Braybrook, Nathan Gerein, Marvin Wadsworth, Christopher Lough and Igor Jakab. Many thanks go to Corey Froese, Dinu Pană, Rastislav Elgr and the Alberta Geological Survey who gave me both financial support and made available data for the area. I want to thank NSERC for financial support, and the Earth and Atmospheric Department for support in the form of teaching and research assistantship. I have to appreciate the software made available by both Midland Valley Exploration and Pangea Software.

Lastly I would like to thank my many friends and family who have helped me stay sane through these difficult years. Most importantly, none of this would have been possible without the love and patience of my family. My parents who have been a constant source of love, concern, support and strength all these years. I would like to express my heart-felt gratitude to my fiancé, Les, who gave me unconditional love, inspiration, support and understanding.

Table of Contents

Chapter 1: Introduction	1
1.1 Previous Work	3
1.2 Stratigraphy	15
1.2.1 Palliser Formation	15
1.2.2 Banff Formation	15
1.2.3 Rundle Group	17
1.2.4 Tobermory Formation	20
1.2.5 Fernie Formation	20
1.2.6 Kootenay Group	22
1.2.7 Blairmore Group	22
1.2.8 Alberta Group	28
1.2.9 Belly River Group	30
1.3 Methods	30
1.4 Presentation and Main Objectives	31
1.5 References	32
Chapter 2: Structure of the Rocky Mountain Thrust Belt in the Crowsnest Pass Area using LiDAR Interpretive Mapping	39
2.1 Introduction	39
2.1.1 Previous Geological Work	42
2.1.2 LiDAR in Structural Geology	43
2.2 Data for the Crowsnest Pass Area	44
2.2.1 Data Collection and Processing	45
2.2.2 Data Interpretation and Geological Map Production	47
2.2.3 Data Collection, Processing, and Interpretation for the Cross-Section Construction	47
2.3 Geological Map and Cross-section of the Crowsnest Pass Area	54
2.3.1 Structures	54
2.3.2 Cross-sections Structure	61
2.4 Discussion	65
2.4.1 Advantages of LiDAR Assisted Mapping Technique	65
2.4.2 Geometry, Kinematics and Dynamics of the Thrusts and Folds	67
2.5 Conclusions	74
2.6 References	76
Chapter 3: Kinematic development of a thrust-related fold in the Rocky Mountain foothills, Crowsnest Pass, Alberta	81
3.1 Introduction	81
3.2 Kinematic Models of Folds Related to Thrusting	85
3.2.1 Fault-Bend Folds	87
3.2.2 Detachment Folds	90
3.2.3 Fault-Propagation Folds	94
3.3 Data Collection and Strain Analysis	102
3.3.1 Fry Method	102

3.3.2	Calcite Strain Gauge Method	108
3.3.3	Strain Ellipsoid Construction	113
3.3.4	Comparing Fry and Calcite Strain Gauge Results	114
3.4	Strain Analysis Results	114
3.4.1	Fry Method	114
3.4.2	Calcite Strain Gauge Method	120
3.4.3	Comparing the Strains	124
3.5	Discussion: Deformation History of the Fold	124
3.5.1	Discussion of Strain Comparisons	124
3.5.2	Comparing Rock Strain to Predictions of Kinematic Models	126
3.6	Conclusions	130
3.7	References	131
	Chapter 4: Conclusions	135
	Appendix A: Well Locations	140
	Appendix B: Field Data	141
	Appendix C: Bedding orientations determined by remote sensing	152
	Appendix D: Strain analysis by Fry method	154
	Appendix E: Calcite strain gauge data	164

List of Tables

Table 3-1:	Table of fold models and their literature references.	86
Table 3-2:	Table of symbols	89
Table 3-3:	The bulk strain ellipses determined from the Fry plots, their errors and the strain ellipsoids.	116
Table 3-4:	Equal volume intra-crystalline strain ellipsoid and errors, determined using the calcite strain gauge method.	121

List of Figures

Figure 1-1: Regional map of the study area.	2
Figure 1-2: Geological map of the Crowsnest Pass area, after MacKay (1933).	4
Figure 1-3: Geological map the Crowsnest Pass area, after Price (1962).	6
Figure 1-4: Geological map of the Crowsnest Pass area, after Norris (1993).	8
Figure 1-5: Geological map of the Grassy Mountain area, after Norris (1994).	12
Figure 1-6: Geological map of the Livingstone Range, after Cooley et al. (2011a).	14
Figure 1-7: Stratigraphic column for the Crowsnest Pass area.	16
Figure 1-8: Massive skeletal limestone of the Livingstone Formation.	18
Figure 1-9: Oolitic limestone of the Baril Formation.	18
Figure 1-10: Mixed skeletal lime packstone and wackestone of the Carnarvon member.	21
Figure 1-11: Fine grained sandstone of the Todhunter member.	21
Figure 1-12: Thickened Number Two coal seam of the Kootenay Group.	24
Figure 1-13: Quartz and chert conglomerate of the Cadomin Formation.	24
Figure 1-14: Quartz sandstone beds of the Dalhousie Formation.	25
Figure 1-15: Exotic volcanic pebble conglomerate beds in the Beaver Mines Formation.	25
Figure 1-16: Cross-bedded sandstone beds of the Mill Creek Formation.	27
Figure 1-17: Porphyritic volcanic unit in the Crowsnest Formation.	27
Figure 1-18: Stratified volcanic breccia of the Crowsnest Formation.	29

Figure 1-19: Well cemented coarse-grained sandstone of the Cardium Formation.	29
Figure 2-1: Regional map of the study area.	40
Figure 2-2: Stratigraphic column for the Crowsnest Pass area.	41
Figure 2-3: Geological map of the Crowsnest Pass area.	pocket
Figure 2-4: Waypoints with 100 m topographic contours.	pocket
Figure 2-5: Hill-shade LiDAR imagery and traced lineaments.	pocket
Figure 2-6: Orientations determined using the computer program Orion.	46
Figure 2-7: Hill-shaded LiDAR imagery showing features associated with stratigraphic units.	48
Figure 2-8: Cross-section from A-A' of the Crowsnest Pass area.	50
Figure 2-9: Cross-section from B-B' of the Crowsnest Pass area.	51
Figure 2-10: Cross-section from C-C' of the Crowsnest Pass area.	52
Figure 2-11: Restored east-west cross-sections for the Crowsnest Pass area.	53
Figure 2-12: Axial projection showing present day geology on Grassy Mountain.	58
Figure 2-13: Three fold types associated with thrust belts and one modified fold type.	60
Figure 2-14: Stereoplot of poles to bedding and mean fold axis.	62
Figure 2-15: Map showing the location of the McConnell thrust trace.	70
Figure 2-16: Block diagram of north end of Bluff Mountain.	72
Figure 3-1: Geological map of the Turtle Mountain area.	82
Figure 3-2: Stratigraphic column for the Crowsnest Pass area.	84
Figure 3-3: Three general fold types associated with thrust belts.	86
Figure 3-4: Fault-bend fold in the southern Appalachians.	88

Figure 3-5: Kinematic models of fault-bend folds proposed in the literature.	88
Figure 3-6: Kinematic models of detachment folds proposed in the literature.	91
Figure 3-7: Detachment fold in the Jura Mountains.	92
Figure 3-8: Kinematic models of fault-propagation folds proposed in the literature.	95
Figure 3-9: Fault-propagation fold in the Turner Valley Structure.	99
Figure 3-10: The direction on the fold of the three orientated thin sections cut from each sample.	103
Figure 3-11: Plotting of a Fry plot.	105
Figure 3-12: Fry plot for thin section ML025A on the profile plane.	105
Figure 3-13: Photomicrograph of thin section ML024A.	107
Figure 3-14: The error for ϕ .	109
Figure 3-15: Most favourably oriented stress axes to produce twinning.	110
Figure 3-16: SEM image showing location of twin where thickness was measured.	112
Figure 3-17: Stereoplot of poles to bedding and mean fold axis.	115
Figure 3-18: The bulk strain ellipses, determined from the equal area Fry plot ellipsoids.	117
Figure 3-19: The bulk strain ellipses, determined assuming no orogen-parallel extension.	118
Figure 3-20: Flinn plot of the Fry method strain ellipsoids.	119
Figure 3-21: The intra-crystalline strain ellipses, determined from the equal area calcite strain gauge ellipsoids.	122
Figure 3-22: Flinn plot of the calcite strain gauge method strain ellipsoids	123

Chapter 1: Introduction

The Rocky Mountain foothills form the eastern margin of the Canadian Cordilleran foreland belt. The foreland belt is a thin-skinned thrust belt that developed between the Late Jurassic and Early Eocene. This was associated with the accretion of a tectonic collage of allochthonous oceanic terranes due to plate motions in the Pacific realm to the west (Price, 1994). The direction of thrust transport is predominately west to east, and progressively lower thrusts, closer to the foreland, generally developed later than higher thrusts near the hinterland (Price, 1994). Crowsnest Pass is located in the Rocky Mountain foothills of the Canadian Cordillera in southern Alberta (Fig. 1-1). A number of studies have focused on the area affected by a catastrophic rock slide, known as the Frank Slide, that took place in 1903 (e.g., Allan, 1931, 1932, 1933; Cruden and Krahn, 1973; Fraser and Gruendig, 1985). The slide came from the forelimb of a well exposed fold, in the hanging wall of the Turtle Mountain thrust. Though there has been extensive research on the rock slide and the related brittle fractures, the earlier history of thrust-related folding is poorly known.

The primary objective of chapter 2 is to determine the deformation history of the Crowsnest Pass area. A revised geological map is constructed using LiDAR (light detection and ranging), a remote sensing technique, along with field observations. Using the revised map, cross-sections were constructed to determine the subsurface structure and to constrain the kinematic history of folding and thrusting. Multiple kinematic models for folds in thrust belts have been proposed in the literature. In chapter 3 two methods of strain analysis are performed on rocks from a fold in the hanging wall of the Turtle Mountain thrust, to determine the bulk and intra-crystalline strain locally in the fold, and to compare actual finite strains with those predicted by the various published models. Understanding the deformation history of the fold in Crowsnest Pass has petroleum implications to

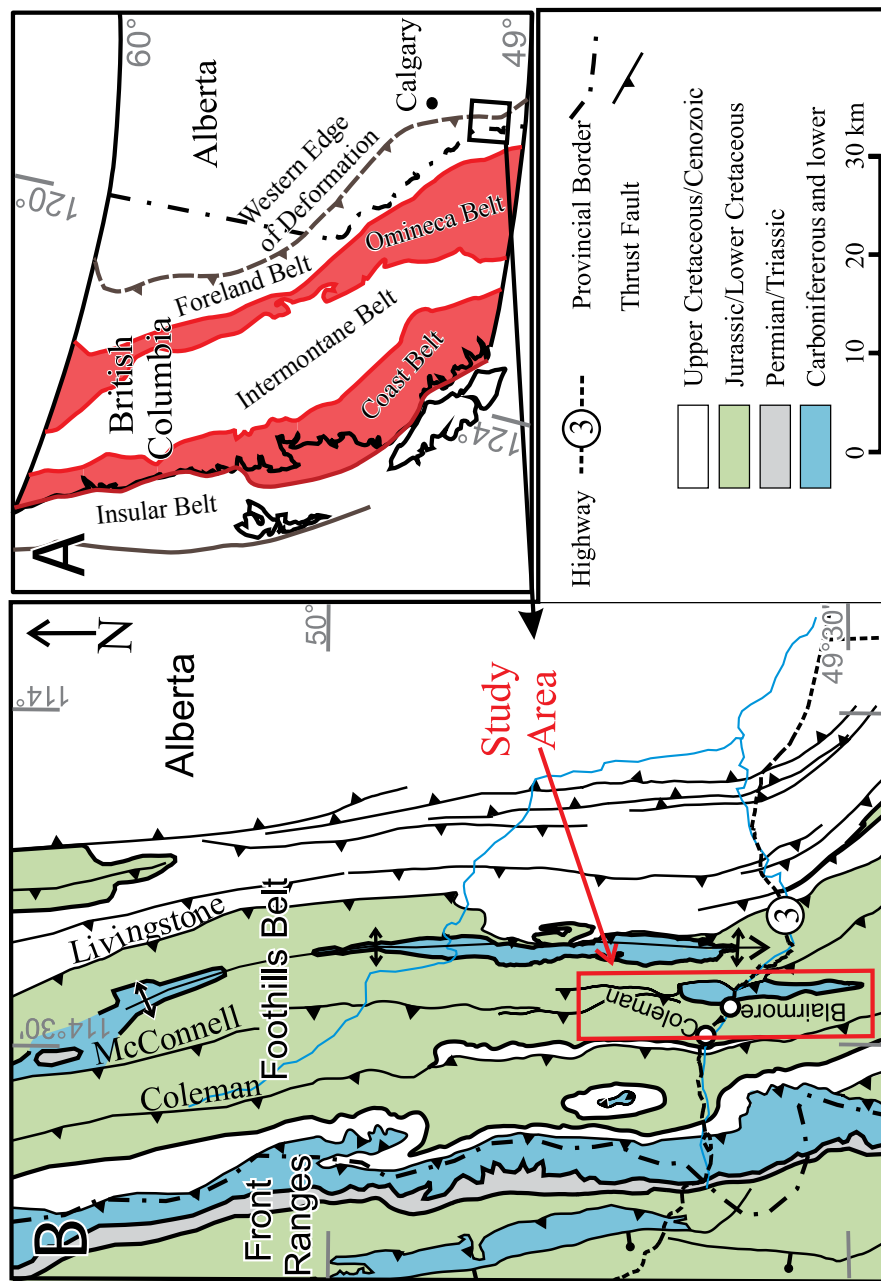


Figure 1-1: Regional map of the study area. (A) Canadian Cordillera map showing belts modified after Wheeler et al., (1991). (B) Regional geological map modified from Cooley et al. (2011a, b).

the Rocky Mountain foothills. The model that best matches the Turtle Mountain fold may potentially be applied to other thrust-related folds in the subsurface. This can improve both subsurface interpretation and location of petroleum reservoirs.

1.1 Previous Work

Following a 1903 catastrophic slope failure (known as the Frank Slide), research in the Crowsnest Pass area was carried out by Allan (1931, 1932, 1933). Subsequent mapping of the study area was carried out by MacKay (1933), Price (1962) and Norris (1955, 1993) (Fig. 1-2, 1-3, 1-4). Larger-scale maps have subsequently been produced for both the Grassy Mountain area (Norris, 1994) and the Livingstone Range (Cooley et al., 2011a; b) (see Fig. 1-5 and 1-6, respectively). Stratigraphic sections through the south end of Bluff Mountain were measured by B.C. Richards in 1997 (in Langenberg et al., 2007). Studies of the slope failure and slope monitoring have also been carried out (e.g., Cruden and Krahn, 1973; Fraser and Gruendig, 1985). Two-dimensional seismic reflection profiles through the area have been used to interpret the structure in the subsurface below the Turtle Mountain anticline (e.g., Begin et al., 1996; Issac and Lawton, 2006). Other work on Turtle Mountain focuses on fractures identified by ground surveying and analysis of digital elevation models (DEMs), and is used for slope monitoring (e.g., Langenberg et al., 2007; Jaboyedoff et al., 2009).

Lasers were invented in the 1950s and their first environmental applications were to detect particles suspended in the atmosphere (Campbell, 2007). LiDAR was developed using laser technology in the 1980s (Campbell, 2007) and its first application to the geosciences took place in the 1990s (e.g., Soeters and van Westen, 1996). The most widespread use of LiDAR in geology has been the mapping of geomorphic features (e.g., Haugerud et al., 2003; Roering, 2008; Notebaert et al., 2009), or recording coastal changes (e.g., Houser

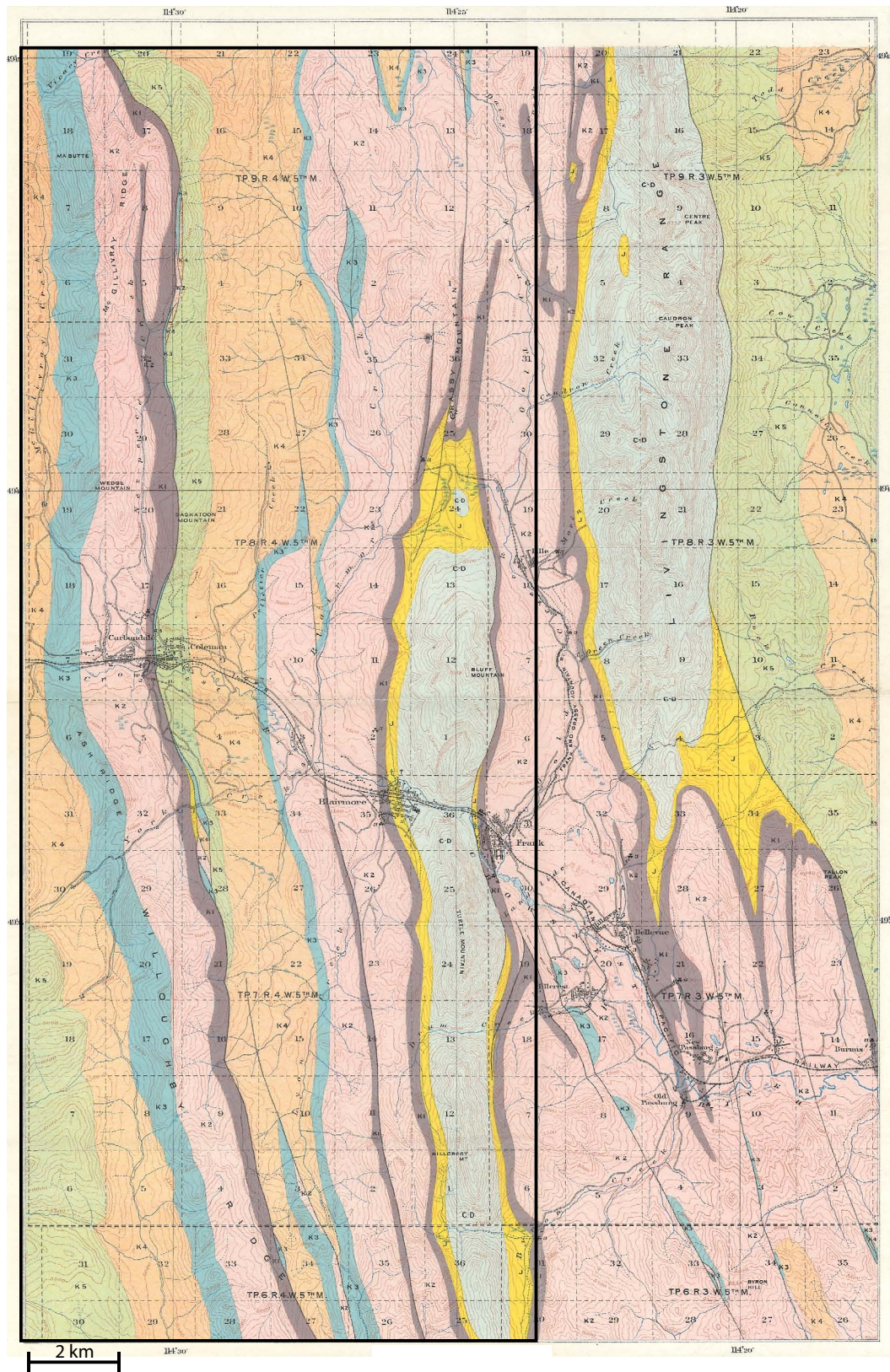


Figure 1-2: Geological map of the Crowsnest Pass area, after MacKay (1933).

Location of study area in the black box.

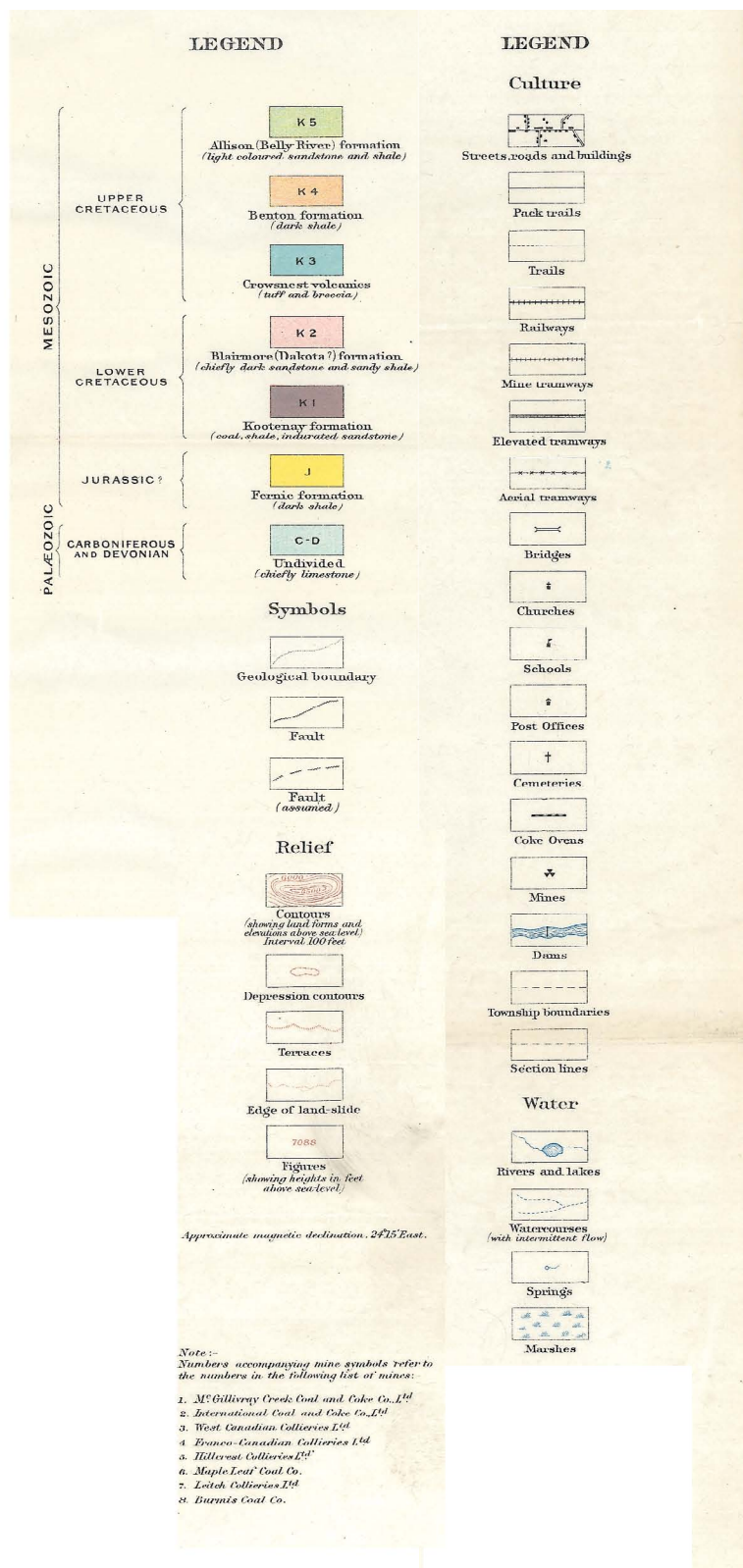


Figure 1-2 (continued): Location and legend to map symbols, after MacKay (1933).

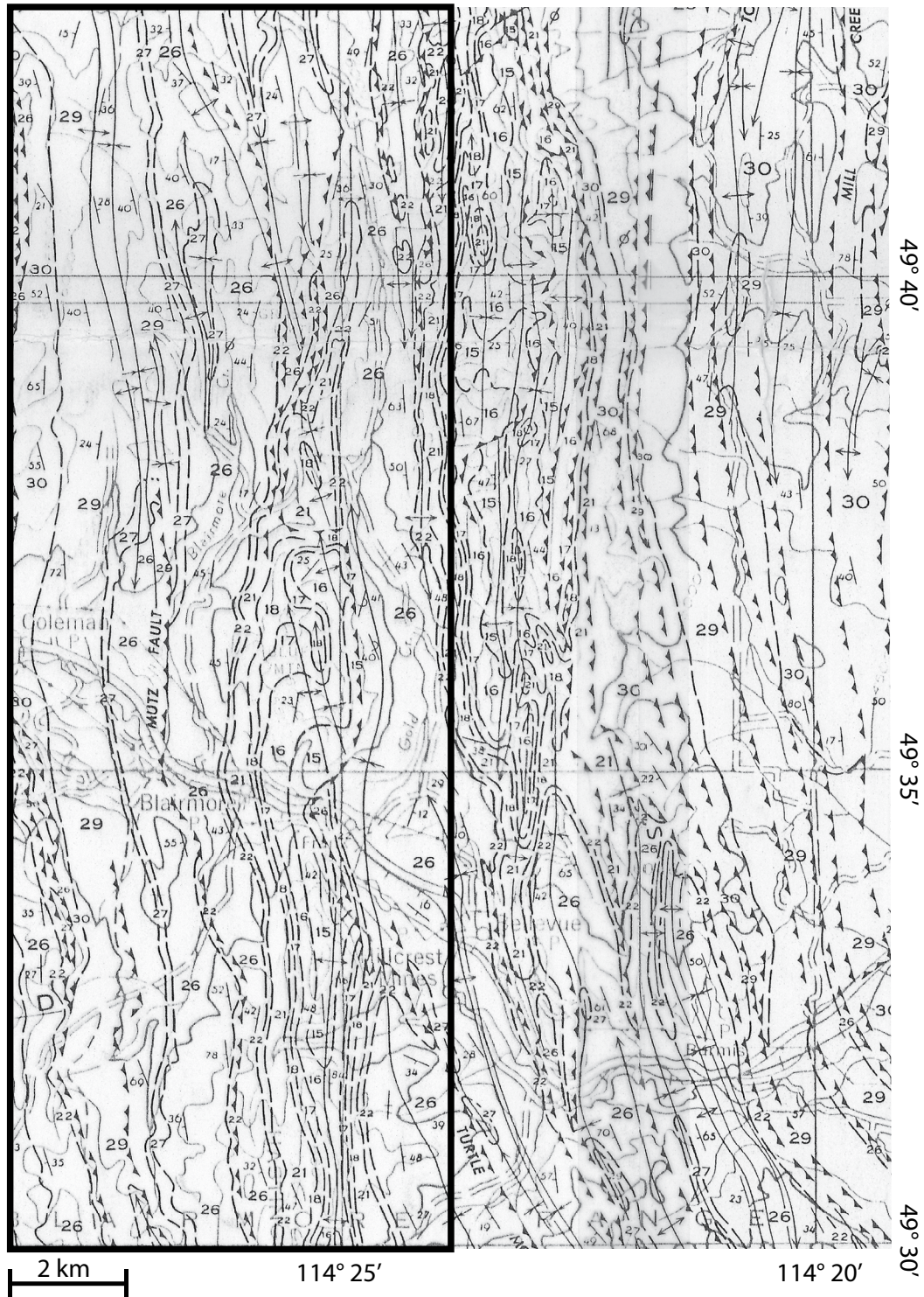


Figure 1-3: Geological map of the Crowsnest Pass area, after Price (1962). Location of study area in the black box.

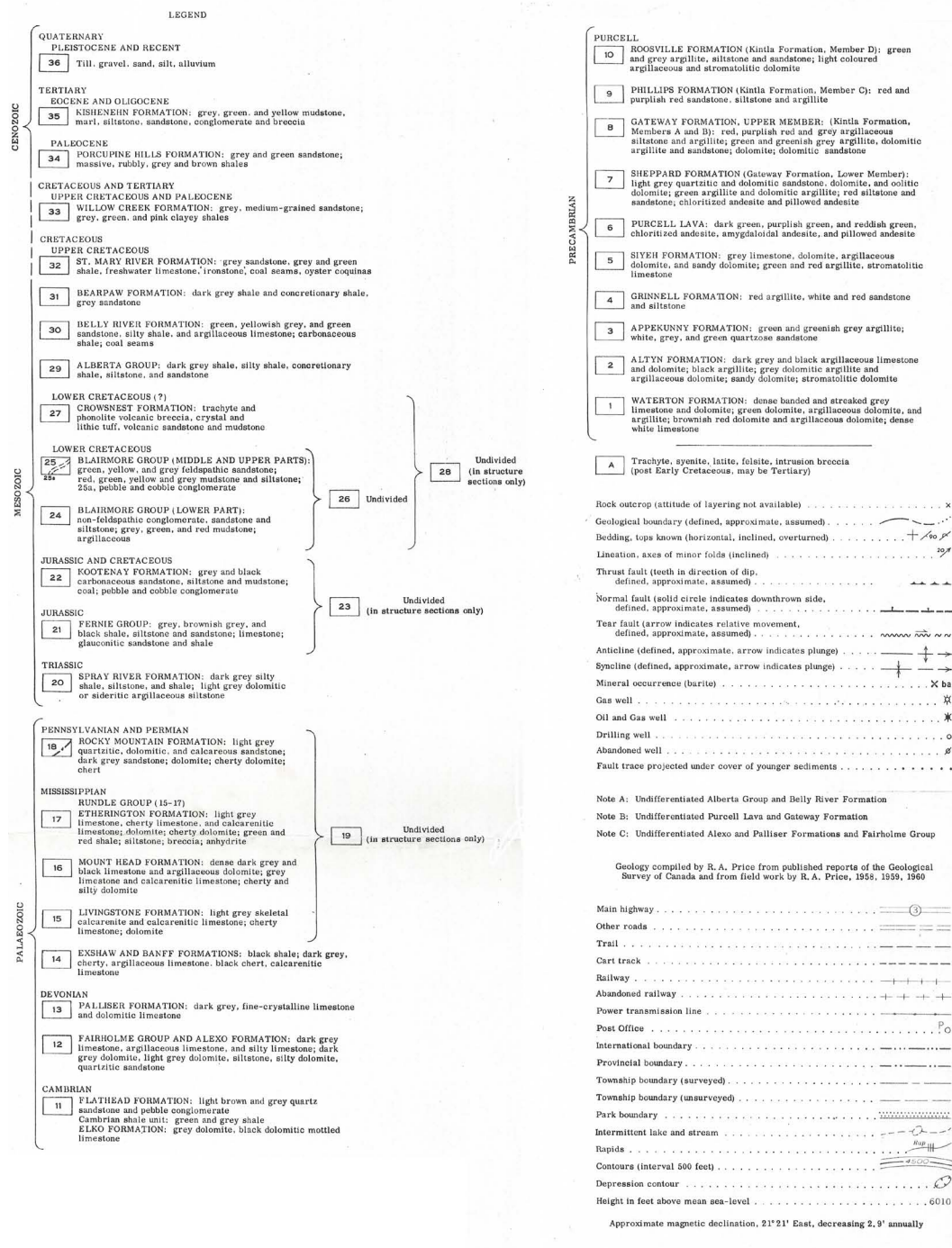


Figure 1-3 (continued): Location and legend to map symbols, after Price (1962).

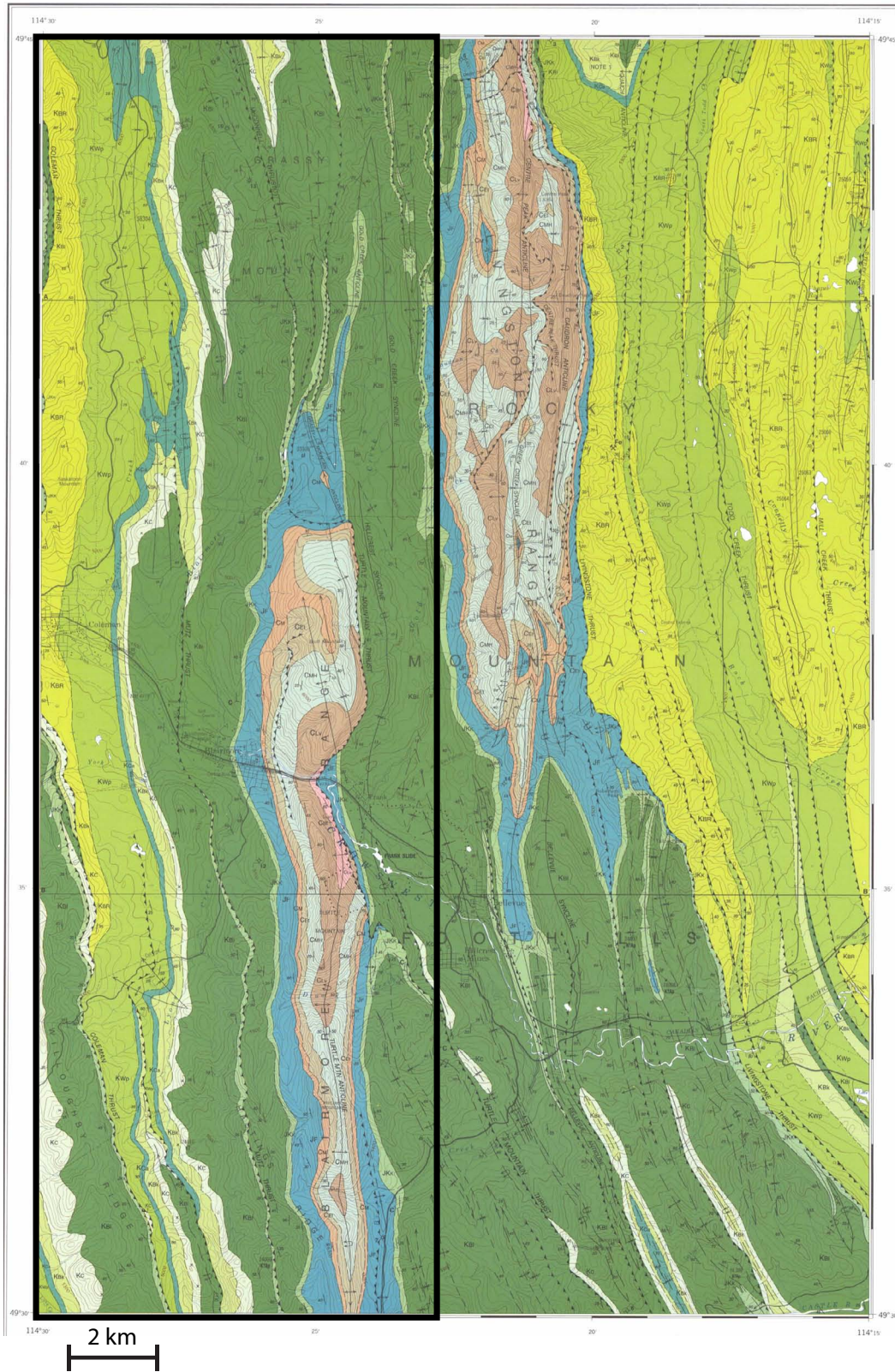


Figure 1-4: Geological map of the Crowsnest Pass area, after Norris (1993). Location of study area in the black box.

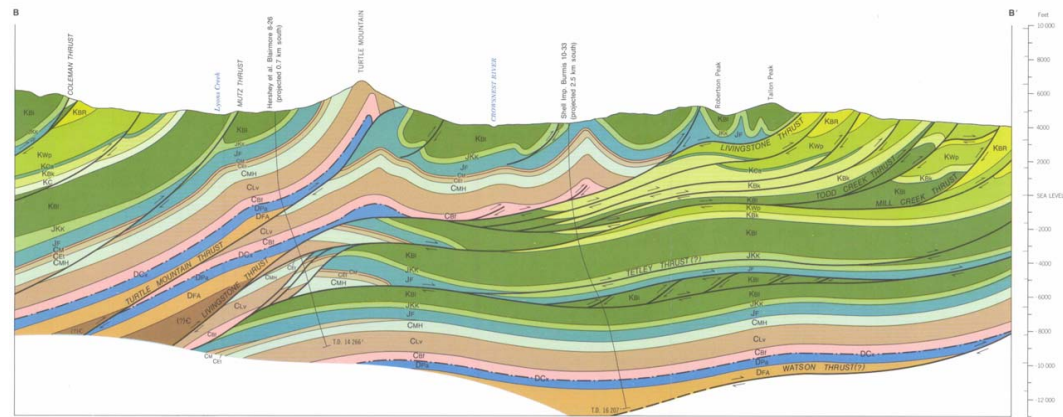


Figure 1-4 (continued): Sections through the Crowsnest Pass area, after Norris (1993). Lines of cross-sections are located on the map. Section A-A' located in the north and B-B' located in the south.

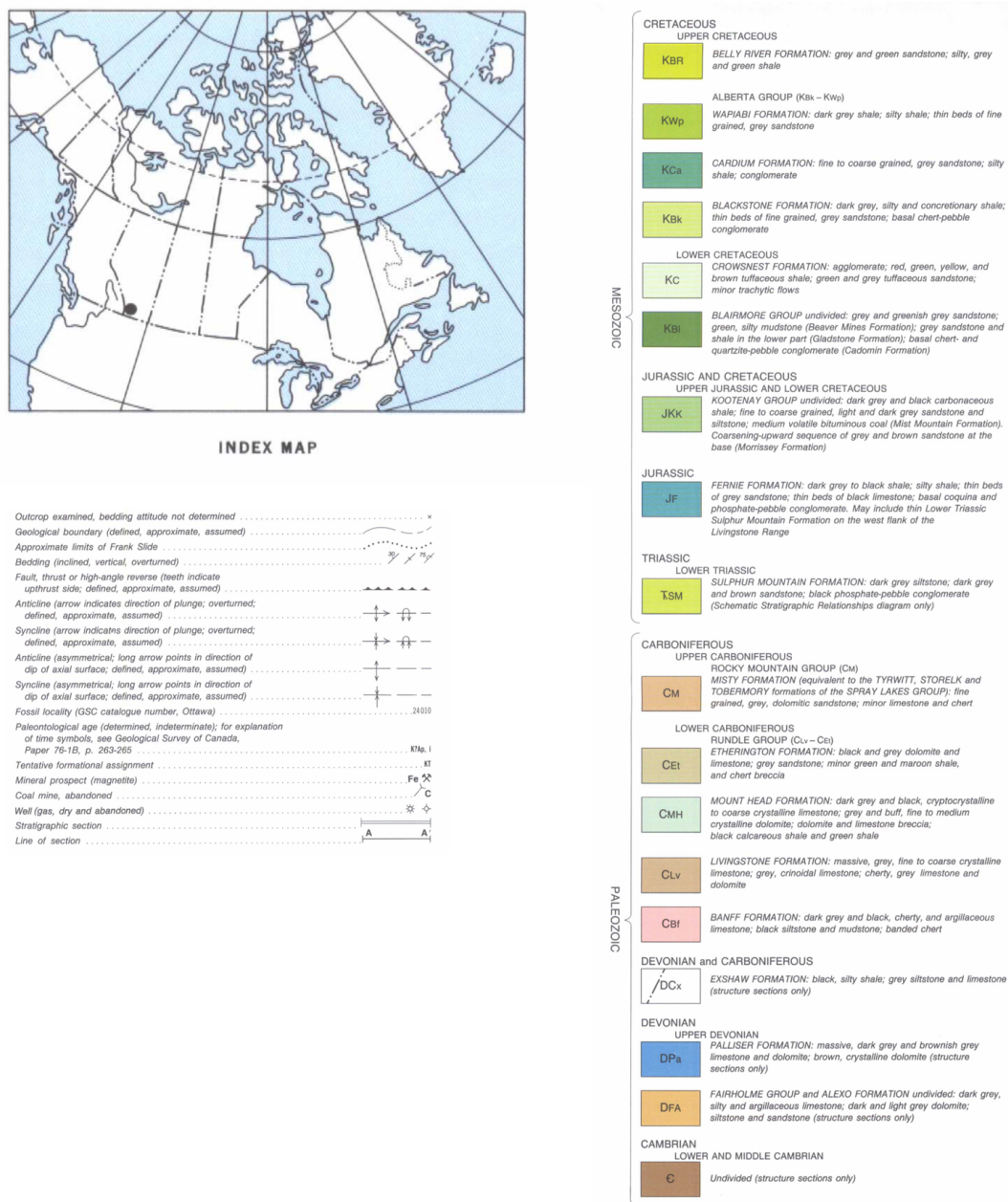


Figure 1-4 (continued): Location and legend to map symbols, after Norris (1993).

et al., 2008). In Alaska, LiDAR-derived topography has been used in areas of poor outcrop to determine bedrock structure (Pavlis and Bruhn, 2011). In the last few years, structural studies based on data from airborne LiDAR have become more popular (e.g., Jaboyedoff et al., 2009; Barth et al., 2012; Grebby et al., 2012; Martinez Torres et al., 2012). LiDAR has been used to gather detailed quantitative data sets on fracture and fold distributions (Pearce et al., 2011).

Air photo stereo-pair have been used to derive three-dimensional data for use in structural geology. Orientation measurements have been made by the use of a DEM derived from the three-dimensional data (Jaboyedoff et al., 2009). COLTOP-3D, a computer program, computed the orientation of each cell of the DEM and showed that there was agreement between remotely measured surfaces and field structure measurements (Jaboyedoff et al., 2009).

Folds that develop in thrust belts have geometries that are related to the slip of the adjacent faults. Kinematic models of fold development have been proposed for different fold geometries found in thrust belts. In many cases, there is disagreement as to which kinematic model better describes an observed fold (Suppe et al., 2004). Kinematic models continue to be added to the literature in efforts to explain observed fold geometries (e.g., Mitra, 1990; Erslev, 1991; Epard and Groshong, 1995; Poblet and McClay, 1996; Mitra, 2003; Tavani et al., 2006; Tavani and Storti, 2011). In many field examples, interpretations are hindered by incomplete knowledge of a fold. In many examples, how a fold develops and which model, if any, more accurately matches its kinematic history have yet to be determined. A simple classification of folds in thrust belts (Suppe, 1983) recognizes three categories: detachment fold, fault-bend fold, and fault-propagation folds (Fig. 3-3). Each model is based on an idealized kinematic process of fold development. The anticline associated with the Turtle Mountain thrust provides an exceptional example of thin-skinned thrust-related folding, in

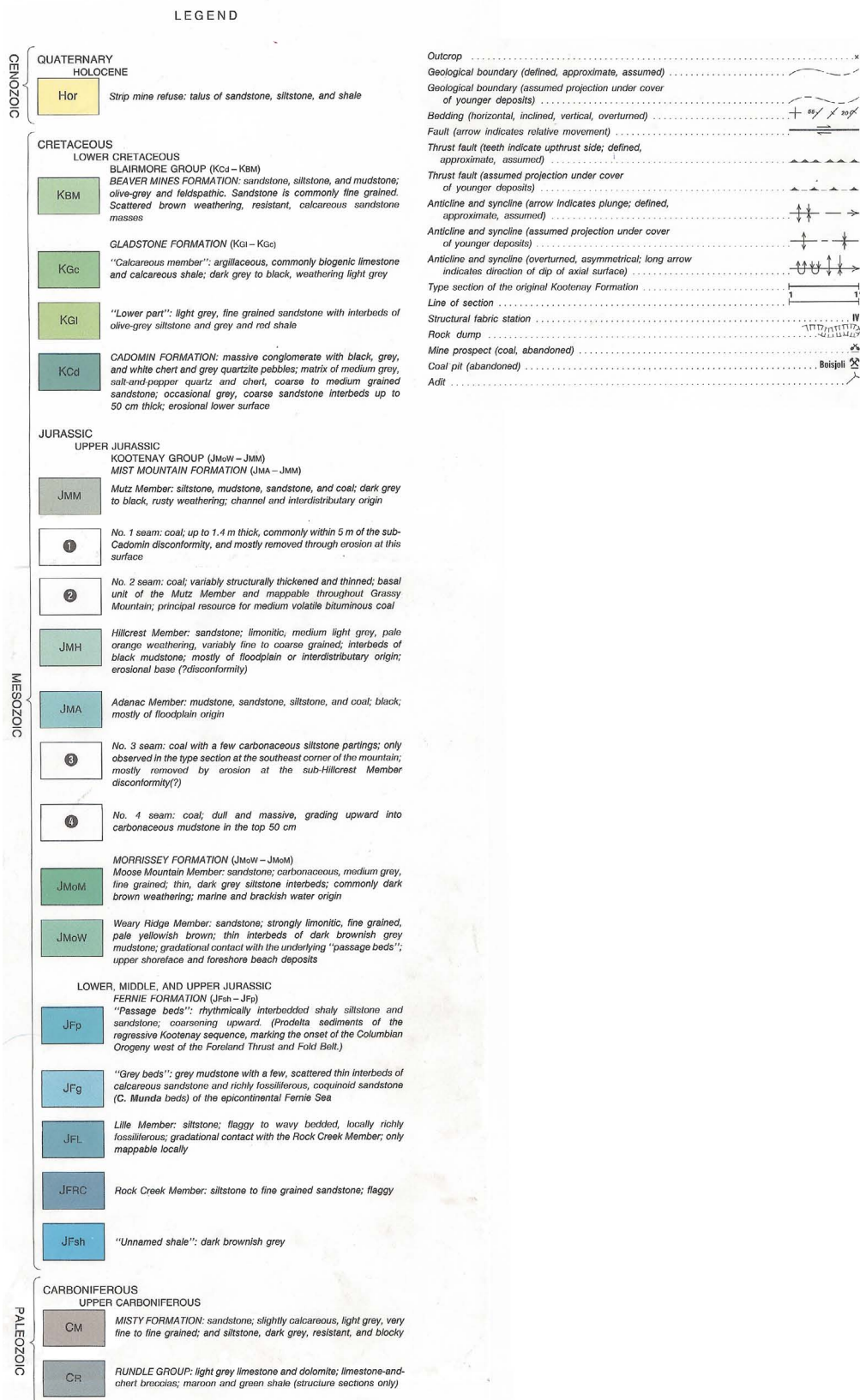


Figure 1-5 (continued): Location and legend to map symbols, after Norris (1994).

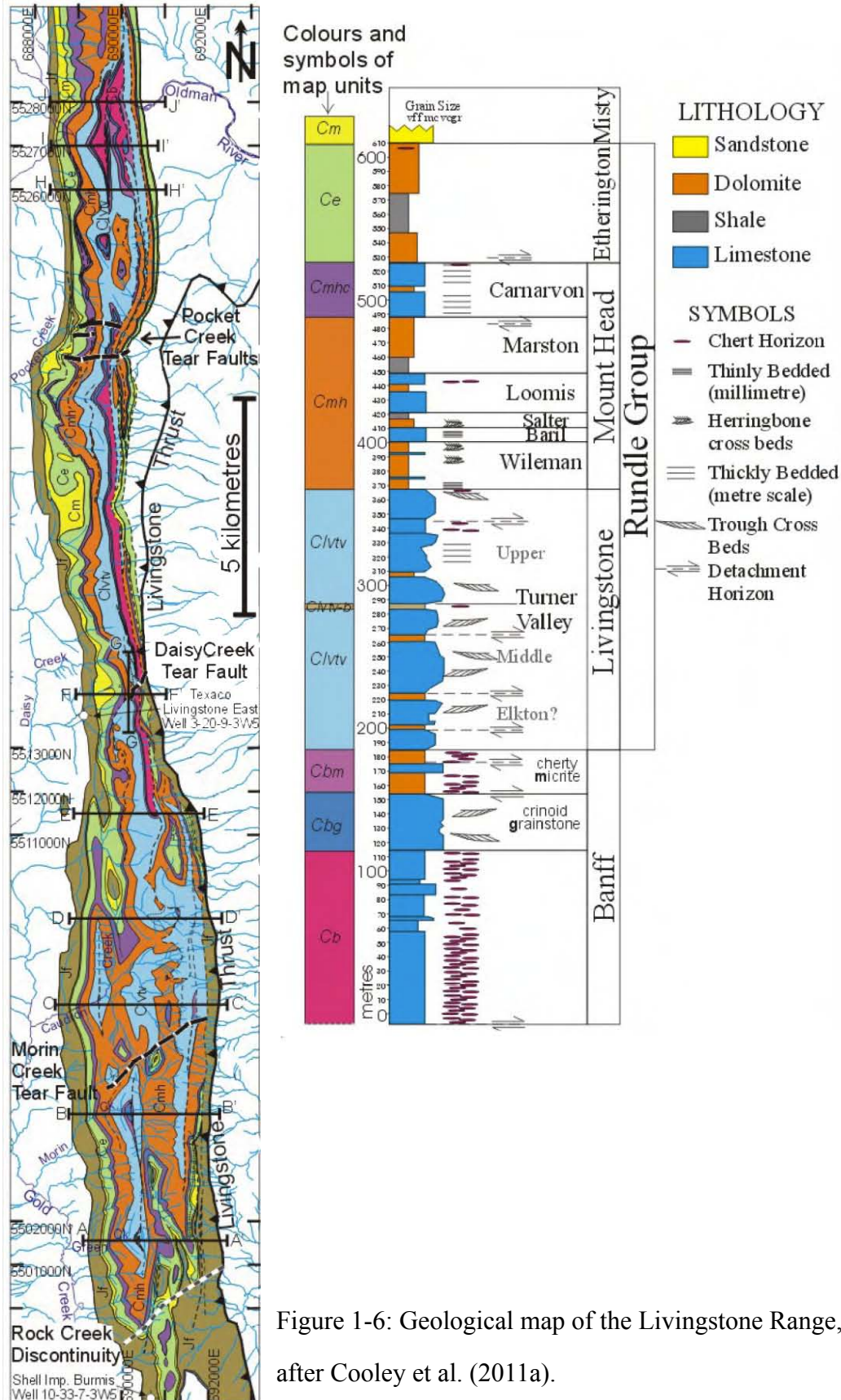


Figure 1-6: Geological map of the Livingstone Range, after Cooley et al. (2011a).

which kinematic models can be applied and tested.

1.2 *Stratigraphy*

The principal rocks of the Crowsnest Pass area (study area of Fig. 1-1) are assigned to a lower Paleozoic succession and an overlying Mesozoic succession. The Paleozoic succession is made up of the Palliser and Banff formations, the Rundle Group and the Etherington Formation. The Mesozoic succession includes the Fernie Formation, and the overlying Kootenay, Blairmore, Alberta, and Belly River groups (see stratigraphic column Fig. 1-7). The stratigraphy is summarized below. More complete accounts of the stratigraphy are given by Jerzykiewicz and Norris (1994), Leckie and Burden (2001), and Langenberg et al. (2007).

1.2.1 Palliser Formation

The Devonian Palliser Formation is made up of a lower grey and dark greyish brown mottled dolomitic limestone, and an upper interbedded succession of dolostone, silty dolostone, and fossiliferous limestone (Meijer Drees et al., 1993). In the Crowsnest Pass area, the Exshaw Formation, which elsewhere overlies the Palliser is not present, and the Banff Formation directly overlies the Palliser (Langenberg et al., 2007).

1.2.2 Banff Formation

The Mississippian Banff Formation consists mainly of argillaceous micritic limestones, that contain nodular or patchy chert (Macqueen and Bamber, 1967). In the Crowsnest Pass area, it is about 60 m thick and contains black mudstone, siltstone, and banded chert (Langenberg et al., 2007). A prominent band of chert that is 10 m thick makes up the top of the formation (Langenberg et al., 2007). Both the Palliser and Banff formations are only visible at the surface on Turtle Mountain.

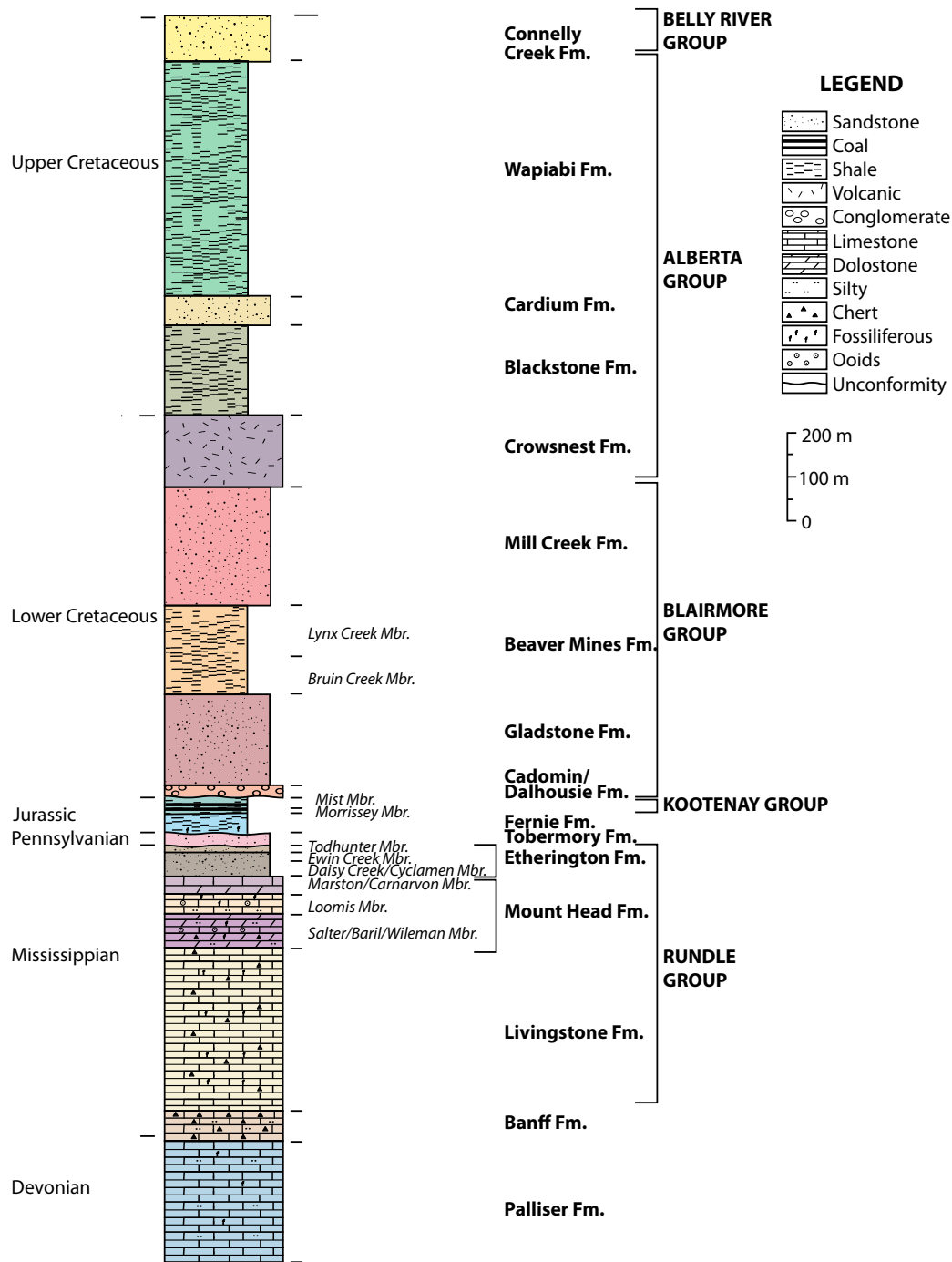


Figure 1-7: Stratigraphic column for the Crowsnest Pass area, Alberta.

1.2.3 Rundle Group

Livingstone Formation

The Mississippian Livingstone Formation is a repetitive succession consisting mainly of massive-bedded echinoderm and bryozoan skeletal limestones, and contains chert nodules (Macqueen and Bamber, 1967). In Crowsnest Pass, it mostly consists of massive, grey, fine to coarse crystalline limestone, with occurrences of cherty limestone and dolostone. Throughout the unit there are grey chert nodules ranging in size up to 30 cm (Fig. 1-8). In the unit, there are thick beds of fossiliferous grainstone containing crinoid ossicles, bivalves, and ooids.

Mount Head Formation

The Mississippian Mount Head Formation also consists of carbonate rocks, and displays alternating limestone and dolostone beds. The formation includes the Wileman, Baril, Salter, Loomis, Marston, and Carnarvon members (Douglas, 1958).

Salter, Baril, and Wileman Members

The Wileman and Salter members consist of fine to medium-grained massive to medium bedded dolomite, and contain sand (Douglas, 1958). The Baril member is recognized based on its composition, containing grey medium to coarsely crystalline and oolitic limestone. There are some units within the Salter and Wileman members that contain peloidal and mixed-skeletal lime grainstones, similar to the Baril member (Fig. 1-9) (Langenberg et al., 2007), which makes recognition of the Baril member difficult in areas of incomplete exposure. The Salter, Baril, and Wileman members could not be separated in this study due to the uncertainty of the location of the Baril member. The dolostone found on



Figure 1-8: Massive skeletal limestone of the Livingstone Formation, showing chert nodules on right side.



Figure 1-9: Oolitic limestone of the Baril Formation.

Bluff Mountain contains white nodules of calcite, possibly representing replaced evaporites, and sedimentary structures such as cross-lamination and wavy laminations. The dolostone weathers grey to yellowish grey.

Loomis Member

The Loomis member is composed of medium to coarsely crystalline, partly oolitic limestone and altered to medium crystalline dolomite towards the base (Douglas, 1958). The unit has a gradational sandy base. In the Crowsnest Pass area, the lowest 8 m contains resistant medium to thickly bedded grey oolitic, mixed skeletal grainstone. The unit coarsens upward and is dark grey, with light olive grey weathering.

Marston Member

The strata of the Marston member are composed of alternating beds of shale and carbonate. The shale is usually green or grey, and the carbonate is a finely crystalline limestone (Douglas, 1958). In Crowsnest Pass, the member consists of grey-brown, well-bedded dolomitic lime packstone, and is interbedded with grey-brown dolomitic lime grainstone containing chert nodules and mudstone. The unit is fairly recessive and is eroded in many places. This unit is approximately 40 m thick in the area.

Carnarvon Member

The Carnarvon member is composed mainly of cryptocrystalline to coarsely crystalline limestone (Douglas, 1958). There are recessive mudstone beds interlayered with the limestone (Langenberg et al., 2007). In the Crowsnest Pass area, the unit contains chert nodules and displays bioturbation. The unit contains grey mixed skeletal lime packstone and wackestone, with 1 to 2% mud and shale (Fig. 1-10). The unit varies in colour from medium to dark grey, with

light grey to olive grey weathering.

Etherington Formation

The Mississippian Etherington Formation consists of fine-grained sandstone and dolomitic packstone. The formation includes the informal Daisy Creek, Cyclamen, and Ewin Creek members, and one formal member, the Todhunter (Langenberg et al., 2007). On Bluff Mountain, the formation is generally recessive; only the Todhunter member is differentiated in some locations. The lower units contain fine, silty sandstone, siltstone and mudstone. In places the sandstone is dolomitic and can be cross-stratified. The Todhunter member is a generally recessive unit making up the top 20 m of the Etherington Formation. The Todhunter member consists of fine grained sandstone that weathers reddish brown (Fig. 1-11). The top of the unit contains interbedded silty, finely crystalline dolomitic packstone and greenish mudstone.

1.2.4 Tobermory Formation

The recessive Pennsylvanian Tobermory Formation is made up of sandstone with minor dolostone, shale, and limestone (Richards et al., 1993). The formation is bounded by disconformities; Mississippian/Pennsylvanian unconformity at the base and the Pennsylvanian/Jurassic unconformity at the top (Langenberg et al., 2007). In Crowsnest Pass, the base of the formation contains sandy conglomerate overlain by silty shale. The remainder of the formation is mainly made up of silty, fine-grained sandstone that contains chert pebbles. In places the unit contains dark grey silty and sandy dolostone and dolomitic sandstone that weather olive grey. The unit is approximately 35 m thick.

1.2.5 Fernie Formation

The Jurassic Fernie Formation comprises lower shales and mudstones, and



Figure 1-10: Mixed skeletal lime packstone and wackestone of the Carnarvon member.



Figure 1-11: Fine grained sandstone of the Todhunter member weathered reddish brown.

coarser clastics in the upper units (Stott, 1998). The recessive formation mainly contains brownish-black silty shale, and is overlain by siltstone and sandstone beds that coarsen upwards. Locally the Fernie Formation also contains thin beds of fossiliferous sandstone containing mollusks and massive limestone beds. This formation is not well exposed in the area.

1.2.6 Kootenay Group

The Kootenay Group comprises three formations: the Morrissey, the Mist Mountain, and the Elk formations. Due to erosional truncation and/or sedimentary thinning, the Elk Formation does not occur in the Crowsnest Pass area (Gibson, 1985). The Kootenay Group is not well exposed in most areas at the surface, due to erosion. Therefore, the Kootenay Group is undivided on the maps presented here. In the Crowsnest Pass area the unit contains dark grey carbonaceous siltstone, sandstone, mudstone and coal. It varies in colour from dark grey and black to pale yellowish brown, and weathers rusty orange. Through the area the number of coal seams varies. In the area there are a total of five coal seams. The Number Five seam is 1.5 to 6 m thick but contains large amounts of shale (MacKay, 1933). The Number Four seam varies in thickness between 3 and 6 m. (Norris, 1994). The Number Three seam is thin at less than 1 m thick (MacKay, 1933). The Number Two seam is 6 to 9 m thick, but has been thickened in the area of Grassy Mountain (Fig. 1-12) (Snyder, 2011). The Number One seam is missing in most of the area and is less than 1 m thick (Mackay, 1933).

1.2.7 Blairmore Group

The Cretaceous Blairmore Group consists of the Cadomin, Dalhousie, Gladstone, Beaver Mines, Mill Creek, and Crowsnest formations (Leckie and Burden, 2001).

Cadomin Formation

The Cadomin Formation consists of resistant chert and quartzite pebble conglomerate (Mellon, 1967). In the Crowsnest Pass area, the unit is dominated by massive to crudely horizontally bedded, clast-supported conglomerate (Leckie and Cheel, 1997). The conglomerate has clasts that range in diameter from 5 to 50 cm and a matrix that is medium grey quartz and chert sandstone (Fig. 1-13). The unit contains beds of sandstone up to 70 cm thick. The thickness of the formation varies through the area from 0 to 30 m.

Dalhousie Formation

The Dalhousie Formation consists predominantly of quartzite sandstone with lenses of conglomerate (Leckie and Cheel, 1997). In the Crowsnest Pass area the unit contains medium bedded quartz sandstone with pebble sized clasts that are made up of approximately 20% chert grains (Fig. 1-14). The unit contains conglomerate beds in places. It is 10 to 20 m thick and has a gradational contact with the underlying Cadomin Formation. Unlike the underlying Cadomin Formation, it is continuous through the area.

Gladstone Formation

The Gladstone Formation consists of white to grey sandstone and shale, which become more calcareous towards the top (Leckie and Burden, 2001). In the Crowsnest Pass area, the formation contains a lower and upper unit. The lower unit contains grey, fine grained sandstone and siltstone interbedded with varicoloured shale. The upper calcareous unit contains limestone beds, up to 5 m thick, together with calcareous silt and shale.

Beaver Mines Formation

The Beaver Mines Formation has a lower part that contains a felspathic



Figure 1-12: Thickened Number Two coal seam of the Kootenay Group on Grassy Mountain.



Figure 1-13: Quartz and chert conglomerate of the Cadomin Formation.



Figure 1-14: Quartz sandstone beds of the Dalhousie Formation.



Figure 1-15: Exotic volcanic pebble conglomerate beds in the Beaver Mines Formation.

sandstone unit with exotic volcanic pebbles (Fig. 1-15) and beds of dark green-grey siltstone (Leckie and Burden, 2001). The upper part consists of interbedded green, fine-grained crossbedded felspathic sandstone, dark green laminated siltstone, and varicoloured shale (Leckie and Burden, 2001). In the Crowsnest Pass area, the lower beds contain dark brown or grey thickly bedded sandstone beds in recessive black shale units. The upper beds contain greenish grey to grey mud, sandstone and conglomerate units that become thinner and finer towards the top of the formation.

Mill Creek Formation

The Mill Creek Formation has two members: the lower Bruin Creek and the upper Lynx Creek (Leckie and Burden, 2001). The lower Bruin Creek member contains interbedded cherty sandstone, varicoloured mudstone, conglomerate, and ash (Leckie and Burden, 2001). The upper Lynx Creek member consists of white, quartz-rich sandstone and dark grey to black shale and siltstone (Leckie and Burden, 2001). Due to lack of continuous outcrop, the members are not separated for this study. Locally in the base of the formation, there are clast-supported conglomerates with igneous pebbles. The formation consists of cross-bedded grey thinly to medium bedded fine grained quartz and chert sandstone and siltstone, interbedded with varicoloured shales (Fig. 1-16).

Crowsnest Formation

The Crowsnest Formation is a localized volcanic unit, comprising thick agglomerate, volcanoclastic debris flows, and ash-fall deposits (Leckie and Burden, 2001). The unit ranges in thickness from 150 to 300 m. The texture varies from porphyritic with light pink and green crystal fragments (up to 30 cm) with a dark grey-black aphanitic matrix (Fig. 1-17), to stratified breccia (Fig. 1-18), to grey-purple thin to thick bedded ash. The formation is highly resistive and is



Figure 1-16: Cross-bedded sandstone beds of the Mill Creek Formation.

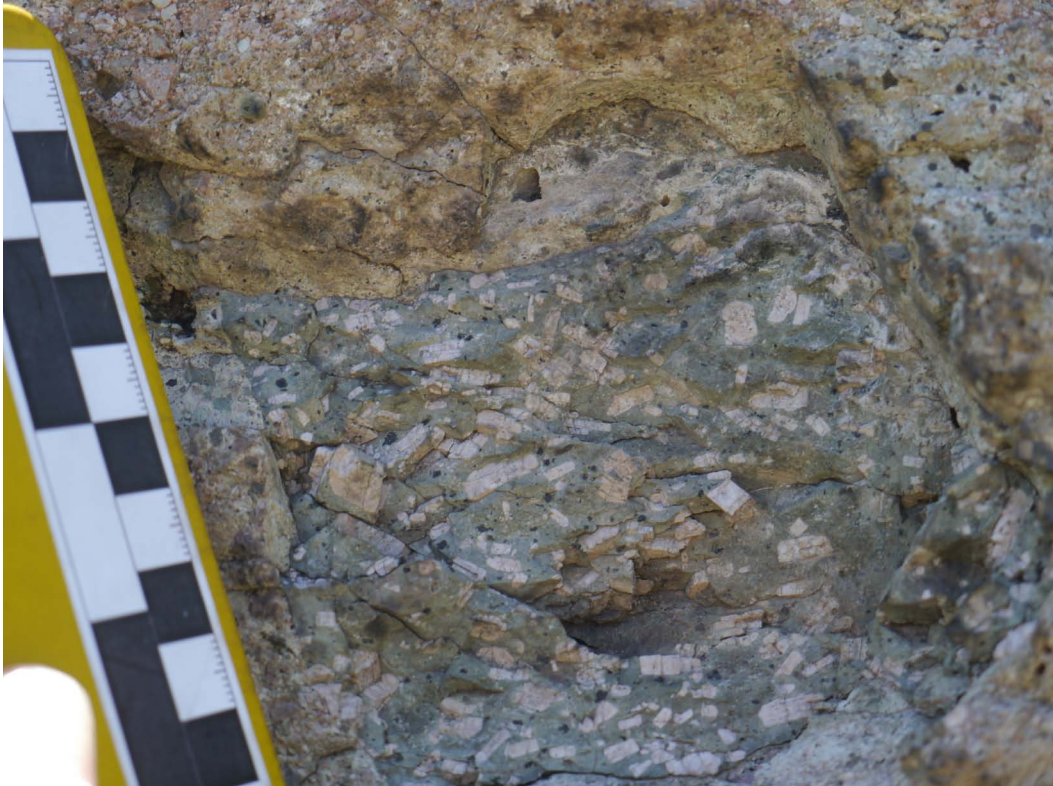


Figure 1-17: Porphyritic volcanic unit in the Crowsnest Formation.

found in many of the ridges in the area.

1.2.8 Alberta Group

The Upper Cretaceous Alberta Group consists of the Blackstone, Cardium, and Wapiabi formations (Jerzykiewicz and Norris, 1994).

Blackstone Formation

The Blackstone Formation contains siltstone, shale, bands of limestone, and chalk layers (Wall and Rosene, 1977). The layers that contain chalk are not seen in the foothills (Wall and Rosene, 1977). In the Crowsnest Pass area, the unit consists of black shale, silty shale, and thin, fine-grained sandstone. Throughout there are units with calcareous matrixes. The formation is approximately 200 m thick in the area, but due to the fissile nature of the shales, the unit is easily eroded and not well exposed.

Cardium Formation

The Cardium Formation comprises mud, sand, and conglomerate layers, and ranges in thickness from 50 to 165 m (Krause et al., 1994). The unit lacks consistent members and is not divided for this study. In the Crowsnest Pass area, the unit is 50 to 100 m thick and consists of well cemented, fine to coarse-grained sandstone, interbedded with black siltstone (Fig. 1-19). The upper part of the unit contains chert clasts and limestone concretions. This formation is resistant to weathering and creates ridges.

Wapiabi Formation

The Wapiabi Formation comprises mudstone, siltstone, sandstone, and localized chert conglomerate (Collom, 2001). Though there are seven members in the formation, due to lack of exposure the formation was not further subdivided. The formation consists of dark grey shale with thin beds of silty shale, and thin

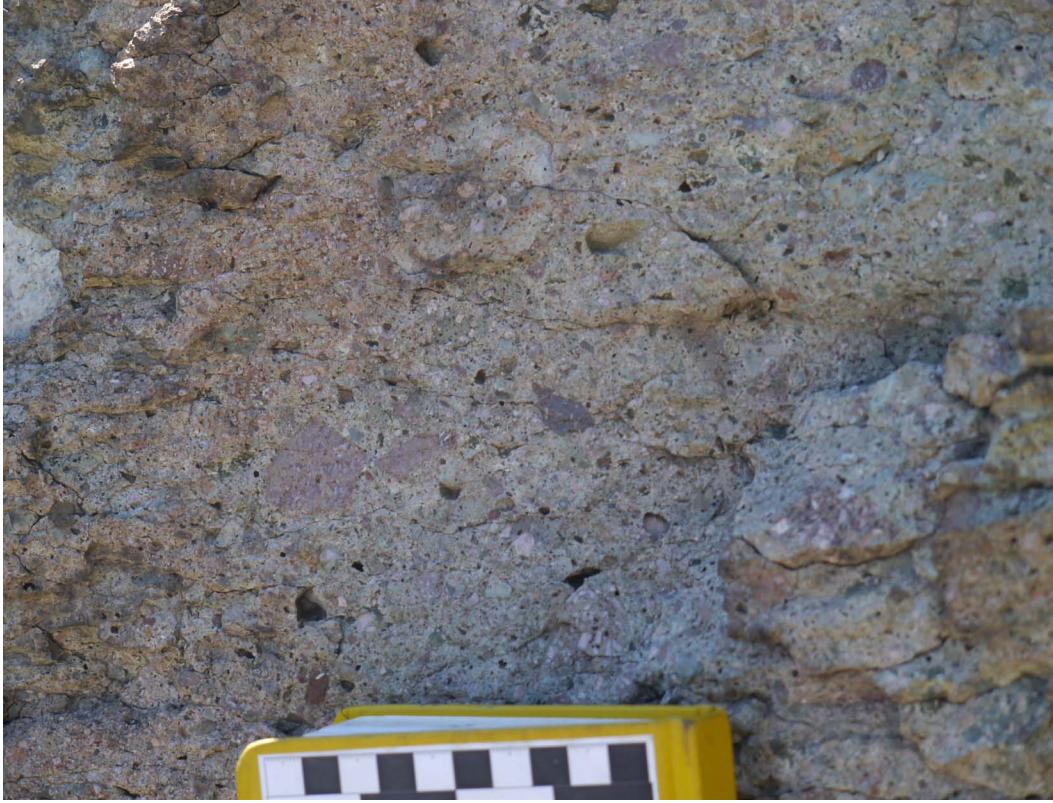


Figure 1-18: Stratified volcanic breccia of the Crowsnest Formation.



Figure 1-19: Well cemented coarse-grained sandstone of the Cardium Formation.

beds of fine grained, grey sands. The formation is approximately 600 m thick. The top of the formation appears to have a gradational contact with the Belly River Group.

1.2.9 Belly River Group

The Upper Cretaceous Belly River Group is subdivided into three formations: stratigraphically, in order, the Connelly Creek, the Lundbreck, and the Drywood Creek formations (Jerzykiewicz and Norris, 1994). The Connelly Creek Formation is several hundred metres thick and contains upward-fining sandstone beds and upward-coarsening sandstone beds interstratified with mudstone (Jerzykiewicz and Norris, 1994). In the Crowsnest Pass area, only the bottom 200 m of the Belly River Group is seen. In the area, the unit consists of medium to thickly cross-bedded, coarse grained quartz sandstone interbedded with thin beds of grey and green shale. Most likely only the Connelly Creek Formation exists in the area, but due to lack of exposure, the group is not subdivided.

1.3 Methods

Field mapping was conducted on exposed rocks in the Crowsnest Pass area. Ten weeks of field work were completed between August 2010 and June 2012, during which over 500 outcrops were visited. Each outcrop location was mapped, and both GPS coordinates and field observations were recorded. Orientation measurements were taken for sedimentary structures, including bedding, and for tectonic structures such as joints and faults.

A revised geological map was produced using field observations and orientations, along with lineaments (approximately 80 m or longer) seen on the LiDAR data. Geological cross-sections were produced using structure contours and well information. The cross-sections oriented approximately perpendicular to strike were constructed to balance (equal areas of rock area before and after

deformation) and were further restored. Balanced cross-sections assume no volume loss and/or out-of-plane motion.

Rock samples were collected in the field from the backlimb, hinge, and forelimb of the fold. They were cut and prepared as thin sections along three planes. The planes are the bedding plane, the profile plane, and a third mutual plane. Strain analysis was performed by two methods: Fry plots (Fry, 1979) and calcite strain gauge (Groshong, 1972). Fry plots were performed on photomicrographs of the thin sections, and analyzed by extensions, FryJ and FryJFit, using the computer program ImageJ. This method which determines the bulk strain of the rock in two-dimensions was described by Waldron and Wallace (2007). The calcite strain gauge method described by Groshong (1972), determines the intra-crystalline strain using twins in the calcite grains. Measurements of different parameters are made on a universal stage. Each parameter is input in a computer program developed by Evans and Groshong (1994), and the output is three-dimensional strain.

1.4 Presentation and Main Objectives

A paper-based format was chosen, which will assist in the publication of this thesis in peer-reviewed publications. This thesis comprises a series of two manuscripts that incorporate geological mapping and the deformation history in the area of Crowsnest Pass. Some repetition between chapters occurs in order for them to stand alone as separate entities.

In Chapter 2, airborne LiDAR and field data are used to produce a revised geological map for the Crowsnest Pass area. LiDAR data were used to aid in mapping, by increasing both area covered in the field and accuracy and by assisting in interpretation in poorly exposed and inaccessible areas. Additionally, revised cross-sections through the area show the geometry of structure below the

surface, and constrain the kinematic history.

Chapter 3 attempts to determine the deformation history of the dominant fold in the study area using strain analysis. Rocks collected from the Turtle Mountain fold were analyzed by two methods: the Fry method (Fry, 1979), which determines the bulk strain, and the calcite strain gauge method (Groshong, 1972), which determines the intra-crystalline strain. The determined strain is compared to the strain predicted by kinematic models proposed in previous research.

Chapter 4 briefly summarizes the major research conclusions.

1.5 References

- Allan, J.A., 1931, Report on Stability of Turtle Mountain, Crowsnest District, Alberta: Edmonton, Dept. of Public Works.
- Allan, J.A., 1932, Second Report on Stability of Turtle Mountain, Crowsnest District: Edmonton, Dept. of Public Works.
- Allan, J.A., 1933, Report on Stability of Turtle Mountain, Alberta and Survey of Fissures Between North Peak and South Peak: Edmonton, Dept. of Public Works.
- Barth, N.C., Toy, V.G., Langridge, R.M., and Norris, R.J., 2012, Scale dependence of oblique plate-boundary partitioning; new insights from LiDAR, central Alpine Fault, New Zealand: *Lithosphere*, v. 4, p. 435-448.
- Begin, N.J., Lawton, D.C., and Spratt, D.A., 1996, Seismic interpretation of the Rocky Mountain thrust front near the Crowsnest deflection, southern Alberta: *Bulletin of Canadian Petroleum Geology*, v. 44, p. 1-13.
- Campbell, J.B., 2007, Introduction to Remote Sensing: New York, The Guilford Press, 625 p.
- Collom, C.J., 2001, Systematic paleontology, biostratigraphy, and paleoenvironmental analysis of the Upper Cretaceous Wapiabi Formation

- and equivalents; Alberta and British Columbia, Western Canada [Doctoral thesis]: Calgary, University of Calgary, 835 p.
- Cooley, M.A., Price, R.A., Dixon, J.M., and Kyser, T.K., 2011a, Along-strike variations and internal details of chevron-style, flexural-slip thrust-propagation folds within the southern Livingstone Range anticlinorium, a paleohydrocarbon reservoir in southern Alberta Foothills, Canada: AAPG Bulletin, v. 95, p. 1821-1849.
- Cooley, M.A., Price, R.A., Kyser, T.K., and Dixon, J.M., 2011b, Stable-isotope geochemistry of syntectonic veins in Paleozoic carbonate rocks in the Livingstone Range anticlinorium and their significance to the thermal and fluid evolution of the southern Canadian foreland thrust and fold belt: AAPG Bulletin, v. 95, p. 1851-1882.
- Cruden, D.M., and Krahn, J., 1973, A Reexamination of the Geology of the Frank Slide: Canadian Geotechnical Journal, v. 10, p. 581-591.
- Douglas, R.J.W., 1958, Mount Head map-area, Alberta: Memoir - Geological Survey of Canada, 241 p.
- Epard, J.L., and Groshong, R.H., Jr., 1995, Kinematic model of detachment folding including limb rotation, fixed hinges and layer-parallel strain: Tectonophysics, v. 247, p. 85-103.
- Erslev, E.A., 1991, Trishear fault-propagation folding: Geology, v. 19, p. 617-620.
- Evans, M.A., and Groshong, R.H., Jr., 1994, Microcomputer techniques and applications; a computer program for the calcite strain-gauge technique: Journal of Structural Geology, v. 16, p. 277-281.
- Fraser, C.S., and Gruendig, L., 1985, The analysis of photogrammetric deformation measurements on Turtle Mountain: Photogrammetric Engineering and Remote Sensing, v. 51, p. 207-216.
- Fry, N., 1979, Random point distributions and strain measurement in rocks:

- Tectonophysics, v. 60, p. 89-105.
- Gibson, D.W., 1985, Stratigraphy, sedimentology and depositional environments of the coal-bearing Jurassic-Cretaceous Kootenay Group, Alberta and British Columbia: Bulletin Geological Survey of Canada, v. 357, p. 108.
- Grebby, S., Cunningham, D., Naden, J., and Tansey, K., 2012, Application of airborne LiDAR data and airborne multispectral imagery to structural mapping of the upper section of the Troodos Ophiolite, Cyprus: International Journal of Earth Sciences, v. 101, p. 1645-1660.
- Groshong, R.H., Jr., 1972, Strain Calculated from Twinning in Calcite: Geological Society of America Bulletin, v. 83, p. 2025-2037.
- Haugerud, R.A., Harding, D.J., Johnson, S.Y., Harless, J.L., Weaver, C.S., and Sherrod, B.L., 2003, High-Resolution Lidar Topography of the Puget Lowland, Washington -A Bonanza for Earth Science: GSA Today, v. 13, p. 4-10.
- Houser, C., Hapke, C., and Hamilton, S., 2008, Controls on coastal dune morphology, shoreline erosion and barrier island response to extreme storms: Geomorphology, v. 100, p. 223-240.
- Issac, J.H., and Lawton, D.C., 2006, The Complex Structure of Turtle Mountain, Fold-Fault Research Project, v. 12: University of Calgary, p. 8-1-8-22.
- Jaboyedoff, M., Couture, R., and Locat, P., 2009, Structural analysis of Turtle Mountain (Alberta) using digital elevation model; toward a progressive failure: Geomorphology, v. 103, p. 5-16.
- Jerzykiewicz, T., and Norris, D.K., 1994, Stratigraphy, structure and syntectonic sedimentation of the Campanian “Belly River” clastic wedge in the southern Canadian Cordillera: Cretaceous Research, v. 15, p. 367-399.
- Krause, F.F., Deutsch, K.B., Joiner, S.D., Barclay, J.E., Hall, R.L., and Hills, L.V., 1994, Cretaceous Cardium Formation of the Western Canada sedimentary

- basin: Canada, Canadian Society of Petroleum Geologists : Calgary, AB, Canada, p. 374-385.
- Langenberg, C.W., Pana, D.I., Richards, B., Spratt, D.A., and Lamb, M.A., 2007, Structural geology of Turtle Mountain near Frank, Alberta: Alberta Geological Survey, Energy Resources Conservation Board, 39 p.
- Leckie, D., and Burden, E.T., 2001, Stratigraphy, sedimentology, and palynology of the Cretaceous (Albian) Beaver Mines, Mill Creek, and Crowsnest formations (Blairmore Group) of southwestern Alberta: Ottawa, Geological Survey of Canada, 103 p.
- Leckie, D.A., and Cheel, R.J., 1997, Sedimentology and depositional history of Lower Cretaceous coarse-grained clastics, Southwest Alberta and Southeast British Columbia: Bulletin of Canadian Petroleum Geology, v. 45, p. 1-24.
- MacKay, B.R., 1933, Geology and coal deposits of Crowsnest Pass area, Alberta: Summary Report of the Geological Survey of Canada, p. 21-67.
- Macqueen, R.W., and Bamber, E.W., 1967, Stratigraphy of Banff Formation and lower Rundle Group (Mississippian), southwestern Alberta: Paper - Geological Survey of Canada, v. 67, 36 p.
- Martinez Torres, L.M., Lopetegui, A., and Eguiluz, L., 2012, Automatic resolution of the three-points geological problem: Computers & Geosciences, v. 42, p. 200-202.
- Meijer Drees, N.C., Johnston, D.I., and Richards, B.C., 1993, The Devonian Palliser Formation and its equivalents, southern Alberta, Canada: Open-File Report - Geological Survey of Canada, 98 p.
- Mellon, G.B., 1967, Stratigraphy and petrology of the Lower Cretaceous Blairmore and Mannville Groups, Alberta Foothills and Plains: Research Council of Alberta, Bulletin, v. 21, 270 p.

- Mitra, S., 1990, Fault-propagation folds; geometry, kinematic evolution, and hydrocarbon traps: AAPG Bulletin, v. 74, p. 921-945.
- Mitra, S., 2003, A unified kinematic model for the evolution of detachment folds: Journal of Structural Geology, v. 25, p. 1659-1673.
- Norris, D.K., 1955, Blairmore, Alberta: Paper - Geological Survey of Canada, v. 55, 36 p.
- Norris, D.K., 1993, Blairmore, Alberta: Calgary, Geological Survey of Canada, Map 1829A, scale 1:50 000.
- Norris, D.K., 1994, Structural style of the Kootenay Group, with particular reference to the Mist Mountain Formation on Grassy Mountain, Alberta: Ottawa, Geological Survey of Canada, 42 p.
- Notebaert, B., Verstraeten, G., Govers, G., and Poesen, J., 2009, Qualitative and quantitative applications of LiDAR imagery in fluvial geomorphology: Earth Surface Processes and Landforms, v. 34, p. 217-231.
- Pavlis, T.L., and Bruhn, R.L., 2011, Application of lidar to resolving bedrock structure in areas of poor exposure; an example from the STEEP study area, Southern Alaska: Geological Society of America Bulletin, v. 123, p. 206-217.
- Pearce, M.A., Jones, R.R., Smith, S.A.F., and McCaffrey, K.J.W., 2011, Quantification of fold curvature and fracturing using terrestrial laser scanning: AAPG Bulletin, v. 95, p. 771-794.
- Poblet, J., and McClay, K., 1996, Geometry and kinematics of single-layer detachment folds: AAPG Bulletin, v. 80, p. 1085-1109.
- Price, R.A., 1962, Fernie map-area, east half, Alberta and British Columbia: Geological Survey of Canada, Map 82 G E 1/2, 65 p.
- Price, R.A., 1994, Cordilleran tectonics and the evolution of the Western Canada sedimentary basin, Geological atlas of the Western Canada sedimentary

- basin: Calgary, AB, Canada, Canadian Society of Petroleum Geologists, p. 12-24.
- Richards, B.C., Bamber, E.W., Higgins, A.C., and Utting, J., 1993, Stratigraphy; Carboniferous The geology of North America, Volume D-1: Canada, Geological Survey of Canada : Ottawa, ON, Canada, p. 202-271.
- Roering, J.J., 2008, How well can hillslope evolution models explain topography? Simulating soil transport and production with high-resolution topographic data: Geological Society of America Bulletin, v. 120, p. 1248-1262.
- Snyder, M., 2011, Structural Geology of Grassy Mountain, southern Alberta [Undergraduate thesis]: Edmonton, University of Alberta, 47 p.
- Soeters, R., and van Westen, C.J., 1996, Slope instability recognition, analysis, and zonation: Special Report - Transportation Research Board, National Research Council, p. 129-177.
- Stott, D.F., 1998, Fernie Formation and Minnes Group (Jurassic and Lowermost Cretaceous), northern Rocky Mountain Foothills, Alberta and British Columbia: Bulletin Geological Survey of Canada, 516 p.
- Suppe, J., 1983, Geometry and kinematics of fault-bend folding: American Journal of Science, v. 283, p. 684-721.
- Suppe, J., Connors, C.D., and Zhang, Y., 2004, Shear fault-bend folding, in McClay, K.R., ed., AAPG Memoir 82: Tulsa, American Association of Petroleum Geologists, p. 303-323.
- Tavani, S., and Storti, F., 2011, Layer-parallel Shortening Templates Associated with Double-edge Fault-propagation Folding, in McClay, K.R., Shaw, J.H., and Suppe, J., eds., Thrust Fault-Related Folding, AAPG Memoir 94: Tulsa, OK, p. 121-135.
- Tavani, S., Storti, F., and Salvini, F., 2006, Double-edge fault-propagation folding: geometry and kinematics: Journal of Structural Geology, v. 28, p. 19-35.

- Waldron, J.W.F., and Wallace, K.D., 2007, Objective fitting of ellipses in the centre-to-centre (Fry) method of strain analysis: *Journal of Structural Geology*, v. 29, p. 1430-1444.
- Wall, J.H., and Rosene, R.K., 1977, Upper Cretaceous stratigraphy and micropaleontology of the Crowsnest Pass-Waterton area, southern Alberta Foothills: *Bulletin of Canadian Petroleum Geology*, v. 25, p. 842-867.
- Wheeler, J.O., Brookfield, A.J., Gabrielse, H., Monger, J.W.H., Tipper, H.W., and Woodsworth, G.J., 1991, Terrane map of the Canadian Cordillera: Ottawa, ON, Canada, Geological Survey of Canada, Map 1713A, scale 1: 2 000 000.

Chapter 2: Structure of the Rocky Mountain Thrust Belt in the Crowsnest Pass Area using LiDAR Interpretive Mapping

2.1 Introduction

The construction of bedrock geological maps by conventional field techniques is limited by areas of inaccessibility and by ground cover due to vegetation, soil, snow, and buildings. Airborne LiDAR (light detection and ranging) data (acquired by remote sensing) have been used in the past to aid in the analysis of geomorphology (e.g., Notebaert et al., 2009), and for landslide assessment and modeling (e.g., Sturzenegger et al., 2007). LiDAR data regarding structural features have also been used to interpret bedrock (e.g., Jaboyedoff et al., 2009; Pavlis and Bruhn, 2011; Grebby et al., 2012). Compared to field techniques, the use of airborne LiDAR data can enable larger areas to be mapped with increased accuracy.

The Crowsnest Pass area (Fig. 2-1) is located in the Rocky Mountain foothills of the Canadian Cordillera in southern Alberta, Canada. The Rocky Mountain foothills are a thin-skinned thrust belt. The stratigraphy in the area is dominated by Paleozoic carbonates overlain by Mesozoic mainly clastic units (Fig. 2-2). A single volcanic unit, the Crowsnest Formation, is present in the Mesozoic succession. Volcanic units are otherwise rare in the Rocky Mountains. The study area, Fig. 2-1, is located near the border of British Columbia and is crossed by Alberta Highway 3. In the middle of the study area, Highway 3 and the Crowsnest River run east-west in a valley, cross-cutting the major structures; a product of superimposed drainage. The towns Frank, Blairmore, and Coleman are located in the valley of the Crowsnest River. The south half of the map area has recently

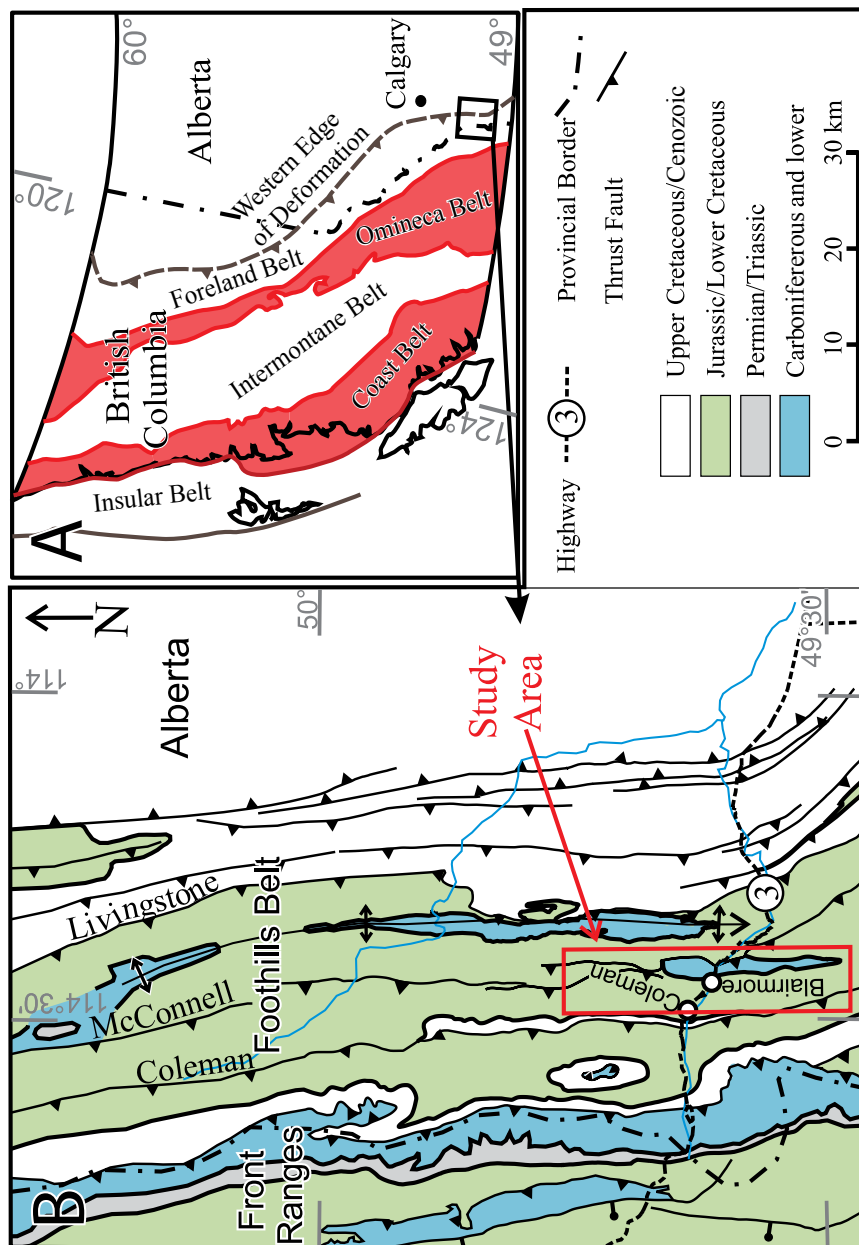


Figure 2-1: Regional map of the study area. (A) Canadian Cordillera map showing belts modified after Wheeler et al., (1991). (B) Regional geological map modified from Cooley et al. (2011a, b).

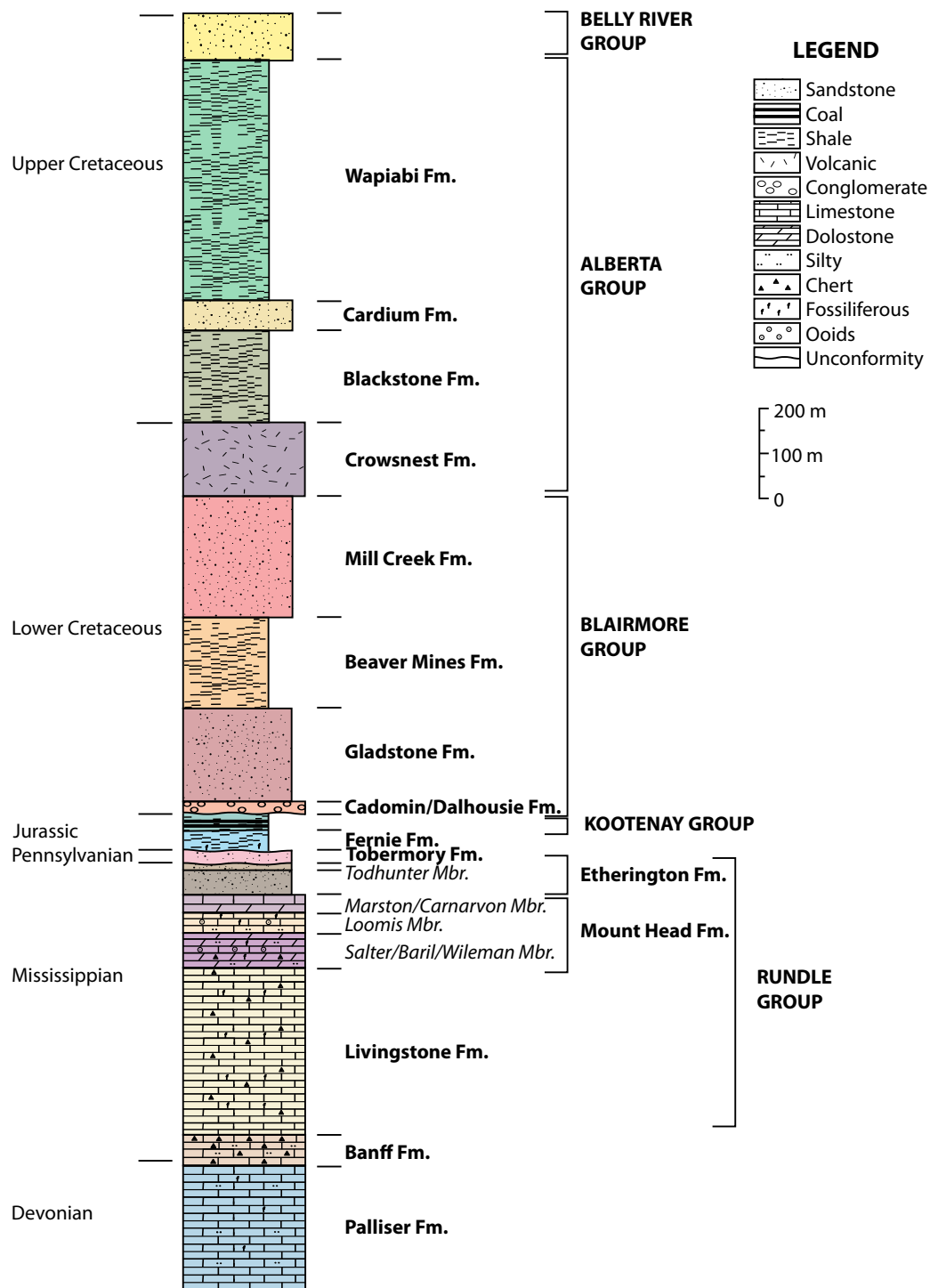


Figure 2-2: Stratigraphic Column for the Crowsnest Pass area, Alberta.

experienced forest fires, making it inaccessible in areas.

The area contains a series of thrusts that generally strike north-south. The hanging walls and footwalls of most thrusts expose Mesozoic units at the surface; however, the Turtle Mountain thrust (Fig. 2-1) exposes Paleozoic carbonates in its hanging wall. Folds occur that have hinges that mainly plunge north.

The anticline in the Turtle Mountain thrust sheet is cored by Paleozoic carbonate rocks. This anticline makes a dominant north-south ridge. The topography of the carbonates is high, due to the resistant nature of the rocks. To the east and west of this anticline, the topography is lower where Mesozoic units are exposed at the surface. However, ridges in the Mesozoic strata mark more resistive units: the Belly River Group, and the Cardium, the Crowsnest, and the Cadomin formations (Fig. 2-2).

2.1.1 Previous Geological Work

Following a 1903 catastrophic slope failure (known as the Frank Slide), research in the Crowsnest Pass area was carried out by Allan (1931, 1932, 1933). Subsequent mapping of the study area was carried out by the Canada Department of Mines and the Geological Survey (MacKay, 1933), Price (1962), and Norris (1955, 1993). Previous larger-scale maps have been produced for both the Grassy Mountain area (Norris, 1994) and the Livingstone Range (Cooley et al., 2011a; b). Stratigraphic sections through the south end of Bluff Mountain were measured by B.C. Richards in 1997 (Langenberg et al., 2007). Studies of the slope failure and slope monitoring have also been carried out (e.g., Cruden and Krahn, 1973; Fraser and Gruendig, 1985). Two-dimensional seismic reflection profiles through the area have been used to interpret the structure in the subsurface below and east of Turtle Mountain (e.g., Begin et al., 1996; Issac and Lawton, 2006). Other work on Turtle Mountain focuses on fractures identified by ground surveying and analysis

of digital elevation models (DEMs) and is used for slope monitoring (e.g., Langenberg et al., 2007; Jaboyedoff et al., 2009).

On Grassy Mountain, located in the northern part of the Crowsnest Pass study area (Fig. 2-3 in pocket, 686000E 5507000N, all grid references Universal Transverse Mercator Projection, Zone 11, North American Datum 1983), Kootenay Group coal is well exposed at the surface. This is a result of historic surface mining. Several studies have been done on the highly deformed and thickened coal in the Grassy Mountain area (e.g., Norris, 1959; Norris, 1994; Snyder, 2011).

Cooley et al. (2011a; b) mapped and developed cross sections through the folds that make up the Livingstone Range to the east. Also studied were the internal structure and fractures, and the fluid flow recorded by the veins during fold development (Cooley et al. 2011a; b).

A number of wells have been drilled in the Crowsnest Pass area for oil and gas exploration. Information from 23 wells was used in this study. This includes locations, deviation surveys, formation tops, and wireline logs. Most of the wells are located in the north and east parts of the map (Fig. 2-4, in pocket, and Appendix A).

2.1.2 LiDAR in Structural Geology

Light detection and ranging (LiDAR) is a high-resolution remote sensing technique that uses laser pulses to measure the distance from a source to the land surface. This results in a set of xyz coordinates which are registered by using points of known ground location (Campbell, 2007). When more than one object is hit (e.g., the laser contacts vegetation above the ground), the ground returns can be separated from the non-ground returns using computer software; this is done by filtering the lowest returns from a point cloud of returns (Campbell, 2007). The resulting bare-earth filtered data are then interpolated to form a regular grid

or DEM (Campbell, 2007). Bare-earth-filtered DEMs, when displayed in shaded-relief images, show subtle topographic features (Pavlis and Bruhn, 2011).

The most widespread use of LiDAR in geology has been the mapping of geomorphic features (e.g., Haugerud et al., 2003; Roering, 2008; Notebaert et al., 2009), or recording coastal changes (e.g., Houser et al., 2008). In Alaska, LiDAR-derived topography has been used in areas of poor outcrop to determine bedrock structure (Pavlis and Bruhn, 2011). In the last few years, structural studies based on data from airborne LiDAR have become more popular (e.g., Jaboyedoff et al., 2009; Barth et al., 2012; Grebby et al., 2012; Martinez Torres et al., 2012). LiDAR data collected with a terrestrial laser scanner, with a horizontal and vertical resolution of 25 mm, has been used to gather detailed quantitative data sets on fracture and fold distributions (Pearce et al., 2011). One study by Jaboyedoff et al. (2009) detected large-scale structural features (e.g., joints and bedding) and determined their orientations using LiDAR data. The Troodos ophiolite, in Cyprus, is an uplifted slice of oceanic crust and lithospheric mantle created through sea-floor spreading (Grebby et al., 2012). Faults and dykes were mapped on this ophiolite using LiDAR; the strikes of lineaments in the LiDAR data were found to be in agreement with field-based structural data (Grebby et al., 2012).

2.2 Data for the Crowsnest Pass Area

LiDAR digital elevation data from 2008, with 1 m horizontal resolution and 30 cm vertical resolution, were made available to the project by Alberta Geological Survey. In addition, infrared orthophotos from 2006 with 0.5 m resolution and aerial photos with 2.5 m resolution were available. Subsurface well information for the area was obtained from the computer program geoSCOUT, made by geoLOGIC Systems.

2.2.1 Data Collection and Processing

The LiDAR data, infrared orthophotos, and aerial photos were brought into the Geographical Information System ArcMap, made by ESRI. The LiDAR data were displayed in hill-shaded relief with different directions of simulated illuminations. All visible lineaments were traced and then separated into three categories: unknown, geomorphological and bedrock. The bedrock lineaments were superimposed on a grid of UTM (Universal Transverse Mercator) coordinates in projection NAD 83 zone 11 (Fig. 2-5 in pocket). These resulting maps were printed on water-resistant paper and used for note-taking in the field.

Field data collection took place over 10 weeks between August 2010 and June 2012. Over 500 outcrops were mapped and located by hand-held Global Positioning System (GPS) receiver (see Fig. 2-4, Appendix B and Appendix C). Orientation measurements were recorded for sedimentary structures including bedding, and for tectonic structures such as joints and faults. The typical accuracy of the orientation measurements was $\pm 3^\circ$. The GPS positional data had a typical positional error of ± 6 m as indicated by the GPS receiver.

Coordinates for the outcrops were imported into ArcMap from the GPS receiver (Appendix B). Orientation measurements were imported into ArcMap as a separate table, and joined to the GPS positional data for plotting.

To determine orientations of bedrock units in unexposed or inaccessible areas, the LiDAR data were loaded into the computer program Orion (from Pangaea Scientific). Points were chosen on the curved lineament marking the trace of a dipping unit across a ridge or a valley (Fig. 2-6). Orion determines a best-fit plane through these points. These orientations, along with their locations, were imported into ArcMap (Appendix C). The error was calculated using multiple measurements made for the same lineament and determining the 95% cone of confidence about the pole to bedding on a stereonet in the computer program

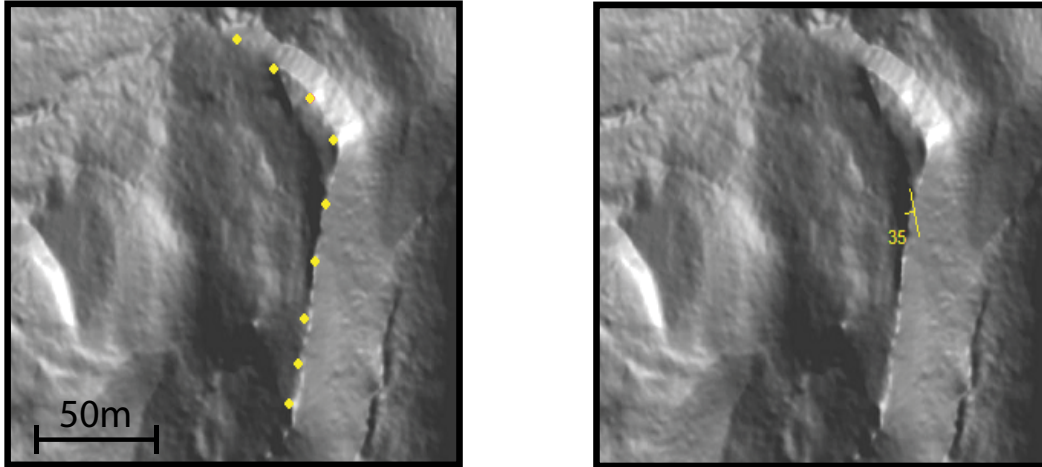


Figure 2-6: Orientations determined using the computer program Orion. Left: the points chosen along a lineament. Right: orientation derived using the best fit plane through the points.

SpheriStat3 (from Pangaea Scientific). The typical error was determined to be $\pm 1.2^\circ$ for strike and $\pm 0.2^\circ$ for dip.

2.2.2 Data Interpretation and Geological Map Production

Boundaries between units were interpreted using field observations, orientations from the program Orion, and lineaments visible on the LiDAR images. Structure contours were established from known boundaries and bedding lineaments and were used to extrapolate boundaries into areas of uncertainty. Maps were exported from ArcMap into Adobe Illustrator for final formatting (Fig. 2-3).

There is a relationship between the characteristics of the image produced by the LiDAR data and the units exposed at the surface (Fig. 2-3). The Paleozoic Rundle Group (Fig. 2-2) makes prominent ridges in the LiDAR, where bedding surfaces can be easily traced (Fig. 2-7). Less resistant units in the Kootenay and Alberta Groups lack topographic features and continuous bedding surfaces (Fig. 2-7). The lowest Blairmore Group units, the Dalhousie and Cadomin formations, are thin, but due to their erosion-resistance, they make conspicuous ridges that are imaged in the LiDAR. The Cadomin Formation has a distinct granular texture in the LiDAR produced by boulders at the surface that range in size from 1 to 10 m (Fig. 2-7). The volcanic Crowsnest Formation forms ridges that appear smooth-textured in the LiDAR imagery (Fig. 2-7). Both the Blackstone and the Wapiabi formations form lows, due to their shaly recessive lithology; in places discontinuous bedding features can be seen in the LiDAR imagery (Fig. 2-7), even in areas of no outcrop. As well, the locations of anthropogenic features such as mines, paths and roads were easy to identify in the LiDAR (Fig. 2-7).

2.2.3 Data Collection, Processing, and Interpretation for the Cross-Section Construction

Unit boundaries were extrapolated into the subsurface using structure

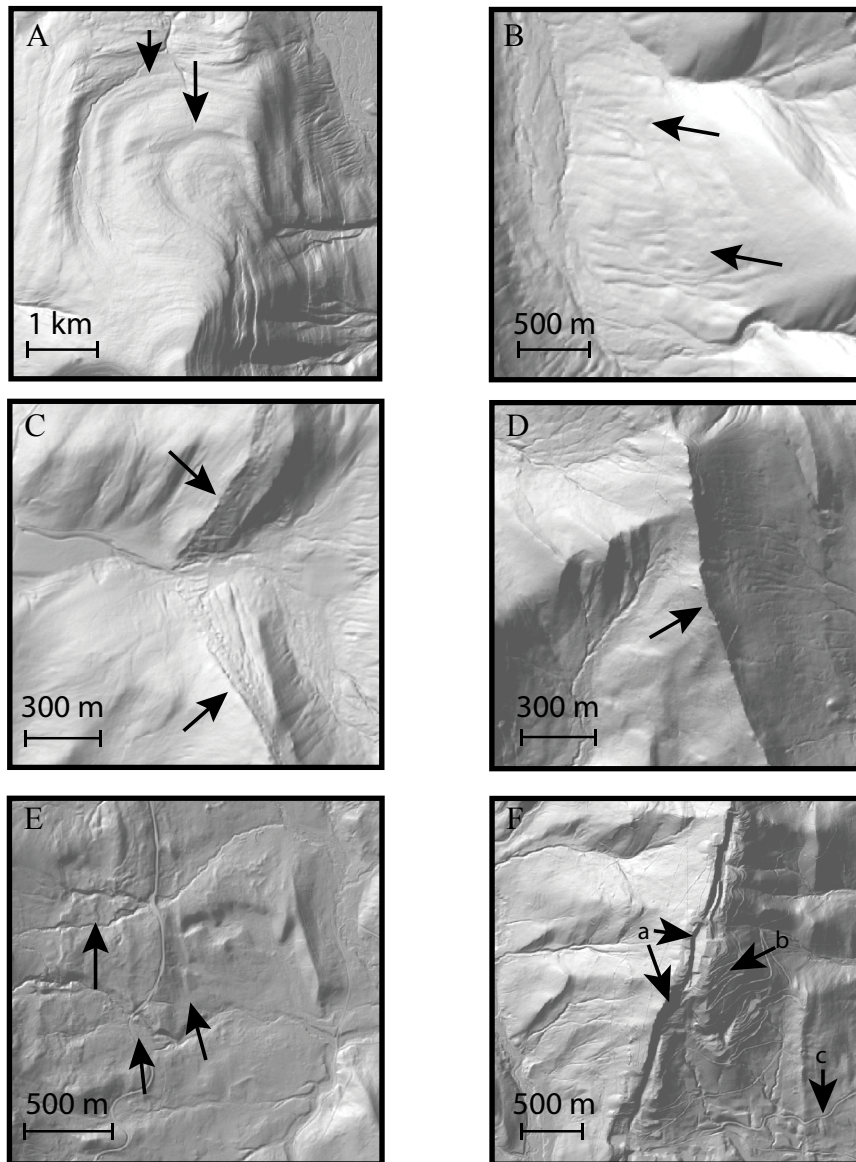


Figure 2-7: Hill-shaded LiDAR imagery showing features associated with units. (A) Prominent ridges of the Paleozoic Rundle Group. (B) Less resistant units in the Kootenay Group lack topographic features and continuous bedding surfaces. (C) The Cadomin Formation has a distinct granular texture in the LiDAR produced by boulders at the surface. (D) The volcanic Crowsnest Formation forms ridges that appear smooth-textured in the LiDAR imagery. (E) The Blackstone Formation in a valley showing discontinuous bedding features in places. (F) Hill-shaded LiDAR imagery showing anthropogenic features such as mines (a), paths (b), and roads (c) on Grassy Mountain.

contours. These were supplemented with stratigraphic picks derived from well data via geoSCOUT (Appendix A). Data from the LiDAR, maps, and wells were imported into the computer program Move (from Midland Valley Exploration Ltd), and were used to create cross-sections. The unit boundaries and faults from the map were imported into Move as shape files generated in ArcMap. Bedding and well information were imported as text files. Seismic profiles from the Turtle Mountain area (Isaac et al., 2008) were imported and located using topography, in the absence of georeferencing information. Three cross-sections were created (Fig. 2-8, 2-9, and 2-10) using all of these data sources, in conjunction with previous work in the area. Wells were projected normal to the two east-west cross-sections, as these were approximately perpendicular to the dominant strike. One cross-section was created north-south through the large anticline structure making up Bluff, Turtle, and Hillcrest Mountains. Wells were not projected onto this section because it is parallel to the dominant strike.

The cross-sections approximately perpendicular to thrust strikes (Fig. 2-8 and 2-9) were constructed to balance. A cross section is balanced when a restored section can be constructed (Fig. 2-11) assuming no volume loss or out-of-plane motion, so that the present-day and restored sections display equal amounts of rock area. Balanced sections are used to constrain subsurface interpretations that are kinematically possible. Balanced cross sections should have structures that are similar to those observed in the field. They should have fault geometries that are reasonable and a deformation sequence that is kinematically possible.

When units in the present day section have the same thicknesses as the restored section, line lengths are the same in the two. Construction of a restored section using this property is known as line length balancing. In contrast where units do not have known constant thickness, construction of the restored section requires the measurement of the cross-sectional areas of units. This is known as

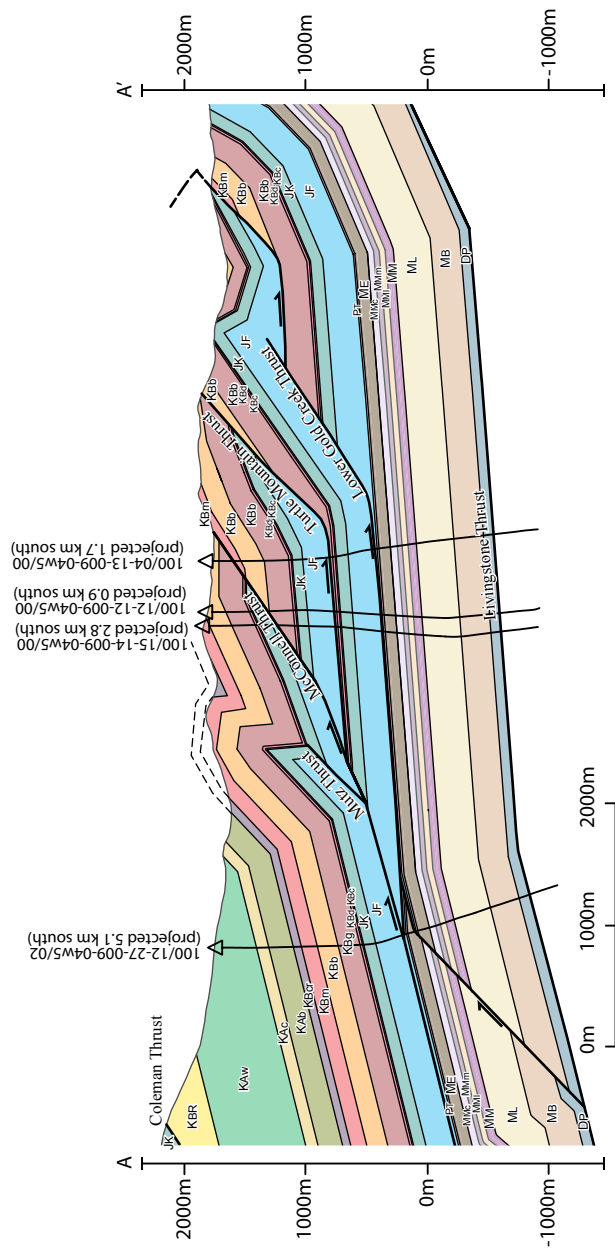


Figure 2-8: Cross-section from A-A' of the Crowsnest Pass area, approximately perpendicular to the dominant strike. Legend on Figure 2-3.

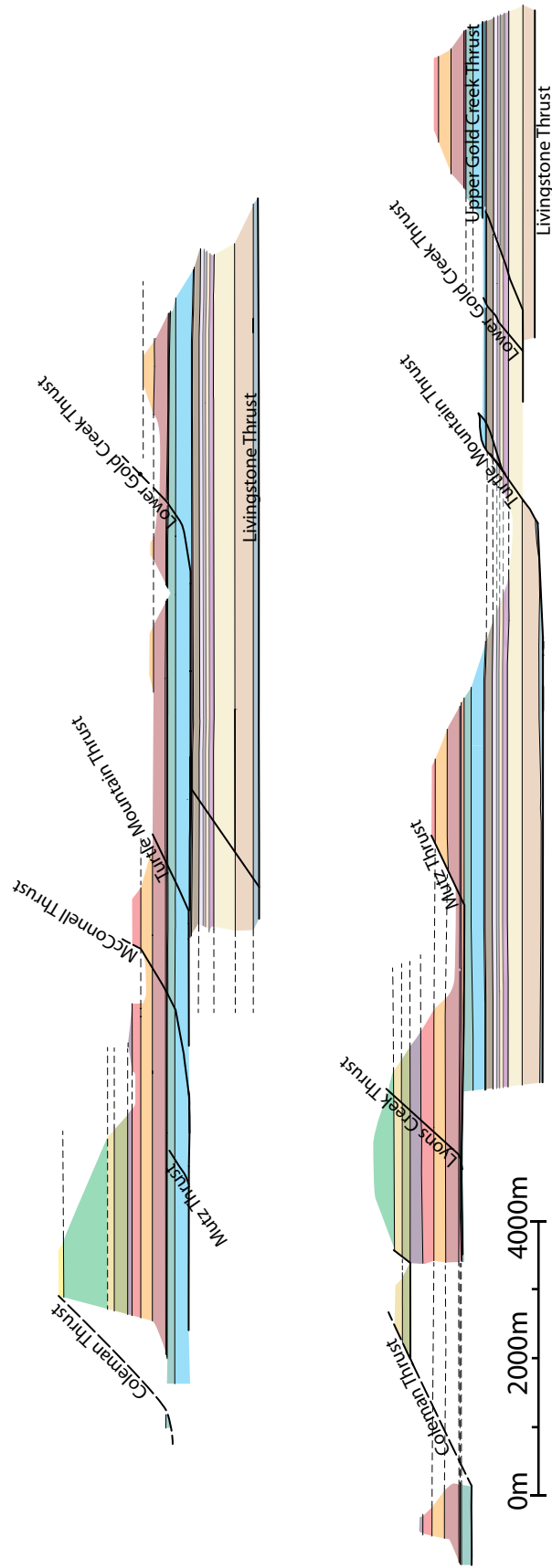


Figure 2-11: Restored east-west cross-sections for the Crowsnest Pass area. Legend on Fig. 2-3. Top section A-A' and bottom section B-B'. Dashed lines indicate eroded portion of the stratigraphy. The dashed faults represents easternmost possible position for the Coleman thrust.

area balancing; this was used on an interpreted detachment fold along the Lower Gold Creek thrust (Fig. 2-8 and 2-11).

2.3 *Geological Map and Cross-section of the Crowsnest Pass Area*

The resulting geological map and cross-sections for the Crowsnest Pass area are shown in Figures 2-3, 2-8, 2-9, and 2-10.

2.3.1 Structures

The map area contains seven main interpreted thrust sheets, which generally strike north-south and dip to the west. Folds in the sheets have axes that generally plunge north. The upper sheets contain Mesozoic mainly clastic units. In these sheets most thrusts display hanging wall flats in the shale units of the Kootenay Group and Fernie Formation. The lower thrust sheets, of the Turtle Mountain, Gold Creek, and Livingstone thrusts, contain both Mesozoic mainly clastic units and Paleozoic carbonate units. The Livingstone thrust sheet is used as a base to the cross-sections. Well and seismic data indicate that its base is approximately planar. In the following sections thrust sheets are named after the thrust located below them.

The Livingstone Thrust

The Livingstone thrust is the lowest mapped thrust, and the thrust sheet is only exposed at the surface on the north-eastern side of the map sheet (Fig. 2-3). The structure of the Livingstone thrust footwall is based on earlier sections in the surrounding area (Langenberg et al., 2006; Cooley et al., 2011a), previous area maps (Norris, 1993) and picks from wells projected along strike; it contains horses with Paleozoic and Mesozoic units that are located above the undeformed basement. The surface trace of the Livingstone thrust lies further east outside the mapped area. The thrust has a hanging wall flat in the Palliser Formation. The

thrust sheet structure changes along strike. In the north, chevron-style anticlines exist in the Paleozoic carbonate units (Cooley et al., 2011a). These are exposed at the surface to the east of the map area. In the south, the anticlines die out, and the Paleozoic units are not exposed at the surface.

In the north, the thrust sheet is continuous and Paleozoic carbonate units underlie the entire cross-section. In the south, the sheet is no longer continuous through the whole section, as the interpreted Turtle Mountain thrust splays off the Livingstone thrust.

In the northeast of the map area, there is a thrust that lies west of the Livingstone thrust, the Caudron Creek thrust (Fig. 2-3). The thrust extends off the top and the east edge of the map. The fault cuts Kootenay Group in the hanging wall, placing it over Gladstone Formation of the Livingstone thrust sheet.

The Gold Creek Thrust System

The Gold Creek thrust system overlies the Livingstone thrust and changes in character from north to south. In the north, the Lower Gold Creek thrust is interpreted as the surface trace of a thrust that dips to the west. This thrust cuts older Kootenay Group and Gladstone Formation in its hanging wall over younger Blairmore Group stratigraphy. In the north, the Upper Gold Creek thrust is interpreted as the surface trace of a thrust that dips to the east. The thrust places younger hanging wall Belly River and Mill Creek formations on top of older footwall Gladstone and Belly River formations. These thrusts mark the east edge of the Gold Creek thrust sheet. The Upper Gold Creek thrust and the Lower Gold Creek thrust meet at a point east of Grassy Mountain (Fig. 2-3, 688000E 5509600N). This point is where the tip of a tectonic wedge (a horse of the Gold Creek thrust system) is exposed at the surface.

The carbonate units are only exposed at the surface in the Gold Creek thrust sheet at one location, north of Bluff Mountain, in a folded area where To-

bermory Formation is exposed in an anticline; however, they are inferred in the subsurface south of this location based on this observation. Further south, in the subsurface, the thrust sheet is interpreted to be more faulted and two horses are present, containing Paleozoic and Mesozoic units (see 2.3.3, below).

The Turtle Mountain Thrust

The surface trace of the Turtle Mountain thrust is located to the east of the dominant ridge that includes Hillcrest, Turtle, and Bluff Mountains (Fig. 2-3). Farther north, the thrust turns west along the north end of Bluff Mountain and then is traced north through Grassy Mountain, in the Kootenay Group. The carbonates are exposed on Bluff, Turtle, and Hillcrest Mountains in an anticline. East of Turtle and Hillcrest Mountains, the thrust trace veers south-east (away from the carbonate cored ridge of Hillcrest Mountain), exposing clastic Kootenay and Blairmore Group units in the thrust sheet (Fig. 2-3).

The thrust has a hanging wall flat in the Palliser Formation, established by the identification of Palliser Formation in the core of the anticline of Turtle Mountain (Langenberg et al., 2007). This has been confirmed in this study by using well data, along with cross-section interpretation (Fig. 2-9). The thrust is interpreted to splay from the Livingstone thrust, in the subsurface to the west of Turtle Mountain (Fig. 2-9). In the north, this thrust cuts up-section in its hanging wall into Mesozoic Kootenay Group, by a hanging wall lateral ramp (Fig. 2-10). To the north, the thrust continues in a hanging wall flat in the Fernie Formation, and no longer visibly branches from the Livingstone thrust sheet, at least within the cross-section (Fig. 2-8).

Strata are clearly folded in the Turtle Mountain thrust sheet. Bluff Mountain is dominated by a north-plunging anticline. The fold continues through Turtle and Hillcrest Mountains where it plunges to the south. The fold is more open on Bluff Mountain than Hillcrest Mountain, where the forelimb of the fold is exposed

at the surface (Fig. 2-3). To the east of the anticline on Hillcrest Mountain, the Turtle Mountain thrust sheet contains a south-plunging syncline. This fold contains the units of the Fernie Formation, and the Kootenay and Blairmore Groups. In the area north of Bluff Mountain, the topographic lineaments are strongly curved in the LiDAR data. This is interpreted to be due to an open anticline with an east-west axial trace (Fig. 2-3).

North of Bluff Mountain, the Turtle Mountain thrust splays into several thrusts in the Kootenay Group, making up an inferred duplex structure. These thrusts appear to include east-vergent features that intersect earlier west-vergent thrusts (Fig. 2-12) (Snyder, 2011). All the splays appear to die out to the north. Also in the north, the Turtle Mountain thrust sheet contains a syncline located in the Crowsnest Formation with a hinge plunging to the north (Fig. 2-3 685000E 5513000N).

The McConnell Thrust

One thrust, identified as the McConnell thrust by Norris (1993), emerges from a poorly exposed area of Kootenay Group in the immediate hanging wall of the Turtle Mountain thrust, along the west side of the Grassy Mountain. The thrust places hanging wall Fernie Formation on top of footwall Blairmore Group, in a hanging wall flat. The thrust sheet contains only Mesozoic units. The ridge of Blairmore Group in the footwall is visible in the LiDAR data, where it runs along the west side of Grassy Mountain (Fig. 2-3). The McConnell thrust sheet contains both a syncline and an anticline. The anticline lies in the Blairmore Group with a mainly horizontal hinge. The syncline is located farther west in the Crowsnest Formation, and plunges to the south.

The Mutz Thrust

The Mutz thrust is located west of the McConnell thrust and the carbon-

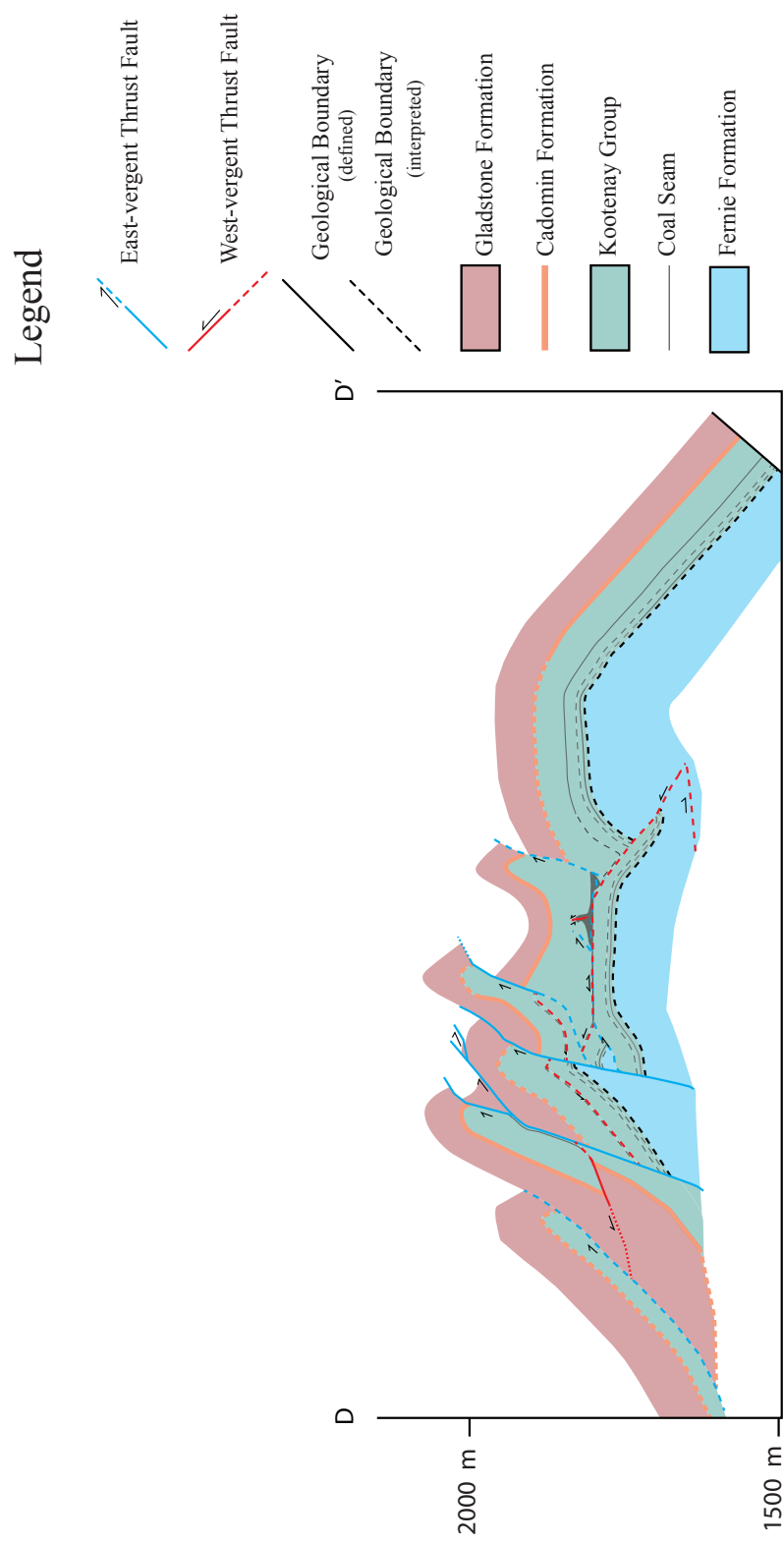


Figure 2-12: Axial projection showing present day geology on Grassy Mountain at natural scale, modified after Snyder (2011). Location of section on Fig. 2-3.

ate-cored anticline making up Turtle and Hillcrest Mountains. The thrust sheet contains Mesozoic clastic units. In the south of the area, the thrust sheet contains lower formations in the Blairmore Group and a flat in the Kootenay Group (Fig. 2-9). The footwall contains recessive units higher in the Blairmore Group.

In the north, the Mutz thrust has a hanging wall flat at the base of the Fernie Formation and is interpreted to splay into several thrusts (Fig. 2-3), which branch upward and westward. The units in these thrust sheets are folded. The first splay branches from the Mutz thrust west of Bluff Mountain and cuts up-section in the hanging wall into folded Blackstone Formation. The second splay branches from the Mutz thrust about 3 km farther north and terminates in folded Blackstone Formation. The kinematic model by Suppe and Medwedeff (1990) of a fault-propagation fold (Fig. 2-13) was applied to this fold in the subsurface. West of Grassy Mountain, the Mutz thrust cuts rapidly up-section in its footwall to Mill Creek Formation. Locally, where the underlying rocks are folded, the thrust appears to cut Crowsnest Formation volcanics and Alberta Group shales in its footwall. To the north, the Mutz thrust loses stratigraphic throw, placing Mill Creek Formation on top of itself.

The syncline interpreted in the footwall of the Mutz thrust has both limbs cut by the thrust. This is significant in that it indicates that the thrust post-dates the fold and therefore suggests out-of sequence movement along the thrust. The traces of the splay thrusts west of the main strand are asymmetrically curved, with a stratigraphic throw that is significantly less than that of the main Mutz thrust.

The Lyons Creek Thrust

The Lyons Creek thrust is locatable only in the south of the area, 1-2 km west of the Mutz thrust. For the southernmost 4.5 km of its mapped trace, the Lyons Creek thrust places Beaver Mines Formation in the hanging wall over Blackstone Formation in the footwall (Fig. 2-3). To the west, it is interpreted to flatten

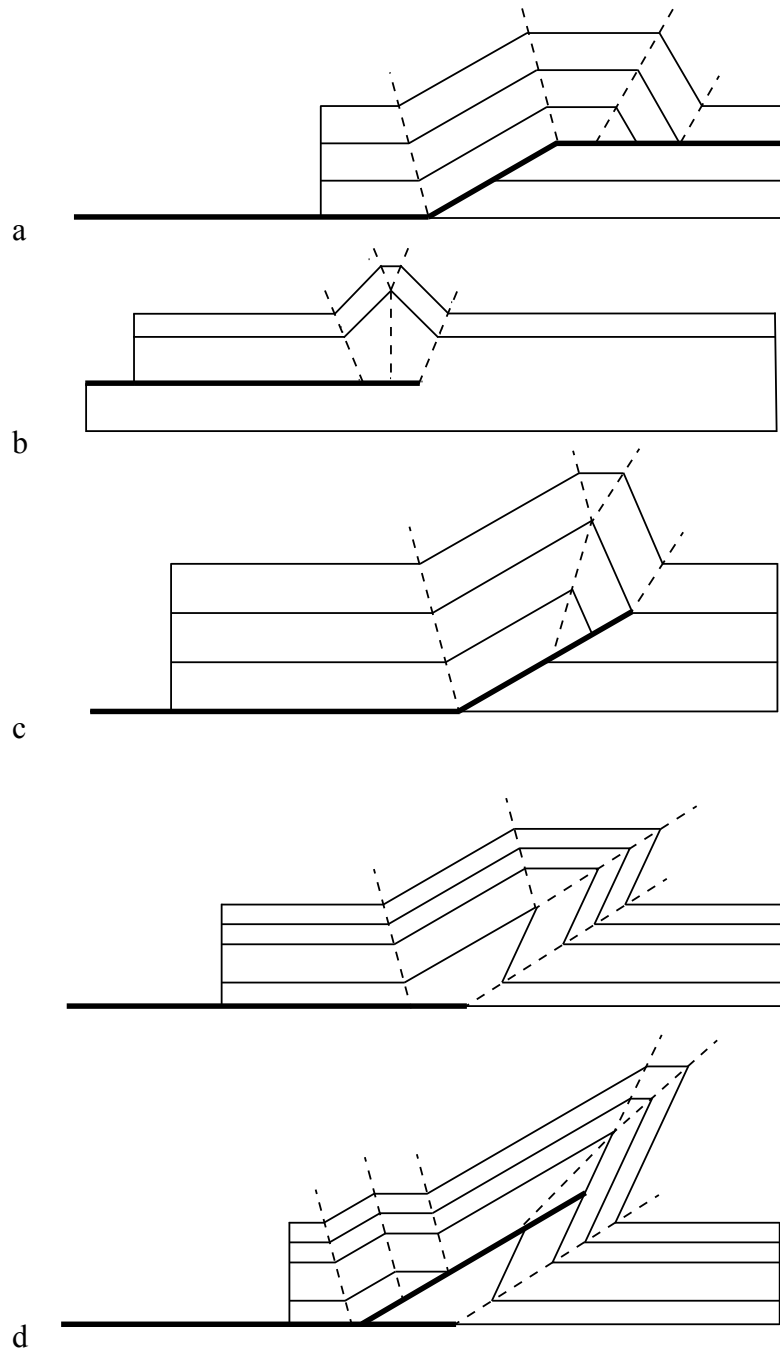


Figure 2-13: Three fold types associated with thrust belts and one modified fold type. The fold types are (a) fault-bend fold, (b) detachment fold and (c) fault-propagation fold (modified after Suppe, 1983; Homza and Wallace, 1995; Suppe and Medwedeff, 1990). Bottom two diagrams of (d) modified fault-propagation fold containing an underlying syncline (revised from McNaught and Mitra, 1993).

into a décollement in the Fernie Formation and is interpreted to splay from the Mutz thrust at depth (Fig. 2-9). Farther north, the thrust cuts rapidly up-section in both the hanging wall and footwall, and offsets the Cardium Formation. The thrust trace appears to die out northward in the Wapiabi Formation.

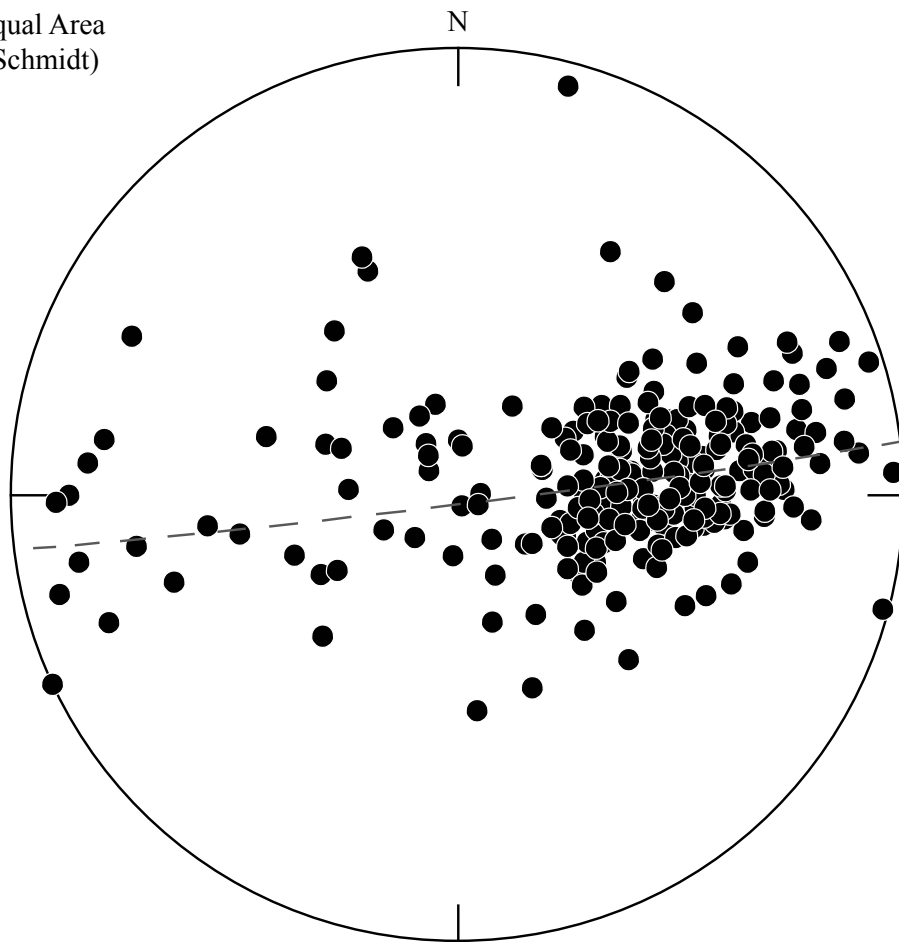
The Coleman Thrust

The surface trace of the Coleman thrust occurs in the southeast parts of the map. Portions of the trace also occur in the northwest parts of the map area. The Coleman thrust sheet includes a ridge of resistant Blairmore Group at the southwest edge of the map sheet (Fig. 2-3). The fault cuts stratigraphically down in the hanging wall towards the north, from the Gladstone Formation to the Kootenay Group. Near the south edge of the map, the Coleman thrust is interpreted to splay. A splay thrust, to the east of the main thrust, contains Crowsnest Formation in the hanging wall and Wapiabi Formation in the footwall. A second splay branches northward into the footwall, duplicating the Cardium Formation in the area, between the Coleman and Lyons Creek thrusts. Just south of Highway 3, there is a third splay east of the Coleman thrust. The hanging wall of the splay exposes Cardium to Beaver Mines Formation, placing them above Wapiabi Formation and Belly River Group in the footwall.

2.3.2 Cross-sections Structure

Three sections (Fig. 2-8, 2-9, and 2-10) through the area show the interpreted subsurface structure. Two of these sections are orientated east-west, in both the north and south portions of the map. These sections are approximately perpendicular to thrust strikes, and parallel to the inferred transport direction, allowing them to be restored (Fig. 2-14 and 2-11). One section oriented north-south, perpendicular to the inferred transport direction, displays the structure through the large anticline making up Bluff, Turtle, and Hillcrest Mountains.

Equal Area
(Schmidt)



Axial

N = 252

Figure 2-14: Stereoplot of poles to bedding for all outcrop locations. The dashed line is the mean fold axis at orientation 083°/88°.

Interpreted East-West Section in North

In the north section, four main thrust sheets seen in the map are interpreted in the subsurface (Fig. 2-8). The lowest thrust is the Livingstone thrust, which is relatively planar and has a footwall flat in the Palliser Formation. Above the Livingstone thrust is the Lower Gold Creek thrust, which has a detachment surface in the Fernie Formation. North of Bluff Mountain (Fig. 2-8) a fold is interpreted to be a detachment fold along the Lower Gold Creek thrust, where the Fernie Formation is thickened into an anticline. To the west is the Turtle Mountain thrust; this thrust displaces material eastward along a footwall flat in the Fernie Formation. Units in the hanging wall are folded, but become planar towards the west.

Further west is the McConnell thrust. It has a detachment surface along a footwall flat in the Fernie Formation. There is an interpreted splay in its hanging wall identified as the Mutz thrust. This splay is not exposed at the surface on the line of section; the units above are folded in a fault propagation fold. On the west edge of the section there is a small portion of Kootenay Group, visible at the surface above the Coleman thrust.

Interpreted East-West Section in South

In the south section, six main thrusts are interpreted in the subsurface (Fig. 2-9). The lowest thrust is the Livingstone thrust; this thrust contains a hanging wall flat in the Banff Formation. This thrust is interpreted to be relatively planar. Above it is the Gold Creek thrust system, which is interpreted to have two horses upon which displacement occurred. The horses contain folded Mesozoic and Paleozoic units. Above the horses is the Turtle Mountain thrust. Units in the Turtle Mountain thrust sheet include Paleozoic and Mesozoic units, from the Palliser to the Mill Creek Formation. The thrust has a hanging wall flat in the Palliser Formation and cuts up-section to the Etherington Formation, below the anticline. The

anticline is tight, with the backlimb dipping around 65° , and contains an over-turned forelimb. The Turtle Mountain thrust splays below the anticline and a small horse is located below. This horse contains folded units from the Mount Head Group to the Tobermory Formation, mapped on the ground by Langenberg et al. (2007).

The Mutz thrust is above the Turtle Mountain thrust, with a hanging wall flat in the Kootenay Group. The Mutz thrust sheet contains units from the Kootenay Group to Wapiabi Formation. The Lyons Creek thrust splays from the Mutz thrust; it is interpreted that there has been only minor displacement along the thrust, inferred from a small offset of units along the fault. The highest thrust is the Coleman thrust; it has two interpreted splays visible in the section. The sheet above the lower splay contains Blackstone and Cardium formations. The sheet above the upper splay has a hanging wall flat in the Kootenay Group, and contains units up to the Crowsnest Formation.

Interpreted North-South Section

In the north-south section, three thrusts are interpreted in the subsurface (Fig. 2-10). The section is sub-parallel to the tight fold making up Turtle and Hillcrest Mountains; apparent thicknesses are distorted by dips into and out of the plane of section. The lowest thrust is the Livingstone thrust, which is interpreted to be relatively planar. In the north, the Livingstone thrust sheet contains Paliser to Gladstone formations. Towards the south, it becomes thinner as the Paliser Formation is lost in a hanging wall cut-off, and units above the Mount Head Group are lost in interpreted footwall cut-offs on the overlying Lower Gold Creek thrust.

The Lower Gold Creek thrust is located above the Livingstone thrust. In the north, the Lower Gold Creek thrust is interpreted to merge with the Turtle Mountain thrust. To the south (below Grassy Mountain), the Lower Gold Creek

thrust is interpreted to splay; the Fernie Formation is tectonically thickened and Paleozoic units emerge as hanging wall cut-offs. Below Bluff Mountain, the units above the Fernie Formation are absent due to the overlying Turtle Mountain thrust.

The Turtle Mountain thrust is interpreted to be present in two locations of the section separated by a region where it has been removed by erosion. It occurs in the north where it contains Blairmore Group with a hanging wall flat in the Beaver Mines Formation. In the south, the Turtle Mountain thrust occurs below Bluff, Turtle, and Hillcrest Mountains. It has a hanging wall flat in the Palliser Formation and cuts up-section to the Fernie Formation towards the north. In Bluff Mountain the units are folded in an open anticline. Further south, more units are exposed at the surface as the Turtle Mountain thrust gets lower in elevation.

2.4 Discussion

2.4.1 Advantages of LiDAR Assisted Mapping Technique

Use of LiDAR data increased the area that could be covered by allowing interpretations to be made in the field. Interpretations were made in the field on maps made from gridded LiDAR data with simulated illumination, along with lineaments picked from the data. The efficiency of fieldwork was increased as LiDAR data could be used to correlate contacts between across-strike traverses. This worked well in areas with units containing distinctive features and lineaments. For example of the Cadomin Formation, contains conglomerate units, was identified in the LiDAR by its granular texture (Fig. 2-7), and resistive units, such as the carbonates of the Mount Head Group and Livingstone Formation, have well defined lineaments along which contacts can be traced (Fig. 2-7).

Features in the LiDAR were used to plan the efficient use of the available field time. Because images derived from the LiDAR data were carried in the field,

areas with complicated geology or lack of LiDAR lineaments could be identified, and more time was assigned to working in these areas. The location of paths and roads were easy to identify in the LiDAR (Fig. 2-7), these were used to gain access to areas. In areas with less resistant units, the location of lineaments was used to indicate possible rock exposure. In areas that were inaccessible, such as the south where there were recent forest fires or where the terrain was dangerous, LiDAR data were used to derive orientations. These orientations, along with the lineaments, were used to fill in portions of the map (Appendix C); 13% of the orientations were derived using lineaments.

The revised map and cross-sections are improved by the use of the LiDAR data. The map, draped over the simulated illuminated surface, allows the relationship between topography and stratigraphy to be seen (Fig. 2-3). Resistive units are seen at the tops of ridges, whereas most valleys contain less resistive shale and sandstone units. In addition, the LiDAR data provided accurate topographic profiles for cross-section construction.

The revised map shows several significant differences in interpretation from previously published maps. In the north area of the map the location of the Gold Creek thrust system is different from previous interpretations by Norris (1993) (Fig. 1-4). LiDAR assisted mapping shows the surface trace of the Gold Creek thrust system is longer and it is located in the middle of the syncline east of Bluff Mountain (Fig. 2-3). In the south, the location of a splay from the Lyons Creek thrust (Fig. 2-3, 683000E 5488000N) was identified from lineaments in the LiDAR data. This splay was not previously identified by Norris (1993) (Fig. 1-4) or Price (1962) (Fig. 1-3). The location of Turtle Mountain thrust east of Turtle and Hillcrest Mountains, where the trace veers south-east, is based on lineaments found in the LiDAR data (Fig. 2-3). The location of this thrust is less curved and further south than the previous interpretation by Norris (1993) (as can be seen by

comparing figures 2-3 and 1-4).

2.4.2 Geometry, Kinematics and Dynamics of the Thrusts and Folds

Geometry of the Principal Thrust Sheets

In the Crowsnest Pass area there are seven main thrusts that strike north-east and dip to the west. The thrusts have listric shapes that flatten with depth. The thrusts have long flats at two main detachment layers, and short frontal ramps through the other layers. At the north end of Bluff Mountain there is a hanging wall lateral ramp along the Turtle Mountain thrust (Fig. 2-10) where it cuts up-section northward from the Palliser to the Fernie Formation. An interpreted duplex structure occurs on Grassy Mountain (Fig. 2-3), where the Turtle Mountain thrust splays into several thrusts in the Kootenay Group.

Previous interpretation of the Crowsnest Pass area by Norris (1993) (Fig. 1-4) show thrusts with steep dips, thrusts with long frontal ramps and short flats, bounding thrust sheets that contain many units. Based on map and cross-section interpretation the subsurface is interpreted in this study to be dominated by the lower Livingstone, Gold Creek, and Turtle Mountain thrust sheets which contain both Paleozoic carbonates and Mesozoic clastic units. The lower thrust sheets are longer than the overlying thrust sheets, which only contain Mesozoic units. This geometry is similar to that developed in the geodynamic models of Stockmal et al. (2007).

Previous interpretation by Norris (1993) (Fig. 1-4) filled the subsurface space below the Turtle Mountain thrust with folded Mesozoic units. Based on map observation and cross-section construction in this study the Gold Creek thrust system was interpreted to contain carbonate units in two horses that sit directly under the Turtle, Bluff, and Hillcrest Mountain anticline, and fill the space

below. This interpretation was based on the presence of Tobermory Formation in outcrop north of Bluff Mountain (Fig. 2-3, 686700E 5504000N), where the Gold Creek thrust sheet is exposed at the surface. This indicates that Paleozoic units are present in this sheet and that the main detachment is below the Fernie Formation/Kootenay Group.

The Gold Creek thrust's amount of separation is different from previous interpretations by Norris (1993) (Fig. 1-4). Norris (1993) showed the Gold Creek thrust with little separation, dying out north of the north cross-section with a short surface trace (approximately 4 km). Cross-section interpretation (Fig. 2-9) in this study showed that the Gold Creek thrust system contains a large amount of shortening that has taken place along thrusts in the north (approximately 6.7 km) and horses in the south (approximately 5.6 km).

Thrust Kinematics

The difference between the total length of the restored and present day cross-sections is 9.2 km in the north section (Fig. 2-8) and 10 km in the south section (Fig. 2-9). Assuming that this difference is equivalent to shortening, a minimum of shortening (difference divided by total restored length) above the Livingstone thrust is approximately 50%. The Livingstone thrust was used as a base to the cross-sections. However, there are thrusts located below; these thrusts would increase total shortening for the area. In the Langford Creek area, north of the study area, Verilleux (1993) determined total displacement of 25 km along a 28 km present day section, which is very similar to the amount of shortening in the study area.

The general order of thrust development based on geometrical relationships in the area is in-sequence, where progressively lower thrusts, closer to the foreland, developed later. Thrust sheets dip to the west, suggesting that deformation proceeded from west to east. However, evidence of out-of-sequence thrusting

was noted at some locations.

The earliest tectonic activity probably occurred in the westernmost parts of the study area. The Coleman thrust had initial displacement along an upper fault followed by displacement along a lower splay. To the south minor movement occurred along the Lyons Creek thrust shown by the small offset along the thrust (Fig. 2-9). The fault dies out to the north, in the shale units of the Blackstone Formation. In the north (Fig. 2-3, 684000E 5508500N) folding produced a syncline in the footwall of the thrust. This syncline has both its limbs cut by the Mutz thrust in an implied out-of-sequence thrust relationship suggesting that it pre-dates the latest motion on the Mutz thrust.

The Mutz thrust was next to develop. In the north splays from the Mutz thrust (Fig. 2-8) were folded with continued displacement over footwall ramps. This geometry can be interpreted as a standard fault-propagation fold (Suppe and Medwedeff, 1990).

Tectonic activity continued in the north on the fault termed the McConnell thrust by Price (1962). In the study area, the McConnell Fault splays from the Mutz thrust and shows little offset in the northern cross-section (Fig. 2-8), where it places Beaver Mines Formation on top of Mill Creek Formation. The thrust dies out south in the complex of thrusts on Grassy Mountain. The lack of offset along the McConnell thrust in the area suggests that it is not closely related to the McConnell thrust known farther north in the Rocky Mountains. Norris (1989), Stockmal et al. (2001) and McMechan (2001) placed the south termination of the McConnell thrust north of the study in the Langford Creek area (Fig. 2-15). Work done north of this termination has an estimated 40 km of displacement (McMechan, 2001), which is substantially more than in the Crowsnest Pass area. The thrust is interpreted to not be related to the McConnell thrust to the north of the study area.

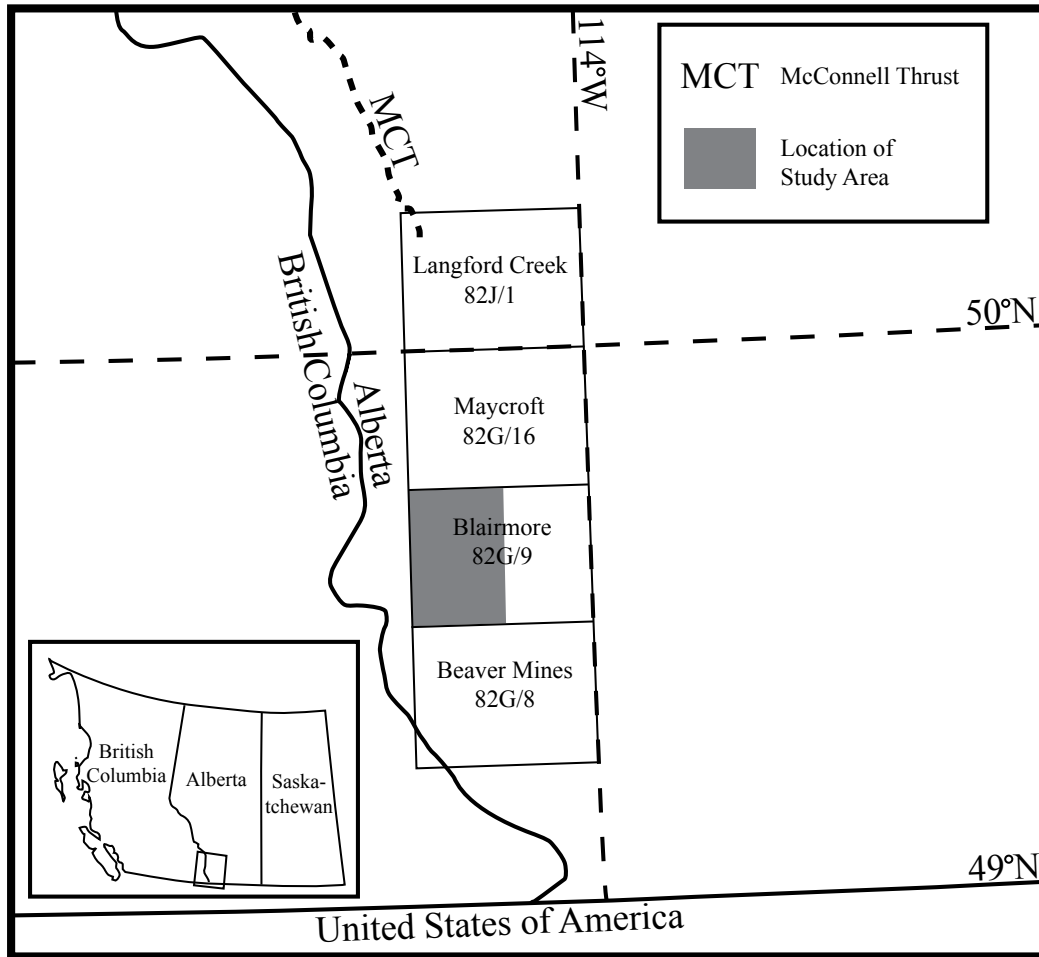


Figure 2-15: Map showing the location of the McConnell thrust trace, after Stockmal et al. (2001). Map-sheets encompassing the Southeastern Cordillera NAT-MAP project area are outlined and labelled. Study area location represented by grey box.

Tectonic activity continued to the east, on the Turtle Mountain thrust. The displacement along the thrust is different from the north to the south. In the north displacement occurs along a flat in the Fernie Formation, and there are several splays in this formation on Grassy Mountain. Variations in the dip of Blairmore Group units in the Turtle Mountain thrust sheet to the north and west of Grassy Mountain suggest that additional fault-propagation or break-thrust folds may be present in this area. Thickened coal on the mountain is interpreted by Snyder (2011) to be affected by west-vergent thrusting followed by east-vergent thrusting (Fig. 2-12), suggesting that there is out-of-sequence thrusting, similar to that developed by the numerical models of Stockmal et al. (2007).

The change in structure and displacement of the Turtle Mountain thrust occurs at the north end of Bluff Mountain. An open transverse fold, with east-west axial trace, is here interpreted as a fault-bend fold (Fig. 2-3 and 2-10), resulting from the Turtle Mountain thrust cutting up-section northward from the Palliser to the Fernie Formation in a lateral hanging wall ramp (Fig. 2-16). A similar relationship has been described along the Brazeau thrust, north of the study area, where Begin and Spratt (2002) interpreted a lateral ramp which cut up-section from the carbonate Cambrian units to the Jurassic shale units, in that the overlying units are folded and the surface trace is curved (Begin and Spratt, 2002).

To the south, the Turtle Mountain thrust sheet contains an anticline that is cored with Paleozoic carbonate units. This relationship between the fault and thrust can be used to make inferences about the kinematics of fold and thrust development. On Turtle Mountain, Langenberg et al. (2007) interpreted the main fold structure as resulting from modified fault-propagation or break-thrust folding, based on the presence of a footwall syncline. In this interpretation, the anticline resulted from the development of an earlier detachment fold above a flat fault segment; a thickened weak layer in the core of the detachment fold allowed the

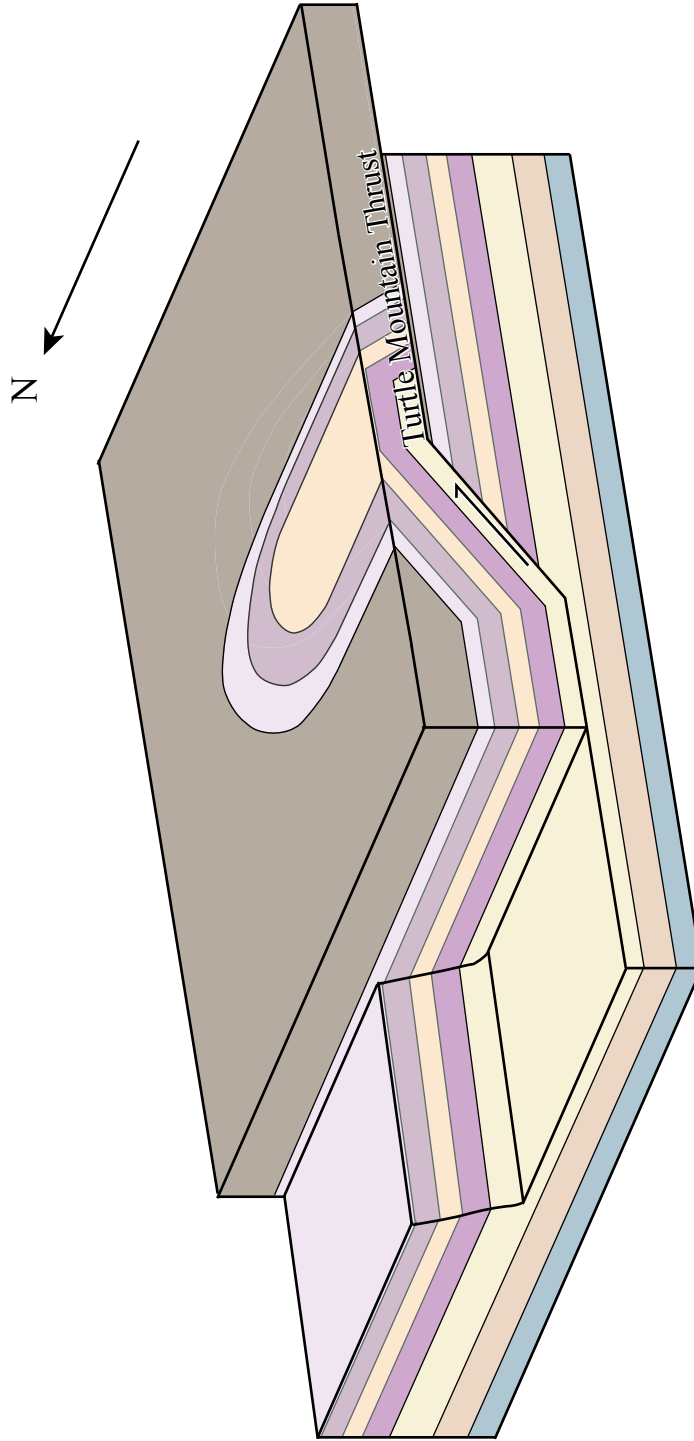


Figure 2-16: Block diagram of north end of Bluff Mountain. The Turtle Mountain thrust contains both a frontal and lateral ramp. The north direction shown by the arrow and legend for colors on Fig. 2-3.

thrust to cut up-section (McNaught and Mitra, 1993) and the underlying syncline was derived from the forelimb of the detachment fold (Fig. 2-13) (McNaught and Mitra, 1993). The south east-west restored cross-section (Fig. 2-11) indicates that the displacement of horses associated with the Gold Creek thrust system created the footwall syncline. The footwall syncline is therefore not associated with the folding of the Turtle Mountain thrust and cannot be used to help interpret it. The structure of the Turtle Mountain fold most closely resembles a fault-propagation fold amongst the basic fold types associated with thrust belts (Fig. 2-13), based on its tightness and the presence of an overturned forelimb.

Tectonic activity continued on the Gold Creek thrust system. Like the Turtle Mountain thrust the structure and displacement is different from the north to the south. In the north displacement occurred along a hanging wall flat in the Fernie Formation, and on a splay along which an interpreted detachment fold occurs. In the south shortening took place along two horses, and thrusting occurred lower in the stratigraphic column. The horses were wedged between lower Paleozoic units and upper Mesozoic units. The Mesozoic units may have been thrust over the horses at this time.

The youngest tectonic activity occurred at approximately 64 Ma as movement along the Livingstone thrust (Cooley et al., 2011b). Most of the movement occurs along a hanging wall flat in the Palliser Formation. This motion is interpreted to have carried the overlying thrust sheets passively eastward at least 10 km (Cooley et al., 2011a).

Mechanics of Thrusting

The thrust sheets in the Crowsnest Pass area contain main detachment surfaces in both the Palliser Formation and the Kootenay Group/Fernie Formation. These detachment surfaces are interpreted to be regionally important weak horizons. Work in the surrounding areas on surface measurements, well informa-

tion, and seismic interpretation (Spratt and Lawton, 1996; Stockmal et al., 2001; Langenberg et al., 2006) shows detachment surfaces in both the Palliser and Fernie formations, and have determined these places to be regional major detachment surfaces. The detachment within the Palliser, which has been noted elsewhere (McMechan, 2001), does not correspond to a notable lithological change. The cause of the weak zone is unknown. Widespread detachment in the Fernie Formation/Kootenay Group caused shortening in the shaly Mesozoic units to be largely independent of the Paleozoic carbonate units below (Fig. 2-8). This interpretation differs from that of Norris (1993) (Fig. 1-4), who interpreted that most of the faults in the area ramp up-section through both the Paleozoic and Mesozoic successions. This interpretation matches the results of Stockmal et al. (2007), who used geodynamic numerical models analogous to the Canadian Rocky Mountains and interpreted Mesozoic thrusts as largely independent of Paleozoic thrusts because of separation by a detachment layer. Geodynamic numerical models also predicted that Paleozoic thrust and thrust sheets should be larger and fewer, and that out-of-sequence thrusting should be common (Stockmal et al., 2007), features that are apparent in the cross-sections presented here (Fig. 2-8 and 2-9).

2.5 Conclusions

LiDAR data used as a mapping tool can increase the area covered in the field and improve accuracy of the resulting map. In areas where connected lineaments are well defined in the LiDAR images, the locations of contacts can be accurately placed between field transverses. The relationship between topography and stratigraphy can be seen in the revised geological map when it is overlaid on the hill-shaded LiDAR data (Fig. 2-3). To aid mapping in inaccessible areas, the lineaments can be used to determine the orientations of dipping bedding planes.

Balanced cross-sections show that the rocks above the Livingstone thrust

have been shortened up to 50% by thrusting and related folding. The anticline making up the ridge of Bluff, Turtle, and Hillcrest Mountains is classified as a fault-propagation fold, based on its tightness and the presence of the overturned limb (in the area of Turtle Mountain) (Fig. 2-9). The cross-section through the structure suggests the syncline to the east is due to the underlying horses that are deformed by the Gold Creek thrust system.

Thrusts in the Crowsnest Pass area have main detachment surfaces in both the Palliser Formation and the Kootenay Group/Fernie Formation. These detachment surfaces are consistent with the position of regional detachment surfaces in the surrounding areas (Spratt and Lawton, 1996). In the Crowsnest Pass area the upper thrust sheets contain only Mesozoic units and are divided into short thrust sheets, whereas the lower Paleozoic units show long sheets. These geometries are similar to those developed from geodynamic numerical models of thrust deformation by Stockmal et al. (2007), that incorporated a strong lower layer and weaker upper layers; during deformation the lower stronger layer develop very long thrust sheets, whereas the upper weaker layers deform into a series of short imbricate thrust sheets.

The general order of thrust development in the area is mainly in-sequence where progressively lower thrusts, closer to the foreland, developed later. There are two implied out-of-sequence thrusting locations. One is where a syncline in the footwall of the Mutz thrust has both limbs cut by the thrust. A second is on Grassy Mountain where thickened coal was created by a series of west-vergent thrusts followed by east-vergent thrusts (Snyder, 2011). The presence of out-of-sequence structures is also consistent with the geodynamic modelling results of Stockmal et al. (2007).

2.6 *References*

- Allan, J.A., 1931, Report on Stability of Turtle Mountain, Crowsnest District, Alberta: Edmonton, Dept. of Public Works.
- Allan, J.A., 1932, Second Report on Stability of Turtle Mountain, Crowsnest District: Edmonton, Dept. of Public Works.
- Allan, J.A., 1933, Report on Stability of Turtle Mountain, Alberta and Survey of Fissures Between North Peak and South Peak: Edmonton, Dept. of Public Works.
- Barth, N.C., Toy, V.G., Langridge, R.M., and Norris, R.J., 2012, Scale dependence of oblique plate-boundary partitioning; new insights from LiDAR, central Alpine Fault, New Zealand: *Lithosphere*, v. 4, p. 435-448.
- Begin, N.J., Lawton, D.C., and Spratt, D.A., 1996, Seismic interpretation of the Rocky Mountain thrust front near the Crowsnest deflection, southern Alberta: *Bulletin of Canadian Petroleum Geology*, v. 44, p. 1-13.
- Begin, N.J., and Spratt, D.A., 2002, Role of transverse faulting in along-strike termination of Limestone Mountain Culmination, Rocky Mountain thrust-and-fold belt, Alberta, Canada: *Journal of Structural Geology*, v. 24, p. 689-707.
- Campbell, J.B., 2007, *Introduction to Remote Sensing*: New York, The Guilford Press, 625 p.
- Cooley, M.A., Price, R.A., Dixon, J.M., and Kyser, T.K., 2011a, Along-strike variations and internal details of chevron-style, flexural-slip thrust-propagation folds within the southern Livingstone Range anticlinorium, a paleohydrocarbon reservoir in southern Alberta Foothills, Canada: *AAPG Bulletin*, v. 95, p. 1821-1849.
- Cooley, M.A., Price, R.A., Kyser, T.K., and Dixon, J.M., 2011b, Stable-isotope geochemistry of syntectonic veins in Paleozoic carbonate rocks in the

- Livingstone Range anticlinorium and their significance to the thermal and fluid evolution of the southern Canadian foreland thrust and fold belt: AAPG Bulletin, v. 95, p. 1851-1882.
- Cruden, D.M., and Krahn, J., 1973, A Reexamination of the Geology of the Frank Slide: Canadian Geotechnical Journal, v. 10, p. 581-591.
- Fraser, C.S., and Gruendig, L., 1985, The analysis of photogrammetric deformation measurements on Turtle Mountain: Photogrammetric Engineering and Remote Sensing, v. 51, p. 207-216.
- Grebby, S., Cunningham, D., Naden, J., and Tansey, K., 2012, Application of airborne LiDAR data and airborne multispectral imagery to structural mapping of the upper section of the Troodos Ophiolite, Cyprus: International Journal of Earth Sciences, v. 101, p. 1645-1660.
- Haugerud, R.A., Harding, D.J., Johnson, S.Y., Harless, J.L., Weaver, C.S., and Sherrod, B.L., 2003, High-Resolution Lidar Topography of the Puget Lowland, Washington -A Bonanza for Earth Science: GSA Today, v. 13, p. 4-10.
- Homza, T.X., and Wallace, W.K., 1995, Geometric and kinematic models for detachment folds with fixed and variable detachment depths: Journal of Structural Geology, v. 17, p. 575-588.
- Houser, C., Hapke, C., and Hamilton, S., 2008, Controls on coastal dune morphology, shoreline erosion and barrier island response to extreme storms: Geomorphology, v. 100, p. 223-240.
- Isaac, J.H., Lawton, D.C., and Langerberg, C.W., 2008, Seismic imaging of the Turtle Mountain structure, southwestern Alberta, Canada: Bulletin of Canadian Petroleum Geology, v. 56, p. 199-208.
- Issac, J.H., and Lawton, D.C., 2006, The Complex Structure of Turtle Mountain, Fold-Fault Research Project, v. 12: University of Calgary, p. 8-1-8-22.

- Jaboyedoff, M., Couture, R., and Locat, P., 2009, Structural analysis of Turtle Mountain (Alberta) using digital elevation model; toward a progressive failure: *Geomorphology*, v. 103, p. 5-16.
- Langenberg, C.W., Beaton, A., and Berhane, H., 2006, Regional evaluation of the coalbed-methane potential of the foothills/mountains of Alberta, Canada: *International Journal of Coal Geology*, v. 65, p. 114-128.
- Langenberg, C.W., Pana, D.I., Richards, B., Spratt, D.A., and Lamb, M.A., 2007, Structural geology of Turtle Mountain near Frank, Alberta: Alberta Geological Survey, Energy Resources Conservation Board, 39 p.
- MacKay, B.R., 1933, Geology and coal deposits of Crowsnest Pass area, Alberta: Summary Report of the Geological Survey of Canada, p. 21-67.
- Martinez Torres, L.M., Lopetegui, A., and Eguiluz, L., 2012, Automatic resolution of the three-points geological problem: *Computers & Geosciences*, v. 42, p. 200-202.
- McMechan, M.E., 2001, Large-scale duplex structures in the McConnell thrust sheet, Rocky Mountains, Southwest Alberta: *Bulletin of Canadian Petroleum Geology*, v. 49, p. 408-425.
- McNaught, M.A., and Mitra, G., 1993, A kinematic model for the origin of foot-wall synclines: *Journal of Structural Geology*, v. 15, p. 805-808.
- Norris, D.K., 1955, Blairmore, Alberta: Paper - Geological Survey of Canada, v. 55, 36 p.
- Norris, D.K., 1959, Type section of the Kootenay Formation, Grassy Mountain, Alberta: *Journal of the Alberta Society of Petroleum Geologists*, v. 7, p. 223-233.
- Norris, D.K., 1989, Geology, Beehive Mountain-Livingstone River area, Alberta-British Columbia, Geological Survey of Canada, 18 p.
- Norris, D.K., 1993, Blairmore, Alberta: Calgary, Geological Survey of Canada,

- Map 1829A, scale 1:50 000.
- Norris, D.K., 1994, Structural style of the Kootenay Group, with particular reference to the Mist Mountain Formation on Grassy Mountain, Alberta: Ottawa, Geological Survey of Canada, 42 p.
- Notebaert, B., Verstraeten, G., Govers, G., and Poesen, J., 2009, Qualitative and quantitative applications of LiDAR imagery in fluvial geomorphology: *Earth Surface Processes and Landforms*, v. 34, p. 217-231.
- Pavlis, T.L., and Bruhn, R.L., 2011, Application of lidar to resolving bedrock structure in areas of poor exposure; an example from the STEEP study area, Southern Alaska: *Geological Society of America Bulletin*, v. 123, p. 206-217.
- Pearce, M.A., Jones, R.R., Smith, S.A.F., and McCaffrey, K.J.W., 2011, Quantification of fold curvature and fracturing using terrestrial laser scanning: *AAPG Bulletin*, v. 95, p. 771-794.
- Price, R.A., 1962, Fernie map-area, east half, Alberta and British Columbia: Geological Survey of Canada, Map 82 G E 1/2, 65 p.
- Roering, J.J., 2008, How well can hillslope evolution models explain topography? Simulating soil transport and production with high-resolution topographic data: *Geological Society of America Bulletin*, v. 120, p. 1248-1262.
- Snyder, M., 2011, Structural Geology of Grassy Mountain, southern Alberta [Undergraduate thesis]: Edmonton, University of Alberta, 47 p.
- Spratt, D.A., and Lawton, D.C., 1996, Variations in detachment levels, ramp angles and wedge geometries along the Alberta thrust front: *Bulletin of Canadian Petroleum Geology*, v. 44, p. 313-323.
- Stockmal, G.S., Beaumont, C., Nguyen, M., and Lee, B., 2007, Mechanics of thin-skinned fold and thrust belts; insights from numerical models: *Special Paper - Geological Society of America*, v. 433, p. 63-98.

- Stockmal, G.S., Lebel, D., McMechan, M.E., and A., M.P., 2001, Structural style and evolution of the triangle zone and the external Foothills, southwestern Alberta: Implications for thin-skinned thrust-and-fold belt mechanics: Bulletin of Canadian Petroleum Geology, v. 49, p. 472-496.
- Sturzenegger, M., Sartori, M., Jaboyedoff, M., and Stead, D., 2007, Regional deterministic characterization of fracture networks and its application to GIS-based rock fall risk assessment: Engineering Geology, v. 94, p. 201-214.
- Suppe, J., 1983, Geometry and kinematics of fault-bend folding: American Journal of Science, v. 283, p. 684-721.
- Suppe, J., and Medwedeff, D.A., 1990, Geometry and kinematics of fault-propagation folding, in Jordan, P., Noack, T., Schmid, S., and Bernoulli, D., eds., *Eclogae Geologicae Helveticae*, v. 83, p. 409-454.
- Veilleux, B.W., 1993, Structural geology of the Langford Creek area, S. W. Alberta [Master thesis]: Edmonton, University of Alberta, 102 p.
- Wheeler, J.O., Brookfield, A.J., Gabrielse, H., Monger, J.W.H., Tipper, H.W., and Woodsworth, G.J., 1991, Terrane map of the Canadian Cordillera: Ottawa, ON, Canada, Geological Survey of Canada, Map 1713A, scale 1: 2 000 000.

Chapter 3: Kinematic development of a thrust-related fold in the Rocky Mountain foothills, Crowsnest Pass, Alberta

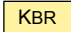
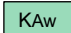



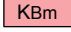
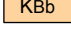
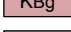


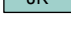
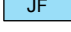
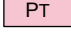



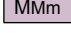


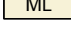

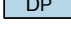

3.1 Introduction

Folds that develop in thrust belts have geometries that are related to the slip on the adjacent faults. Kinematic models of fold development have been proposed for different fold geometries found in thrust belts. In many cases, there is disagreement as to which kinematic model better describes an observed fold (Suppe et al., 2004). Kinematic models continue to be added to the literature in efforts to explain observed fold geometries (e.g., Mitra, 1990; Erslev, 1991; Epard and Groshong, 1995; Poblet and McClay, 1996; Mitra, 2003; Tavani et al., 2006; Tavani and Storti, 2011). In many field examples, interpretations are hindered by incomplete knowledge of a fold. In many examples, how a fold develops and which model, if any, more accurately matches its kinematic history have yet to be determined.

The Crowsnest Pass area (Fig. 3-1) is located in the Rocky Mountain foothills of the Canadian Cordillera in southern Alberta, Canada. The Rocky Mountain foothills are a thin-skinned thrust belt. The stratigraphy in the area is dominated by Paleozoic carbonates overlain by Mesozoic mainly clastic units (Fig. 3-2). A single volcanic unit, the Crowsnest Formation, is present in the Mesozoic succession. Volcanic units are otherwise rare in the Rocky Mountains.

The area contains a series of thrusts that generally strike north-south. The hanging walls and footwalls of most thrusts expose Mesozoic units at the surface; however, the Turtle Mountain thrust (Fig. 3-1) exposes Paleozoic carbonates in its hanging wall. Hillcrest and Turtle Mountains are located in the folded hang-

LEGEND

	Belly River Group		
	Alberta Group	38	Upright
	Wapiabi Formation	79	Overtured
	Cardium Formation	72	Way-up Unknown
	Blackstone Formation	NJ118 x	Sample Locations
	Blairmore Group	▼	Thrust Trace (Defined)
	Crowsnest Formation	▼-▼	Thrust Trace (Approximate)
	Mill Creek Formation	▼-▼-▼	Thrust Trace (Based on remote sensing)
	Beaver Mines Formation	▼-▼-▼-▼	Thrust Trace (Interpreted)
	Gladstone Formation	—	Member Boundary (Defined)
	Dalhousie Formation	---	Member Boundary (Approximate)
	Cadomin Formation	- - -	Member Boundary (Based on remote sensing)
	Kootenay Group	—	Formation Boundary (Defined)
	Fernie Formation	---	Formation Boundary (Approximate)
	Tobermory Formation	- - -	Formation Boundary (Based on remote sensing)
	Etherington Formation	↔-↕-↔	Anticline (arrow indicates approximate direction of plunge; upright; overtured)
	Todhunter Member	A—A'	Line of Section
	Mount Head Formation		
	Carnarvon Member		
	Marston Member		
	Loomis Member		
	Salter/Baril/Wileman Member		
	Livingstone Formation		
	Banff Formation		
	Palliser Formation		
	Unknown		

Universal Transverse Mercator projection;
North American Datum 1983

Figure 3-1 (continued): Legend to map symbols.

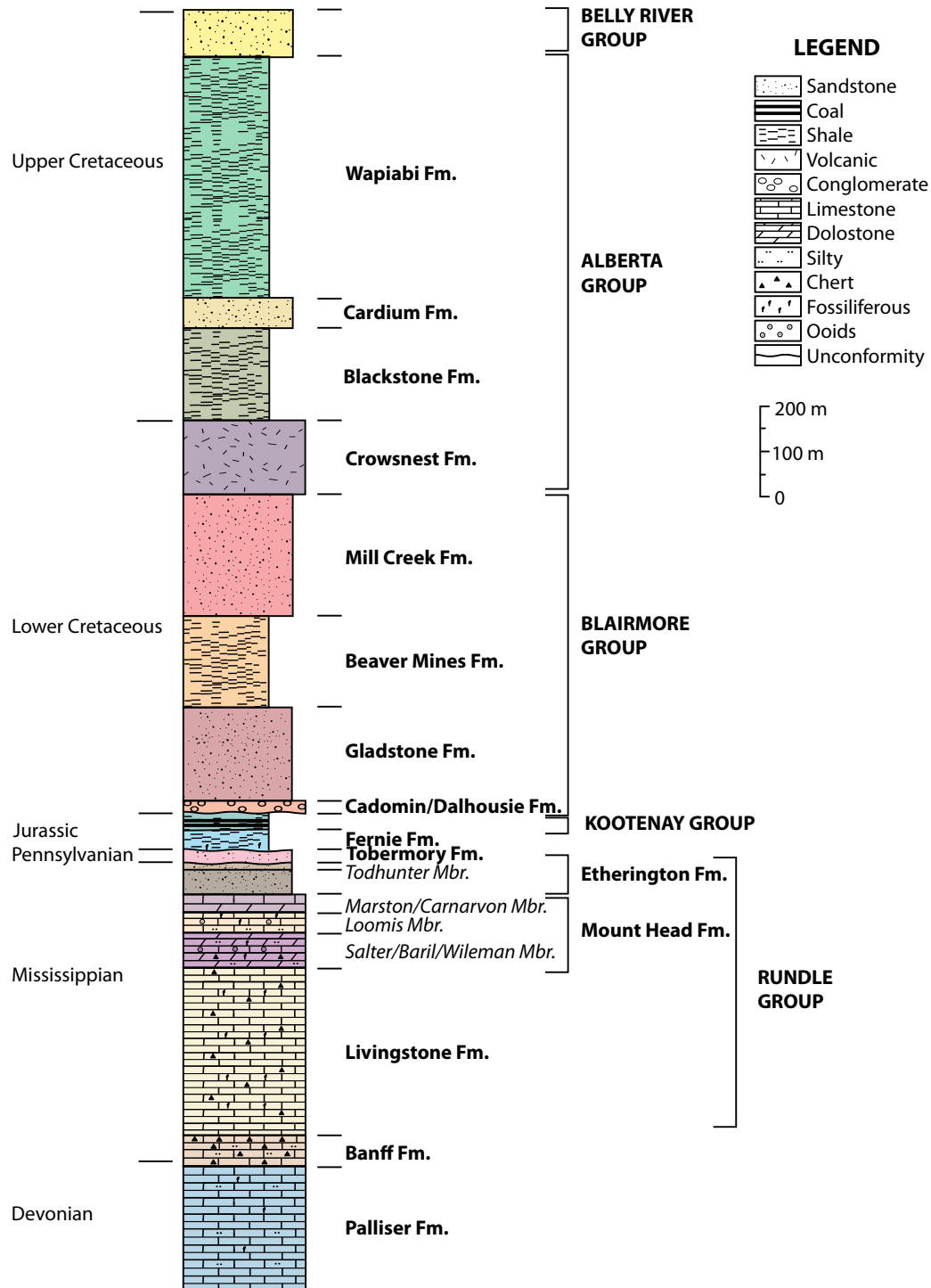


Figure 3-2: Stratigraphic column for the Crowsnest Pass area, Alberta.

ing wall of the Turtle Mountain thrust. These mountains provide an exceptional example of thin-skinned thrust-related folding, in which kinematic models can be applied and tested.

In this paper, two methods of strain analysis are performed to determine the bulk and intra-crystalline strain locally in the fold, and to compare actual finite strains with those predicted by the various published models. The predicted finite strain for each model was determined from the geometry of the published model. Understanding the deformation history of the fold in Crowsnest Pass has petroleum implications to the Rocky Mountain foothills. The fold model that best matches the Turtle Mountain fold may be applicable to folds in the subsurface.

3.2 Kinematic Models of Folds Related to Thrusting

A simple classification of folds in thrust belts (Suppe, 1983) recognizes three categories: detachment fold, fault-bend fold, and fault-propagation folds. Each model is based on an idealized kinematic process of fold development (Fig. 3-3). Detachment folds are created as units buckle above a planar décollement at a location where the amount of slip changes. Both fault-bend and fault-propagation folds form over non-planar faults. Fault-bend folds are associated with bending of the hanging wall block over ramps and flats in the footwall of a fault. Fault-propagation folds form where the thrust slip declines to zero at a thrust tip, and involve variations in both the dip and the slip along the fault plane. Over the last 30 years, kinematic models for each of the three categories have been added to the literature (e.g., Suppe, 1983; Mitra, 1990; Suppe and Medwedeff, 1990; Erslev, 1991; Homza and Wallace, 1995; Tavani and Storti, 2006). Models and their literature references discussed in this study are summarized in Table 3-1. Most of these kinematic models are constructed using angular folds with constant layer-thickness ('kink construction') for convenience, and assume plane strain.

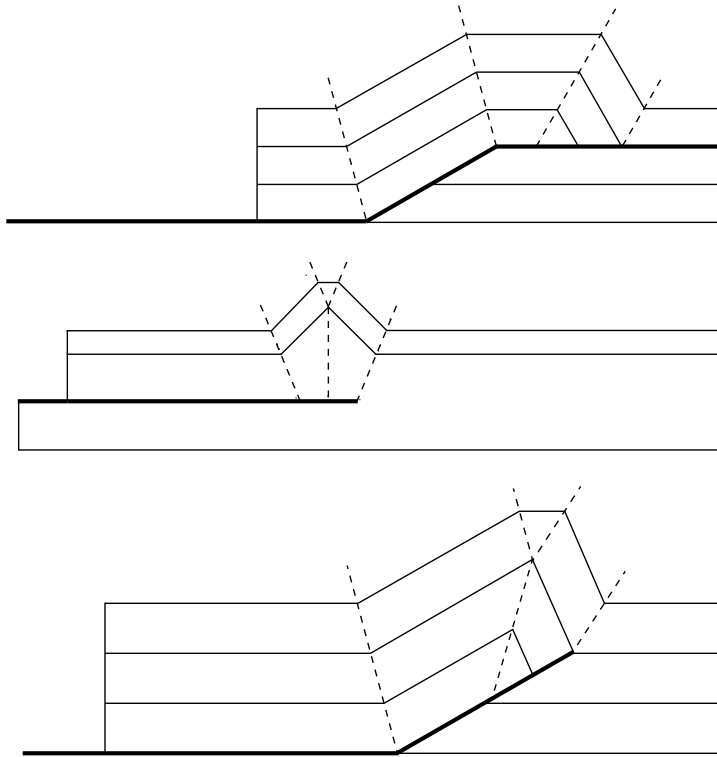


Figure 3-3: Three general fold types associated with thrust belts. The fold types are respectively, fault-bend fold (modified after Suppe, 1983), detachment fold (modified after Homza and Wallace, 1995) and fault-propagation fold (modified after Suppe and Medwedeff, 1990).

<u>Model</u>	<u>Literature Reference</u>
Fault-bend folds	
<i>A</i>	Suppe, 1983
<i>B</i>	Suppe et al., 2004
<i>C</i>	Suppe et al., 2004
<i>D</i>	Tavani and Storti, 2006
Detachment folds	
<i>i</i>	Homza and Wallace, 1995
<i>ii</i>	Homza and Wallace, 1995
<i>iii</i>	Epard and Groshong, 1995
<i>iv</i>	Epard and Groshong, 1995
<i>v</i>	Wilkerson et al., 2007
Fault-propagation folds	
<i>a</i>	Suppe and Medwedeff, 1990
<i>b</i>	Suppe and Medwedeff, 1990
<i>c</i>	Mitra, 1990
<i>d</i>	Mitra, 1990
<i>e</i>	McNaught and Mitra, 1993
<i>f</i>	Erslev, 1991
<i>g</i>	Erslev and Mayborn, 1997
<i>h</i>	Tavani et al., 2006

Table 3-1: Table of kinematic fold models and their literature references.

3.2.1 Fault-Bend Folds

Fault-bend folds occur where a fault ramps between upper and lower décollements (“flats”) that are bedding parallel. With shortening, rocks in the hanging wall change shape as they are displaced over the changes in fault dip. The fault-bend model has been applied to folds in many areas, following Suppe’s (1983) study of examples in the southern Appalachians (Fig. 3-4). The earliest kinematic model (model *A* in Fig. 3-5) is based on the assumptions of: preservation of layer thickness; conservation of bed length; layer-parallel slip; and constant displacement of the hanging wall on the hinterland side of the model (Suppe, 1983). As a result of these assumptions, interlimb angles (β) (Table 3-2 and Fig. 3-5, model *A*) are equal on either side of the fold axial surface; the fault ramp and backlimb of the fold have equal dips; the fault must propagate through the model at the start of translation before hanging wall translation; and no distortion occurs where layers are horizontal. In the backlimb and forelimb of the fold, the direction of shortening is at a high angle to the axial surface, but shortening is larger in the forelimb.

Based on observed seismic and field examples, Suppe et al. (2004) developed modifications of model *A* (here models *B* and *C*) which include distortion in the layer above the fault. In both models, the assumptions (of model *A*) are relaxed only in the weak décollement layer at the base of the ramp, which results in a backlimb dip lower than the fault ramp dip. Model *B* contains bedding-parallel simple shear in the décollement layer, and along the ramp the slip declines to zero at the base of the hanging wall (no basal fault slip)(Suppe et al., 2004). The strain for model *B* cannot be predicted from ramp geometry for the lower décollement layer as it is dependent on the amount of shear. Shear in the upper units is similar to model *A*, but changes depending on the dip of bedding in the backlimb, which is not equal to the dip of the fault ramp. Model *C* involves pure-shear in

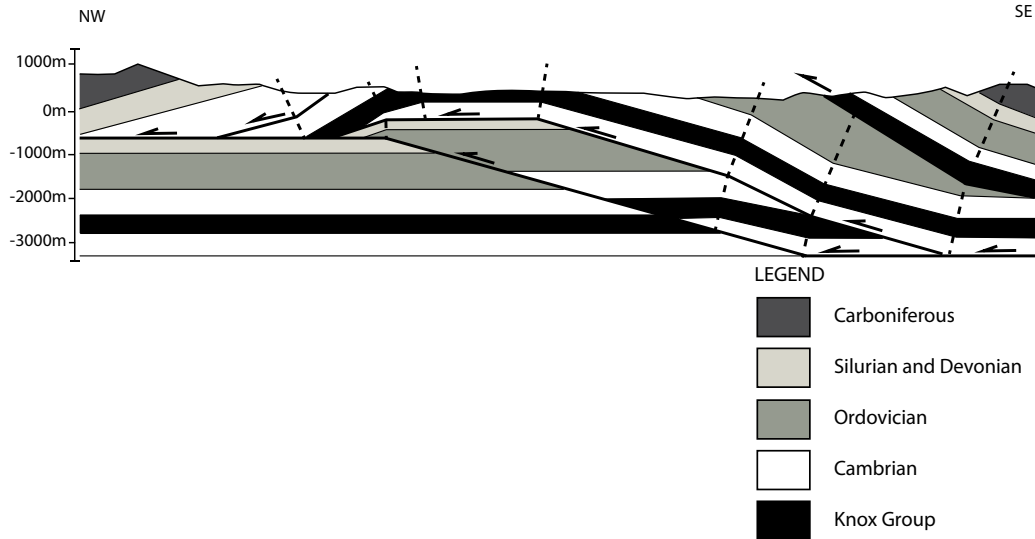


Figure 3-4: Fault-bend fold in the southern Appalachians (modified from Suppe, 1983). Section is at natural scale (vertical exaggeration 1:1).

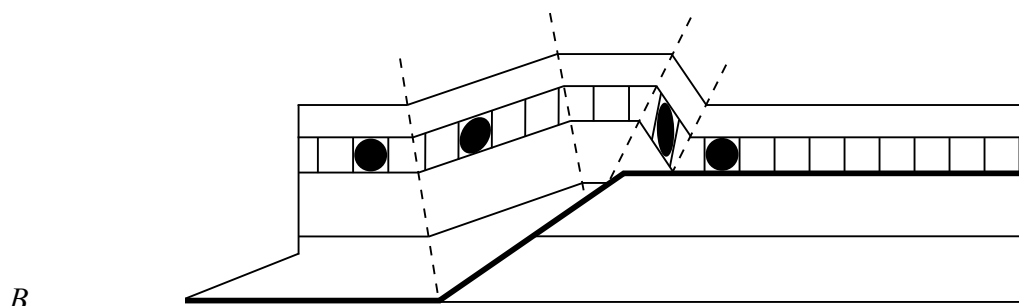
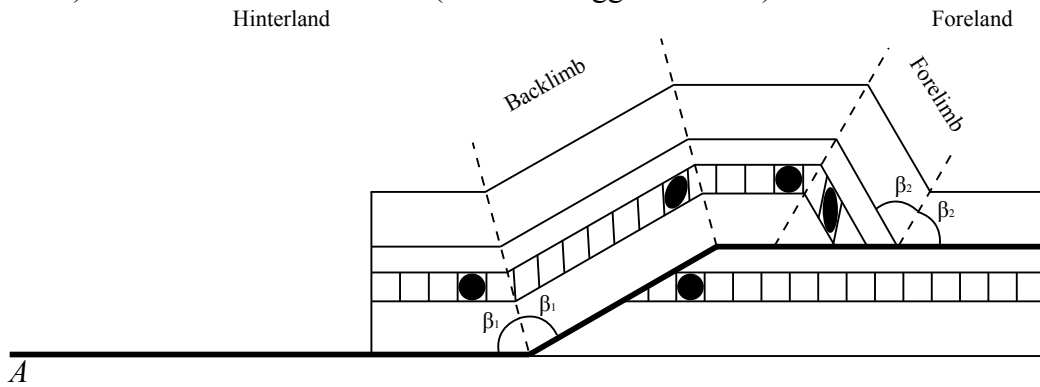


Figure 3-5: Kinematic models of fault-bend folds proposed in the literature, here models A-D (modified A after Suppe, 1983; B and C after Suppe et al., 2004; D after Tavani and Storti, 2006). Ellipses show finite strain that is calculated from fold geometry. β_1 are the interlimb angles of the backlimb and β_2 are the interlimb angles of the forelimb.

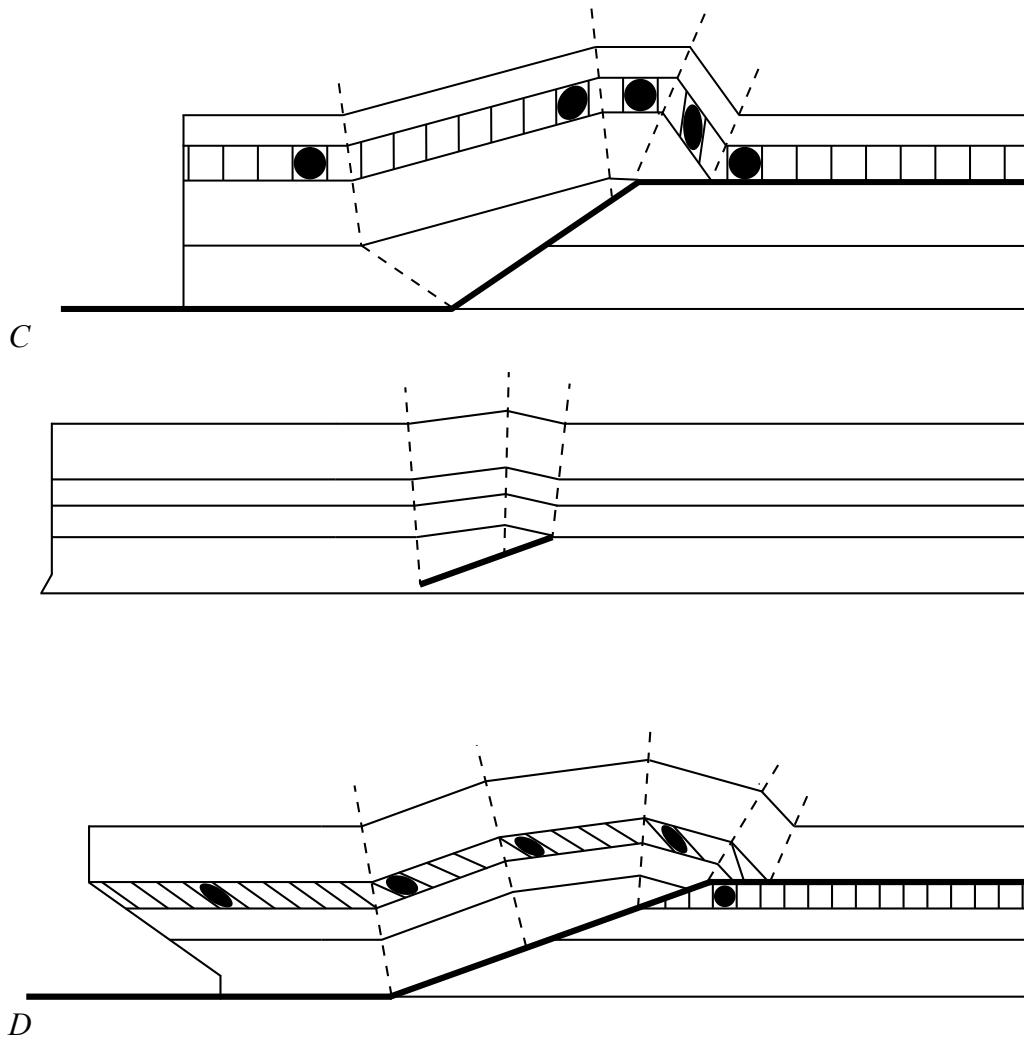


Figure 3-5: continued.

<u>Symbol</u>	<u>Definition</u>
β	Fold interlimb angle on either side of the fold axial surface
S_1	Stretch for long axis of strain ellipsoid
S_2	Stretch for intermediate axis of strain ellipsoid
S_3	Stretch for short axis of strain ellipsoid
a	Axial ratio equal to S_1/S_2
b	Axial ratio equal to S_2/S_3
k	Shape factor of strain ellipsoid equal to a/b
R_s	Strain ratio or ellipticity
Φ	Orientation of long axis of strain ellipse relative to horizontal

Table 3-2: Table of symbols.

the décollement layer, resulting in shortening of the layer parallel to bedding, and thickening perpendicular to bedding (Suppe et al., 2004). The strain associated with the upper units of model *C* is similar to the previous model, and also cannot be determined for the décollement layer from fault dip alone.

Tavani and Storti (2006) observed that the previous models have an unlikely kinematic pathway involving complete fault-propagation before hanging wall translation. They proposed a model (model *D*) as an end-member to fault-propagation fold model *g* (see below), which relaxes the assumptions about the fold's kinematic pathway. Initially, the thrust ramp nucleates somewhere within the stack of layers and then propagates upward and downward, creating an anticline in the hanging wall prior to forward translation (Tavani and Storti, 2006). When either the upper or lower fault tip joins a flat décollement, the anticline is transported toward the foreland (Tavani and Storti, 2006). The layers containing shear have noticeably different strain than the previous models. The orientation of the shortening direction is at a low angle to the axial surface, and the strain may be larger on the backlimb than the forelimb.

3.2.2 Detachment Folds

Detachment folds occur where a fault surface is relatively horizontal and the slip declines to zero at a fault tip. The units are folded to accommodate shortening above the fault tip. Kinematic models for detachment folds are shown in Fig. 3-6, *i-v*. Classic detachment folds have been associated with décollements in the Jura Mountains, Switzerland (Fig. 3-7) (Mitra, 2003). The simplest kinematic model (Fig. 3-6, model *i*) is based on the assumptions that: there are incompetent layers in the centre of the fold which do not preserve thickness but preserve area; the competent units above form parallel folds which conserve bed lengths and thicknesses; these competent layers deform by flexural slip; the deformation

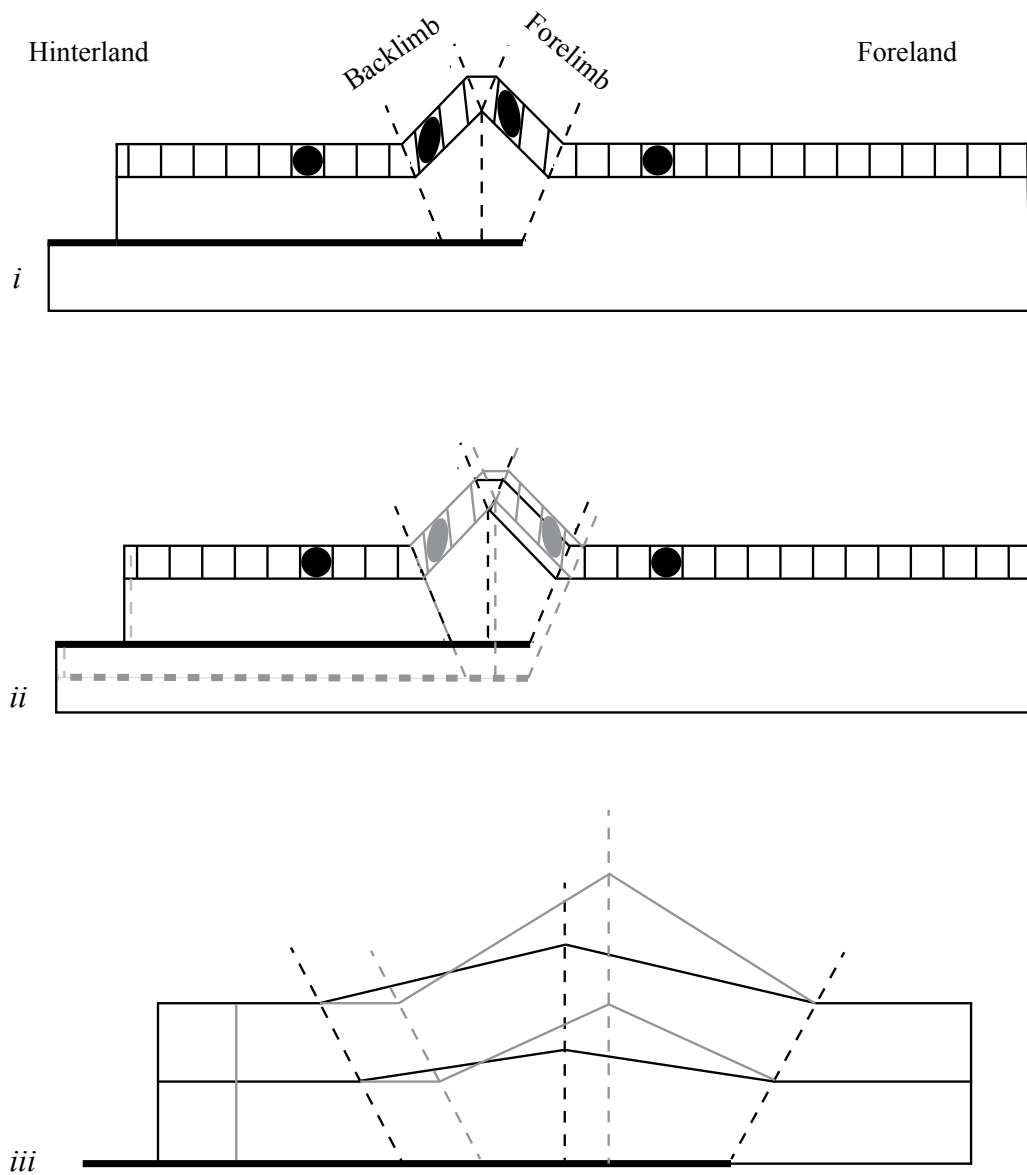


Figure 3-6: Kinematic models of detachment folds proposed in the literature, here models *i-v* (modified *i* and *ii* after Homza and Wallace, 1995; *iii* and *iv* after Epard and Groshong, 1995; *v* after Wilkerson et al., 2007). Ellipses show finite strain that is calculated from fold geometry. Grey indicates geometry and strain with further deformation.

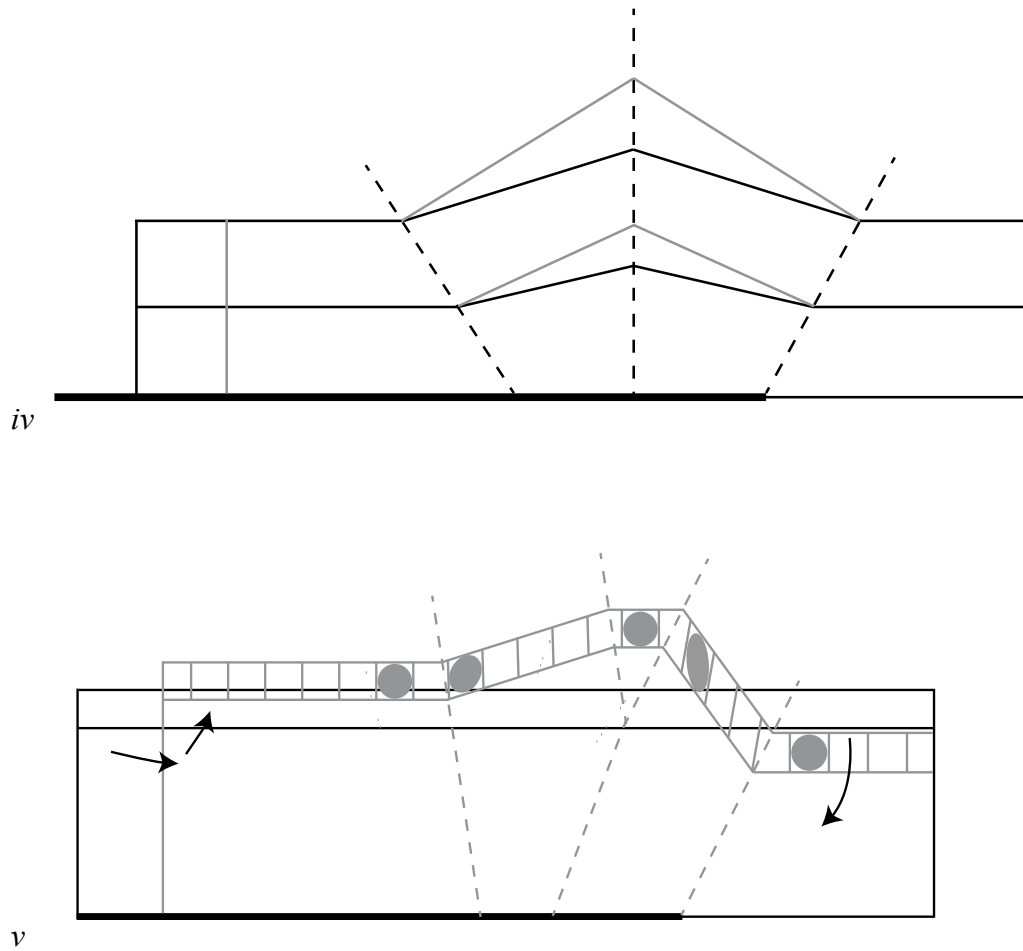


Figure 3-6: continued

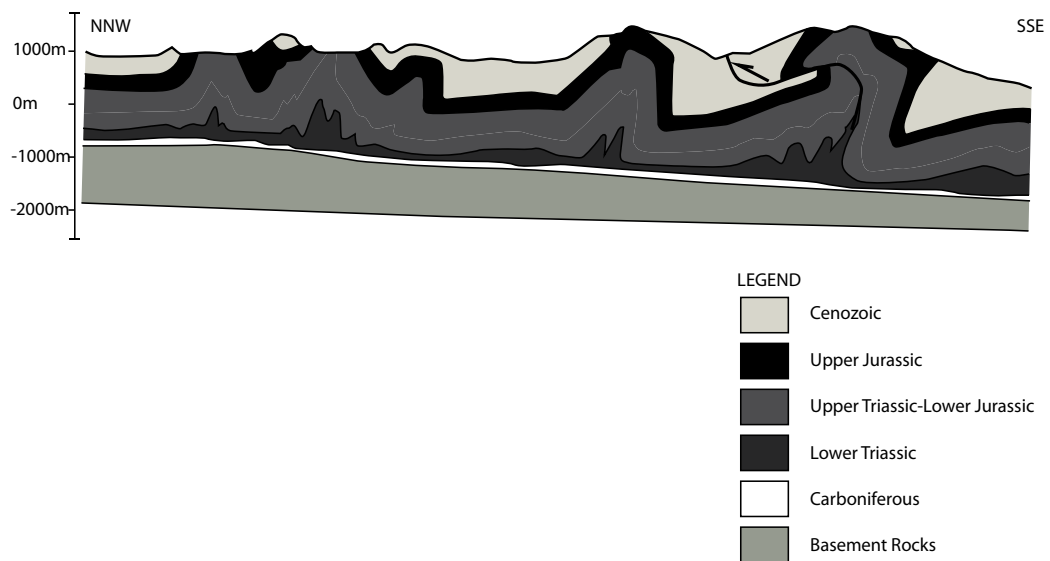


Figure 3-7: Detachment fold in the Jura Mountains (modified from Mitra, 2003).

The section is at natural scale (vertical exaggeration 1:1).

is restricted between the outer axial surfaces of the fold; and detachment depth is constant (Homza and Wallace, 1995). As a result of these assumptions, fold growth is limited because it requires a linear increase in area with increased shortening, requiring hinges to migrate and fold limbs to change length during fold growth (Homza and Wallace, 1995). The strain associated with the fold model can be readily determined for the upper competent layer. The strain is the same in both limbs of the fold, and the direction of shortening is at a high angle to the axial surface.

Based on observed fold shapes, Homza and Wallace (1995) developed another model (model *ii*) that could have fixed-hinge fold growth. In order to do this, they relaxed the assumption that detachment depth remains constant. In model *ii*, the detachment depth either increases or decreases with fold progression; with increased detachment depth, the height of the fold increases and with decreased detachment depth, the fold widens (Homza and Wallace, 1995). The strain associated in the upper competent layer with model *ii* is the same as model *i*.

Epard and Groshong (1995) proposed two end member models (model *iii* and *iv*) that relax the assumptions of constant bed length and layer thickness in model *i*, but are instead area balanced (Epard and Groshong, 1995). Model *iii* has fixed hinge fold growth, where no material can move through the fold axial surfaces (Epard and Groshong, 1995). Model *iv* has migrating hinges, where material can move through the axial surfaces. The distance between the outer axial surfaces remains constant (Epard and Groshong, 1995). Due to thickness changes through the limbs of the fold, the strain does not show a simple relationship to dip. Wilkerson et al. (2007) introduced a kinematic model, model *v*, based on observed thickness changes in the incompetent unit outside the detachment fold anticline in the Nucios Fold Complex in the Monterrey Salient, Mexico. It was observed that

there can be higher elevation in the hinterland than the foreland. Model *v* relaxes the assumption that deformation takes place only between the outer axial surfaces of the fold. Therefore, shortening can be by either hinge-migration or limb-rotation (Wilkerson et al., 2007). The strain related to model *v* is similar to model *i*, as the shortening direction is typically at a high angle to the axial surface. However, the strain is different in each limb, and larger in the forelimb.

3.2.3 Fault-Propagation Folds

Fault-propagation folds are formed during shortening when rocks are transported above a fault ramp which contains a propagation fault tip, where the slip declines to zero. Above the fault tip, the rocks are deformed by folding. Kinematic models for fault-propagation folds are shown in Fig. 3-8, *a-h*. Examples of fault-propagation folds have been described in the Turner Valley structure in southern Alberta (Fig. 3-9) (Mitra, 1990) and in the Meilin anticline of the western Taiwan overthrust belt near Chiayi (Suppe and Medwedeff, 1990). The simplest kinematic model purposed (Suppe and Medwedeff, 1990) (model *a*) is based on the assumptions that: the fold has hanging wall rocks that are unsheared at the hinterland side; the fault ramp propagates up-section and towards the foreland from a starting point on a lower flat; there is conservation of bed length; layer thickness remains constant; and material rolls through the fold axial surfaces. As a result of the assumptions, the model balances (due to both constant layer thickness and bed length), the dip of the backlimb and the fault ramp are equal, and the interlimb angles (β) are equal (Table 3-2). The strain associated with model *a* is zero outside the limbs of the fold. In the backlimb of the fold there is lower strain than in the forelimb, and in both limbs the shortening direction is oblique to bedding and at a high angle to the fold's axial surfaces. The backlimb strain is identical to fault-bend fold model *A*.

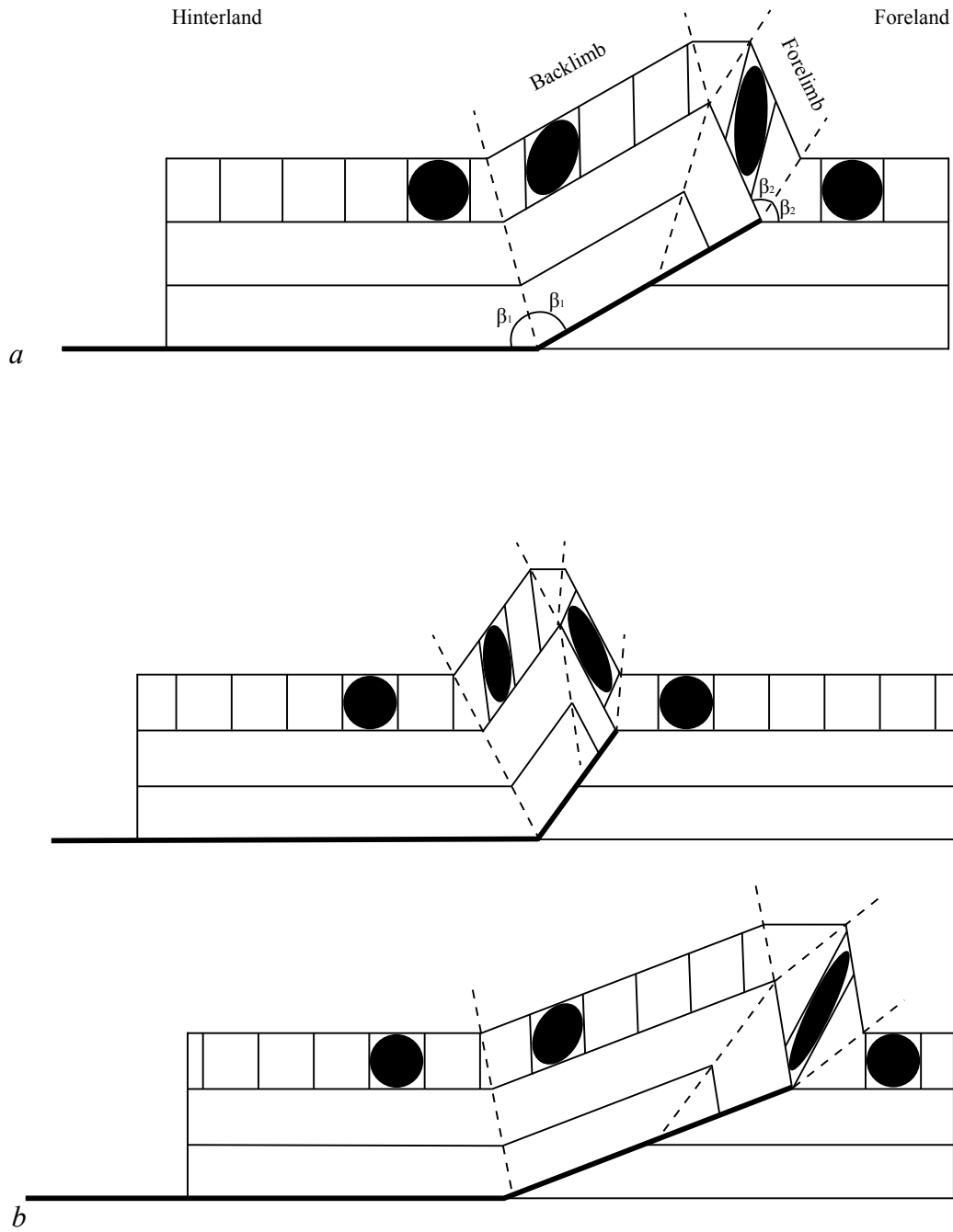
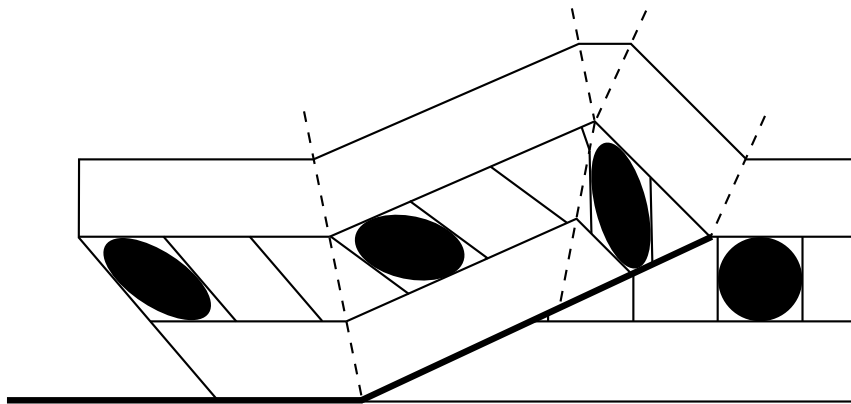
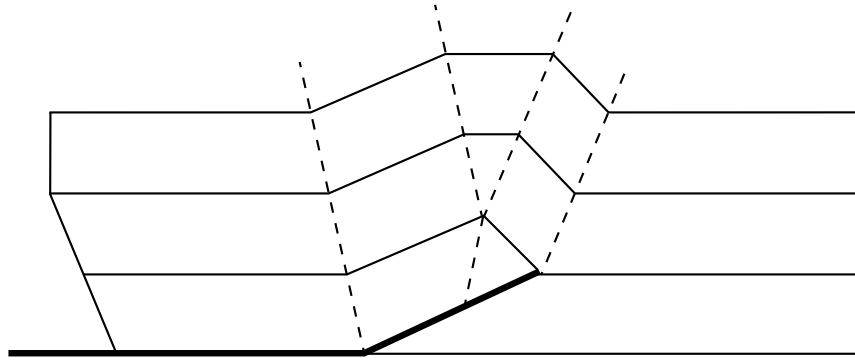
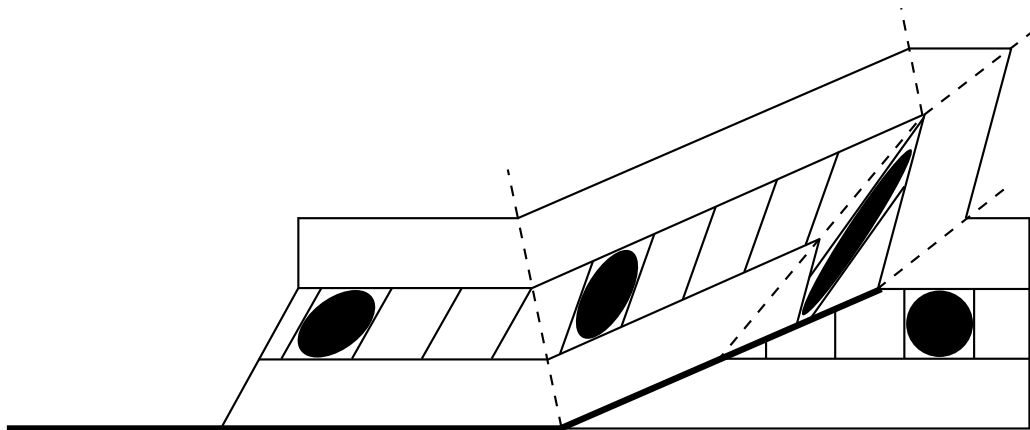


Figure 3-8: Kinematic models of fault-propagation folds proposed in the literature, here models *a-h* (modified *a* and *b* after Suppe and Medwedeff, 1990; *c* and *d* after Mitra, 1990; *e* after McNaught and Mitra, 1993; *f* after Erslev, 1991; *g* after Erslev and Mayborn, 1997; *h* after Tavani et al., 2006). Ellipses show finite strain that is calculated from fold geometry. β_1 are the interlimb angles of the backlimb and β_2 are the interlimb angles of the forelimb.



c



d

Figure 3-8: continued

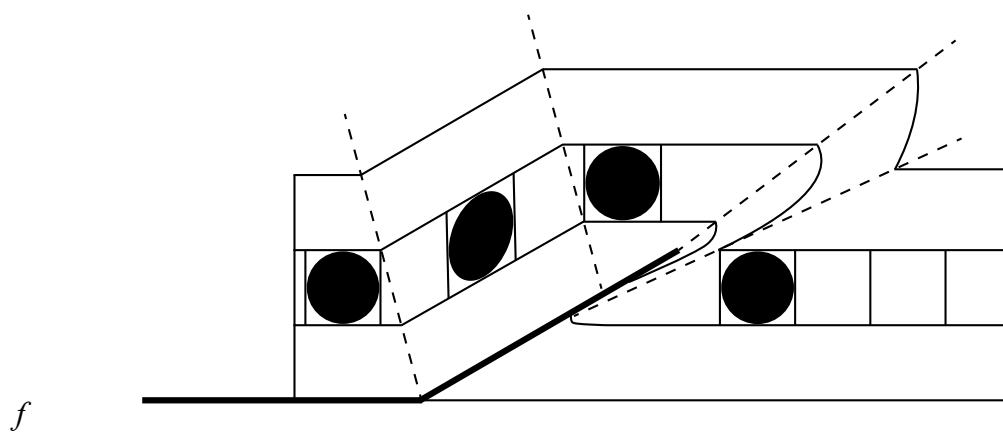
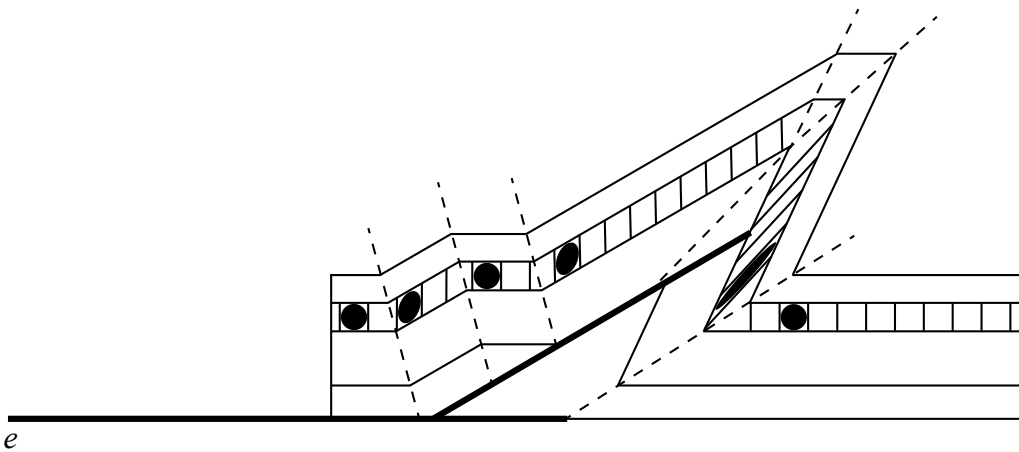
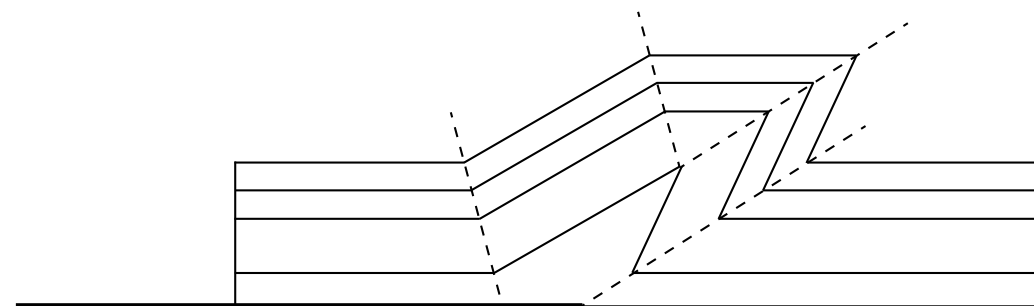
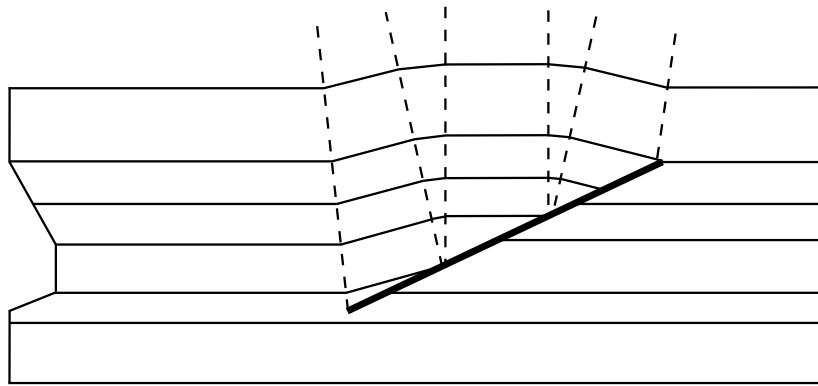
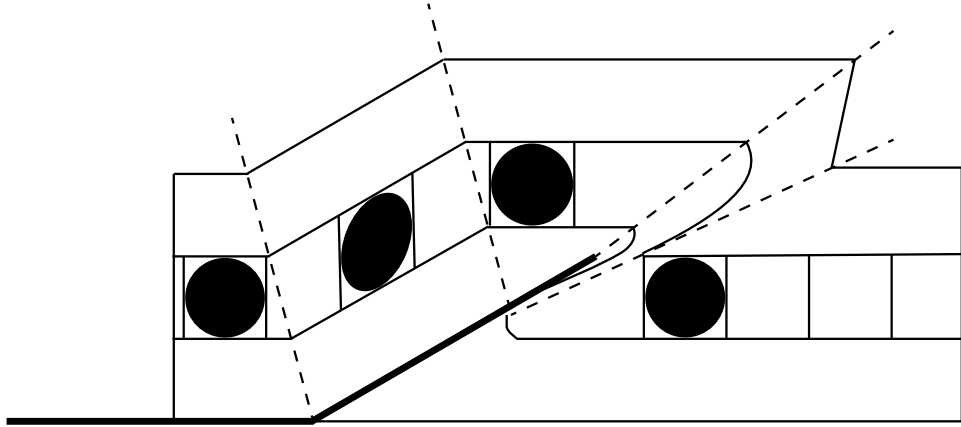


Figure 3-8: continued

σ



h

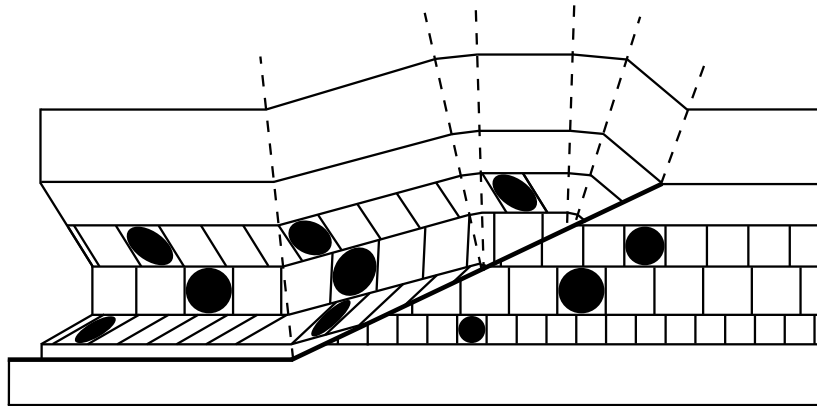


Figure 3-8: continued

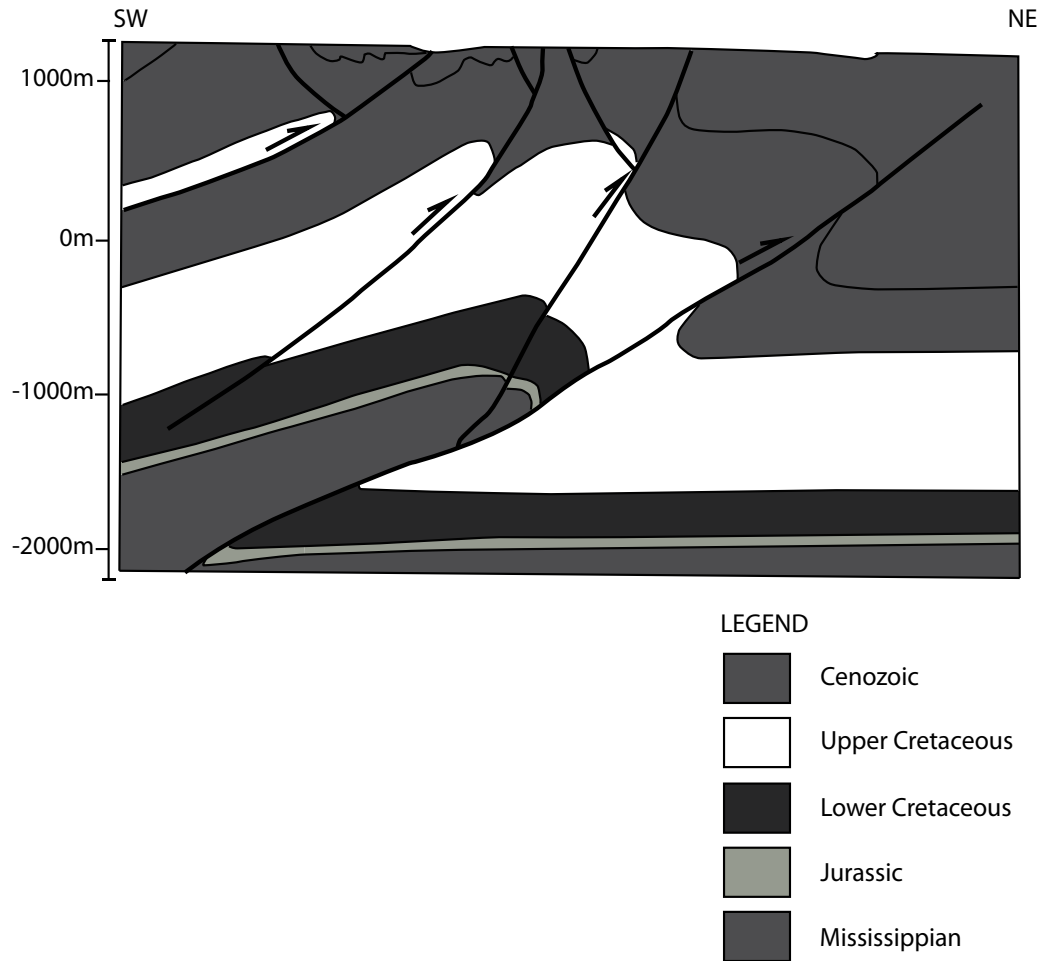


Figure 3-9: Fault-propagation fold in the Turner Valley Structure (modified from Mitra, 1990). The section is at natural scale (vertical exaggeration 1:1).

Based on the speculation that beds might not roll through the axial surfaces, Suppe and Medwedeff (1990) purposed a fixed axial surface model (model *b*). The model removes the assumption that material rolls through the forelimb axial surfaces. Therefore, layer thickness cannot remain constant and there is thickening or thinning in the forelimb of the fold, depending on the ramp angle. This implies that the interlimb angles (β) can no longer be equal. The strain orientation associated with model *b* resembles model *a*. In the backlimb of the fold, the strain is larger with higher angle ramps, whereas on the forelimb, the strain is larger with lower angle ramps.

Mitra (1990) proposed two models which relax the assumption that there is no shear in the hanging wall on the hinterland side of the fault-propagation fold. Both models (model *c* and *d*) involve thickness changes and are area balanced. In *c*, the interlimb angles (β) remain constant through fold progression. The lower units involve bed thickness changes, which take place as the fold progresses; the upper units have constant bed thicknesses (Mitra, 1990). Unlike model *a*, in the lower units of model *c* the shortening direction in the backlimb is at a low angle to the axial surface, and the amount depends on the shear in the hanging wall on the hinterland side. In model *d*, the interlimb (β) angles change as the fault propagates, and thickness changes are distributed throughout the fold (Mitra, 1990). The strain for model *d* has approximately the same direction as model *a*, but is greater.

Model *e* is based on the occurrence, in natural examples, of observed footwall synclines that the previous models could not explain (McNaught and Mitra, 1993). The model relaxes the assumption that the ramp fault develops at the beginning of deformation. The footwall syncline is the result of the development of an earlier detachment fold above a flat fault segment; a thickened weak layer in the core of the detachment fold allows the thrust to cut up section (McNaught and

Mitra, 1993). The underlying syncline is derived from the forelimb of the detachment fold (Fig. 3-8) (McNaught and Mitra, 1993). The strain for model *e* shows similar orientations to model *a*, but differs in that in the forelimb it is larger. In the backlimb there may be areas of zero strain, depending on how the fold develops.

Erslev (1991) observed curved fold forelimbs in naturally occurring fault-propagation folds and that the hinge tightened downward towards the fault. Model *f* is based on this observation and relaxes the assumption that there are planar limbs. Model *f* contains a concentrated triangular zone of shear expanding upward from the thrust tip, distributed into the overlying units. The shear zone expands upward and outwards by simple and oblique shear (at an angle to bedding) (Erslev, 1991). The strain predicted for the backlimb of model *f* is the same as the model *a*. In the forelimb of the fold, in the triangular zone of shear, it is impossible to predict the strain (due to the heterogeneity of shear). The model predicts a large zone with no strain on the crest of the structure, which is broader than the other models.

Erslev and Mayborn (1997) also proposed model *g*. In the triangular zone of shear, model assumptions are the same as model *f*. However, in the units above, folds are assumed to have “kink” style similar to model *a*. The strain associated with model *g* in the lower units is the same as model *f*.

Tavani et al. (2006) made the observation in naturally occurring fault-propagation folds that the dip of the backlimb is often shallower than the dip of the ramp. Based on this observation, they relaxed the assumptions that at the beginning of deformation both the fault ramp and tip develop, and that there is no shear in the hanging wall on the hinterland side. They put forward a model *h*, where the deformation along the ramp is initially localized at a nucleation point or segment in the layers (Tavani et al., 2006). The initial configuration consists of a basal décollement and a thrust ramp which propagates both upward and down-

ward from its starting point or segment. There is hanging wall shear in the layers through which the ramp propagates, and the layer-parallel shear for each layer depends on amount and timing of deformation along the ramp (Tavani et al., 2006). The amount of strain in model h depends on the amount of shear that takes place during fault propagation. The strain in model h varies throughout the model. In the forelimb and backlimb of the fold, the shortening direction is at varying angles to the fold's axial surface depending on the hanging wall shear. However, in the crest region of the structure, there are areas where the strain is zero.

3.3 Data Collection and Strain Analysis

Rock samples were collected between August 2010 and June 2012. Coarse grainstone samples were collected from the backlimb, hinge, and forelimb of the anticline associated with the Turtle Mountain thrust (Fig. 3-1). Three orientated thin sections were cut from each sample, along the fold profile plane, the bedding plane, and a third plane mutually perpendicular to the other two (Fig. 3-10). Strain analysis was performed to determine the bulk and intra-crystalline strain locally in the fold, and compared to that predicted by the models.

3.3.1 Fry Method

The Fry (1979) method determines the two-dimensional bulk finite strain using the measurements of the distances and directions between object centres. The Fry method produces usable results only if the objects are anticlustered: statistically, the centres of objects tend to be separated by a minimum distance. Typically, this occurs in well sorted sedimentary rocks where the spacing of object centres is determined by grain size. In deformed rocks, the objects' centres become closer together in the direction of shortening and further apart in the direction of maximum stretch; these are proportional to the strain ellipse diameters (Fry, 1979). This technique uses an image of the deformed rock in which the

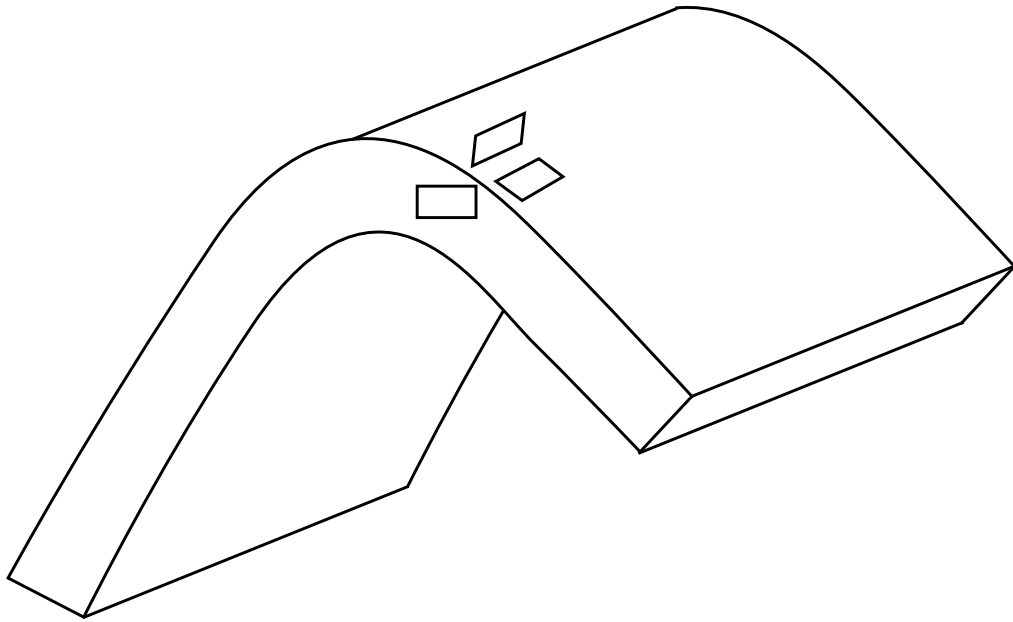


Figure 3-10: The direction on the fold of the three orientated thin sections cut from each sample, along the fold profile plane, the bedding plane, and a third plane mutually perpendicular to the other two.

position of each object centre is determined. The Fry plot was first performed on tracing paper over the original image (Fig. 3-11). In this technique, a reference point is marked on the centre of the tracing paper. The reference point is placed over one object centre. The centres of all the other adjacent objects are marked on the tracing paper. The reference point is moved to another object, keeping the orientation of the paper constant, and the process is repeated (Fry, 1979). The Fry plot shows the frequency with which points have neighbouring points at different distances in different directions (Fry, 1979). In the centre of the Fry plot (Fig. 3-12), there is a vacancy because neighbouring object centres can be no closer than the sum of their radii. That is, the objects are anticlustered. Depending on the degree of anticlustering, there may be a high density rim (Fig. 3-12) around the vacancy, representing the statistically most common distance between neighbouring objects. In deformed rocks, the vacancy represents the shape of the finite strain ellipse (Fry, 1979). With a random distribution no central vacancy field appears (Waldron and Wallace, 2007). For the Fry method to be useful and accurate it depends on the degree of anticlustering, the number of objects, and closeness of objects (Waldron and Wallace, 2007).

The Fry method has a number of limitations. Amongst these limitations are the large number of objects required to make quantitative results, and the subjective visual interpretation of the shape of the elliptical vacancy in the middle of the plot (Fry, 1979). A Fry plot performed on a poorly sorted sample results in a blurred vacancy. This problem can be reduced by using a method suggested by Erslev (1988) which normalizes the centre-to-centre distance between two objects. This is done by dividing the interparticle distance between two objects by the sum of the average radii of the two objects.

Thin sections were photographed using 20X magnification on a petrographic microscope. The thin sections contained small numbers of sections

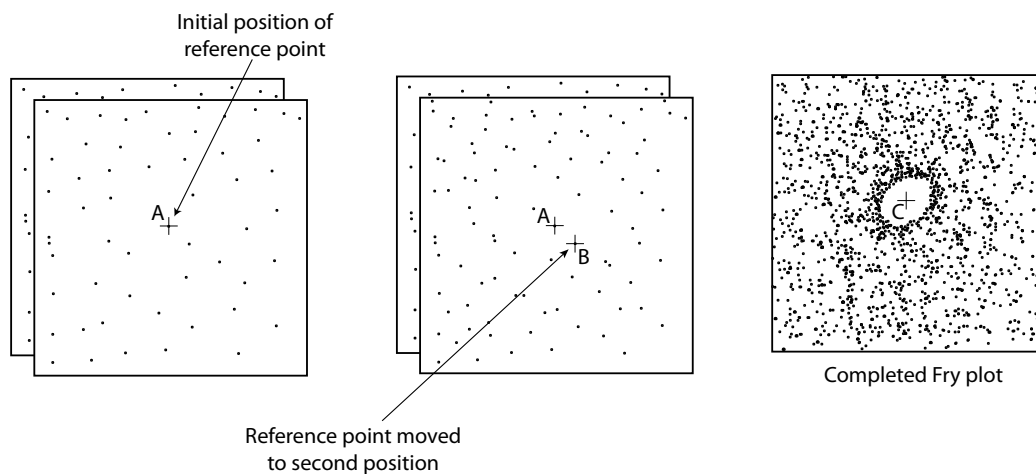


Figure 3-11: Plotting of an original Fry plot. The reference point is moved through all the successive positions (a and b) and the centers of grains are traced; the vacant area (c) in the center represents the strain ellipse.



Figure 3-12: Fry plot for thin section ML025A profile plane. Showing both the strain ellipse and the surrounding elliptical annulus.

through crinoids and other identifiable fossils, along with large numbers of twined calcite grains. The number of crinoid fossils (elliptical objects) was not sufficient for Fry plots. The more irregular shaped grains were believed to be original echinoderm fragments, together with cement overgrowth that is hard to distinguish (Fig. 3-13). The grains are evenly spaced and have an interlocking geometry, with stylolites between them. The samples contained limestone cement matrix with mixed-skeletal fragments and dolomite crystals. Since the grains are original to the sample, and therefore would have originally been randomly distributed, they were all used for strain analysis. The photomicrographs were brought into the program Adobe Illustrator and the individual calcite crystals were outlined. The traced crystal images were brought into the image analysis program ImageJ.

Computer techniques assist in the interpretation of the object data. The Fry method was originally performed on rocks where the centres of the objects could be determined visually (elliptical/circular objects). With the use of computer programs, irregular shaped grains can now be used. The program ImageJ identifies each traced object and determines: the object's area, the location of the object's centre, the lengths of the major and minor axes, and the orientation of the major axis. From the information determined, normalized Fry plots were produced using the computer program FryJ (Waldron and Wallace, 2007).

Computer methods can also assist in determination of the best-fit elliptical boundary for the elliptical vacancy, reducing observer subjectivity (Waldron and Wallace, 2007). This improves the location of the strain ellipse when the shape of the vacancy is poorly defined (Appendix D). The program FryJFit used to fit strain ellipses was developed by Waldron and Wallace (2007) using the ImageJ macro language. The FryJFit program uses the plot information determined by FryJ and outputs a best fitting ellipse. This is done by an iterative point-count density method which determines the ellipse that shows the largest difference

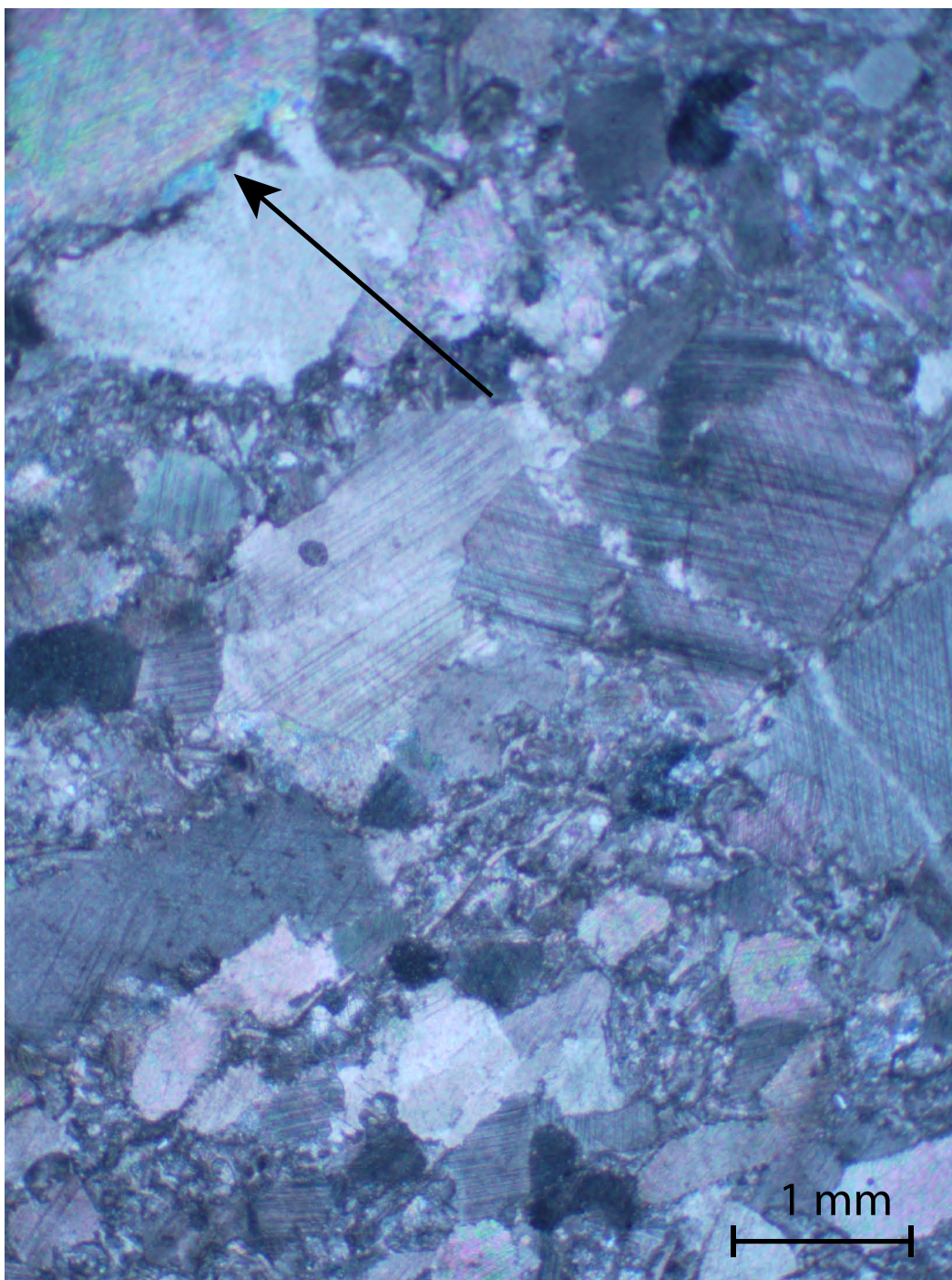


Figure 3-13: Photomicrograph of thin section ML024A from the profile plane in polarized light, shows both interlocking geometry of calcite grains and stylolites (shown by arrow).

(contrast) between the density of points in the ellipse and a surrounding elliptical annulus. In a successful fit, this annulus contains the highest point density (Waldron and Wallace, 2007). The best-fit ellipse is described by a strain ratio (R_s) and an orientation (ϕ) relative to horizontal (Table 3-2 and Appendix D).

The error for ϕ or R_s can be investigated by graphing the variability of density contrast against ϕ or R_s while keeping the other variables fixed. When contrast is plotted against ϕ , contrast rises to a peak around the best-fit value of ϕ . The width of the peak (relative to the scatter of values) is an indicator of the error associated with the best-fit value (Fig. 3-14). A similar procedure is used for R_s . The results for most sections indicate that ϕ is determined with a precision typically $\pm 3^\circ$ and R_s with a precision of ± 0.05 .

3.3.2 Calcite Strain Gauge Method

The calcite strain gauge method measures the internal strain magnitude and direction using twin sets in moderately deformed calcite. The theory used to determine the strain is that during twinning, part of a grain is rotated in simple shear by a fixed amount, which is controlled by the crystallography (Evans and Groshong, 1994). Each calcite grain has three stress axis orientations which are most favourable for producing twins. When the imposed stress acts parallel to these orientations, twinning in the grain is favoured. The principal stress and strain axes are assumed to be statistically parallel for small strains; the favoured stress axes are estimates of the finite strain axes. For a single crystal the pole to the twin plane, the c-axis of the calcite and the favoured maximum compressive stress axis are all coplanar, and perpendicular to the twin plane (Fig. 3-15) (Groshong, 1972). The angle between the favoured stress axis and the twin plane is known to be 45° ; between the c-axis and the twin plane pole the angle is 26.5° (Groshong, 1972).

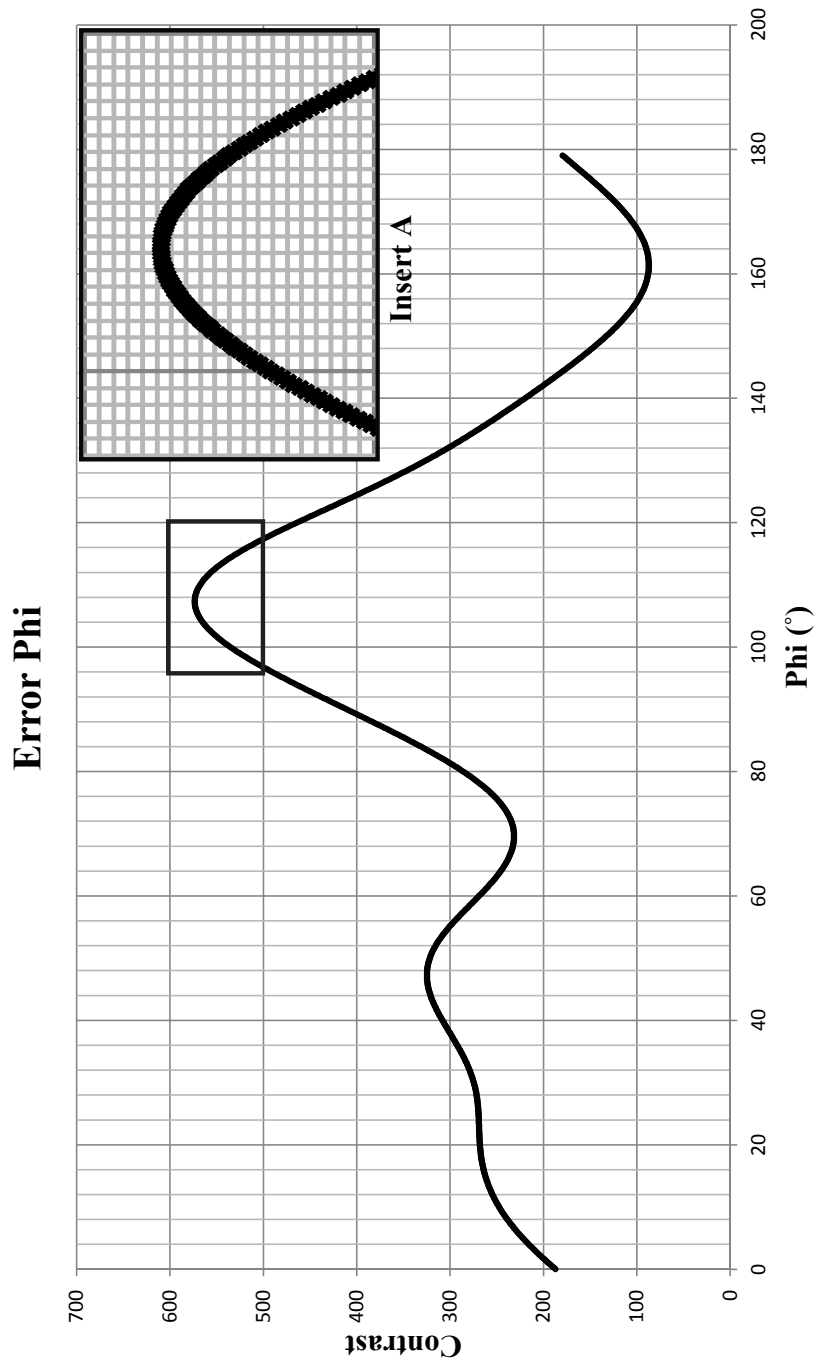


Figure 3-14: The error for phi determined by graphing the variability of density contrast against phi while keeping the other variables fixed. The contrast rises to a peak around the best-fit value of phi. The width of the peak (relative to the scatter of values) is an indicator of the error associated with the best-fit value. Contrast is unitless as it is the difference in the density of points between the inner ellipse and outer elliptical annulus. Insert A is an enlarged area of the black box on the graph.

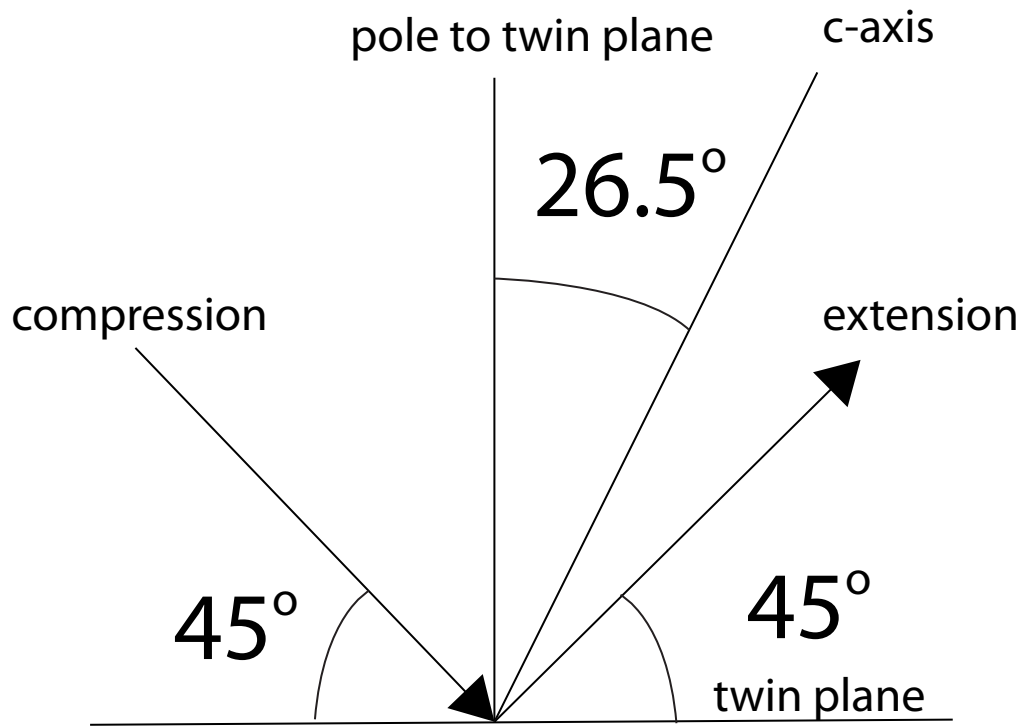


Figure 3-15: Most favourably oriented stress axes to produce twinning, modified from Groshong (1972).

Studies of calcite twinning (Burkhard, 1993) recognize two categories of twins, termed 'thick' and 'thin'. Thick twins are defined to have thicknesses greater than 5 μ (Burkhard, 1993). Thin twins tend to range in thickness from 5 to 1 μ (Burkhard, 1993). Straight thin twins are associated with lower temperature deformation, less than 200°C, and straight thick twins are associated with higher deformation temperatures, ranging from 150 – 300°C.

In the method proposed by Evans and Groshong (1994), measurements of several parameters are made on the thin sections, using a universal stage. These parameters include: the c- axis orientation, twin set orientation (determined as a pole), average thickness of the thick and thin twins, number of both thick and thin twins, and grain-width. Calculations are made to correct the thin twin width using the ratio of 0.5 of the inner width for the thick twins, due to the difficulty in measuring thin twins using a microscope. This ratio has been determined as a best estimate by comparing calculated strain to experimental values (Groshong, 1974).

The samples in this study lacked thick twins. Therefore, more accurate twin measurements were made using a scanning electron microscope (SEM). The samples were etched for 12 seconds in 10% acetic acid; it was found that this duration produced the best visibility of twin planes while preserving the integrity of the samples. SEM images were collected on grains from which previous measurements were taken; because of the homogeneity of the limestones, individual grain locations were determined comparing SEM images with gridded photomicrographs. In the SEM images, individual twins were established and true thicknesses were determined using plane orientations from the previous universal stage work (Fig. 3-16). The range of thin twin widths was between 1.18 and 3.00 μ . A value 2.00 μ is used in the strain analysis. Groshong (1974) determined that a small change in twin width does not produce a dramatic difference in computed strain magnitude or direction.

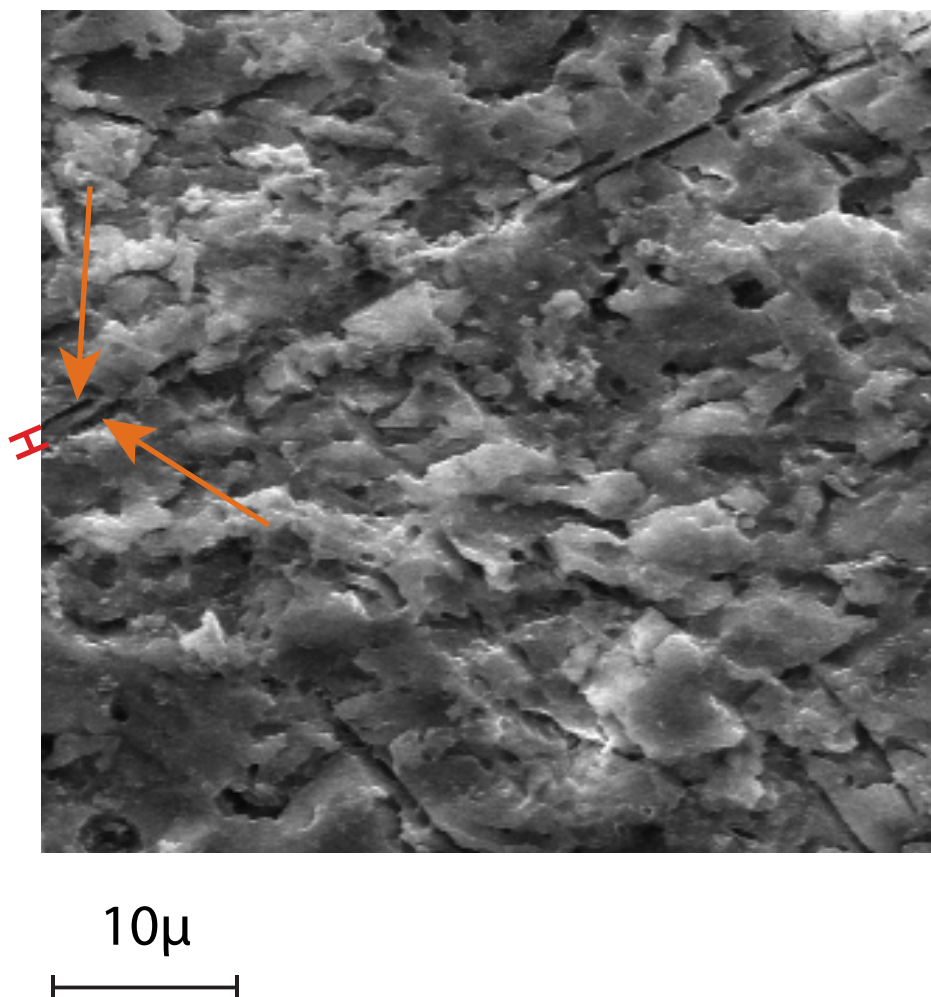


Figure 3-16: SEM image showing location of twin where thickness was measured on grain 8 of thin section ND177A profile plane. Arrows pointing to the edges of the thin twin and thickness shown by red line.

The shear strain is calculated for each twin set, and a least squares solution is used to find the strain axes for the sample (Evans and Groshong, 1994). The accuracy of the estimates of the strain axes can be improved by further “noise reduction”. The difference between the expected value and the measured twin-set strain is noise. Twenty percent of the grains are removed that have the largest deviations (Groshong et al., 1984). The strain axes, noise reduction, and the standard error are calculated using the calcite strain gauge computer program written by Evans and Groshong (1994) (Appendix E). For a more complete discussion of the techniques and the computer program, refer to Evans and Groshong (1994).

3.3.3 Strain Ellipsoid Construction

From each of the three mutually perpendicular thin sections, the Fry method produced three bulk strain ellipses, in two-dimensions. From these strain ellipses, the program by Mookerjee and Nickleach (2011) that runs in Mathematica, created best-fit equal volume strain ellipsoids. The program by Mookerjee and Nickleach (2011) was used where necessary to determine the elliptical section within an arbitrarily oriented plane through the centre of the ellipsoid.

Both the Fry and calcite strain gauge methods determine the relative magnitudes of the principal strains, not their absolute values. The results were normalized based on two different assumptions. The first normalization method assumes no volume change. The strain ellipses are determined for constant volume, such that the product of the principal strains $S_1 S_2 S_3 = 1$ (Table 3-2). Because this assumption led to orogen-parallel stretches > 1 , and because of evidence for pressure solution in the rocks, a second normalization method was used. In the second normalization method it is assumed that there is no orogen-parallel extension. This assumption is more plausible regionally as the fold is cylindrical and there is no evidence of deformation or movement in the direction of the fold axis. This

normalization assumes that the strain along the fold axis is zero and all the deformation is parallel to the fold profile plane. The principal strains are adjusted such that the stretch along the regional mean fold axis (Fig. 3-17) is equal to 1, which results in a change in the ellipsoid's volume.

3.3.4 Comparing Fry and Calcite Strain Gauge Results

Both the Fry method and the calcite strain gauge method were performed on each collected sample. The strain was compared on two-dimensional planes. For each method, strain ellipses were determined for specific planes in each of the samples. Sample results are shown in Appendix D and E.

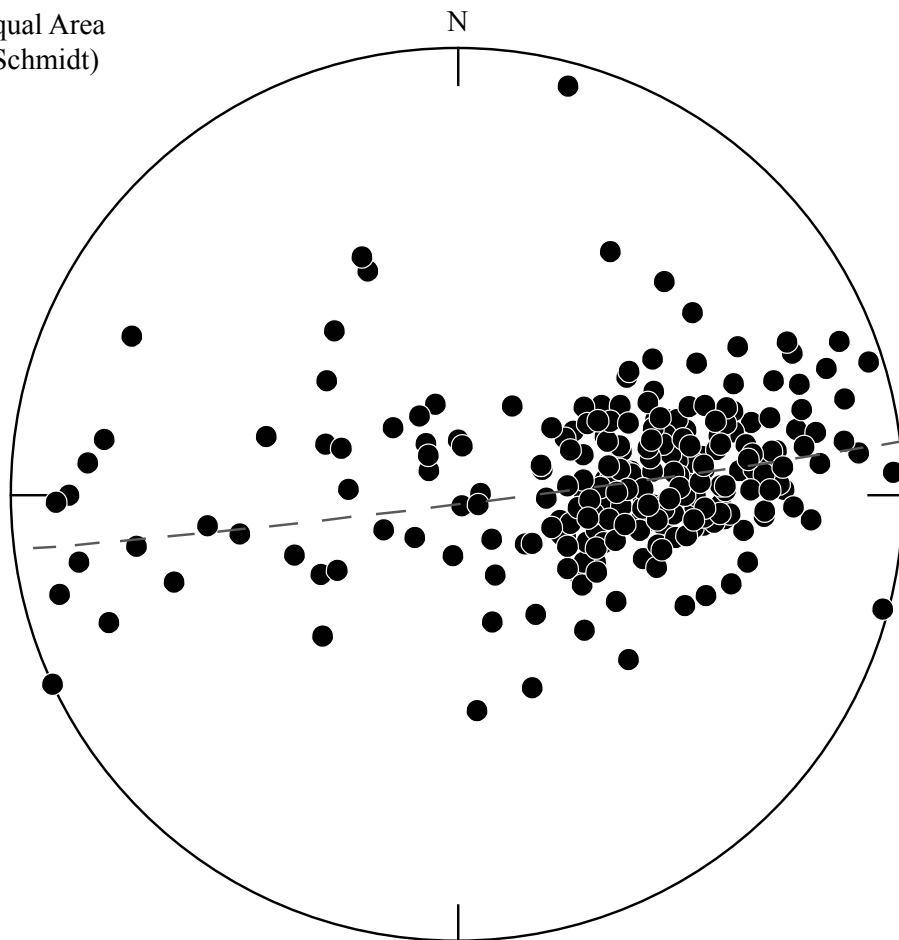
3.4 Strain Analysis Results

3.4.1 Fry Method

The ellipses determined from the Fry plots (Appendix D), their errors, and the strain ellipsoids are shown in Table 3-3. Strain ellipses (from constant volume strain ellipsoids) for the profile plane, the bedding plane, and the horizontal plane are displayed with their approximate location on the cross-section through the fold (Fig. 3-18). The strain ratio varies in the profile plane from 1.08 to 1.77, in the bedding plane from 1.06 to 2.02, and in the horizontal plane from 1.05 to 1.77. The strain ellipse results were normalized to a stretch of 1.0 along the fold axis in the horizontal direction (Fig. 3-19). The size of the ellipses in all but three are reduced by normalization, suggesting that either orogen-parallel stretch or volume loss has occurred.

The shapes of the strain ellipsoids are represented using a Flinn Plot in Fig. 3-20. They are plotted based on the axial ratios a and b , where the k value is equal to a/b , where a is S_1/S_2 , b is S_2/S_3 (Table 3-2). The plot also shows the shape factor k where $k = a/b$. Values of k that are less than one represent ellipsoids that

Equal Area
(Schmidt)



Axial

N = 252

Figure 3-17: Stereoplot of poles to bedding for all outcrop locations. The dashed line is the mean fold axis at orientation 083°/88°.

Fry Method Ellipses

SECTION	Orientation 255°/90°					Orientation Bedding					Orientation Third Plane						
	R _s	Phi	Error R _s	Error Phi	Phi	Strike	Dip	Rs	Phi	Error Rs	Error Phi	Strike	Dip	Rs	Phi	Error Rs	Error Phi
LA033A	1.30	119.7	0.50	2.5		190	49	2.03	162.7	0.06	1.7	346	48	1.13	170.1	0.03	2.7
ML023A	1.10	72.6	0.20	3.2		202	76	1.27	159.3	0.05	0.8	346	18	1.33	5.9	0.05	4.5
ND177A	1.27	21.0	0.02	3.0		127	39	1.33	154.4	0.02	2.5	166	28	1.17	5.9	0.02	2.9
ML024A	1.21	58.4	0.05	5.7		206	31	1.53	22.5	0.04	2.0	346	65	1.85	31.3	0.03	2.1
ND176A	1.27	51.0	0.03	2.7		74	30	1.10	90.0	0.02	2.6	166	88	2.40	136.4	0.07	0.6
LA036A	1.36	67.8	0.03	2.8		148	28	1.56	66.3	0.03	1.9	346	64	1.29	164.7	0.02	2.9
ML025A	1.37	84.8	0.02	2.2		332	9	1.38	151.9	0.02	2.9	166	81	1.16	1.1	0.02	2.4
ML026A	1.24	164.6	0.03	3.4		7	36	1.28	64.9	0.03	4.1	166	56	1.18	97.6	0.04	3.5
ND178A	1.78	94.0	0.04	1.5		0	72	1.08	137.8	0.02	2.9	166	88	1.18	41.2	0.02	2.5
NJ118A	1.23	48.0	0.02	2.8		163	76	1.61	91.6	0.03	0.6	346	14	1.00	15.0	0.00	0.1

Fry Method Ellipsoid

SECTION	Fold Location	From Hinge	S ₁	Trend	Plunge	S ₂	Trend	Plunge	S ₃	Trend	Plunge	Ellipticity
LA033A	back	346m	1.63	188.6	26.9	1	60.6	50.5	0.72	293.3	26.6	2.28
ML023A	back	39m	1.36	147.7	40.4	1	243.2	6.4	0.86	340.6	48.9	1.59
ND177A	back	12.6m	1.32	148.5	15.1	1	246.0	25.8	0.76	31.2	59.5	1.74
ML024A	back	2.4m	1.67	3.7	25.5	1	249.1	41.1	0.72	115.7	38.2	2.32
ND176A	hinge		1.52	180.0	48.1	1	89.7	0.2	0.65	359.5	41.9	2.33
LA036A	hinge		1.19	302.9	55.8	1	37.8	3.3	0.88	130.0	34.0	1.36
ML025A	hinge		1.12	358.0	7.1	1	197.0	82.5	0.76	88.3	2.4	1.46
ML026A	fore	2.9m	1.17	76.3	0.3	1	167.4	75.2	0.85	346.2	14.8	1.37
ND178A	fore	8.8m	1.20	352.0	44.9	1	163.0	44.7	0.61	257.5	4.5	1.97
NJ118A	fore	400m	1.38	248.2	56.8	1	75.9	33.0	0.90	343.6	3.5	1.53

Table 3-3: The bulk strain ellipses determined from the Fry plots, their errors and the strain ellipsoids.

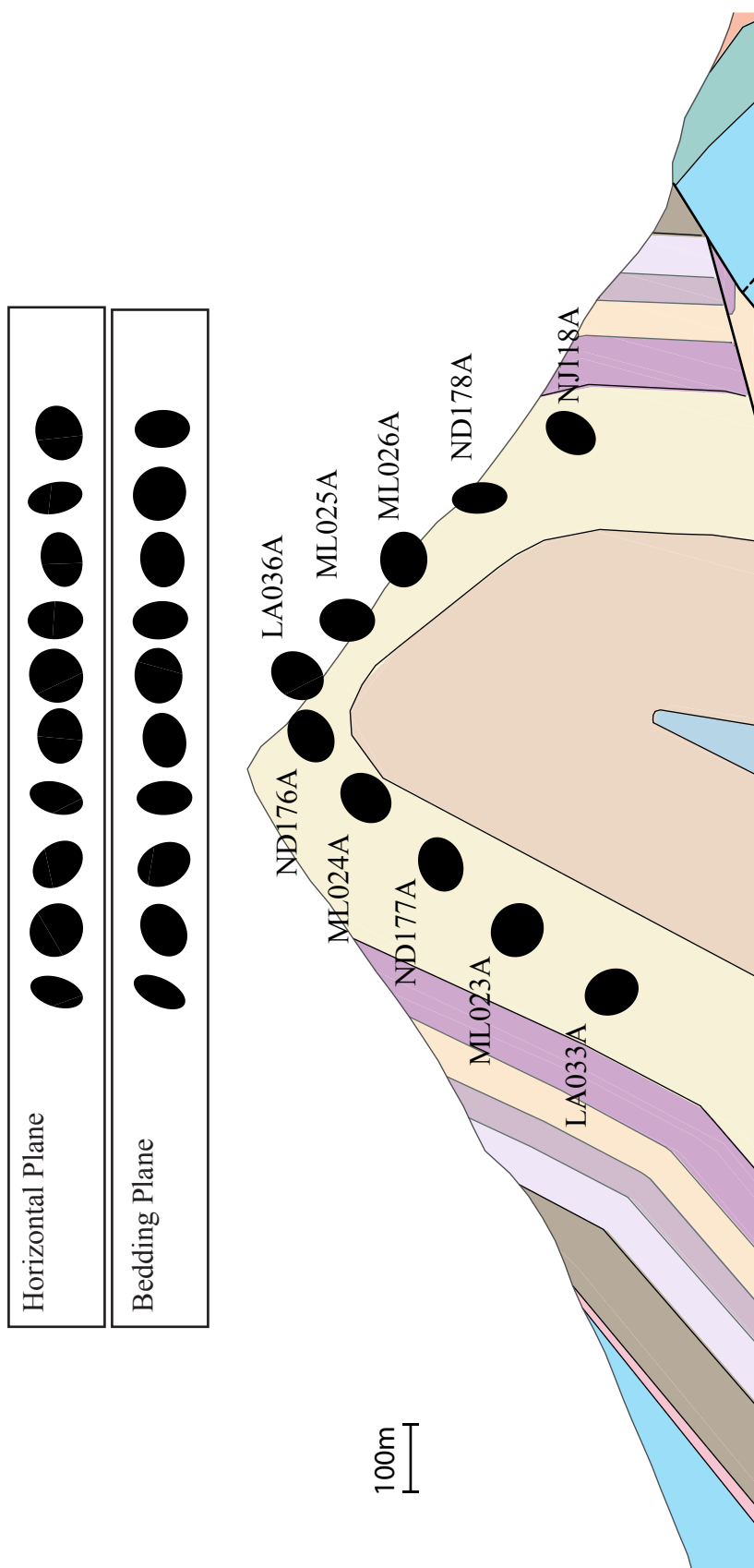


Figure 3-18: The bulk strain ellipses, determined from the equal area Fry plot ellipsoids. All three strains are plotted along with their approximate locations on the fold. Strain in the bedding and horizontal planes above cross-section. Strain in the profile plane is plotted on the cross-section through Turtle Mountain. The legend is located on Fig. 3-1.

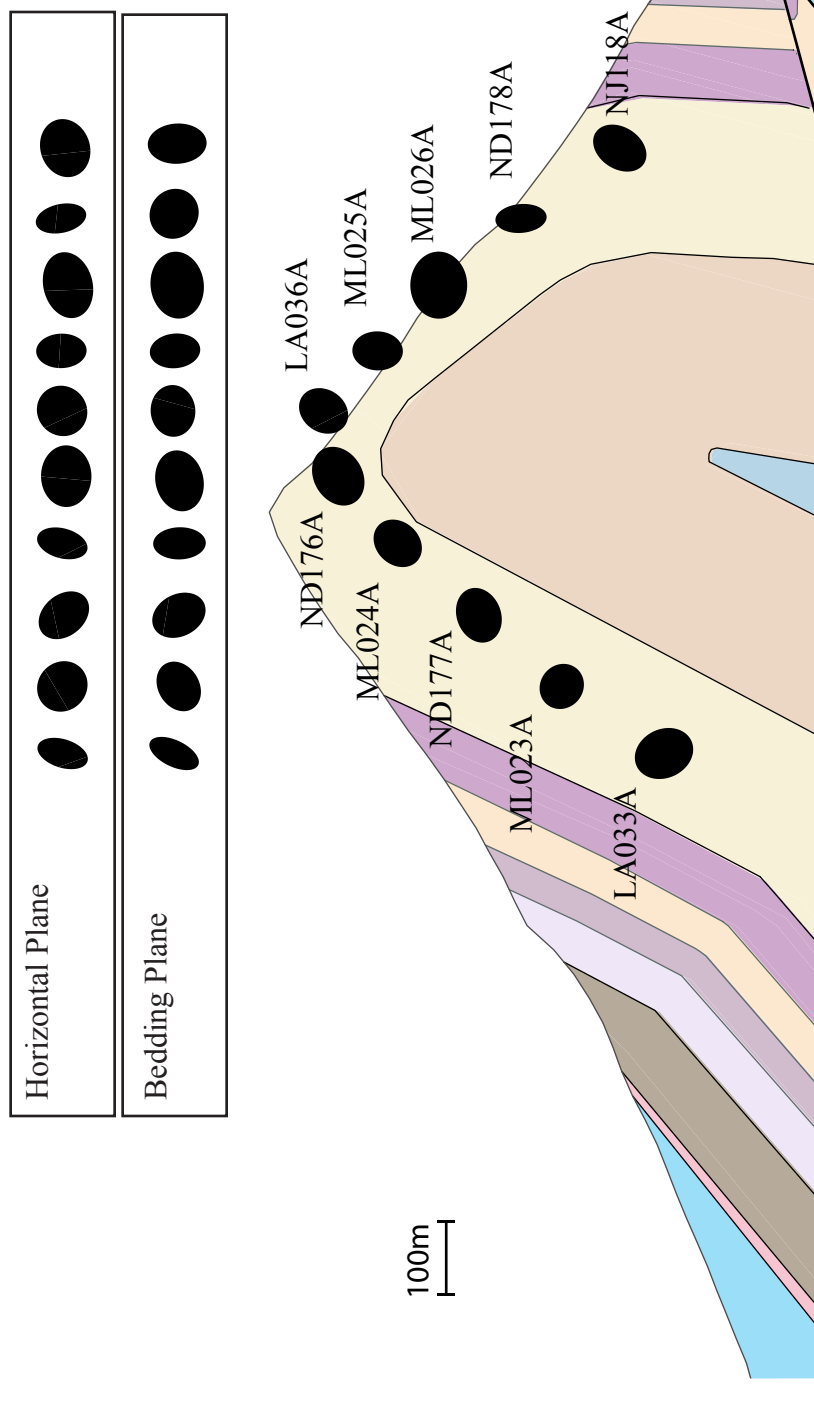


Figure 3-19: The bulk strain ellipses, determined assuming no orogen-parallel extension (length of 1.0 along the hinge). All three strains are plotted along with their approximate locations on the fold. Strain in the bedding and horizontal planes above cross-section. Strain in the profile plane is plotted on the cross-section through Turtle Mountain. The legend is located on Fig. 3-1.

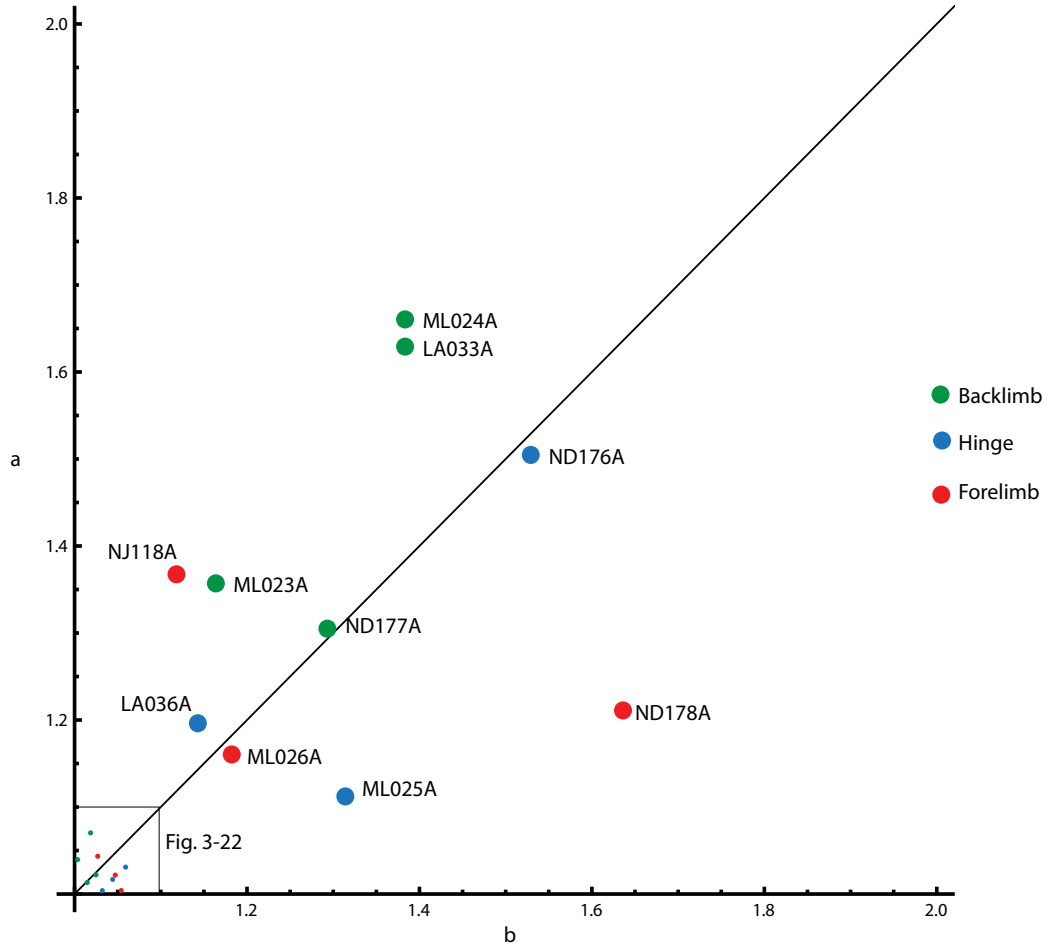


Figure 3-20: Flinn plot of the Fry method strain ellipsoids. The k value is equal to a/b , where a is S_1/S_2 , b is S_2/S_3 and S is the stretch. Insert is figure 3-22 scaled to fit plot axes; this is the flinn plot of calcite strain gauge method.

are oblate in shape and values of k that are greater than one represent ellipsoids that are prolate. The k values associated with the backlimb range from 1.00 to 1.21, the hinge range from .85 to 1.05, and the forelimb range from .74 to 1.24. The obtained ellipticity or strain ratio (R_s), where $R_s = a/b$, of the ellipsoids values ranges from 1.37-2.33.

3.4.2 Calcite Strain Gauge Method

The twins found in the limestone collected from the area contained mainly thin, straight twins, with up to three twin sets per grain, which usually extended across the entire grain. The amount of twinning ranges from intensely to slightly twinned, or rarely, to untwined. The thickness of twins is mainly a function of deformation temperature, and is not sensitive to factors such as differential stress, strain rate, grain size, or grain orientation (Ferrill, 1991; Burkhard, 1993). The twins would be classified as type I by Burkhard (1993), which suggests a deformation temperature of less than 200°C, with very low strain.

The intra-crystalline strain ellipsoid results and their errors, determined using the calcite strain gauge method (Appendix E), are shown in Table 3-4. The ellipses in the profile bedding and horizontal planes are plotted, along with their approximate locations on the fold (Fig. 3-21). Due to the low amount of strain, a thin white line has been placed showing the location of the long axes of the ellipses. The standard error, the average of the computed errors on the x- and y-axis magnitudes, ranges from 13 to 47% for the samples. The ellipsoids are represented on a Flinn Plot (Fig. 3-22), and have k values for the backlimb that range from .94 to 1.11, for the hinge range from .94 to .99, and for the forelimb range from .92 to 1.00 (Table 3-2). Though the Flinn plot for the intra-crystalline strain shows highly variable ellipsoid shapes, the overall strain is so low that small changes in strain or small errors in the results may change the shape from prolate to oblate.

Calcite Strain Gauge Method Strain Ellipses

SECTION	Orientation 255°/90°		Orientation Bedding				Orientation 360°/00°	
	Rs	Phi	Strike	Dip	Rs	Phi	Rs	Phi
LA033A	1.005	90.0	190	49	1.020	62.1	1.023	141.5
ML023A	1.022	10.3	202	76	1.043	174.0	1.040	63.1
ND177A	1.040	163.7	127	39	1.018	170.9	1.016	178.8
ML024A	1.031	102.4	206	31	1.015	19.7	1.038	116.4
ND176A	1.023	160.5	74	30	1.030	78.1	1.023	47.7
LA036A	1.005	49.0	148	28	1.022	90.2	1.022	8.4
ML025A	1.027	62.8	332	9	1.051	121.1	1.052	55.4
ML026A	1.009	9.4	7	36	1.052	131.9	1.070	37.9
ND178A	1.054	162.9	0	72	1.042	159.8	1.010	145.7
NJ118A	1.058	46.3	163	76	1.029	127.8	1.031	69.6

Calcite Strain Gauge Method Ellipsoid

SECTION	Fold Location	From Hinge	S ₁	Trend	Plunge	S ₂	Trend	Plunge	S ₃	Trend	Plunge	Ellipticity	Standard Error (%)
LA033A	back	346m	1.011	309.6	14.1	1.001	99.7	73.8	0.988	217.6	7.8	1.02	15
ML023A	back	39m	1.028	207.2	5.2	0.989	299.3	22.3	0.984	104.9	67.1	1.04	26
ND177A	back	12.6m	1.021	97.0	19.0	1.001	190.8	11.0	0.977	309.4	67.8	1.05	22
ML024A	back	2.4m	1.052	153.6	41.8	0.982	248.5	5.4	0.966	344.5	47.7	1.09	47
ND176A	hinge		1.040	172.5	41.2	1.010	71.3	12.5	0.951	328.0	46.1	1.09	18
LA036A	hinge		1.017	178.5	61.5	1.007	83.6	2.6	0.976	352.2	28.3	1.04	23
ML025A	hinge		1.024	221.3	35.2	1.010	18.2	52.5	0.967	123.2	11.3	1.06	23
ML026A	fore	2.9m	1.030	231.8	8.2	1.009	73.6	81.2	0.962	322.2	3.2	1.07	27
ND178A	fore	8.8m	1.019	118.0	3.0	1.017	26.8	21.8	0.964	215.5	68.0	1.06	29
NJ118A	fore	400m	1.037	214.8	37.4	0.994	325.8	25.1	0.969	80.9	42.1	1.07	13

Table 3-4: Equal volume intra-crystalline strain ellipsoid and errors, determined using the calcite strain gauge method.

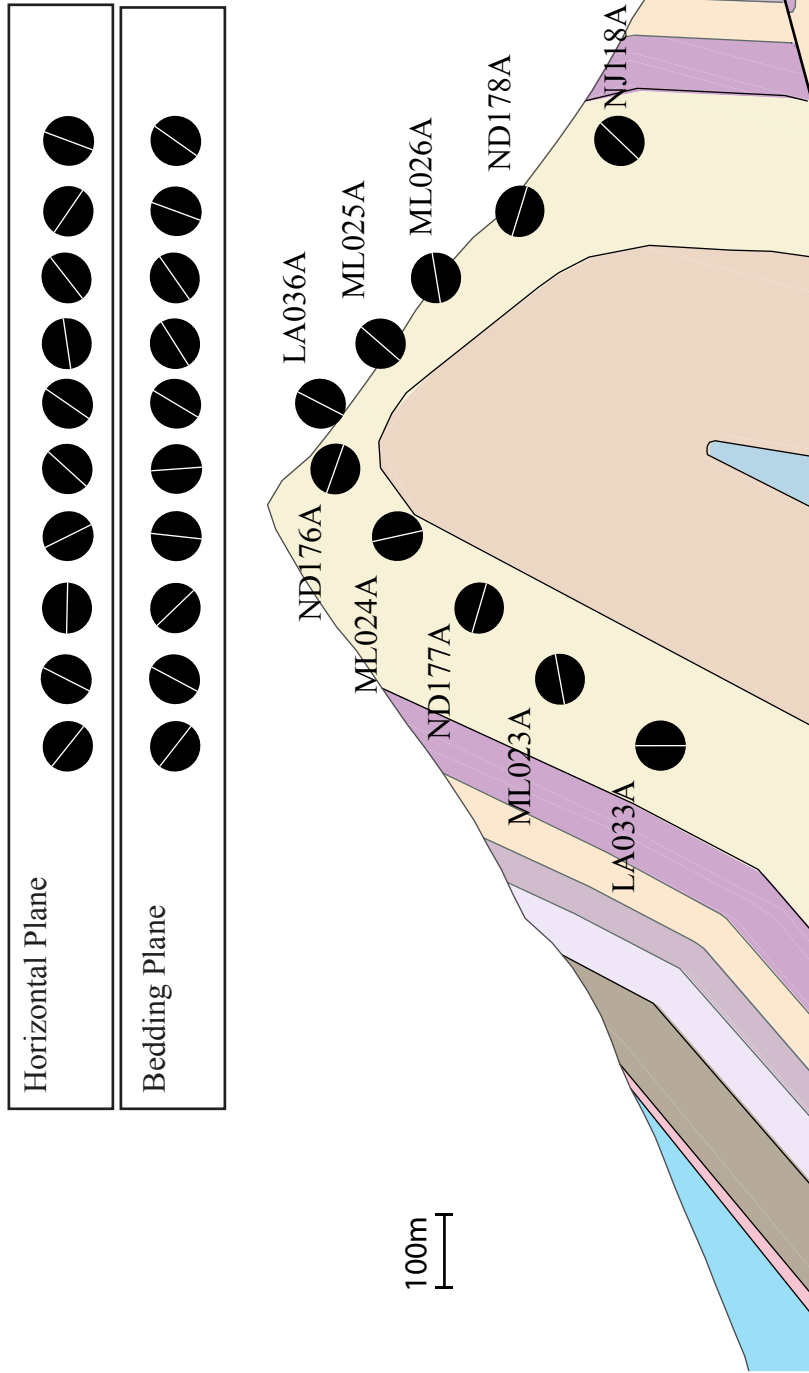


Figure 3-21: The intra-crystalline strain ellipses, determined from the equal area calcite strain gauge ellipsoids. Due to the low amount of strain a thin white line has been placed showing the location of the long axes of the strain ellipses. All three strains are plotted along with their approximate locations on the fold. Strain in the bedding and horizontal planes above cross-section. Strain in the profile plane is plotted on the cross-section through Turtle Mountain. The legend is located on Fig. 3-1.

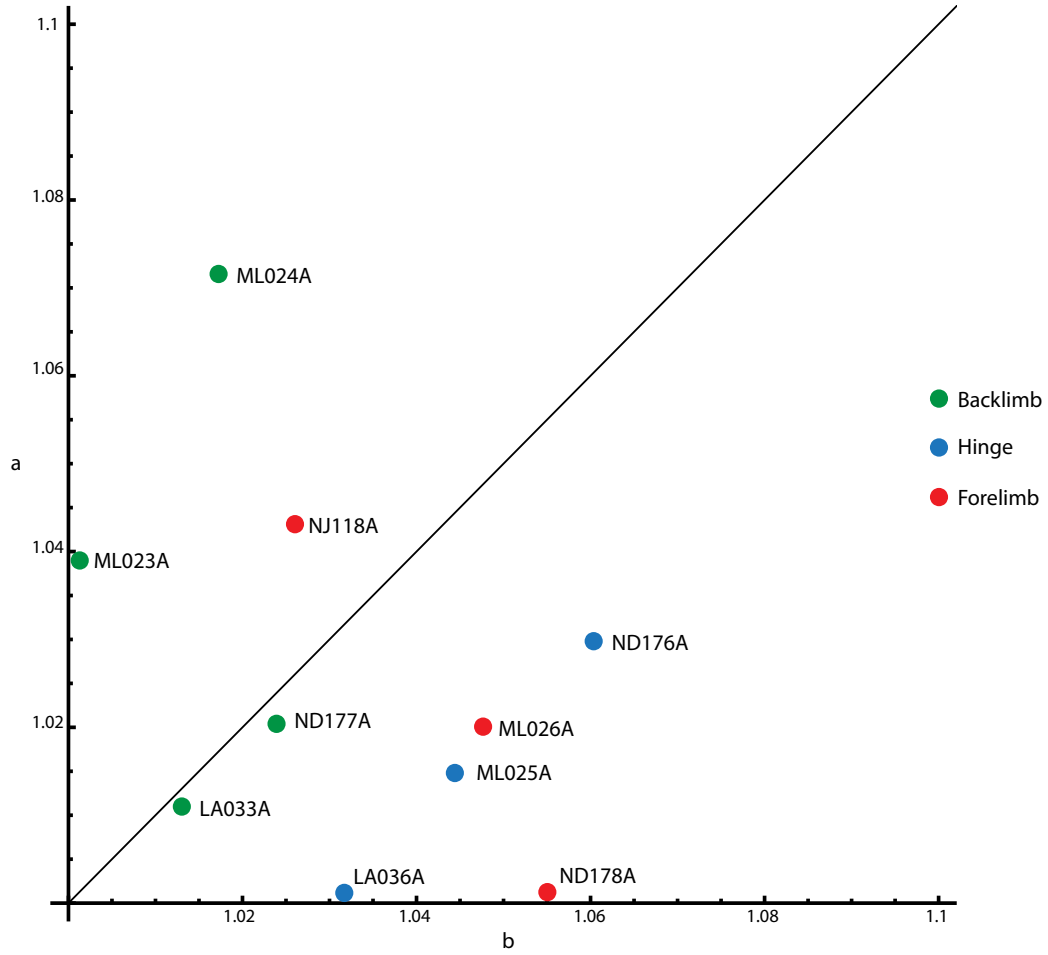


Figure 3-22: Flinn plot of the calcite strain gauge method strain ellipsoids. The k value is equal to a/b , where a is S_1/S_2 , b is S_2/S_3 and S is the stretch.

The strain ellipsoids have ellipticity values ranging from 1.02-1.09.

3.4.3 Comparing the Strains

The strain ellipses observed from each method are noticeably different. The range of ellipticity determined by the Fry method ranges from 1.37 to 2.33 and is an order of magnitude larger in the same samples than that determined by the calcite strain gauge (1.02-1.09). The principal strain axis directions and the Flinn plots are very different when both methods are compared. The difference in long axis orientation of the strain ellipses ranges from 2°-89° in the same samples. In the horizontal plane the range varies between 24°-73°. This indicates that the bulk strain (including all mechanisms such as grain boundary sliding, mass transfer, and intra-crystalline strain) of the rock, determined using the Fry method, is different from the internal strain (intra-crystalline strain) of the grains, determined from the calcite strain gauge method.

3.5 Discussion: Deformation History of the Fold

3.5.1 Discussion of Strain Comparisons

The large difference between both the magnitudes and ellipticity values indicate the twinning accounts for only a small part of the bulk strain, and that other deformation mechanisms must exist. Stylolites and the interlocking crystal shapes help to account for this difference. Groshong (1972) proposed that under larger strain, grain-boundary interactions may increase the rigidity of crystals undergoing twinning, causing twin strain values to be smaller than the total strain. Thin sections show interlocking grain geometries and stylolites which indicates high strain (Fig. 3-13). The presence of stylolites indicates that there is likely to have been strain by mass transfer, in addition to the intra-crystalline strain.

The principal strain axis directions and the Flinn plots are very different

when the bulk and intra-crystalline strains are compared. These results suggest that the deformation associated with the bulk strain records a different (over-printed) deformation event additional to the internal strain. This result contrasts with that of Gonzalez-Casado et al. (2003), studying a synclinorium structure within the Basque-Cantabrian Basin of Spain, where the principal strain axis directions from the Fry method and the calcite strain gauge method were very similar; interpreted to indicate that the twinning was simultaneous with other deformation mechanisms. In the case of Turtle Mountain, the results of this study strongly suggest that intra-crystalline strain was not simultaneous with the solution mass transfer processes that led to most of the distortion seen in the Fry plots.

The intra-crystalline strain results suggest that intra-crystalline strain may have taken place prior to folding. The long strain axis of each strain ellipse, determined by the calcite strain gauge method, is at a high angle to bedding (Fig. 3-21); in the bedding plane the long axis directions are approximately north-south. These two observations suggest that the intra-crystalline strain is related to original shortening when bedding was approximately horizontal. Geodynamic numerical models by Stockmal et al. (2007), constructed with strength parameters similar to rock in the Canadian Cordilleran thrust belt, suggest that the lower stronger layers underwent significant layer-parallel shortening before thrusting occurred. This would account for the small intra-crystalline strain that records deformation prior to folding.

The bulk strain determined by the Fry method is associated with both deformational events. The early, mainly intra-crystalline strain was overprinted by the large strain associated with the folding deformation. The presence of interlocking grain boundaries and grains that contain straight twins extending across the entire grain (showing no further intra-crystalline strain) indicated that further strain was by mass transfer. The presence of stylolites indicates volume loss by

pressure solution.

3.5.2 Comparing Rock Strain to Predictions of Kinematic Models

In this section, the strain associated with the folding deformation, from Turtle Mountain samples, will be compared to the kinematic fault-propagation folds models, described in section 3.2.3. This is because amongst the three basic types of folds associated with thrust belts described in section 3.2, the structure of the Turtle Mountain fold (Fig. 3-18) most closely resembles a fault-propagation fold (Fig. 3-3). This is based on its tightness and the presence of an overturned forelimb.

In the discussion that follows, the small component of intra-crystalline strain has not been removed from the bulk strain values determined by the Fry (1979) method. Because the bulk strains are an order of magnitude larger than the intra-crystalline strains, strains associated with folding can be satisfactorily approximated by the bulk strain values. The results are displayed assuming (i) constant volume deformation and (ii) no extension to the main fold axis. (Fig. 3-18 and 3-19).

The bulk strain associated with the Turtle Mountain fold has both varying orientations and amounts of shortening, indicating that strain is very heterogeneous (Fig. 3-18). On the backlimb of the fold, the sample furthest from the fold hinge, the strain is higher and the shortening direction is at a high angle to the axial surface. The strain in the next sample to the east is very low. Then in the two samples closest to the hinge, the strain increases and the shortening directions are at low angles to the axial surface. Strain on the hinge of the fold is large and the shortening directions are at high angles to the axial trace. On the forelimb of the fold, close to the hinge, the strain is low and the shortening direction is at a low

angle to the axial trace. Further from the hinge, on the forelimb of the fold, the strain is larger and the direction of shortening is at a high angle to the axial trace. There are areas on both the backlimb and forelimb of the fold where the strain is low. The strain on the forelimb has shortening directions that change orientation (almost 90°).

In a second profile, the strain associated with folding is assumed to be plane strain where there is no orogen-parallel extension (Fig. 3-19). The horizontal stretch along the hinge is normalized to 1.0 and the other dimensions of the strain ellipsoid are either reduced or increased accordingly. Most of the ellipses decreased in size, indicating an overall reduction in the volume of the strain ellipsoid. This reduction in size indicates volume loss within the Turtle Mountain fold. There is other evidence of volume loss shown by a decrease in thickness of units in the backlimb (approximately 5%) and forelimb of the fold (approximately 8%), the presence of stylolites, and interlocking grain geometry. All of the eight kinematic models considered in section 3.2.3 are area balanced, based on an assumption of constant-volume deformation, and therefore cannot completely represent the Turtle Mountain fold. However, the strain predicted by the models can be compared to the distortion component of strain observed in the Turtle Mountain fold.

Both model *a* and *b* have similar predicted strains, though based on different assumptions. The strain associated with both models predicts constant strain through both the backlimb and forelimb of the fold. This is unlike the strain determined in the study area which varies in both limbs. Model *a* is based on assumptions that layer thickness stays constant through the fold. Cross-sections through the Turtle Mountain structure display layer thickness changes. Furthermore, in model *b*, the structure has a forelimb dip that is parallel to the backlimb axial surface (Mosar and Suppe, 1992). Therefore, the forelimb cannot be overturned,

as occurs at Turtle Mountain. Models *a* and *b* cannot be used to explain the Turtle Mountain fold structure.

The strain associated with model *c* changes with the amount of shear during fault propagation. There are associated thickness changes in the lower layers due to assumptions inherent in the model. Though this model has both varying strain and thickness changes, it predicts constant strain on both the backlimb and forelimb of the fold. Model *d* additionally predicts thickness changes. However, in model *d*, the strain is both very high and constant on both limbs of the fold. Neither model predicts the varying strain seen in the limbs of the Turtle Mountain fold.

The strain associated with model *e*, though varied in the backlimb, has only two values. It is either zero or has a shortening direction that is at a high angle to the axial surface. This is different from the Turtle Mountain fold, where strain is not just varied in amount, but also in that the larger strain has varied shortening orientation directions. The footwall of the Turtle Mountain fold contains a footwall syncline, a structure predicted by model *e* (Langenberg et al., 2007). Structure through the subsurface indicates that the footwall syncline is associated with the movement on the Lower Gold Creek thrust. Therefore, model *e* does not represent the Turtle Mountain fold well because it does not predict the observed strain or structure.

Both model *f* and *g* contain a zone of shear that expands upward and outward from the thrust tip. The strain associated with this zone is impossible to predict kinematically due to the heterogeneity of the shear. The strain results for the Turtle Mountain fold also show heterogeneity. However, the heterogeneous strain associated with models *f* and *g* is restricted to the shear zone. The heterogeneous strain from the Turtle Mountain fold is throughout the fold, and is not restricted to a small zone. Therefore, the strain predicted by kinematic models *f* and *g* is not a

good fit for the Turtle Mountain fold.

Due to the assumptions of model *h*, hanging wall shear is created in the layers through which the ramp propagates. This shear creates strain that has highly variable orientations in the different layers of the forelimb and backlimb of the fold. Model *h*, shown in Fig. 3-8, is simplified to show one nucleation segment; however, it is possible for a fault to develop from multiple nucleation sites of varying length (Tavani et al., 2006). Multiple nucleation sites will cause the shear to vary throughout the fold and increase the number of axial surfaces, leading to zones with lower strain. Because samples collected from the area were not all collected in precisely the same layer (Fig. 3-1), the varying strain orientations could be due to varying shear in the layers of the fold. Multiple nucleation sites could also explain the low strain values found in both of the limbs of the fold. The strain associated with model *h* best represents the Turtle Mountain fold and is a possible kinematic model for its development.

Further work has been done on model *h* by Tavani and Storti (2011), which includes volume loss. Tavani and Storti (2011) based their results on pressure solution cleavage found on anticlines in the Pyrenees in France and Spain, and the Apennines in Italy. In these anticlines, the pressure solution cleavage was associated with layer-parallel shortening. The amount and locations of this shortening varied depending on: the location of nucleation sites; ramp angle; rock properties; slip rates; and propagation rates (Tavani and Storti, 2011). The maximum values of layer-parallel shortening was found to always be located within the forelimb; layer-parallel shortening increases upward and downward from the initial fault tips (Tavani and Storti, 2011). These results agree with the thickness changes measured on the Turtle Mountain fold. Measurements made on layer thickness through the anticline implied that the most volume loss was to the forelimb of the fold at 8%.

3.6 *Conclusions*

Strain was determined by two methods at various locations in Paleozoic carbonate rocks of the Turtle Mountain anticline. The Fry method measures the bulk strain at the scale of a thin section. This bulk strain may include strain from many processes. Based on observations in the field and in thin section, pressure solution was important deformation mechanism. The calcite strain gauge in contrast measures only one component of strain: that occurring by twinning within the crystals. The strain determined by Fry plots and the calcite strain gauge are very different, indicating the bulk strain is different from the intra-crystalline strain. This suggests that there were two separate deformational events. The intra-crystalline strain results show shortening directions at low angles to the bedding plane (Fig. 3-21). This probably indicates that deformation took place when the units were horizontal prior to folding. Geodynamic numerical models of thin-skinned thrust belts (Stockmal et al., 2007) suggest that the strata in advance of a developing thrust wedge are significantly shortened before being faulted; this can account for the bedding parallel shortening.

The bulk strain was used to determine the strain associated with the folding deformation. Because the bulk strains are an order of magnitude larger than the intra-crystalline strains, strains associated with folding can be satisfactorily approximated by the bulk strain values. Constant-volume ellipsoids suggest significant orogen-parallel extension, which is unlikely on regional grounds. When the strain is normalized assuming no orogen-parallel extension, the resulting ellipsoids show volume loss up to 16%. Evidence of volume loss is also seen in the thin sections, as stylolites and interlocking grain geometry, and by decreases of layer thickness within the Turtle Mountain fold. The strain associated with the folding deformation (Fig. 3-18 and 3-19) is very heterogeneous.

Compared with models for folds associated with thrust belts (Fig. 3-3), the

style of the Turtle Mountain anticline most closely resembles a fault-propagation fold. This is based on the tightness of the fold and the presence of an overturned forelimb. Of the eight kinematic models for fault-propagation folds (Fig. 3-8, *a-h*), the distortion on the Turtle Mountain fold best matches that predicted by the model of Tavani et al. (2006), which predicts heterogeneous strain due to hinterland shear in the hanging wall, as a fault propagates from a nucleation site (Tavani et al., 2006). Further work on natural folds by Tavani and Storti (2011) incorporates volume loss into the model, consistent with evidence of volume loss in the Turtle Mountain fold. Though strain results and structure of the Turtle Mountain fold are complex, results of this study suggest that the models proposed by Tavani et al. (2006) and Tavani and Storti (2011) best match the deformational history of this fold. Thus the Turtle Mountain thrust probably propagated both up and down section from nucleation sites on the thrust ramp as the fold developed, resulting in highly heterogeneous deformation and significant volume loss by pressure solution in some areas of the fold.

The findings of this study have petroleum implications to the Rocky Mountains. The Tavani et al. (2006) and the Tavani and Storti (2011) models that best match the Turtle Mountain fold can be applied to other thrust-related folds located in the subsurface. This can improve both subsurface interpretation and location of petroleum reservoirs.

3.7 *References*

- Burkhard, M., 1993, Calcite twins, their geometry, appearance and significance as stress-strain markers and indicators of tectonic regime: a review: *Journal of Structural Geology*, v. 15, p. 351-368.
- Epard, J.L., and Groshong, R.H., Jr., 1995, Kinematic model of detachment fold-

- ing including limb rotation, fixed hinges and layer-parallel strain: *Tectonophysics*, v. 247, p. 85-103.
- Erslev, E.A., 1988, Normalized center-to-center strain analysis of packed aggregates: *Journal of Structural Geology*, v. 10, p. 201-209.
- Erslev, E.A., 1991, Trishear fault-propagation folding: *Geology*, v. 19, p. 617-620.
- Erslev, E.A., and Mayborn, K.R., 1997, Multiple geometries and modes of fault-propagation folding in the Canadian thrust belt: *Journal of Structural Geology*, v. 19, p. 321-335.
- Evans, M.A., and Groshong, R.H., Jr., 1994, Microcomputer techniques and applications; a computer program for the calcite strain-gauge technique: *Journal of Structural Geology*, v. 16, p. 277-281.
- Ferrill, D.A., 1991, Calcite twin widths and intensities as metamorphic indicators in natural low-temperature deformation of limestone: *Journal of Structural Geology*, v. 13, p. 667-675.
- Fry, N., 1979, Random point distributions and strain measurement in rocks: *Tectonophysics*, v. 60, p. 89-105.
- Gonzalez-Casado, J.M., Jimenez-Berrocso, A., Garcia-Cuevas, C., and Elorza, J., 2003, Strain determinations using inoceramid shells as strain markers; a comparison of the calcite strain gauge technique and the Fry method: *Journal of Structural Geology*, v. 25, p. 1773-1778.
- Groshong, R.H., Jr., 1972, Strain Calculated from Twinning in Calcite: *Geological Society of America Bulletin*, v. 83, p. 2025-2037.
- Groshong, R.H., Jr., 1974, Experimental Test of Least-Squares Strain Gage Calculation Using Twinned Calcite: *Geological Society of America Bulletin*, v. 85, p. 1855-1863.
- Groshong, R.H., Jr., Teufel, L.W., and Gasteiger, C., 1984, Precision and accuracy of the calcite strain-gage technique: *Geological Society of America Bul-*

- letin, v. 95, p. 357-363.
- Homza, T.X., and Wallace, W.K., 1995, Geometric and kinematic models for detachment folds with fixed and variable detachment depths: *Journal of Structural Geology*, v. 17, p. 575-588.
- Langenberg, C.W., Pana, D.I., Richards, B., Spratt, D.A., and Lamb, M.A., 2007, Structural geology of Turtle Mountain near Frank, Alberta: Alberta Geological Survey, Energy Resources Conservation Board, 39 p.
- McNaught, M.A., and Mitra, G., 1993, A kinematic model for the origin of foot-wall synclines: *Journal of Structural Geology*, v. 15, p. 805-808.
- Mitra, S., 1990, Fault-propagation folds; geometry, kinematic evolution, and hydrocarbon traps: *AAPG Bulletin*, v. 74, p. 921-945.
- Mitra, S., 2003, A unified kinematic model for the evolution of detachment folds: *Journal of Structural Geology*, v. 25, p. 1659-1673.
- Mookerjee, M., and Nickleach, S., 2011, Three-dimensional strain analysis using Mathematica: *Journal of Structural Geology*, v. 33, p. 1467-1476.
- Mosar, J., and Suppe, J., 1992, Role of shear in fault-propagation folds, in McClay, K.R., ed.: *Thrust Tectonics*, p. 123-132.
- Poblet, J., and McClay, K., 1996, Geometry and kinematics of single-layer detachment folds: *AAPG Bulletin*, v. 80, p. 1085-1109.
- Stockmal, G.S., Beaumont, C., Nguyen, M., and Lee, B., 2007, Mechanics of thin-skinned fold and thrust belts; insights from numerical models: *Special Paper - Geological Society of America*, v. 433, p. 63-98.
- Suppe, J., 1983, Geometry and kinematics of fault-bend folding: *American Journal of Science*, v. 283, p. 684-721.
- Suppe, J., Connors, C.D., and Zhang, Y., 2004, Shear fault-bend folding, in McClay, K.R., ed., *AAPG Memoir 82: Tulsa, American Association of Petroleum Geologists*, p. 303-323.

- Suppe, J., and Medwedeff, D.A., 1990, Geometry and kinematics of fault-propagation folding, in Jordan, P., Noack, T., Schmid, S., and Bernoulli, D., eds., *Eclogae Geologicae Helvetiae*, v. 83, p. 409-454.
- Tavani, S., and Storti, F., 2006, Fault-bend folding as an end-member solution of (double-edge) fault-propagation folding: *Terra Nova*, v. 18, p. 270-275.
- Tavani, S., and Storti, F., 2011, Layer-parallel Shortening Templates Associated with Double-edge Fault-propagation Folding, in McClay, K.R., Shaw, J.H., and Suppe, J., eds., *Thrust Fault-Related Folding*, AAPG Memoir 94: Tulsa, OK, p. 121-135.
- Tavani, S., Storti, F., and Salvini, F., 2006, Double-edge fault-propagation folding: geometry and kinematics: *Journal of Structural Geology*, v. 28, p. 19-35.
- Waldron, J.W.F., and Wallace, K.D., 2007, Objective fitting of ellipses in the centre-to-centre (Fry) method of strain analysis: *Journal of Structural Geology*, v. 29, p. 1430-1444.
- Wilkerson, M.S., Smaltz, S.M., Bowman, D.R., Fischer, M.P., and Higuera-Diaz, I.C., 2007, 2-D and 3-D modeling of detachment folds with hinterland inflation: A natural example from the Monterrey Salient, northeastern Mexico: *Journal of Structural Geology*, v. 29, p. 73-85.

Chapter 4: Conclusions

In the Cordilleran foothills of southern Alberta, the Crowsnest Pass area displays a close relationship between topography, stratigraphy, and structure. LiDAR (light detection and ranging) is a high-resolution remote sensing technique, from which the data can be used to make a ‘bare-earth’ filtered map with the vegetation removed. In this terrain, the use of LiDAR assisted mapping increased the area that could be covered in field mapping and improved the accuracy of the resulting map. The LiDAR data are used as a tool to identify lineaments. The lineaments help to locate bedding and other geological boundaries, and to derive orientations in inaccessible areas.

The relationship between topography and stratigraphy can be seen in a revised geological map for the Crowsnest Pass area, in which the geological map is overlaid on the hill-shaded LiDAR data (Fig. 2-3). Improved cross-sections (Fig. 2-8, 2-9 and 2-10) for the area were made using the geological map and well information and differ substantially from those of Norris (1993) (Fig. 1-4). The cross-sections display seven major thrusts. The Livingstone thrust is fairly planar and was used as a base to the cross-sections. The Turtle Mountain thrust changes structure from the north to the south; to the south of a lateral ramp beneath Bluff Mountain, Paleozoic carbonate units are incorporated into the hanging wall. The higher McConnell, Mutz, Lyons Creek, and Coleman thrust sheets only contain Mesozoic units. The improved geological map and cross-sections reveal information about the area that was previously unknown. The main detachment surfaces for the area are within the Fernie Formation/Kootenay Group and the Palliser Formation. Spratt and Lawton (1996) established these units as main detachment surfaces in the surrounding areas, by surface measurements and seismic interpretation. In the study area, the upper thrusts have smaller sheets that only contain Mesozoic units above and including the Fernie Formation/Kootenay

Group, whereas the lower thrust sheets are longer and contain both Paleozoic and Mesozoic units. Using geodynamic numerical models analogous to the Canadian Rockies, Stockmal et al. (2007) determined that very long sheets develop in lower stronger layers. On the improved geological map, evidence of out-of-sequence thrusting occurs where the Mutz thrust cuts both limbs of a footwall syncline, and in the thickened coal on Grassy Mountain, suggests that there was west-vergent thrusting followed by east-vergent thrusting (Snyder, 2011), which on the basis of geodynamic modelling that out-of-sequence thrusting Stockmal et al. (2007) propose is common in thin-skinned thrust belts.

Mapping of the Turtle Mountain thrust sheet shows that it is folded into an anticline cored by Paleozoic rocks. The fold is more open on in the north (Bluff Mountain) than in the south (Hillcrest Mountain), where the forelimb of the fold is exposed at the surface (Fig. 2-3). To the east of the anticline on Hillcrest Mountain, the hanging wall of the Turtle Mountain thrust contains a south-plunging syncline. Amongst the fold types commonly described from thrust belts, the most prominent fold structure in the hanging wall of the Turtle Mountain thrust most closely resembles a fault-propagation fold (Fig. 2-13). This is based on the tightness of the fold and the presence of an overturned forelimb (Fig. 2-9). Subsurface structure revealed that the footwall syncline, previously used to classify the fold (Langenberg et al., 2007), is due to deformation along the underlying Gold Creek thrust system.

The results of strain analysis on rocks collected from the folded hanging wall of the Turtle Mountain thrust were compared to predictions of kinematic models proposed for folds in thrust belts. Strain analysis was performed using two methods to determine the bulk and the intra-crystalline strain. The intra-crystalline strain determined by the calcite strain gauge method of Groshong (1972) showed shortening directions at low angles to bedding, indicating that

it was associated with horizontal shortening prior to folding. This matches the predictions of Stockmal et al. (2007) derived from geodynamic numerical models. The strain associated with the folding deformation was determined from the bulk strain. Strains associated with folding can be satisfactorily approximated by the bulk strain values, because the bulk strains are an order of magnitude larger than the intra-crystalline strains. The strain was normalized so as to assume no orogen-parallel extension. In most ellipses the size was reduced by this normalization, suggesting volume loss. Evidence for volume loss was also seen in layer thickness measurements, and in the thin sections, where there were stylolites and the grains had an interlocking geometry.

The strain associated with the folding deformation was found to be heterogeneous, with both varying amounts and shortening orientations (Fig. 3-19). The strain best matches that predicted by a fault-propagation fold model proposed by Tavani et al. (2006) (Model *h*; Fig. 3-8; Chapter 3). This model has hanging wall shear in the hinterland due to the propagation of a fold from a fault nucleation site. This model predicts highly heterogeneous strain like that seen in the Turtle Mountain fold. Further work by Tavani and Storti (2011) incorporated layer-parallel shortening by pressure solution into the model showing that volume loss is at a maximum in the forelimb. This agrees with the volume loss interpreted on the Turtle Mountain fold. The results presented in the study indicate that the Turtle Mountain fold provides an exceptional example from which the deformation history can be determined. From the improved Crowsnest Pass map and strain analysis, the model proposed by Tavani et al. (2006) and Tavani and Storti (2011) best matches the deformational history of the Turtle Mountain fold.

The cross-sections are constructed to balance, which assumes that there is no volume loss. However, it was found that up to 8% volume loss had probably occurred during thrust-related folding, at least in certain areas on Turtle Mountain.

This amount of volume loss is comparable to the 4% expected for shortening of about 30% in carbonate cored fault-propagation folds (Tavani and Storti, 2011). This recorded volume loss is impossible to determine through the entire area as many samples would need to be collected in the subsurface. Tavani and Storti (2011) determined that the volume loss is confined to small portions of the crests and forelimbs of the folds they analyzed. Therefore, the assumptions used to construct the cross-sections are approximately valid for all but small areas around the anticline.

References

- Groshong, R.H., Jr., 1972, Strain Calculated from Twinning in Calcite: Geological Society of America Bulletin, v. 83, p. 2025-2037.
- Langenberg, C.W., Pana, D.I., Richards, B., Spratt, D.A., and Lamb, M.A., 2007, Structural geology of Turtle Mountain near Frank, Alberta: Alberta Geological Survey, Energy Resources Conservation Board, 39 p.
- Spratt, D.A., and Lawton, D.C., 1996, Variations in detachment levels, ramp angles and wedge geometries along the Alberta thrust front: Bulletin of Canadian Petroleum Geology, v. 44, p. 313-323.
- Stockmal, G.S., Beaumont, C., Nguyen, M., and Lee, B., 2007, Mechanics of thin-skinned fold and thrust belts; insights from numerical models: Special Paper - Geological Society of America, v. 433, p. 63-98.
- Snyder, M., 2011, Structural Geology of Grassy Mountain, southern Alberta [Undergraduate thesis]: Edmonton, University of Alberta, 47 p.
- Tavani, S., and Storti, F., 2011, Layer-parallel Shortening Templates Associated with Double-edge Fault-propagation Folding, in McClay, K.R., Shaw, J.H., and Suppe, J., eds., Thrust Fault-Related Folding, AAPG Memoir 94: Tulsa, OK, p. 121-135.
- Tavani, S., Storti, F., and Salvini, F., 2006, Double-edge fault-propagation folding:

geometry and kinematics: Journal of Structural Geology, v. 28, p. 19-35.

Appendix A: Well Locations

This appendix accompanies chapter 2 and is a complete list of well locations.

Well	Location
1	100/06-31-006-03w5/00
2	100/06-05-007-03w5/00
3	100/13-08-007-03w5/00
4	100/09-16-007-04w5/00
5	100/08-26-007-04w5/00
6	100/09-11-008-04w5/00
7	100/11-12-008-04w5/00
8	100/07-35-008-04w5/00
9	100/04-12-009-04w5/00
10	100/06-11-009-04w5/00
11	100/12-12-009-04w5/02
12	100/04-13-009-04w5/00
13	100/07-14-009-04w5/00
14	100/15-14-009-04w5/00
15	100/13-18-009-03w5/00
16	100/03-20-009-03w5/00
17	100/12-27-009-04W5/03
18	100/16-29-009-05W5/00
19	100/06-14-008-05W5/00
20	100/07-14-006-03W3/00
21	100/10-21-009-03W5/00
22	100/13-28-008-03W5/02
23	100/15-33-007-03W5/00

Appendix B: Field Data

This appendix accompanies chapter 2 and is a complete list of field data.

Waypoint	Longitude	Latitude	UTM Easting	UTM Northing	Azimuth	Inclination	Type	Stratigraphic Unit
ND001	-114.499	49.634	680615.4	5500909.4	172	26	bedding	
ND002	-114.496	49.634	680783.9	5500934.6	216	28	bedding	Belly River
ND003	-114.476	49.631	682225.0	5500699.2				Crowsnest
ND004	-114.477	49.633	682205.0	5500829.1				Crowsnest
ND005	-114.476	49.631	682292.7	5500627.3				Crowsnest
ND006	-114.471	49.627	682628.4	5500255.0	194	54	bedding	
ND007	-114.473	49.628	682508.3	5500357.9				Beaver Mines
ND008	-114.474	49.629	682422.9	5500436.2	170	55	bedding	Blackstone
ND009	-114.481	49.636	681867.0	5501162.0	187	70	bedding	
ND010	-114.480	49.635	681961.2	5501109.0				Cardium
ND011	-114.497	49.630	680730.7	5500504.1	184	30	bedding	Belly River
ND012	-114.480	49.650	681904.5	5502803.1				
ND013	-114.479	49.685	681863.9	5506630.3	165	52	bedding	Wapiabi
ND014	-114.482	49.697	681585.6	5507935.2				Wapiabi
ND015	-114.481	49.703	681613.1	5508632.9	163	31	bedding	Wapiabi
ND016	-114.479	49.710	681712.5	5509447.7	183	37	bedding	
ND017	-114.478	49.717	681828.7	5510203.8				Wapiabi
ND018	-114.472	49.736	682147.3	5512389.5				Wapiabi
ND019	-114.475	49.740	681912.6	5512782.5				Wapiabi
ND020	-114.439	49.600	685072.2	5497300.7				Cadomin
ND021	-114.439	49.593	685066.2	5496527.1				
ND022	-114.446	49.582	684628.0	5495343.5				Dalhousie
ND023	-114.490	49.558	681523.7	5492463.0	178	41	bedding	Cadomin
ND024	-114.493	49.557	681299.8	5492381.2				
ND025	-114.500	49.545	680847.7	5491042.1				Crowsnest
ND026	-114.498	49.546	680970.3	5491200.0				
ND027	-114.503	49.615	680395.0	5498839.9	182	34	bedding	Cadomin
ND028	-114.485	49.551	681884.8	5491694.7	173	32	bedding	Cadomin
ND029	-114.499	49.548	680889.9	5491357.0				Crowsnest
ND030	-114.461	49.565	683563.3	5493393.8	194	26	bedding	Cardium
ND031	-114.454	49.570	684051.6	5493936.1	180	56	bedding	
ND032	-114.443	49.572	684885.3	5494183.4	26	70	bedding	Cadomin
ND033	-114.446	49.571	684641.6	5494062.3				
ND034	-114.447	49.570	684590.4	5494000.0	170	74	bedding	
ND035	-114.497	49.637	680690.1	5501227.9	198	28	bedding	Belly River
ND036	-114.450	49.602	684245.2	5497448.6	157	32	bedding	
ND037	-114.450	49.596	684298.3	5496800.5	160	64	bedding	Cadomin
ND038	-114.450	49.596	684270.3	5496797.2	167	30	bedding	
ND039	-114.453	49.596	684039.2	5496878.0	155	45	bedding	
ND040	-114.454	49.596	683957.0	5496793.7	145	44	bedding	
ND041	-114.457	49.596	683766.6	5496780.6	179	62	bedding	Beaver Mines
					70	58	joint	Beaver Mines
					30	32	joint	Beaver Mines
ND042	-114.459	49.595	683594.5	5496683.2	186	54	bedding	

<u>Waypoint</u>	<u>Longitude</u>	<u>Latitude</u>	<u>UTM</u> <u>Easting</u>	<u>UTM</u> <u>Northing</u>	<u>Azimuth</u>	<u>Inclination</u>	<u>Type</u>	<u>Stratigraphic</u> <u>Unit</u>
ND043	-114.460	49.597	683515.4	5496874.2	184	51	bedding	
ND044	-114.465	49.595	683215.9	5496639.5	174	58	bedding	Crowsnest
ND045	-114.470	49.667	682527.4	5504680.5	184	51	bedding	Cardium
ND046	-114.469	49.666	682657.7	5504585.5	174	58	bedding	Blackstone
ND047	-114.463	49.665	683059.1	5504451.4				Crowsnest
ND048	-114.461	49.665	683188.9	5504482.8				Blackstone
ND049	-114.460	49.666	683306.3	5504645.5	162	86	bedding	Cardium
ND050	-114.453	49.665	683817.1	5504450.1				Crowsnest
ND051	-114.450	49.662	684054.4	5504140.7				
ND052	-114.449	49.662	684064.7	5504130.6				
ND053	-114.449	49.661	684061.5	5504055.5				
ND054	-114.445	49.660	684381.7	5503935.9				
ND055	-114.440	49.657	684729.6	5503624.2	175	24	bedding	
ND056	-114.435	49.658	685124.0	5503752.9				
ND057	-114.463	49.707	682891.7	5509093.5	166	39	bedding	Cardium
ND058	-114.461	49.714	683031.2	5509951.1				Crowsnest
ND059	-114.459	49.713	683205.4	5509832.0	162	53	bedding	Mill Creek
ND060	-114.457	49.711	683362.8	5509626.0	163	28	bedding	
ND061	-114.455	49.710	683458.2	5509467.2	172	50	bedding	
ND062	-114.455	49.710	683507.4	5509448.4	178	58	bedding	Mill Creek
					243	28	slickenline	Mill Creek
ND063	-114.453	49.710	683596.5	5509488.3				Mill Creek
ND064	-114.454	49.716	683534.6	5510214.7	158	56	bedding	Mill Creek
ND065	-114.441	49.719	684438.1	5510547.5	184	34	bedding	Mill Creek
ND066	-114.444	49.718	684215.8	5510385.3	161	38	bedding	Mill Creek
ND067	-114.446	49.717	684085.1	5510308.6				Crowsnest
ND068	-114.447	49.718	684008.5	5510411.0	166	43	bedding	Mill Creek
ND069	-114.449	49.719	683896.9	5510458.5	5	72	bedding	Mill Creek
ND070	-114.451	49.717	683712.5	5510319.6	150	42	bedding	
ND071	-114.431	49.720	685187.9	5510649.5	120	6	bedding	
ND071	-114.431	49.720	685187.9	5510649.5	133	24	slickenline	
ND072	-114.430	49.723	685233.5	5511053.3	328	26	bedding	Mill Creek
ND073	-114.436	49.742	684720.9	5513066.1	340	82	bedding	
ND074	-114.436	49.741	684700.0	5512950.0				Crowsnest
ND075	-114.437	49.739	684661.8	5512758.1	148	31	bedding	Mill Creek
ND076	-114.443	49.743	684246.0	5513141.0				
ND077	-114.444	49.743	684170.9	5513194.9	359	58	bedding	
ND078	-114.449	49.753	683732.9	5514239.2				
ND079	-114.433	49.741	684961.0	5512987.6				Crowsnest
ND080	-114.433	49.744	684911.2	5513284.1	231	11	bedding	
ND081	-114.444	49.722	684203.6	5510802.8	167	26	bedding	
ND082	-114.446	49.727	684081.3	5511369.2				
ND083	-114.465	49.712	682752.3	5509701.4	169	50	bedding	Cardium
ND084	-114.500	49.604	680597.3	5497598.1	173	36	bedding	Cadomin
ND085	-114.500	49.604	680614.7	5497564.5	191	34	bedding	Cadomin
ND086	-114.501	49.601	680588.8	5497257.1				Gladstone
ND087	-114.484	49.747	681232.1	5513568.8	155	15	bedding	
ND088	-114.479	49.747	681618.7	5513521.2	201	27	bedding	Cardium
ND089	-114.478	49.744	681679.6	5513221.4				Cardium
ND090	-114.479	49.742	681660.9	5512971.1				Wapiabi

<u>Waypoint</u>	<u>Longitude</u>	<u>Latitude</u>	<u>UTM</u> <u>Easting</u>	<u>UTM</u> <u>Northing</u>	<u>Azimuth</u>	<u>Inclination</u>	<u>Type</u>	<u>Stratigraphic</u> <u>Unit</u>
ND091	-114.475	49.744	681934.1	5513272.7	53	9	bedding	Cardium
ND092	-114.478	49.751	681693.9	5513964.9				Wapiabi
ND093	-114.488	49.749	680966.5	5513775.7				Wapiabi
ND094	-114.491	49.749	680769.7	5513702.1				Wapiabi
ND095	-114.495	49.747	680488.9	5513519.4	169	36	bedding	Belly River
ND096	-114.495	49.747	680461.9	5513508.7				Belly River
ND097	-114.468	49.733	682465.1	5511981.6	178	61	bedding	Cardium
ND098	-114.494	49.515	681387.5	5487717.9				Crowsnest
ND099	-114.493	49.517	681483.2	5487993.4	160	29	bedding	Crowsnest
ND100	-114.494	49.517	681387.1	5487996.8	167	41	bedding	
ND101	-114.492	49.520	681531.8	5488336.1	151	34	bedding	Crowsnest
ND102	-114.491	49.522	681583.7	5488506.1	184	38	bedding	Crowsnest
ND103	-114.490	49.523	681623.9	5488614.4				Crowsnest
ND104	-114.490	49.523	681650.7	5488661.2	168	44	bedding	Crowsnest
ND105	-114.489	49.524	681708.2	5488734.2	160	49	bedding	Mill Creek
ND109	-114.390	49.739	688073.7	5512882.2	182	47	bedding	
ND110	-114.390	49.740	688061.8	5512993.4	191	47	bedding	
					206	31	fault	
					116	30	slickenline	
					322	36	bedding	
					196	58	fault	
ND111	-114.460	49.695	683154.5	5507811.6	178	34	bedding	Cardium
ND112	-114.459	49.694	683234.2	5507718.4	188	34	bedding	
ND113	-114.434	49.669	685141.9	5505039.4				
ND114	-114.438	49.675	684854.1	5505658.7	172	42	bedding	
ND115	-114.438	49.677	684829.2	5505923.7	188	25	bedding	Beaver Mines
ND116	-114.438	49.678	684803.0	5505971.6	187	37	bedding	Beaver Mines
ND117	-114.439	49.681	684735.7	5506318.5	173	23	bedding	Beaver Mines
ND118	-114.442	49.693	684472.4	5507693.6	209	29	bedding	Beaver Mines
ND119	-114.448	49.700	684031.1	5508389.5				
ND120	-114.459	49.707	683220.4	5509190.7	176	58	bedding	Crowsnest
ND121	-114.467	49.702	682638.5	5508593.2				Wapiabi
ND122	-114.421	49.721	685883.1	5510821.5	88	76	bedding	
ND123	-114.407	49.728	686849.7	5511576.6	178	48	bedding	
					184	51	fault	
					226	43	slickenline	
					111	52	fault	
					233	46	slickenline	
					191	54	bedding	
ND124	-114.406	49.729	686945.4	5511689.4	179	50	bedding	Beaver Mines
ND125	-114.397	49.734	687530.4	5512340.6	166	88	bedding	
ND126	-114.398	49.734	687520.5	5512335.8	182	64	bedding	Cadomin
ND127	-114.398	49.734	687490.6	5512315.9	170	78	bedding	
ND128	-114.399	49.734	687413.0	5512271.8	166	68	bedding	Gladstone
ND129	-114.400	49.734	687327.6	5512291.1	175	64	bedding	
ND130	-114.401	49.734	687262.5	5512279.5	173	76	bedding	
ND131	-114.394	49.736	687791.1	5512519.4	0	80	bedding	
ND132	-114.392	49.739	687944.5	5512831.0	152	22	bedding	Beaver Mines
ND133	-114.391	49.741	687971.0	5513055.4	178	36	bedding	
ND134	-114.390	49.739	688065.4	5512926.6				

<u>Waypoint</u>	<u>Longitude</u>	<u>Latitude</u>	<u>UTM</u> <u>Easting</u>	<u>UTM</u> <u>Northing</u>	<u>Azimuth</u>	<u>Inclination</u>	<u>Type</u>	<u>Stratigraphic</u> <u>Unit</u>
ND135	-114.390	49.740	688062.1	5512985.7				
ND136	-114.385	49.744	688396.7	5513471.0				Dalhousie
ND137	-114.385	49.744	688405.1	5513467.8				Dalhousie
ND138	-114.449	49.734	683823.5	5512140.1				
ND139	-114.481	49.525	682296.6	5488886.2	160	46	bedding	
ND140	-114.482	49.525	682218.9	5488912.5	163	43	bedding	
ND141	-114.481	49.526	682279.6	5489027.3	163	43	bedding	
ND142	-114.479	49.528	682439.2	5489191.7	145	28	bedding	Gladstone
ND143	-114.477	49.524	682602.2	5488732.0	157	62	bedding	
ND144	-114.473	49.519	682923.0	5488246.2	192	40	bedding	
ND145	-114.469	49.517	683174.8	5487998.6				Crowsnest
ND146	-114.464	49.516	683545.6	5487866.1	268	49	bedding	
ND147	-114.463	49.516	683633.5	5487957.2	171	30	bedding	Cardium
ND148	-114.459	49.517	683889.6	5488010.8	151	27	bedding	Crowsnest
ND149	-114.470	49.516	683141.5	5487906.1	157	11	bedding	
ND150	-114.450	49.732	683781.5	5511986.7	195	88	bedding	Beaver Mines
ND151	-114.452	49.733	683578.7	5512072.3				Beaver Mines
ND152	-114.455	49.733	683380.2	5512058.9	172	60	bedding	Mill Creek
ND153	-114.456	49.733	683314.0	5512017.5	170	54	bedding	
					329	34	fault	
					75	29	slickenline	
ND154	-114.458	49.732	683203.3	5511906.7	169	28	bedding	Cardium
					270	76	fault	Cardium
					265	7	slickenline	Cardium
ND155	-114.440	49.725	684534.4	5511249.3	165	8	bedding	
ND156	-114.439	49.727	684562.0	5511410.3	84	16	bedding	
ND157	-114.458	49.560	683859.7	5492834.9	68	48	bedding	Crowsnest
ND158	-114.467	49.555	683215.4	5492214.6	113	46	bedding	
ND159	-114.471	49.542	682952.3	5490760.1	204	34	bedding	
ND160	-114.499	49.600	680688.7	5497153.9	213	16	bedding	Kootenay
ND161	-114.497	49.601	680869.1	5497323.3	172	14	bedding	
ND162	-114.497	49.600	680881.5	5497149.4	183	35	bedding	Cardium
ND163	-114.380	49.744	688720.3	5513454.3	41	32	bedding	Cardium
ND164	-114.394	49.565	688441.2	5493498.8	139	29	bedding	
ND165	-114.395	49.564	688348.2	5493449.5				
ND166	-114.396	49.564	688266.9	5493400.7	269	62	bedding	
ND167	-114.397	49.564	688238.5	5493390.7	304	79	bedding	
ND168	-114.405	49.563	687626.1	5493265.4	147	60	bedding	
ND169	-114.410	49.562	687277.7	5493204.8	174	79	bedding	Wileman
ND170	-114.412	49.562	687176.9	5493189.2	158	81	bedding	Livingstone
ND171	-114.416	49.561	686870.9	5493014.7	95	9	bedding	Livingstone
ND172	-114.416	49.561	686854.8	5493020.7	170	24	bedding	
ND173	-114.416	49.561	686844.5	5493033.4	175	36	bedding	
ND174	-114.416	49.561	686881.5	5493021.8	46	50	bedding	
ND175	-114.415	49.561	686910.3	5493021.8	15	58	bedding	
ND176	-114.415	49.560	686910.3	5492938.5	74	30	bedding	
ND177	-114.416	49.560	686898.7	5492943.5	127	39	bedding	
ND178	-114.415	49.560	686916.3	5492944.9	0	72	bedding	
ND179	-114.408	49.657	687050.8	5503708.5	278	38	bedding	
ND180	-114.409	49.656	687018.1	5503658.1	297	30	bedding	

<u>Waypoint</u>	<u>Longitude</u>	<u>Latitude</u>	<u>UTM</u> <u>Easting</u>	<u>UTM</u> <u>Northing</u>	<u>Azimuth</u>	<u>Inclination</u>	<u>Type</u>	<u>Stratigraphic</u> <u>Unit</u>
ND181	-114.410	49.655	686951.4	5503528.9	221	31	bedding	
ND182	-114.409	49.653	686980.1	5503228.6	81	29	bedding	
ND183	-114.409	49.652	686993.8	5503195.0				
ND184	-114.410	49.650	686959.6	5502962.9	212	12	bedding	
ND185	-114.410	49.649	686988.3	5502839.0				
ND186	-114.409	49.648	687012.9	5502759.4	350	77	bedding	
ND187	-114.414	49.649	686646.4	5502806.8	252	26	bedding	
ND188	-114.415	49.651	686614.2	5503070.5	285	30	bedding	
ND189	-114.415	49.652	686604.6	5503185.0	0	10	bedding	
ND190	-114.412	49.658	686773.3	5503819.0	351	62	bedding	Fernie
ND191	-114.409	49.668	686939.2	5504968.5				Dalhousie
NJ001	-114.498	49.596	680805.9	5496737.7				Kootenay
NJ002	-114.497	49.591	680915.7	5496206.6	154	31	bedding	Cadomin
NJ003	-114.491	49.592	681330.1	5496252.2	314	36	bedding	Crowsnest
NJ004	-114.491	49.588	681337.4	5495853.9				Cardium
NJ005	-114.490	49.588	681373.8	5495854.4	134	56	bedding	Cardium
NJ006	-114.490	49.589	681422.1	5495908.4	122	54	bedding	Crowsnest
NJ007	-114.489	49.589	681458.9	5495915.7	152	29	bedding	Blackstone
NJ008	-114.492	49.586	681264.8	5495647.5	178	31	bedding	Kootenay
NJ009	-114.491	49.587	681329.4	5495715.9	96	45	bedding	
NJ010	-114.491	49.587	681351.7	5495741.1	126	52	bedding	
NJ011	-114.491	49.586	681341.5	5495664.3	189	33	bedding	
NJ012	-114.489	49.585	681481.5	5495485.2	156	43	bedding	
NJ013	-114.490	49.584	681424.2	5495451.8	166	36	bedding	Cadomin
NJ014	-114.490	49.584	681438.1	5495376.0	154	39	bedding	Dalhousie
NJ015	-114.493	49.580	681212.6	5494956.2	182	24	bedding	Gladstone
NJ016	-114.494	49.580	681121.7	5494916.0	178	49	bedding	Beaver Mines
NJ017	-114.498	49.579	680898.9	5494791.4				
NJ018	-114.438	49.659	684870.9	5503848.6	175	20	bedding	Gladstone
NJ019	-114.437	49.663	684943.1	5504281.6				Gladstone
NJ020	-114.434	49.664	685135.3	5504468.3	199	18	bedding	Gladstone
NJ021	-114.434	49.665	685192.1	5504538.6	189	28	bedding	Gladstone
NJ022	-114.431	49.666	685362.9	5504679.2	186	29	bedding	
NJ023	-114.430	49.667	685443.9	5504766.0	196	30	bedding	Cadomin
NJ024	-114.430	49.669	685460.5	5504967.7	191	41	bedding	Cadomin
NJ025	-114.406	49.740	686884.4	5512919.6				Beaver Mines
NJ026	-114.408	49.741	686745.0	5513068.3	266	87	bedding	
NJ027	-114.409	49.741	686662.4	5513087.1	359	79	bedding	Beaver Mines
NJ028	-114.415	49.740	686262.1	5512936.9	173	80	bedding	
NJ029	-114.489	49.516	681731.0	5487821.8				Crowsnest
NJ030	-114.490	49.514	681701.8	5487623.0				Crowsnest
NJ031	-114.491	49.514	681642.4	5487580.1	145	44	bedding	Crowsnest
NJ032	-114.437	49.684	684874.4	5506661.6	160	30	bedding	
NJ033	-114.434	49.685	685072.0	5506798.3	183	58	bedding	Beaver Mines
NJ034	-114.431	49.686	685286.7	5506910.2				Cardium
NJ035	-114.431	49.686	685332.2	5506916.5	181	39	bedding	Cardium
NJ036	-114.429	49.687	685423.7	5506957.4	164	50	bedding	Blackstone
NJ037	-114.427	49.687	685591.6	5506979.1	179	55	bedding	Cadomin
NJ038	-114.429	49.690	685442.7	5507365.4				Cadomin
NJ039	-114.407	49.523	687687.0	5488840.3	177	87	bedding	Wileman

<u>Waypoint</u>	<u>Longitude</u>	<u>Latitude</u>	<u>UTM</u> <u>Easting</u>	<u>UTM</u> <u>Northing</u>	<u>Azimuth</u>	<u>Inclination</u>	<u>Type</u>	<u>Stratigraphic</u> <u>Unit</u>
NJ040	-114.412	49.524	687310.6	5488958.8	159	40	bedding	Livingstone
NJ041	-114.415	49.525	687094.2	5488987.9	179	29	bedding	Livingstone
NJ042	-114.416	49.525	687017.6	5489068.8	157	34	bedding	Wileman
NJ043	-114.417	49.525	686951.5	5489070.9	166	30	bedding	
NJ044	-114.417	49.525	686946.4	5489081.7	176	36	bedding	
NJ045	-114.502	49.650	680284.3	5502719.2	164	37	bedding	Dalhousie
NJ046	-114.502	49.650	680310.1	5502732.0	144	21	bedding	Kootenay
NJ047	-114.499	49.648	680543.5	5502527.8				Crowsnest
NJ048	-114.435	49.566	685469.1	5493496.9	184	49	bedding	Beaver Mines
NJ049	-114.434	49.566	685550.0	5493565.2	185	55	bedding	
NJ050	-114.435	49.567	685489.9	5493633.3	181	47	bedding	
NJ051	-114.432	49.566	685657.9	5493533.0	182	52	bedding	
NJ052	-114.431	49.564	685750.5	5493272.0	183	46	bedding	Cadomin
NJ053	-114.431	49.562	685762.5	5493094.1	195	39	bedding	Cadomin
NJ054	-114.430	49.563	685828.0	5493199.2	177	45	bedding	Kootenay
NJ055	-114.424	49.562	686242.6	5493166.4	172	56	bedding	Etherington
NJ056	-114.424	49.562	686294.7	5493158.8	173	46	bedding	Carnarvon
NJ057	-114.420	49.562	686579.6	5493152.7	162	69	bedding	Livingstone
NJ058	-114.434	49.564	685572.3	5493334.8	170	50	bedding	
NJ059	-114.435	49.562	685513.5	5493092.9	179	59	bedding	Beaver Mines
NJ060	-114.438	49.560	685243.9	5492897.6	190	31	bedding	Dalhousie
NJ061	-114.438	49.558	685245.1	5492614.8	190	43	bedding	Dalhousie
NJ062	-114.441	49.555	685089.0	5492297.1	186	44	bedding	Beaver Mines
NJ063	-114.442	49.552	684980.9	5491912.4	198	54	bedding	Dalhousie
NJ064	-114.447	49.548	684659.7	5491452.6	185	48	bedding	
NJ065	-114.449	49.547	684526.8	5491413.7	173	55	bedding	Beaver Mines
NJ066	-114.452	49.547	684294.3	5491335.4	188	35	bedding	
NJ067	-114.455	49.548	684109.4	5491440.4				
NJ068	-114.462	49.577	683446.3	5494742.2	178	50	bedding	Cardium
NJ069	-114.458	49.576	683756.4	5494611.6	233	10	bedding	Crowsnest
NJ070	-114.415	49.685	686480.5	5506766.7				Kootenay
NJ071	-114.415	49.685	686433.3	5506824.9	190	24	bedding	Cadomin
NJ072	-114.416	49.687	686364.8	5507033.3	191	59	bedding	
NJ073	-114.417	49.693	686284.9	5507743.1	175	62	bedding	Cadomin
NJ074	-114.417	49.697	686291.2	5508148.2	180	52	bedding	
NJ075	-114.418	49.698	686157.2	5508292.4	185	50	bedding	
NJ076	-114.419	49.699	686111.9	5508337.3	178	40	bedding	
NJ077	-114.421	49.699	685987.8	5508409.5				
NJ078	-114.420	49.698	686032.6	5508239.5	193	56	bedding	Beaver Mines
NJ079	-114.419	49.695	686135.9	5507928.1	160	16	bedding	Beaver Mines
NJ080	-114.429	49.714	685317.4	5509992.5	158	22	bedding	Beaver Mines
					160	16	bedding	Beaver Mines
NJ081	-114.431	49.715	685202.8	5510089.8	158	22	bedding	
					081	65	fracture	
					210	82	fracture	
NJ083	-114.431	49.711	685189.6	5509659.9	305	56	fracture	
NJ084	-114.430	49.709	685280.6	5509419.1	205	22	bedding	Beaver Mines
NJ085	-114.429	49.706	685383.8	5509117.9	212	32	bedding	
NJ086	-114.431	49.705	685198.7	5508987.2	227	34	bedding	Beaver Mines
NJ087	-114.430	49.708	685256.3	5509338.7	172	76	bedding	Beaver Mines

<u>Waypoint</u>	<u>Longitude</u>	<u>Latitude</u>	<u>UTM</u> <u>Easting</u>	<u>UTM</u> <u>Northings</u>	<u>Azimuth</u>	<u>Inclination</u>	<u>Type</u>	<u>Stratigraphic</u> <u>Unit</u>
NJ088	-114.416	49.671	686463.2	5505289.4	184	83	bedding	
NJ089	-114.413	49.672	686632.2	5505382.9	008	84	bedding	
					150	80	bedding	
					193	76	fault	
					282	62	slickenline	
					018	86	bedding	
					011	60	bedding	
					321	50	fault	
NJ090	-114.411	49.672	686774.0	5505340.2	083	46	slickenline	Cadomin
NJ091	-114.414	49.672	686554.9	5505399.9	353	76	bedding	
NJ092	-114.415	49.672	686499.5	5505340.9	285	38	bedding	
					154	31	bedding	
					330	79	fault	
NJ093	-114.439	49.714	684618.3	5509972.3	137	62	slickenline	
NJ094	-114.440	49.713	684547.0	5509922.2				
NJ095	-114.448	49.717	683952.9	5510326.3				Crowsnest
NJ096	-114.463	49.706	682882.2	5509085.4				
NJ097	-114.449	49.718	683897.5	5510445.5	175	70	bedding	
NJ098	-114.472	49.682	682336.5	5506361.3				Cardium
NJ099	-114.470	49.681	682479.4	5506275.8	174	36	bedding	Cardium
NJ100	-114.462	49.682	683085.8	5506369.3	156	54	bedding	
NJ101	-114.460	49.682	683205.2	5506389.1	342	64	bedding	Blackstone
NJ102	-114.458	49.682	683341.9	5506344.6	176	24	bedding	
NJ103	-114.384	49.635	688905.0	5501344.1				Mill Creek
NJ104	-114.377	49.614	689479.4	5499003.5	172	35	bedding	Mill Creek
NJ105	-114.376	49.612	689556.9	5498801.7	112	33	bedding	
NJ106	-114.374	49.607	689700.8	5498273.9	123	61	bedding	
NJ107	-114.380	49.608	689258.2	5498302.3	136	16	bedding	Beaver Mines
NJ108	-114.404	49.603	687584.1	5497770.4	226	19	bedding	Gladstone
NJ109	-114.407	49.607	687368.9	5498117.6	168	66	bedding	Gladstone
NJ110	-114.400	49.661	687624.9	5504194.6	161	4	bedding	Mill Creek
NJ111	-114.395	49.653	688014.0	5503298.4	136	32	bedding	Beaver Mines
NJ112	-114.394	49.658	688056.0	5503881.7	160	32	bedding	Mill Creek
NJ113	-114.388	49.656	688528.9	5503664.8	175	50	bedding	Dalhousie
NJ114	-114.403	49.560	687824.7	5493005.9	19	84	bedding	Cadomin
NJ115	-114.408	49.558	687477.1	5492708.1	358	81	bedding	Etherington
NJ116	-114.408	49.558	687451.8	5492726.0	183	79	bedding	Etherington
NJ117	-114.409	49.559	687340.2	5492871.7	177	74	bedding	
NJ118	-114.410	49.559	687332.6	5492867.2	163	76	bedding	
NJ119	-114.410	49.560	687319.5	5492881.7	272	77	bedding	
NJ120	-114.415	49.560	686901.1	5492903.0	70	32	bedding	
NJ121	-114.415	49.560	686906.3	5492916.3	212	11	bedding	
NJ122	-114.420	49.560	686570.8	5492926.1	212	85	bedding	
NJ123	-114.420	49.561	686564.1	5492970.0	171	77	bedding	
NJ124	-114.377	49.533	689771.0	5490056.9	357	71	bedding	Beaver Mines
NJ125	-114.384	49.531	689296.5	5489791.4	46	86	bedding	Beaver Mines
NJ126	-114.385	49.529	689257.9	5489592.5	41	61	bedding	Beaver Mines
NJ127	-114.397	49.507	688472.4	5487034.8	47	57	bedding	Kootenay
NJ128	-114.394	49.521	688608.2	5488656.6	20	24	bedding	
NJ129	-114.393	49.522	688703.2	5488698.2				Dalhousie

<u>Waypoint</u>	<u>Longitude</u>	<u>Latitude</u>	<u>UTM</u> <u>Easting</u>	<u>UTM</u> <u>Northings</u>	<u>Azimuth</u>	<u>Inclination</u>	<u>Type</u>	<u>Stratigraphic</u> <u>Unit</u>
MV036	-114.423	49.623	686122.6	5499955.0	213	26	bedding	Marston
MV037	-114.423	49.624	686120.7	5500004.5				Marston
MV038	-114.423	49.624	686135.9	5500063.5				Marston
MV039	-114.422	49.624	686201.1	5500068.2	237	26	bedding	Marston
MV040	-114.421	49.625	686288.3	5500107.2	216	15	bedding	Marston
MV041	-114.420	49.625	686291.9	5500161.8				Marston
MV042	-114.421	49.626	686260.5	5500215.2	194	19	bedding	Marston
MV043	-114.421	49.627	686271.1	5500360.3	208	26	bedding	Marston
MV044	-114.421	49.627	686233.9	5500402.0				Carnarvon
MV045	-114.422	49.628	686203.0	5500437.6	182	27	bedding	Carnarvon
MV046	-114.422	49.628	686180.0	5500409.2	265	40	bedding	Carnarvon
MV047	-114.422	49.627	686199.6	5500395.0	105	84	bedding	Carnarvon
					269	50	bedding	
					33	71	fault plane	
MV048	-114.422	49.627	686166.5	5500394.1	224	44	bedding	Carnarvon
					172	87	thrust fault	
MV049	-114.425	49.627	685938.4	5500350.5	182	16	bedding	Carnarvon
MV050	-114.428	49.625	685729.2	5500158.6				Carnarvon
MV051	-114.436	49.624	685209.1	5500014.3	174	46	bedding	Fernie
MV052	-114.428	49.608	685843.4	5498217.8				Loomis
MV053	-114.426	49.607	685984.0	5498072.4				Livingstone
MV054	-114.430	49.609	685654.9	5498371.6	168	63	bedding	Marston
MV055	-114.419	49.669	686200.8	5505080.8	183	14	bedding	Fernie
MV056	-114.411	49.670	686805.3	5505106.8	10	65	bedding	Fernie
MV057	-114.419	49.671	686234.2	5505273.5	337	13	bedding	Fernie
MV058	-114.420	49.671	686148.8	5505244.0	222	18	bedding	Fernie
MV059	-114.419	49.676	686207.7	5505787.1	324	15	bedding	Kootenay
					1	59	bedding	
MV060	-114.419	49.677	686180.4	5505919.3				Kootenay
MV061	-114.431	49.610	685610.0	5498486.5				Carnarvon
MV062	-114.430	49.611	685676.4	5498532.1	265	84	joint	Carnarvon
					333	36	joint	
MV063	-114.429	49.611	685709.3	5498560.6	175	53	bedding	Marston
MV064	-114.428	49.611	685774.1	5498549.6	172	61	bedding	Loomis
MV065	-114.428	49.611	685800.5	5498563.6	183	44	bedding	Loomis
MV066	-114.427	49.613	685840.2	5498747.1	171	41	bedding	Loomis
MV067	-114.426	49.614	685900.2	5498891.9	175	41	bedding	Salter/Wileman
MV068	-114.426	49.615	685959.7	5498999.5				Salter/Wileman
MV069	-114.425	49.616	686010.8	5499120.0	169	40	bedding	Salter/Wileman
MV070	-114.424	49.617	686062.0	5499248.6				Salter/Wileman
MV071	-114.424	49.618	686096.3	5499356.2				Salter/Wileman
MV072	-114.422	49.619	686199.7	5499500.2				
MV073	-114.421	49.620	686254.9	5499612.8	205	4	bedding	Salter/Wileman
					229	5	bedding	
					196	72	joint	
					114	89	joint	
MV074	-114.420	49.621	686306.3	5499677.5	177	90	joint	Loomis
MV075	-114.420	49.621	686352.6	5499636.5				Salter/Wileman
MV076	-114.423	49.620	686123.2	5499590.4	305	68	joint	Salter/Wileman
MV077	-114.424	49.614	686065.1	5498952.8	185	50	bedding	Salter/Wileman

<u>Waypoint</u>	<u>Longitude</u>	<u>Latitude</u>	<u>UTM</u> <u>Easting</u>	<u>UTM</u> <u>Northing</u>	<u>Azimuth</u>	<u>Inclination</u>	<u>Type</u>	<u>Stratigraphic</u> <u>Unit</u>
MV078	-114.424	49.614	686042.7	5498914.8	186	48	bedding	Salter/Wileman
MV079	-114.425	49.613	686039.8	5498830.4	188	44	bedding	Salter/Wileman
MV080	-114.426	49.612	685950.4	5498681.0				Baril
MV081	-114.423	49.607	686204.7	5498080.2	187	54	bedding	Livingstone
MV082	-114.447	49.637	684320.8	5501372.7				Blairmore
MV083	-114.446	49.637	684398.3	5501376.2				Blairmore
MV084	-114.444	49.638	684549.8	5501495.6	199	36	bedding	Blairmore
MV085	-114.445	49.639	684491.7	5501645.0				Blairmore
MV086	-114.441	49.642	684777.0	5502001.7	180	44	bedding	Cadomin
MV087	-114.439	49.642	684871.2	5502001.1				Kootenay
MV088	-114.437	49.643	685009.6	5502089.0				Kootenay
MV089	-114.436	49.643	685133.9	5502099.8				Fernie
MV090	-114.433	49.645	685342.8	5502312.6	200 86	25 72	bedding joint	Kootenay
MV091	-114.451	49.642	683993.9	5501892.4	160	40	bedding	Blairmore
MV092	-114.419	49.625	686398.9	5500082.6				Marston
MV093	-114.418	49.625	686448.5	5500155.5				Carnarvon
MV094	-114.417	49.626	686564.8	5500233.5				Carnarvon
MV095	-114.416	49.627	686585.4	5500335.6				Carnarvon
MV096	-114.415	49.628	686676.9	5500437.1	64	16	bedding	Etherington
MV097	-114.414	49.630	686750.6	5500715.2				Etherington
MV098	-114.414	49.631	686709.1	5500860.5				Etherington
MV099	-114.414	49.632	686705.3	5500955.0	255	24	bedding	Etherington
MV100	-114.415	49.633	686679.0	5501021.0				Etherington
MV101	-114.415	49.633	686658.7	5501011.7	201	21	bedding	Etherington
MV102	-114.415	49.634	686676.3	5501106.2				Etherington
MV103	-114.415	49.635	686639.8	5501205.9				Etherington
MV104	-114.415	49.635	686628.6	5501305.0				Etherington
MV105	-114.416	49.636	686581.5	5501380.6	180	23	bedding	Etherington
MV106	-114.416	49.636	686573.0	5501326.4				Etherington
MV107	-114.416	49.635	686579.3	5501252.9				Etherington
MV108	-114.416	49.634	686545.6	5501162.4	214	24	bedding	Etherington
MV109	-114.417	49.633	686484.2	5501014.6				Etherington
MV110	-114.426	49.623	685935.0	5499863.9				Carnarvon
MV111	-114.426	49.622	685917.7	5499792.1	165	38	bedding	Carnarvon
MV112	-114.435	49.639	685173.9	5501636.5				Kootenay
MV113	-114.431	49.641	685454.7	5501869.9				Fernie
MV114	-114.448	49.646	684217.0	5502358.9	200	39	bedding	Blairmore
MV115	-114.444	49.651	684516.4	5502937.0	185	24	bedding	Blairmore
MV116	-114.443	49.651	684567.3	5503009.8	214	35	bedding	Blairmore
MV117	-114.440	49.654	684789.3	5503273.6	185	34	bedding	Blairmore
MV118	-114.439	49.654	684815.5	5503309.6				Blairmore
MV119	-114.432	49.658	685322.1	5503762.2				Kootenay
MV120	-114.452	49.639	683973.8	5501612.1				Blairmore
MV121	-114.452	49.636	683943.2	5501243.6	185	37	bedding	Blairmore
MV122	-114.451	49.633	684058.6	5500962.9				Blairmore
MV123	-114.451	49.629	684069.6	5500454.7	185	40	bedding	Blairmore
MV124	-114.445	49.618	684540.4	5499328.0				Blairmore
MV125	-114.442	49.612	684783.1	5498655.0	151	24	bedding	Kootenay
MV126	-114.442	49.612	684766.5	5498656.4				Cadomin

<u>Waypoint</u>	<u>Longitude</u>	<u>Latitude</u>	<u>UTM</u> <u>Easting</u>	<u>UTM</u> <u>Northing</u>	<u>Azimuth</u>	<u>Inclination</u>	<u>Type</u>	<u>Stratigraphic</u> <u>Unit</u>
MV127	-114.443	49.612	684706.3	5498682.0	201	20	bedding	Cadomin
MV128	-114.448	49.631	684294.7	5500687.2				Blairmore
MV129	-114.448	49.631	684309.9	5500701.0	183	36	bedding	Blairmore
MV130	-114.447	49.630	684382.9	5500676.5				Blairmore
MV131	-114.444	49.631	684572.1	5500742.1				Blairmore
MV132	-114.443	49.631	684654.6	5500790.6				Blairmore
MV133	-114.442	49.632	684698.5	5500803.2	184	58	bedding	Blairmore
MV134	-114.442	49.631	684732.1	5500802.4				Blairmore
MV135	-114.441	49.632	684773.0	5500820.0	184	68	bedding	Cadomin
MV136	-114.441	49.632	684817.7	5500826.7	187	34	bedding	Cadomin
MV137	-114.440	49.631	684857.4	5500787.5	174	40	bedding	Kootenay
MV138	-114.439	49.632	684916.4	5500829.0	202	50	bedding	Kootenay
MV139	-114.438	49.634	685021.2	5501036.7	194	38	bedding	Kootenay
MV140	-114.437	49.634	685033.1	5501079.9				Kootenay
MV141	-114.437	49.634	685034.6	5501099.5				Cadomin
MV145	-114.436	49.635	685103.5	5501248.7	206	47	bedding	Cadomin
MV146	-114.436	49.635	685133.0	5501208.2	194	21	bedding	Kootenay
MV147	-114.436	49.635	685113.7	5501185.7	183	36	bedding	Kootenay
MV148	-114.440	49.631	684869.6	5500711.4	186	22	bedding	Kootenay
MV149	-114.440	49.630	684850.5	5500621.8				Kootenay
MV150	-114.440	49.629	684844.1	5500541.2	184	37	bedding	Kootenay
MV151	-114.441	49.628	684821.0	5500468.2				Kootenay
MV152	-114.441	49.628	684799.3	5500392.7	177	26	bedding	Kootenay
MV153	-114.441	49.626	684774.9	5500165.6	161	43	bedding	Kootenay
MV154	-114.442	49.625	684719.7	5500114.0	185	46	bedding	Cadomin
MV155	-114.442	49.624	684762.2	5499988.4	159	46	bedding	Kootenay
MV156	-114.442	49.624	684715.3	5499960.5	180	42	bedding	Cadomin
MV157	-114.442	49.623	684727.3	5499872.4				Cadomin
MV159	-114.443	49.624	684678.5	5499956.2	164	40	bedding	Blairmore
MV160	-114.444	49.625	684608.0	5500075.5				Blairmore
MV161	-114.445	49.626	684545.7	5500140.2	167	50	bedding	Blairmore
MV162	-114.445	49.626	684501.3	5500172.3				Blairmore
MV163	-114.448	49.626	684282.6	5500134.6				Blairmore
MV164	-114.448	49.626	684274.0	5500144.6				Blairmore
MV165	-114.449	49.626	684260.9	5500133.5	172	31	bedding	Blairmore
MV166	-114.435	49.626	685235.5	5500156.8	175	56	bedding	Fernie
MV167	-114.434	49.626	685310.2	5500266.0				Fernie
MV168	-114.434	49.627	685337.2	5500292.4				Tobermory
MV169	-114.434	49.627	685338.5	5500328.2				Tobermory
MV170	-114.433	49.627	685366.4	5500345.3				Etherington
MV171	-114.433	49.628	685356.2	5500437.9				Etherington
MV172	-114.433	49.629	685372.0	5500521.7				Etherington
MV173	-114.433	49.630	685397.6	5500674.4				Etherington
MV174	-114.431	49.631	685501.4	5500738.8				Tod Hunter
MV175	-114.428	49.632	685707.5	5500867.5				Etherington
MV176	-114.427	49.635	685788.5	5501269.7				Etherington
MV177	-114.427	49.636	685763.8	5501290.9				Etherington
MV178	-114.427	49.636	685760.1	5501318.5				Etherington
MV179	-114.428	49.636	685705.9	5501361.4				Etherington
MV180	-114.428	49.636	685675.4	5501367.0				Etherington

<u>Waypoint</u>	<u>Longitude</u>	<u>Latitude</u>	<u>UTM</u> <u>Easting</u>	<u>UTM</u> <u>Northing</u>	<u>Azimuth</u>	<u>Inclination</u>	<u>Type</u>	<u>Stratigraphic</u> <u>Unit</u>
MV181	-114.429	49.637	685603.9	5501407.2	183	38	bedding	Etherington
MV182	-114.406	49.664	687216.3	5504460.9	347	67	bedding	Blairmore
MV183	-114.406	49.663	687185.0	5504424.1				Blairmore
MV184	-114.408	49.663	687049.0	5504372.9				Blairmore
MV185	-114.410	49.663	686891.0	5504370.9	346	67	bedding	Fernie
MV186	-114.409	49.661	686975.7	5504213.2				Cadomin
MV187	-114.409	49.659	687001.4	5503946.6				Kootenay
MV188	-114.409	49.659	686986.1	5503918.0	154	64	bedding	Kootenay
MV189	-114.409	49.656	686971.0	5503651.0	237	35	bedding	Tod Hunter
MV190	-114.410	49.655	686960.3	5503513.5				Etherington
MV191	-114.410	49.654	686912.4	5503414.2				Carnarvon
MV192	-114.410	49.654	686952.2	5503383.5	246	35	bedding	Carnarvon
MV193	-114.412	49.655	686787.4	5503437.0				Carnarvon
MV194	-114.412	49.655	686753.9	5503537.6				Etherington
MV195	-114.414	49.656	686666.2	5503579.5	265	31	bedding	Etherington
MV196	-114.417	49.657	686430.2	5503729.7	228	10	bedding	Fernie
MV197	-114.416	49.658	686500.9	5503855.8				Fernie
MV198	-114.415	49.659	686547.8	5503927.7				Fernie
MV199	-114.414	49.659	686632.3	5503940.0				Fernie
MV200	-114.414	49.663	686642.5	5504328.9				Fernie
MV201	-114.425	49.603	686047.1	5497716.6	160	68	bedding	Wileman
MV202	-114.424	49.602	686138.8	5497557.4	167	50	bedding	Livingstone
MV203	-114.424	49.602	686156.6	5497534.6				Livingstone
MV204	-114.423	49.602	686197.6	5497516.6				Livingstone
MV205	-114.422	49.601	686236.2	5497488.3				Livingstone
MV206	-114.422	49.601	686255.5	5497466.4				Livingstone
MV207	-114.422	49.601	686292.7	5497431.1	186	65	bedding	Livingstone
MV208	-114.421	49.600	686333.2	5497396.4				Livingstone
MV209	-114.420	49.600	686387.1	5497312.8				Livingstone
MV210	-114.419	49.598	686480.9	5497118.5	158	64	bedding	Livingstone
MV211	-114.419	49.596	686521.3	5496919.6	190	61	bedding	Livingstone
MV212	-114.423	49.601	686212.0	5497502.7				Livingstone
MV213	-114.424	49.602	686161.0	5497530.8				Livingstone
MV214	-114.424	49.602	686113.3	5497602.4	168	72	bedding	Livingstone
MV215	-114.425	49.657	685822.2	5503656.8				Fernie
MV216	-114.422	49.656	686029.8	5503521.3	250	28	bedding	Tod Hunter
MV217	-114.423	49.655	686022.9	5503427.5	227	34	bedding	Etherington
MV218	-114.423	49.654	686002.1	5503397.8				Etherington
MV219	-114.424	49.653	685910.2	5503235.8				Etherington
MV220	-114.424	49.653	685948.0	5503223.4	208	50	bedding	Etherington
MV221	-114.424	49.652	685946.4	5503169.6				Etherington
MV222	-114.424	49.651	685938.3	5503060.3				Etherington
MV223	-114.424	49.650	685905.0	5502956.1	205	39	bedding	Etherington
MV225	-114.425	49.646	685857.7	5502403.3				Etherington
MV227	-114.428	49.645	685693.1	5502290.7				Tobermory

Appendix C: Bedding orientations determined by remote sensing

This appendix accompanies chapter 2 and is a complete list orientations derived from the computer program Orion, using the lineaments in the LiDAR data.

<u>UTM Easting</u>	<u>UTM Northing</u>	<u>Azimuth</u>	<u>Inclination</u>
681585	5493541	175.2	34
680833	5491886	165.5	30
681915	5490853	177.6	18
681365	5490489	172.3	34
681501	5489911	173.7	25
682670	5487137	156.2	36
682518	5486931	150.4	31
683332	5486774	139.6	41
684111	5487706	161.4	28
684397	5486734	137.8	36
684659	5486683	159.8	42
685338	5486898	158.8	47
685421	5486462	160.7	47
685893	5487492	168.6	58
684801	5488339	161.2	33
683579	5488768	165.7	51
684235	5490137	180.3	32
684505	5489340	163	35
685074	5487268	156.5	38
685604	5487472	161	39
685038	5489586	156.6	46
685142	5489094	160.9	38
686208	5490403	184.6	24
685243	5490273	170.9	41
686592	5487777	169.4	38
687347	5488106	169.1	30
687122	5489692	167.6	39
687044	5491125	168.8	34
686576	5492243	170.4	56
686446	5492614	169.5	54
686601	5491809	169.7	54
686010	5490110	172.9	39
685722	5491371	188.9	30
685214	5494176	176	45
680365	5512521	160.1	33
682917	5511972	167.3	35
686611	5512483	204.4	29

<u>UTM Easting</u>	<u>UTM Northing</u>	<u>Azimuth</u>	<u>Inclination</u>
686362	5512055	152.9	8
682985	5511040	163.2	31
684184	5509864	168.7	38
683837	5509284	346	37
680189	5510448	178.3	89
682721	5509763	160.9	33
684195	5508838	202.8	29
685123	5507665	171.9	34
685162	5506385	174.5	25
684330	5505924	171.4	23
684148	5504560	163.5	19
680777	5504929	171.1	42
680774	5507820	164.5	46
683533	5505263	174	33
686818	5506849	142.9	32
687479	5502483	348.4	58
687450	5501868	357.9	63
687084	5501368	352.2	54
682905	5513804	173.6	31
682870	5513443	162.4	37
683156	5513810	183.1	43

Appendix D: Strain analysis by Fry method

This appendix accompanies chapter 3 and is a complete list of fry plots collected from thin sections. Information included is the sample numbers, the thin section orientations and directions for orientating fry plots (N for north, S for south, E for east, and W for west). Locations shown in Fig. 3-1.

LA033A

Thin Section Orientation: 255°/90°

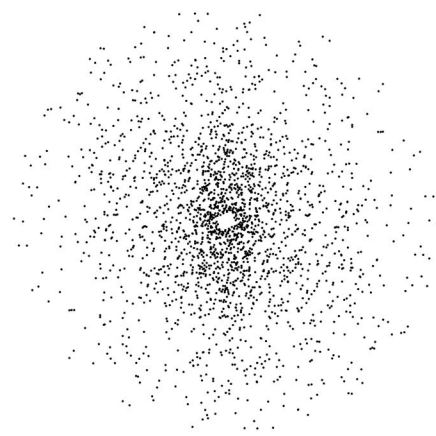
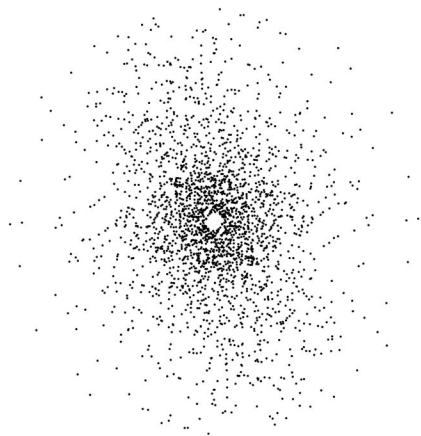
Thin Section Orientation: 190°/49°

NE

SW

S

N



Thin Section Orientation: 346°/48°

N

S



ML023A

Thin Section Orientation: 255°/90°

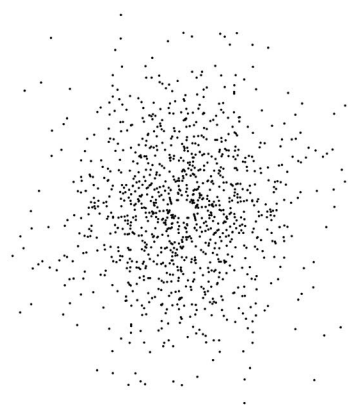
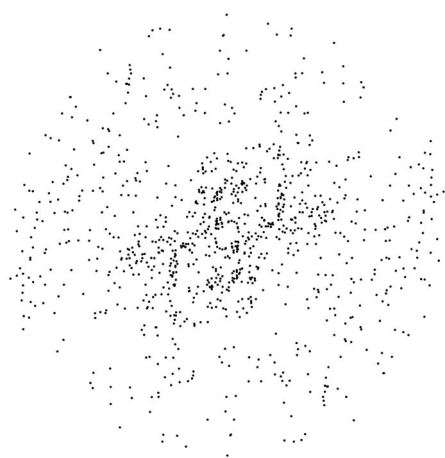
Thin Section Orientation: 202°/76°

SW

NE

S

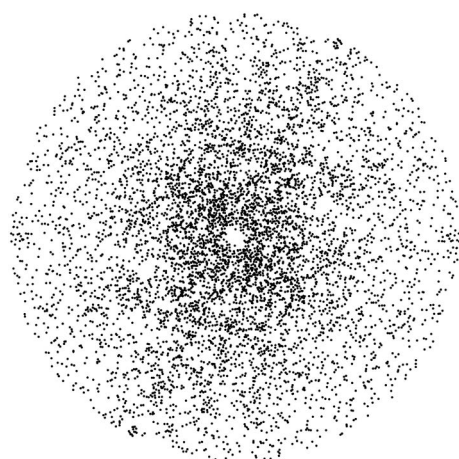
N



Thin Section Orientation: 346°/18°

N

S

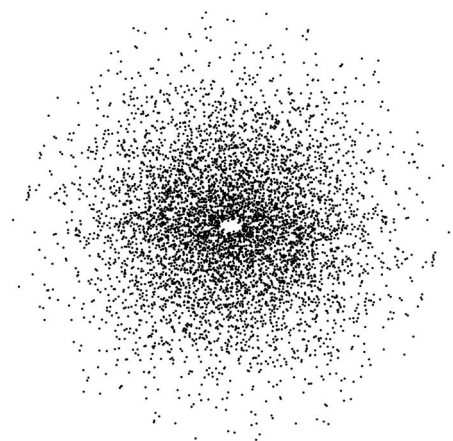


ND177A

Thin Section Orientation: $255^{\circ}/90^{\circ}$

SW

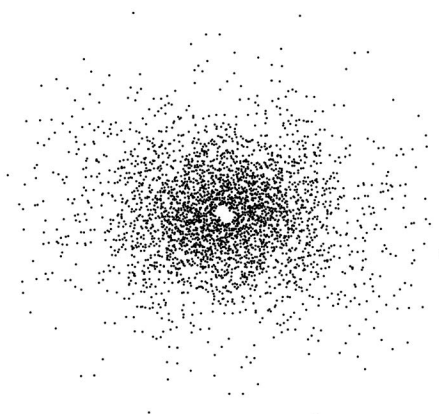
NE



Thin Section Orientation: $127^{\circ}/39^{\circ}$

NW

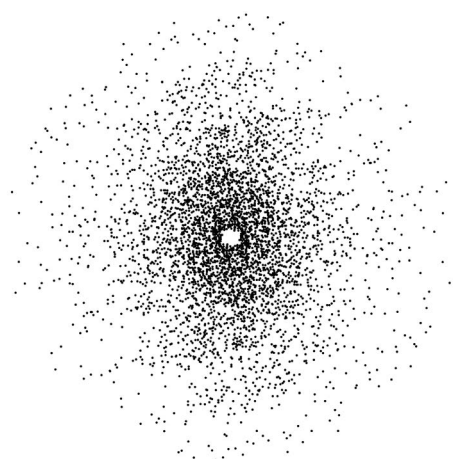
SE



Thin Section Orientation: $166^{\circ}/28^{\circ}$

S

N

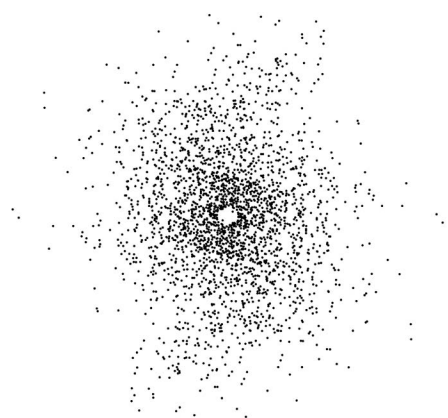


ML024A

Thin Section Orientation: $255^{\circ}/90^{\circ}$

SW

NE



Thin Section Orientation: $206^{\circ}/31^{\circ}$

NE

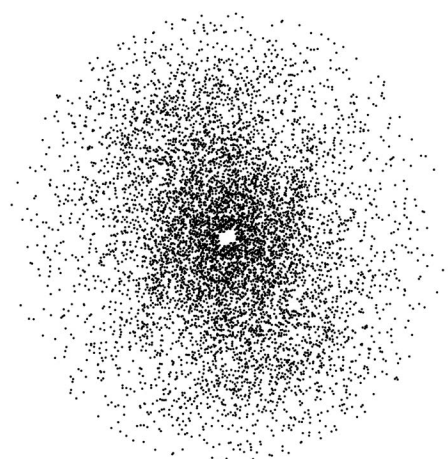
SW



Thin Section Orientation: $346^{\circ}/65^{\circ}$

S

N

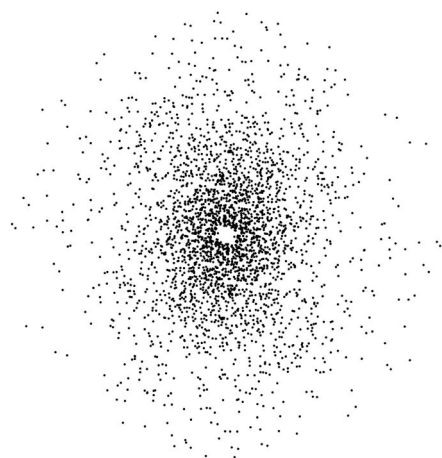


ND176A

Thin Section Orientation: 255°/90°

SW

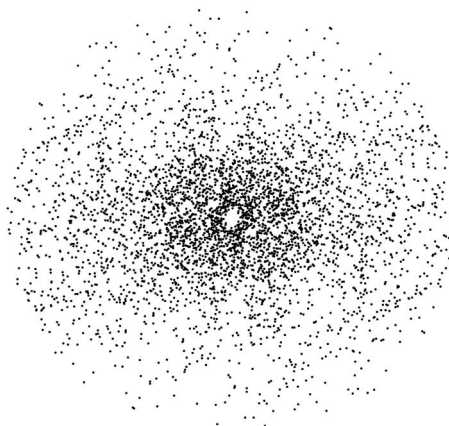
NE



Thin Section Orientation: 074°/30°

W

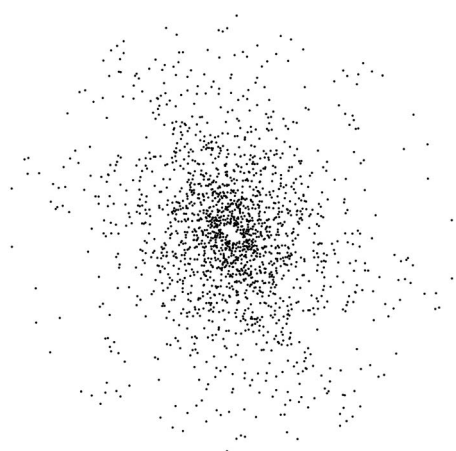
E



Thin Section Orientation: 166°/88°

N

S



LA036A

Thin Section Orientation: 255°/90°

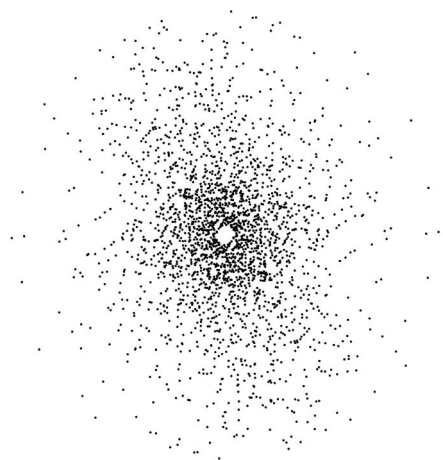
Thin Section Orientation: 148°/28°

NE

SW

NW

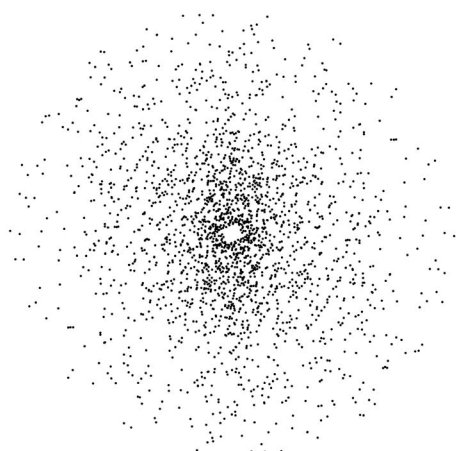
SE



Thin Section Orientation: 346°/64°

S

N

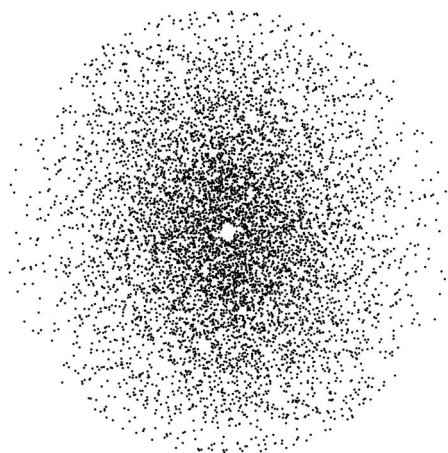


ML025A

Thin Section Orientation: $255^{\circ}/90^{\circ}$

NE

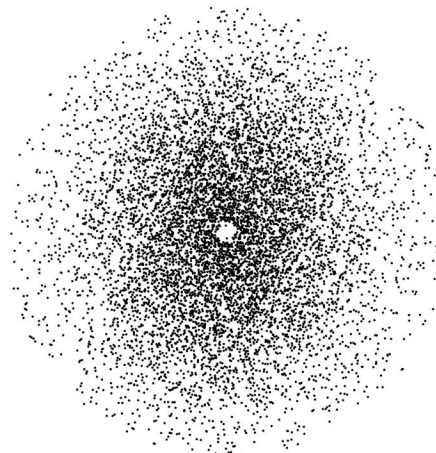
SW



Thin Section Orientation: $332^{\circ}/09^{\circ}$

NW

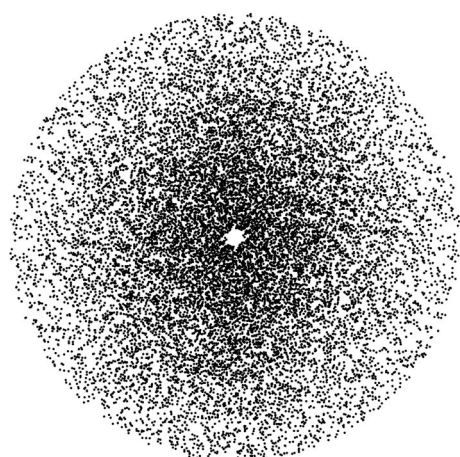
SE



Thin Section Orientation: $166^{\circ}/81^{\circ}$

S

N

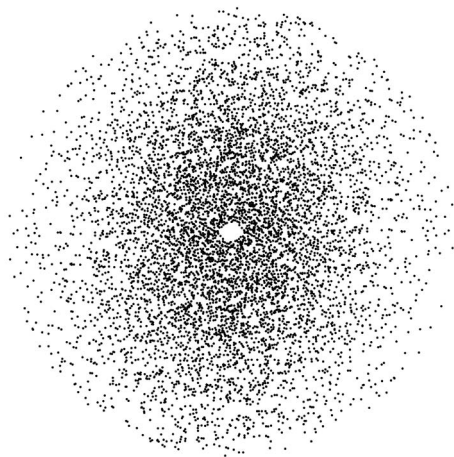


ML026A

Thin Section Orientation: $255^{\circ}/90^{\circ}$

NE

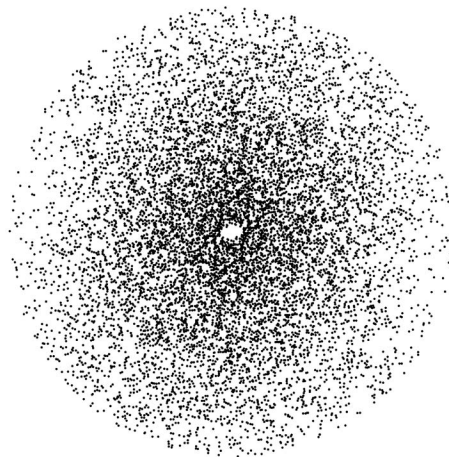
SW



Thin Section Orientation: $007^{\circ}/36^{\circ}$

S

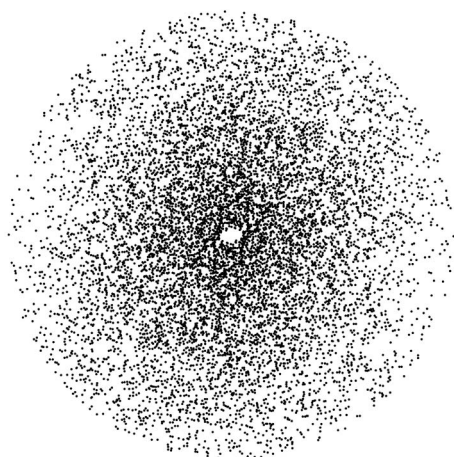
N



Thin Section Orientation: $166^{\circ}/56^{\circ}$

N

S



ND178A

Thin Section Orientation: 255°/90°

SW

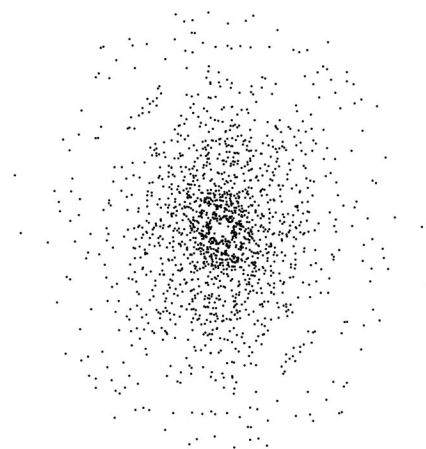
NE



Thin Section Orientation: 000°/72°

S

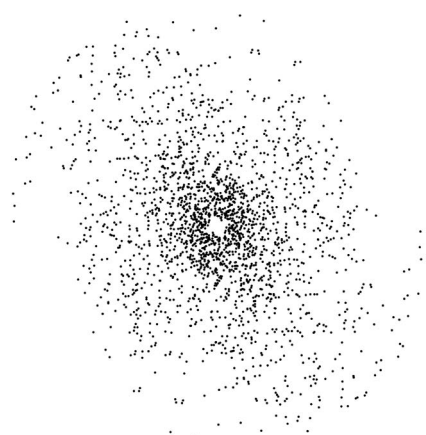
N



Thin Section Orientation: 166°/40°

N

S



NJ118A

Thin Section Orientation: 255°/90°

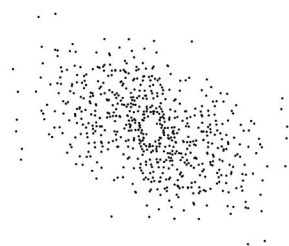
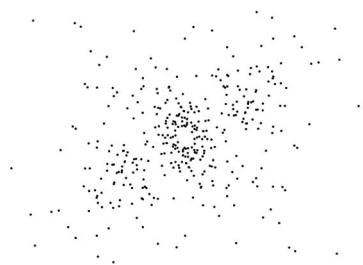
Thin Section Orientation: 163°/76°

SW

NE

N

S



Thin Section Orientation: 346°/14°

N

S

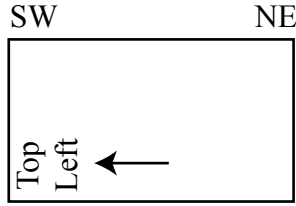


Appendix E: Calcite strain gauge data

This appendix accompanies chapter 3 and is a complete list data collected for the calcite strain gauge method. Information included is the sample numbers, the thin section orientations and directions for orientating thin section on the universal stage (N for north, S for south, E for east, and W for west). Collected data includes: grain number; bearing and plunge of c-axis in degrees; dip direction of stage for the c-axis (2 is to the east and 4 is to the west); bearing and plunge of the pole to the twin plane in degrees; dip direction of stage for the twin plane (1 to the north and 3 to the south); number of thin twins; thickness of thin twins; number of thick twins; inner thickness of thick twins; and grain width perpendicular to twins in μ .

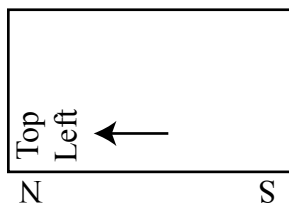
LA033A Thin Section Orientation 255°/90°

Grain Number	Bearing of C-Axis (°)	Plunge of C-Axis (°)	Dip Direction of Stage	Bearing of Twin Pole (°)	Plunge of Twin Pole (°)	Dip Direction to Stage	Number Thin Twins	Thickness Thin Twins	Number Thick Twins	Inner Thickness Thick Twins	Grain Width Perpendicular to Twins (μ)
1	103	7	4	80	6	3	70	2	0	0	800
2	274	7	2	301	1	3	21	2	0	0	680
3	356	16	4	26	20	1	31	2	0	0	440
4	338	11	2	316	1	1	11	2	0	0	690
5	338	11	2	1	10	3	18	2	0	0	560
6	203	9	4	230	6	1	39	2	0	0	1100
7	63	5	4	85	6	1	26	2	0	0	470
8	289	16	2	265	6	3	16	2	0	0	480
9	291	11	2	312	10	3	19	2	0	0	410
10	261	16	4	284	9	1	40	2	0	0	1980
11	297	14	2	321	3	3	21	2	0	0	270
12	317	5	4	295	6	3	25	2	0	0	380
13	131	15	2	113	0	1	64	2	0	0	1240
14	131	15	2	158	17	3	68	2	0	0	1580
15	127	7	4	105	12	1	82	2	0	0	1500
16	127	7	4	152	25	1	58	2	0	0	1560
17	55	2	4	82	4	1	37	2	0	0	690
18	55	2	4	36	5	3	32	2	0	0	860
19	48	6	2	69	6	1	34	2	0	0	490
20	299	3	2	327	6	3	39	2	0	0	1080
21	299	3	2	285	34	1	9	2	0	0	860
22	69	4	4	46	10	1	22	2	0	0	450
23	14	5	4	352	13	1	43	2	0	0	1200
24	14	5	4	41	16	1	60	2	0	0	1100
25	305	2	2	334	18	3	25	2	0	0	810



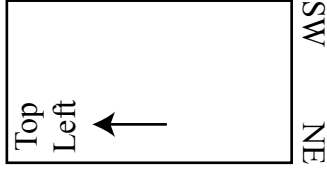
LA033A Thin Section Orientation 190°/49°

Grain Number	Bearing of C-Axis (°)	Plunge of C-Axis (°)	Dip Direction of Stage	Bearing of Twin Pole (°)	Plunge of Twin Pole (°)	Dip Direction to Stage	Number Thin Twins	Thickness Thin Twins	Number Thick Twins	Inner Thickness Thick Twins	Grain Width Perpendicular to Twins (μ)
1	211	10	4	186	28	1	45	2	0	0	1440
2	32	7	4	58	10.5	1	50	2	0	0	840
3	99	0.5	2	80	16	3	30	2	0	0	1100
4	99	0.5	2	126	13	3	8	2	0	0	1020
5	142	19	4	167	14	3	16	2	0	0	800
6	142	19	4	122.5	1	1	19	2	0	0	770
7	320	4	4	347	5.5	3	25	2	0	0	610
8	43.5	3	4	69	12.5	1	44	2	0	0	1120
9	43.5	3	4	19	12	1	45	2	0	0	1260
10	352	4	2	17	7	3	4	2	0	0	300
11	5	7	2	341	3.5	3	46	2	15	10	960
12	209	4	4	186	6	1	36	2	0	0	840
13	209	4	4	233	1	3	83	2	0	0	1040
14	333	1	2	0	5.5	3	20	2	0	0	940
15	72	1	2	97	7.5	3	18	2	0	0	750
16	328	7	4	301	14	3	58	2	13	5	1020
17	156	5	4	133	12	1	81	2	2	5	1520
18	156	5	4	179	21.5	1	52	2	0	0	1220
19	45	4	4	71	16	1	51	2	0	0	1780
20	45	4	4	21	13.5	1	7	2	0	0	1700
21	2	4	4	27.5	10	1	28	2	0	0	1020
22	274	5	2	297	13.5	3	25	2	0	0	1040
23	274	5	2	250	6	3	12	2	0	0	1020
24	274	4	4	249	9.5	1	28	2	0	0	2000
25	131	5	2	108	8	1	3	2	0	0	260



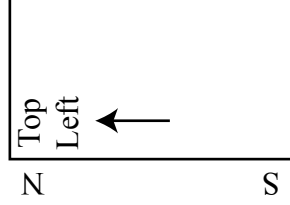
ML023A Thin Section Orientation 255°/90°

Grain Number	Bearing of C-Axis (°)	Plunge of C-Axis (°)	Dip Direction of Stage	Bearing of Twin Pole (°)	Plunge of Twin Pole (°)	Dip Direction to Stage	Number Thin Twins	Thickness Thin Twins	Number Thick Twins	Inner Thickness Thick Twins	Grain Width Perpendicular to Twins (μ)
1	264	4	4	242	9	3	20	2	0	0	830
2	81	5	4	99	26	1	13	2	0	0	720
3	248	16	4	265	2	1	115	2	0	0	920
4	66	2	2	41	12	3	14	2	0	0	1060
5	33	1	2	60	8	1	64	2	0	0	630
6	288	3	4	311	13	3	11	2	0	0	165
7	264	9	4	242	30	3	8	2	0	0	530
8	117	4	4	142	2	1	20	2	0	0	1000
9	282	4	4	309	18	3	37	2	0	0	1120
10	52	5	2	26	7	3	10	2	0	0	410
11	48	3	2	74	4	3	36	2	4	0	620
12	60	15	2	37	33	1	5	2	0	0	670
13	168	11	2	194	24	3	38	2	0	0	720
14	341	14	2	322	31	1	44	2	0	0	1760
15	198	4	2	222	1	1	57	2	0	0	510
16	61	1	2	85	4	1	11	2	0	0	500
17	64	1	2	40	2	1	10	2	0	0	210
18	55	8	4	32	6	3	4	2	0	0	180
19	155	3	2	131	2	3	31	2	0	0	160
20	224	2	2	242	12	3	77	2	0	0	690
21	332	1	2	324	26	3	33	2	0	0	830
22	231	8	2	209	24	1	36	2	0	0	1000
23	43	18	4	22	32	3	11	2	0	0	310
24	306	0	2	310	24	3	9	2	0	0	840
25	348	0	2	333	18	3	33	2	0	0	600



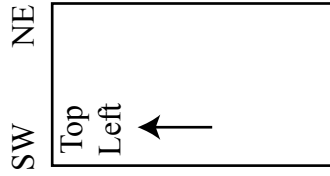
ML023A Thin Section Orientation 202°/76°

Grain Number	Bearing of C-Axis (°)	Plunge of C-Axis (°)	Dip Direction of Stage	Bearing of Twin Pole (°)	Plunge of Twin Pole (°)	Dip Direction to Stage	Number Thin Twins	Thickness Thin Twins	Number Thick Twins	Inner Thickness Thick Twins	Grain Width Perpendicular to Twins (μ)
1	115	25	4	95	8.5	3	38	2	0	0	880
2	272	8	2	295	5	1	13	2	0	0	480
3	272	8	2	250	1	3	29	2	0	0	550
4	12	6	4	347	12	1	42	2	0	0	540
5	125.5	7	4	154.5	0.5	3	33	2	0	0	660
6	42	4	4	66	9	1	57	2	0	0	600
7	42	4	4	20	9	1	18	2	0	0	710
8	46	8	4	70.5	16	3	51	2	0	0	670
9	228	4	4	255	12	3	38	2	0	0	540
10	130	9	4	106	18.5	1	50	2	0	0	900
11	162	15	4	150	35	3	17	2	0	0	970
12	196	6	4	175	19	3	34	2	0	0	740
13	340	3	2	318	13	3	39	2	0	0	660
14	340	3	2	4	21	3	24	2	0	0	740
15	218	3	2	244	2	3	92	2	0	0	1120
16	10	6	4	37.5	1	3	26	2	0	0	340
17	255	5	2	283	3.5	1	21	2	0	0	540
18	8	14	4	30	5	1	32	2	0	0	240
19	131	13	4	106	5	3	21	2	0	0	770
20	1	3	2	27	17	3	11	2	0	0	265
21	39	12	2	14	5	3	22	2	0	0	1700
22	350	9	4	325	4	3	58	2	0	0	940
23	292	10	2	270	3	3	35	2	0	0	700
24	292	10	2	314.5	6	3	18	2	0	0	670
25	309	4	4	333	5	3	22	2	0	0	580



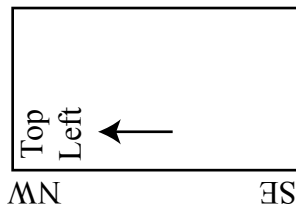
ND177A Thin Section Orientation 255°/90°

Grain Number	Bearing of C-Axis (°)	Plunge of C-Axis (°)	Dip Direction of Stage	Bearing of Twin Pole (°)	Plunge of Twin Pole (°)	Dip Direction to Stage	Number Thin Twins	Thickness Thin Twins	Number Thick Twins	Inner Thickness Thick Twins	Grain Width Perpendicular to Twins (μ)
1	105	4	2	88	28	3	9	2	0	0	650
2	30	10	4	3	10	1	10	2	0	0	530
3	73	6	2	101	15	1	45	2	0	0	940
4	355	6	2	330	4	1	17	2	0	0	500
5	355	6	2	19.5	3	3	38	2	0	0	470
6	279	5	2	301.5	12	3	12	2	0	0	520
7	279	5	2	256	5.5	3	50	2	0	0	520
8	264	10	4	290	7	1	20	2	0	0	1200
9	170	7	4	143	0.5	3	27	2	0	0	650
10	170	7	4	195	2	1	111	2	0	0	790
11	86.5	6	4	114	9	1	14	2	0	0	520
12	37	6	4	62	7	3	29	2	0	0	500
13	250	8	4	279	8	3	14	2	0	0	700
14	298	9	2	321	5	1	19	2	0	0	590
15	298	9	2	274	9	1	38	2	0	0	730
16	291	4	4	319	10.5	1	8	2	0	0	250
17	34	9	4	9	12	3	4	2	0	0	340
18	34	9	4	54	21.5	3	12	2	0	0	260
19	292	9	2	267.5	9	3	71	2	0	0	880
20	292	9	2	314.5	19	3	16	2	0	0	850
21	99	3	4	126	17	1	26	2	0	0	950
22	76	2	4	50	1	1	40	2	0	0	1540
23	76	2	4	90	20	3	39	2	0	0	1240
24	111	8	4	137	14	1	20	2	0	0	1300
25	9	8	4	342	14.5	1	12	2	0	0	300



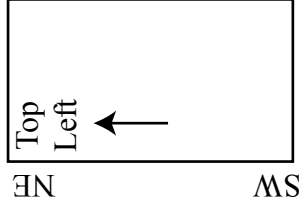
ND177A Thin Section Orientation 127°/39°

Grain Number	Bearing of C-Axis (°)	Plunge of C-Axis (°)	Dip Direction of Stage	Bearing of Twin Pole (°)	Plunge of Twin Pole (°)	Dip Direction to Stage	Number Thin Twins	Thickness Thin Twins	Number Thick Twins	Inner Thickness Thick Twins	Grain Width Perpendicular to Twins (μ)
1	104	3	4	83	14	3	22	2	0	0	1120
2	104	3	4	128	5.5	3	68	2	0	0	840
3	48	2	4	75	2	1	90	2	0	0	1180
4	48	2	4	25	3	3	49	2	0	0	1260
5	109	10	2	83.5	0.5	3	33	2	0	0	1100
6	34	5	2	56	12	3	23	2	0	0	1100
7	34	5	2	11	1	1	139	2	0	0	960
8	234	5	2	260	7	3	26	2	0	0	490
9	312	3	4	339	10	1	19	2	0	0	530
10	242	10	2	219	5	3	16	2	0	0	240
11	242	10	2	263.5	4	3	8	2	0	0	300
12	273	7	4	298	20	3	58	2	0	0	1240
13	273	7	4	251	20	3	8	2	0	0	1260
14	316	7	2	340.5	8	1	11	2	0	0	170
15	316	7	2	289	18	1	5	2	0	0	170
16	320	15	2	346	14	3	20	2	0	0	610
17	320	15	2	301.5	32.5	3	58	2	0	0	900
18	334	5	4	308	8	1	18	2	0	0	270
19	102	10	4	79	3	1	6	2	0	0	780
20	49	7	2	23	7	3	27	2	0	0	340
21	49	7	2	70	24	3	9	2	0	0	500
22	89.5	4	2	113	0.5	1	72	2	0	0	750
23	89.5	4	2	66.5	11	3	6	2	0	0	920
24	15	2	4	352	19	1	33	2	0	0	470
25	17	1	2	352	15	1	83	2	0	0	1080



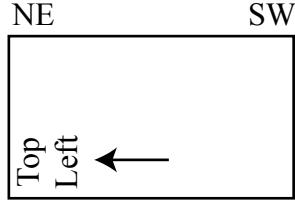
ML024A Thin Section Orientation 255°/90°

Grain Number	Bearing of C-Axis (°)	Plunge of C-Axis (°)	Dip Direction of Stage	Bearing of Twin Pole (°)	Plunge of Twin Pole (°)	Dip Direction to Stage	Number Thin Twins	Thickness Thin Twins	Number Thick Twins	Inner Thickness Thick Twins	Grain Width Perpendicular to Twins (μ)
1	281	22	2	293	3	1	26	2	0	0	380
2	306	28	4	321	6	1	31	2	0	0	430
3	259	29	2	243	9	3	67	2	0	0	740
4	255	41	2	282	22	3	44	2	0	0	630
5	324	46	4	306	28	3	49	2	0	0	1020
6	284	5	4	312	1	1	65	2	0	0	1580
7	321	14	4	344	1	3	10	2	0	0	1020
8	83	15	2	111	1	1	8	2	0	0	290
9	172	11	2	155	37	1	39	2	0	0	540
10	302	6	2	331	4	3	78	2	0	0	580
11	256	10	4	284	18	1	37	2	0	0	450
12	165	5	2	143	11	3	21	2	0	0	375
13	179	1	2	154	1	1	92	2	0	0	530
14	264	7	2	288	9	1	28	2	0	0	650
15	2	17	2	29	14	1	50	2	0	0	630
16	42	8	2	17	19	3	65	2	0	0	800
17	311	15	4	332	4	3	51	2	0	0	1720
18	331	12	2	354	9	1	82	2	0	0	760
19	287	11	2	309	14	3	55	2	5	10	460
20	106	5	2	132	3	3	81	2	0	0	600
21	156	5	2	133	8	3	71	2	1	10	690
22	80	4	4	103	8	1	57	2	0	0	690
23	177	7	2	151	1	1	87	2	0	0	530
24	23	14	2	356	11	1	21	2	0	0	240
25	125	4	2	154	18	3	25	2	0	0	610



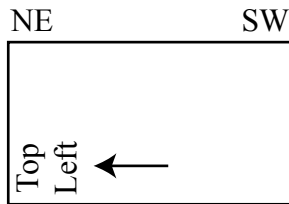
ML024A Thin Section Orientation 206°/31°

Grain Number	Bearing of C-Axis (°)	Plunge of C-Axis (°)	Dip Direction of Stage	Bearing of Twin Pole (°)	Plunge of Twin Pole (°)	Dip Direction to Stage	Number Thin Twins	Thickness Thin Twins	Number Thick Twins	Inner Thickness Thick Twins	Grain Width Perpendicular to Twins (μ)
1	15	18	2	40	24	1	109	2	0	0	1240
2	15	18	2	349	23	1	21	2	0	0	1340
3	4	10	2	336	3	1	63	2	0	0	830
4	58	2	2	40	26	1	35	2	0	0	1020
5	69	10	2	43	15.5	3	13	2	0	0	1380
6	69	10	2	90	27	3	43	2	0	0	1220
7	216	3	2	240	16	3	37	2	0	0	830
8	216	3	2	193	16	3	53	2	0	0	880
9	213	7	2	239	12	3	72	2	0	0	1160
10	35.5	11	4	8	11	3	27	2	5	10	550
11	45	2	4	18	8	3	39	2	0	0	610
12	224	5	4	246	10	1	10	2	0	0	180
13	224	5	4	201	0.5	1	22	2	0	0	380
14	85.5	12	2	62.5	7.5	1	12	2	0	0	410
15	85.5	12	2	109	14	1	48	2	0	0	460
16	26	11	4	2	23	3	26	2	0	0	210
17	227	4	2	251	19	3	18	2	0	0	430
18	227	4	2	204	15	3	28	2	0	0	590
19	35	3	4	9	13	3	43	2	0	0	860
20	35	3	4	60	3	3	65	2	0	0	640
21	310	7	2	331	27	3	15	2	0	0	430
22	310	7	2	283	11	3	10	2	0	0	490
23	325	8	2	352	22	1	28	2	0	0	730
24	27	2	4	53	13	1	13	2	0	0	430
25	27	2	4	4	12	1	34	2	0	0	650



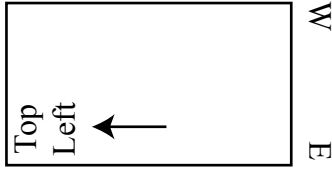
ND176A Thin Section Orientation 255°/90°

Grain Number	Bearing of C-Axis (°)	Plunge of C-Axis (°)	Dip Direction of Stage	Bearing of Twin Pole (°)	Plunge of Twin Pole (°)	Dip Direction to Stage	Number Thin Twins	Thickness Thin Twins	Number Thick Twins	Inner Thickness Thick Twins	Grain Width Perpendicular to Twins (μ)
1	242	5	4	270	5	1	139	2	0	0	1630
2	230	3	2	205	19	1	45	2	0	0	750
3	356	6	4	333	14.5	3	44	2	0	0	400
4	356	6	4	19.5	25	3	26	2	0	0	470
5	172	7	2	195	18	3	8	2	0	0	480
6	112	5	2	88	3	3	25	2	0	0	460
7	214	2	4	238	6	1	41	2	0	0	820
8	214	2	4	191	6	1	45	2	0	0	680
9	53.5	9	4	79.5	2	1	85	2	0	0	800
10	69	1	4	47	8	1	27	2	0	0	660
11	69	1	4	93	10	1	112	2	0	0	780
12	4	4	4	337	2	3	47	2	0	0	490
13	4	4	4	30	10	1	63	2	0	0	570
14	83	2	4	60.5	6	1	53	2	0	0	890
15	83	2	4	110	13	1	91	2	0	0	940
16	95	4	4	70	3	3	49	2	0	0	560
17	95	4	4	109	27	1	31	2	0	0	550
18	321	10	4	297	10	1	97	2	0	0	680
19	321	10	4	344.5	13.5	1	23	2	0	0	810
20	264	10	4	239	1	3	49	2	0	0	650
21	264	10	4	287	22	1	24	2	0	0	630
22	351	2	2	327	12	3	21	2	0	0	1300
23	351	2	2	18	16	3	36	2	0	0	1160
24	80	7	4	104	5.5	3	54	2	0	0	750
25	80	7	4	57	12	3	22	2	0	0	750



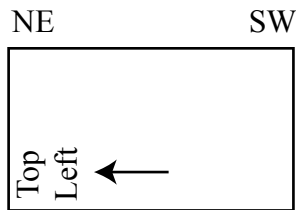
ND176A Thin Section Orientation 074°/30°

Grain Number	Bearing of C-Axis (°)	Plunge of C-Axis (°)	Dip Direction of Stage	Bearing of Twin Pole (°)	Plunge of Twin Pole (°)	Dip Direction to Stage	Number Thin Twins	Thickness Thin Twins	Number Thick Twins	Inner Thickness Thick Twins	Grain Width Perpendicular to Twins (μ)
1	71	5	4	43	15	1	15	2	0	0	720
2	27	10	2	1	10	1	6	2	0	0	490
3	27	10	2	40	38	1	12	2	0	0	410
4	184	12	2	209	7	3	44	2	0	0	500
5	60	10	4	41	30	3	80	2	5	5	1220
6	9	5	2	33.5	14	3	29	2	0	0	420
7	9	5	2	345	18	3	15	2	0	0	750
8	210	10	2	233	3	3	5	2	0	0	110
9	354	2	4	17	22	1	14	2	0	0	550
10	258	8	2	282	7	1	38	2	0	0	580
11	258	8	2	236	25	1	28	2	0	0	610
12	321	3	2	298	10	3	20	2	0	0	540
13	134.5	3	2	110	15	3	27	2	0	0	550
14	134.5	3	2	158	13	3	14	2	0	0	450
15	127	4	4	103	13	3	51	2	0	0	480
16	127	4	4	151	0.5	3	38	2	0	0	680
17	68	3	2	91	7	1	7	2	0	0	170
18	68	3	2	45	13	1	12	2	0	0	340
19	280	2	4	303.5	2.5	1	9	2	0	0	330
20	280	2	4	256	4	3	15	2	0	0	380
21	312	7	4	336	2	3	8	2	0	0	250
22	312	7	4	289	9	3	11	2	0	0	190
23	238	11	2	213	6	3	19	2	0	0	720
24	286	7	4	262.5	1	3	18	2	5	10	530
25	286	7	4	308	15	1	24	2	0	0	700



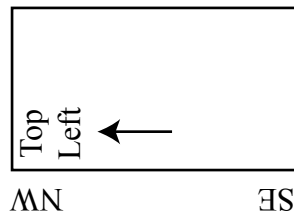
LA036A Thin Section Orientation 255°/90°

Grain Number	Bearing of C-Axis (°)	Plunge of C-Axis (°)	Dip Direction of Stage	Bearing of Twin Pole (°)	Plunge of Twin Pole (°)	Dip Direction to Stage	Number Thin Twins	Thickness Thin Twins	Number Thick Twins	Inner Thickness Thick Twins	Grain Width Perpendicular to Twins (μ)
1	304	9	4	328	14	1	43	2	0	0	260
2	21	21	4	358	5	3	38	2	0	0	620
3	353	11	4	329.5	4	3	19	2	0	0	335
4	32	4	2	6	17.5	1	36	2	0	0	610
5	4	4	4	340	7	3	119	2	0	0	920
6	191	7	4	165	19	1	10	2	0	0	325
7	194	11	4	175.5	26	3	36	2	0	0	670
8	194	11	4	222	10	3	45	2	0	0	630
9	167	6	2	190	8.5	1	63	2	0	0	280
10	28.5	9	2	4	24	1	9	2	0	0	345
11	337	9	4	3	9	1	90	2	0	0	460
12	14.5	4	4	37	10	1	27	2	0	0	920
13	14.5	4	4	350	10	1	54	2	0	0	1100
14	9	7	4	346	11	1	26	2	0	0	540
15	180	9	4	156.5	13	3	28	2	0	0	350
16	63	1	2	45	15	3	78	2	0	0	420
17	47	17	4	75	15	3	16	2	0	0	450
18	1	8	4	23	27	1	43	2	0	0	630
19	1	8	4	338	20	1	14	2	0	0	510
20	189	15	4	218	25	1	66	2	0	0	1040
21	38	5	2	11	15.5	3	25	2	3	10	700
22	38	5	2	58.5	23	3	51	2	3	5	470
23	169	8	4	145	22	1	9	2	0	0	500
24	49	13	2	73.5	21	3	40	2	0	0	630
25	49	13	2	28	34	3	51	2	0	0	550



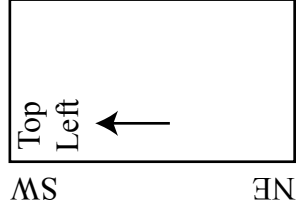
LA036A Thin Section Orientation 148°/28°

Grain Number	Bearing of C-Axis (°)	Plunge of C-Axis (°)	Dip Direction of Stage	Bearing of Twin Pole (°)	Plunge of Twin Pole (°)	Dip Direction to Stage	Number Thin Twins	Thickness Thin Twins	Number Thick Twins	Inner Thickness Thick Twins	Grain Width Perpendicular to Twins (μ)
1	108	13	4	84	1.5	3	33	2	0	0	450
2	216	9	4	240	8	1	37	2	0	0	400
3	316	5	4	343.5	3	1	59	2	0	0	860
4	316	5	4	303	36	1	36	2	0	0	800
5	271	5	2	296	10	3	25	2	0	0	890
6	271	5	2	246	12	3	19	2	0	0	590
7	50	8	4	24	0.5	1	26	2	0	0	240
8	338	6	4	315	1	3	37	2	4	5	430
9	338	6	4	0	1	1	9	2	0	0	460
10	103	7	2	73.5	10	1	47	2	0	0	830
11	74	3	4	50	7	1	7	2	0	0	190
12	179	4	4	203	0.5	1	55	2	0	0	690
13	54	6	4	29	16	1	11	2	0	0	500
14	353	8	4	17	2	1	7	2	0	0	510
15	349	6	4	321	14	1	56	2	0	0	710
16	86	15	2	61	3	3	11	2	0	0	360
17	339	5	2	313	5	3	33	2	0	0	570
18	339	5	2	3.5	18	3	46	2	0	0	510
19	262	2	4	284	14	3	12	2	0	0	270
20	69	4	2	45	5.5	3	9	2	0	0	250
21	69	4	2	90	20.5	3	13	2	0	0	300
22	324	8	2	353	10	3	20	2	0	0	270
23	274	3	2	296	9.5	1	3	2	0	0	320
24	274	3	2	251	15	1	30	2	0	0	220
25	101	8	4	123.5	3	1	17	2	0	0	500



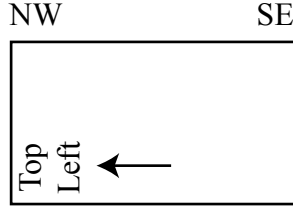
ML025A Thin Section Orientation 255°/90°

Grain Number	Bearing of C-Axis (°)	Plunge of C-Axis (°)	Dip Direction of Stage	Bearing of Twin Pole (°)	Plunge of Twin Pole (°)	Dip Direction to Stage	Number Thin Twins	Thickness Thin Twins	Number Thick Twins	Inner Thickness Thick Twins	Grain Width Perpendicular to Twins (μ)
1	283	4	4	311	6	1	28	2	0	0	540
2	330	4	4	307	5	1	29	2	0	0	370
3	109	1	2	129	14	3	29	2	2	5	450
4	358	6	2	335	4	3	27	2	0	0	335
5	114	5	2	142	7	1	32	2	0	0	380
6	53	12	2	25	26	3	22	2	0	0	640
7	265	10	2	294	6	3	20	2	0	0	255
8	60	2	2	77	17	1	20	2	0	0	255
9	60	2	2	34	3	3	31	2	0	0	400
10	249	14	2	278	14	3	29	2	0	0	480
11	249	14	2	229	27	3	35	2	0	0	490
12	62	9	4	86.5	7	3	11	2	0	0	240
13	62	9	4	39	4	3	22	2	0	0	225
14	303	13	2	330.5	14	3	26	2	0	0	960
15	200.5	12	2	174	11	1	43	2	8	4	800
16	75	8	4	54	23	3	4	2	0	0	300
17	306	13	4	327.5	5	3	18	2	0	0	660
18	306	13	4	283	13	1	22	2	0	0	1020
19	82	8	4	109	7	3	42	2	0	0	430
20	152	26	2	131	7	1	87	2	0	0	285
21	100	7	4	126.5	9	1	44	2	0	0	530
22	100	13	2	129	7	3	23	2	0	0	490
23	194	24	2	173	5.5	1	73	2	0	0	890
24	194	24	2	217	12.5	3	58	2	0	0	860
25	278	12	2	304.5	4	3	69	2	0	0	760



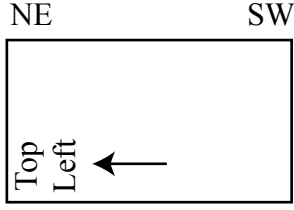
ML025A Thin Section Orientation 332°/09°

Grain Number	Bearing of C-Axis (°)	Plunge of C-Axis (°)	Dip Direction of Stage	Bearing of Twin Pole (°)	Plunge of Twin Pole (°)	Dip Direction to Stage	Number Thin Twins	Thickness Thin Twins	Number Thick Twins	Inner Thickness Thick Twins	Grain Width Perpendicular to Twins (μ)
1	124	4	2	101.5	11.5	1	16	2	0	0	315
2	124	4	2	149	11	1	9	2	0	0	300
3	163.5	6	4	141	17	1	24	2	0	0	760
4	163.5	6	4	189	17	1	30	2	0	0	720
5	247	6	2	270	16.5	1	10	2	0	0	670
6	247	6	2	222	17	1	13	2	0	0	550
7	60	4	4	44	26	1	20	2	0	0	590
8	60	4	4	87	7	1	12	2	0	0	620
9	304	7	2	329	22	1	33	2	0	0	820
10	278	8	4	303	15	1	10	2	0	0	620
11	118	6	2	97	19	1	21	2	0	0	390
12	118	6	2	143	11	1	9	2	0	0	470
13	314	2	2	290	10.5	1	42	2	0	0	760
14	314	2	2	338	9	1	13	2	0	0	630
15	46	6	2	20	14	3	15	2	0	0	440
16	273	6	4	250	3	3	15	2	0	0	245
17	198	7	4	175	2.5	3	10	2	0	0	450
18	198	7	4	220	5	3	14	2	0	0	380
19	89	3	2	67.5	12	1	42	2	0	0	680
20	89	3	2	113	6	1	7	2	0	0	390
21	298	13	2	274	4	3	44	2	0	0	570
22	298	13	2	324	4	3	25	2	0	0	780
23	355	13	2	21	6	3	39	2	0	0	580
24	98	2	2	73	10	1	50	2	0	0	760
25	98	2	2	106	32	3	20	2	0	0	790



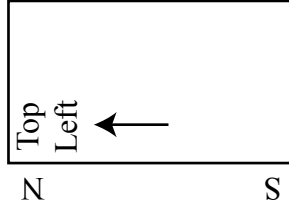
ML026A Thin Section Orientation 255°/90°

Grain Number	Bearing of C-Axis (°)	Plunge of C-Axis (°)	Dip Direction of Stage	Bearing of Twin Pole (°)	Plunge of Twin Pole (°)	Dip Direction to Stage	Number Thin Twins	Thickness Thin Twins	Number Thick Twins	Inner Thickness Thick Twins	Grain Width Perpendicular to Twins (μ)
1	289	11	2	259	13	3	15	2	0	0	625
2	321	9	4	297	12	1	25	2	0	0	1260
3	262	1	2	289	19	1	33	2	10	20	1140
4	76	14	2	45	15	3	0	0	20	10	800
5	270	1	4	250	22	3	7	2	0	0	520
6	304	10	4	329	25	3	40	2	0	0	420
7	343	2	4	324	11	1	57	2	0	0	440
8	236	4	4	269	7	3	23	2	0	0	240
9	236	4	4	223	11	1	35	2	0	0	340
10	295	31	4	311	8	3	80	2	0	0	480
11	51	5	2	23	20	3	26	2	0	0	475
12	337	11	4	5	21	3	9	2	0	0	500
13	337	11	4	311	26	3	32	2	0	0	480
14	297	2	4	318	19	3	10	2	0	0	1000
15	306	2	4	325	21	3	11	2	0	0	840
16	48	10	2	80	35	1	26	2	0	0	360
17	306	2	4	281	21.5	1	8	2	0	0	360
18	283	15	4	310	13	1	11	2	0	0	480
19	27	6	4	2	5	3	59	2	0	0	475
20	358	23	2	346	6	3	71	2	0	0	380
21	311	11	2	333	27	3	21	2	0	0	320
22	272	5	2	300	5	1	88	2	0	0	780
23	55	18	4	34	4	1	49	2	0	0	560
24	55	18	4	76	20	1	23	2	0	0	500
25	302	3	2	277	12	3	27	2	0	0	520



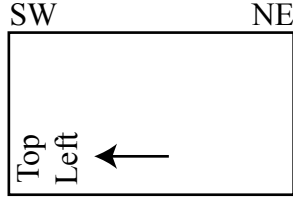
ML026A Thin Section Orientation 166°/56°

Grain Number	Bearing of C-Axis (°)	Plunge of C-Axis (°)	Dip Direction of Stage	Bearing of Twin Pole (°)	Plunge of Twin Pole (°)	Dip Direction to Stage	Number Thin Twins	Thickness Thin Twins	Number Thick Twins	Inner Thickness Thick Twins	Grain Width Perpendicular to Twins (μ)
1	295	1	2	277	17	1	18	2	0	0	480
2	293.5	7	4	315.5	1	3	46	2	0	0	390
3	120.5	1	2	146	12	3	14	2	0	0	330
4	120.5	1	2	99	13	3	18	2	0	0	300
5	131	8	4	105	5.5	3	22	2	0	0	690
6	255	7	4	279	9	3	29	2	0	0	360
7	46	11	4	20	7	1	47	2	0	0	810
8	46	11	4	66.5	23	1	11	2	0	0	800
9	279	3	2	305.5	7.5	3	23	2	0	0	340
10	194	1	2	171	5	1	19	2	0	0	390
11	194	1	2	221	12	1	9	2	0	0	550
12	99	6	2	125	8.5	3	28	2	0	0	470
13	357	8	4	24	13	3	28	2	0	0	610
14	320	1	2	297	12	3	22	2	0	0	660
15	320	1	2	341	11	1	21	2	0	0	520
16	353	6	2	329	7	3	24	2	0	0	390
17	69	10	4	97	13	1	24	2	0	0	590
18	132	4	2	111	27.5	1	10	2	0	0	600
19	259	6	2	284	6	1	131	2	0	0	2050
20	259	6	2	240	20	1	20	2	0	0	2300
21	92	4	4	70.5	2	3	25	2	0	0	980
22	35	3	2	61	7	3	11	2	0	0	450
23	266	8	4	289	15	3	44	2	0	0	600
24	13	1	4	349	5	3	20	2	0	0	370
25	13	1	4	40	1	1	12	2	0	0	350



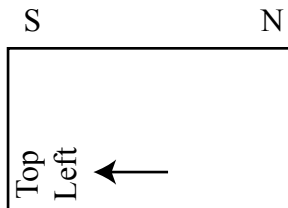
ND178A Thin Section Orientation 255°/90°

Grain Number	Bearing of C-Axis (°)	Plunge of C-Axis (°)	Dip Direction of Stage	Bearing of Twin Pole (°)	Plunge of Twin Pole (°)	Dip Direction to Stage	Number Thin Twins	Thickness Thin Twins	Number Thick Twins	Inner Thickness Thick Twins	Grain Width Perpendicular to Twins (μ)
1	84	4	4	112	4	3	26	2	0	0	790
2	21	4	4	357	9.5	1	7	2	0	0	570
3	69	4	2	45	16	3	21	2	0	0	470
4	69	4	2	94.5	17	3	70	2	0	0	1160
5	128	3	4	101.5	13	3	112	2	0	0	820
6	55	15	2	30	16	3	54	2	0	0	1500
7	85	5	4	61	5.5	3	18	2	0	0	310
8	351	12	2	325	4.5	3	71	2	0	0	920
9	106	13	4	133.5	0.5	3	4	2	0	0	600
10	232	8	2	254	0.5	1	36	2	0	0	220
11	349	2	4	326	12	3	39	2	0	0	920
12	349	2	4	15	7	1	51	2	0	0	720
13	289	8	4	314	23	3	30	2	0	0	790
14	65	6	4	41	20	3	30	2	0	0	780
15	276	8	2	298	22	1	19	2	0	0	760
16	276	8	2	255	0.5	3	52	2	0	0	850
17	23	8	2	359.5	5	3	16	2	0	0	1240
18	293	4	4	322	1	3	4	2	0	0	460
19	45	7	4	18	9.5	1	32	2	0	0	1140
20	45	7	4	67	3.5	1	72	2	0	0	1500
21	145	1	2	169.5	5	3	37	2	0	0	790
22	145	1	2	119	4	1	83	2	0	0	710
23	8.5	2	4	32	0.5	3	24	2	0	0	440
24	43	4	4	72.5	2	3	19	2	0	0	280
25	77	3	4	50	9.5	3	59	2	0	0	920



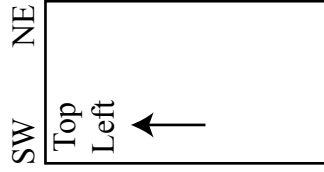
ND178A Thin Section Orientation 000°/72°

Grain Number	Bearing of C-Axis (°)	Plunge of C-Axis (°)	Dip Direction of Stage	Bearing of Twin Pole (°)	Plunge of Twin Pole (°)	Dip Direction to Stage	Number Thin Twins	Thickness Thin Twins	Number Thick Twins	Inner Thickness Thick Twins	Grain Width Perpendicular to Twins (μ)
1	357	8	4	332	7	1	7	2	0	0	310
2	357	8	4	23	13.5	1	39	2	0	0	310
3	169	9	2	195	12	1	11	2	0	0	430
4	340	4	2	6.5	18	3	57	2	0	0	790
5	326	9	4	349	23	1	12	2	0	0	820
6	326	9	4	300	10	1	107	2	0	0	860
7	332	4	4	353	17	3	4	2	0	0	330
8	192	8	2	169	16	1	68	2	0	0	760
9	192	8	2	220	6	1	33	2	0	0	570
10	238	8	4	265	6	3	79	2	0	0	1640
11	356	5	4	24	10	3	63	2	0	0	700
12	84	11	2	64	30.5	1	12	2	0	0	310
13	316	9	2	343.5	13	3	62	2	0	0	720
14	316	9	2	293	7	3	40	2	0	0	740
15	50	4	2	72.5	1	3	73	2	0	0	1400
16	5	2	2	342	5	1	7	2	0	0	300
17	5	2	2	29	5	1	21	2	0	0	310
18	304	3	2	332	12	3	23	2	0	0	840
19	355	2	4	19.5	3	3	139	2	0	0	1120
20	355	2	4	329	4	3	26	2	0	0	900
21	346.5	1	4	14.5	7.5	3	28	2	0	0	320
22	71	4	4	84	32	3	17	2	0	0	1120
23	241	11	4	250	39	1	31	2	0	0	1240
24	7	4	4	344	9	3	44	2	0	0	1220
25	7	4	4	34.5	2	3	146	2	0	0	1080



NJ118A Thin Section Orientation 255°/90°

Grain Number	Bearing of C-Axis (°)	Plunge of C-Axis (°)	Dip Direction of Stage	Bearing of Twin Pole (°)	Plunge of Twin Pole (°)	Dip Direction to Stage	Number Thin Twins	Thickness Thin Twins	Number Thick Twins	Inner Thickness Thick Twins	Grain Width Perpendicular to Twins (μ)
1	90	3	4	108	26	3	14	2	0	0	200
2	29	13	2	2	6	3	14	2	0	0	230
3	45	10	2	21	26	3	11	2	0	0	180
4	25	10	4	50.5	22	1	13	2	0	0	190
5	91	3	4	114	10	3	15	2	0	0	120
6	8	5	2	345	2	3	9	2	0	0	140
7	15	4	4	351	10	3	4	2	0	0	230
8	321	3	2	297	2	1	6	2	0	0	120
9	346	8	4	320.5	3	3	10	2	0	0	120
10	44	7	2	16.5	18	3	6	2	0	0	1460
11	74	2	2	55	21.5	3	12	2	0	0	360
12	168	10	2	140	8	1	12	2	0	0	160
13	99	12	2	77	5	1	12	2	0	0	600
14	99	12	2	122	1	3	15	2	0	0	540
15	1	6	4	338	14	1	36	2	0	0	420
16	24	3	4	51	8	1	26	2	0	0	480
17	9	15	4	34.5	23	1	51	2	0	0	720
18	30	3	4	56.5	11.5	1	13	2	0	0	210
19	331	5	2	305	5	3	21	2	0	0	540
20	270	3	4	293	9	1	21	2	0	0	390
21	270	3	4	248	14.5	1	18	2	0	0	330
22	22	5	4	48	4	1	6	2	0	0	130
23	44	11	2	66	1	3	21	2	0	0	560
24	100	5	2	121	1	3	8	2	0	0	1880
25	100	5	2	80	7	1	3	2	0	0	1820



NJ118A Thin Section Orientation 163°/76°

Grain Number	Bearing of C-Axis (°)	Plunge of C-Axis (°)	Dip Direction of Stage	Bearing of Twin Pole (°)	Plunge of Twin Pole (°)	Dip Direction to Stage	Number Thin Twins	Thickness Thin Twins	Number Thick Twins	Inner Thickness Thick Twins	Grain Width Perpendicular to Twins (μ)
1	70	2	4	47	3	1	10	2	0	0	275
2	70	2	4	93	0.5	1	12	2	0	0	265
3	354	13	4	22	20.5	3	18	2	0	0	810
4	13	15	2	41	15	1	41	2	0	0	400
5	66	8	4	39	14	3	4	2	0	0	85
6	353	3	4	329	4	3	14	2	0	0	790
7	144	11	4	170	9.5	1	17	2	0	0	540
8	136	4	4	164	6	3	14	2	0	0	760
9	210	3	2	185	0.5	3	7	2	0	0	530
10	210	3	2	231	7	3	19	2	0	0	560
11	108	2	4	81	7	3	23	2	0	0	500
12	108	2	4	130	13	3	21	2	0	0	520
13	352	7	2	17	7	3	31	2	0	0	930
14	352	7	2	331	3	1	29	2	0	0	800
15	42	4	2	18	7	3	12	2	0	0	290
16	42	4	2	65	0.5	1	10	2	0	0	260
17	91	4	2	68	22	1	5	2	0	0	360
18	6	20	4	30.5	24	1	5	2	0	0	260
19	68	3	2	41	11	3	24	2	0	0	450
20	50	11	4	24	24	1	15	2	0	0	230
21	79	10	4	109	10	1	24	2	0	0	540
22	267	9	4	244	2	1	20	2	0	0	230
23	160	4	4	137	4	3	27	2	0	0	720
24	160	4	4	175	30	1	44	2	0	0	740
25	56	2	4	32	15	3	59	2	0	0	1000

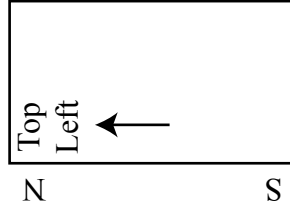


Figure 2-3: Orientation of bedding and interpreted unit boundaries superimposed on hill-shaded LiDAR imagery. With data from Norris (1993), Langenberg et al. (2007) and Snyder (2011). Cross-section A-A', B-B' and C-C' showing the subsurface structure in natural scale.

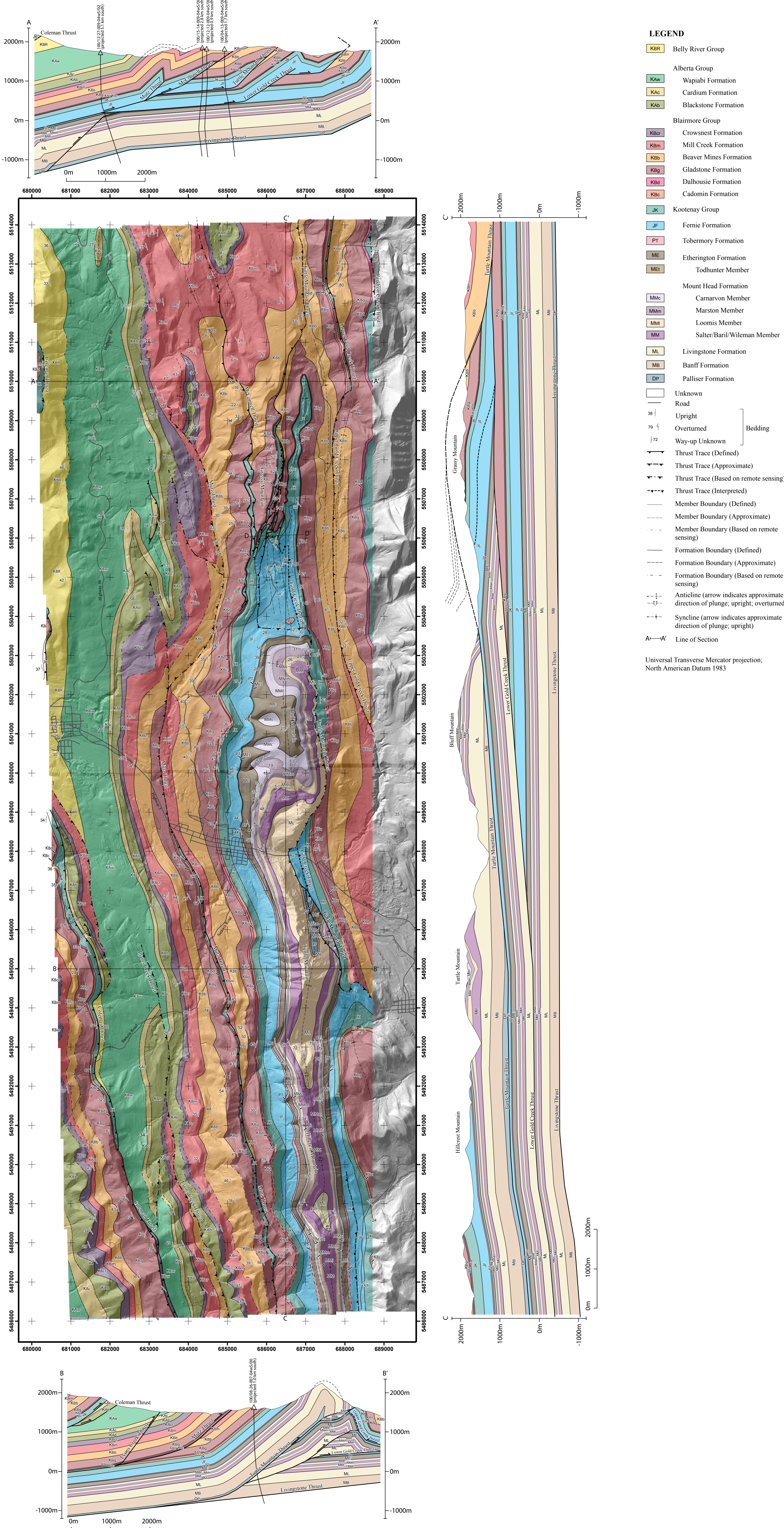


Figure 2-5: Lineaments traced and superimposed on hill-shade LiDAR imagery.

